

Determination of Residual Stress in Components Manufactured using Laser Powder Bed Fusion (L-PBF)

This thesis is submitted in accordance with the requirements of

The University of Liverpool for the degree of

Doctor in Philosophy

by Rodrigo Magana Carranza

December 2020



UNIVERSITY OF
LIVERPOOL

Declaration

I hereby declare that except where specific reference is made to the work of others, the contents of this dissertation are original and have not been submitted in whole or in part for consideration for any other degree or qualification in this, or to any other university. This dissertation is my own work and contains nothing which is the outcome of work done in collaboration with others.

Rodrigo Magana Carranza

December 2020

Abstract

The research reported in this thesis focuses on understanding the development of residual stresses in the Laser Powder Bed Fusion (L-PBF) process. All Laser Powder-Bed Fusion (L-PBF) parts contain residual stresses because of the high energy input, and the rapid heating and cooling rates of the part throughout the manufacturing process. The process parameters used for the L-PBF process affect the development of the residual stresses in the components significantly generating deformation leading to critical distortion and structural failure of the parts during manufacturing or in service. The aim of this research is to understand the complex evolution of residual stresses in the L-PBF process through the use of in-situ measurements and to understand the effect of the process parameters and process-material relationship on the development of residual forces, from which residual stresses can be inferred, with the use of a Force Transducer Device (FTD).

With the experimental work presented in this thesis, it has been demonstrated that in-situ measurements give a good understanding of the complex evolution of residual stresses in the L-PBF process which are difficult to obtain by post-process methods. The in-process measurements revealed the interlayer forces developed in the L-PBF process, which provide a successful way to understand the effect of the material properties and process parameters on the development of residual stresses. The results presented in this thesis showed that residual forces developed in the build vary depending on the process parameters used and on the material properties of the metal powder being used.

A study of the effect of the process parameters on the development of residual stress was conducted, where different scan strategies were analysed. Amongst Stripe, Meander and Chessboard, Meander had the lowest residual force development with 40% less than in the Stripe scan strategy for different metal powders. The effect of the energy density was also tested. A variation from the exposure time from 60 μs , 70 μs and 80 μs showed that for higher energy input higher the residual stresses developed in the L-PBF samples; however, induced porosity for lower energy input can affect the mechanical properties of the final part.

The experimental work reported in this thesis showed the important influence that material properties of the different metal powders have on the development of residual forces in the L-PBF process, which has not been previously studied in the literature. The process parameters and process conditions used in L-PBF were shown to have different effects for

different metal powders. These differences could be related to a specific property of each metal alloy; however, it was difficult to correlate the development of residual stresses to a particular material property. Material properties, such as the phase transformation, were shown to have an effect on the forces developed and part distortion in the L-PFB process. From four tested metal powders, Maraging steel was shown to develop much lower residual forces during the process (over 50%) compared to the rest of the metals tested; this could be due to the low phase transformation upon rapid cooling from austenite (α') to martensite (γ) of the Maraging steel. The phase transformation for Maraging steel leads to volumetric expansion during cooling, which subsequently results in a reduction of the residual stresses.

Process parameters such as the gas used as the inert atmosphere in the L-PFB chamber affected the strains developed in the process and the part deformation of the final component for Maraging steel samples, which has not been previously reported in the literature. Results showed that Maraging steel samples exhibited deformation that was the inverse of the deformation observed in the samples from the other metal powders when using Argon (Ar) gas to create the inert atmosphere; however, the use of Nitrogen (N_2) gas in Maraging steel changed the direction of the part deformation after releasing the samples from the base plate, this could be because Nitrogen (N_2) works as a martensite stabilizer retaining the austenite transformation.

Acknowledgements

The author would like to thank everyone who has supported this research project, in particular, Professor Chris Sutcliffe, Professor Eann Patterson, and the Renishaw Additive Manufacturing Product Division members for their invaluable supervision and guidance. Thanks, are also given to all the technical members of staff at the University of Liverpool whom have provided guidance in the design and manufacture of the experimental equipment. I would like to thank CONACyT Mexico and Renishaw for their financial support for this project. Finally, to all my friends and family for their love, patience and constant support over this time.

Contents

Declaration	i
Abstract	i
Acknowledgements.....	i
Contents.....	i
Figures.....	i
Tables	i
Nomenclature.....	i
1 Introduction.....	1
1.1 Applications of L-PBF.....	6
1.2 Motivation.....	10
1.3 Aims and Objectives	12
1.4 Experimental Plan.....	13
1.5 Thesis Structure.....	15
1.6 List of publications.....	16
2 Literature Review.....	17
2.1 Background of Additive Manufacturing (AM) and Powder Bed Fusion (PBF)	17
2.2 Materials in L-PBF and their Applications.....	24
2.2.1 Steel and Iron-based Alloys	24
2.2.2 Titanium and Titanium Alloys	25
2.2.3 Nickel-based Superalloys.....	26
2.3 Development of Residual Stress in L-PBF	27
2.3.1 Thermal Gradient Mechanism.....	29
2.3.2 Thermal Contraction.....	30
2.3.3 Theoretical Model	30
2.4 Measurement Techniques of Residual Stress in L-PBF	35
2.4.1 Destructive and Non-destructive Methods	36
2.4.2 In-process Measurements of Residual Stress in PBF	43
2.5 Methods to Model and Predict Residual Stress in PBF	47

2.6	Process dependence on Residual Stress.....	51
2.6.1	Process Parameters and Material Properties	53
2.6.2	Scanning Parameters.....	58
2.7	Knowledge Gap in Literature.....	62
3	Materials and Methods.....	64
3.1	Materials Used	64
3.1.1	Ti-6Al-4V ELI-0406 Alloy	64
3.1.2	Inconel 625-0404 Alloy.....	65
3.1.3	Inconel 718-0405 Alloy.....	65
3.1.4	Maraging Steel M300.	66
3.2	Manufacturing Equipment	66
3.2.1	Manufacturing Process.....	69
3.2.2	Scanning Parameters.....	72
3.3	Software Packages.....	75
3.3.1	Creo 5.0 (PTC, USA)	75
3.3.2	QuantAM 4.1.0.76 (Renishaw, UK)	75
3.3.3	ImageJ/FIJI 1.48 (National Institute of Health, US)	75
3.3.4	InstruNet World Plus v3.7 (GW Instruments, US).....	75
3.3.5	Abaqus Student Edition 2017 (Dassault Systèmes, France).....	76
3.3.6	ExaSIM v2.2 (Ansys Inc., US).....	76
3.3.7	Conform Surfaces 1.2 (University of Liverpool, UK).....	76
3.4	Measurement Equipment	76
3.4.1	Image Correlation System Q-400 (Dantec Dynamics, DNK).....	76
3.4.2	Instron® 5984 tensile testing machine (Instron, USA)	77
3.4.3	SEM JOEL JSM 7001f (Joel Ltd, U.K.).....	77
3.4.4	SmartScope® ZIP 300 (OGP, UK)	77
3.5	Measurement Methods	77
3.5.1	Melt pool and Microstructure Analysis	77
3.5.2	Relative Density of Solids.....	78
3.5.3	Tensile Testing.....	79

3.5.4	Part Deformation after Removal	79
3.5.5	In-situ Measurements of Strains Developed in L-PFB.....	80
3.6	Experimental Arrangements.....	95
3.6.1	Effect of the Processing Parameters on Residual Stress and Part Deformation using Ti-6Al-4V	96
3.6.2	Effect of the Material Properties and Processing Parameters using Nickel-based Alloys.....	101
3.6.3	Melt Pool Characteristics.....	102
4	Experimental Results.....	105
4.1	Effect of Processing Parameters on Residual Stress and Part Deformation for Ti-6Al-4V	105
4.1.1	Effect of the Laser Power	106
4.1.2	Effect of the Scan Strategy and Layer Thickness.....	113
4.1.3	Analysis of the Part Deformation.....	128
4.2	In-situ Measurements of Developed Strains in L-PFB for Nickel-based Super Alloys: Inconel 625, Inconel 718 and Maraging Steel.....	131
4.2.1	Effect of the Scan Strategy	131
4.2.2	Effect of the Metal Alloy.....	133
4.2.3	Effect of the Inert Gas Atmosphere.....	137
4.2.4	Effect of the Energy Density	144
4.3	Melt Pool Characteristics.....	148
4.3.1	Three-dimensional Optical Measurements	149
4.3.2	Section Measurements.....	152
5	Discussion	168
5.1	Experimental Results.....	169
5.1.1	Effect of the processing parameters for Ti-6AL-4V.....	169
5.1.2	Effect of the Material Properties	174
5.1.3	Effect of the inert gas atmosphere.....	176
5.1.4	Effect of the Energy Density	177
5.1.5	Melt pool characteristic.....	179

5.2	Proposal Design for High-Temperature FTD.....	180
6	Conclusions.....	184
	List of contributions to knowledge:	186
	Future Work	187
7	References.....	189
	Appendix 1.....	203
	Appendix 2.....	214

Figures

Figure 1: Classification of metal AM processes (adapted from [18]).....	3
Figure 2: Operating principle of the Laser Powder Bed Fusion (L-PBF) process (from [9]).....	4
Figure 3: SEM micrograph of the CoCr-01 alloy powder (from [24]).....	4
Figure 4: Metal Additive Manufacturing (AM) leading companies (from [14])	6
Figure 5: 3D Printer engine fuel nozzle used for the LEAP-1C jet engine [34].....	8
Figure 6: Comparison of front axle differential using traditional manufacturing vs metal 3D printed part [33].....	8
Figure 7: Experimental plan flow chart Phase 1 using Ti-6Al-4V and Phase 2 using Nickel based alloys	14
Figure 8: Classification of Additive Manufacturing Technologies (from [2]).....	18
Figure 9: Schematic principles from the different AM processes: a) Stereolithography (SL) process (from [52]), b) Laminated Object Manufacturing (LOM) process (from [53]), c) Fused Deposition Modelling FDM (from [54]) and d) Selective Laser Sintering (SLS) process (from [55])	19
Figure 10: SLM 500HL machine multi-laser technology and schematic of the multi laser system (from [57] and [58]).....	21
Figure 11: Definitions of the axes and planes discussed with respect to the build layers (from [59]).....	22
Figure 12: AM applications timeline (from [64]).....	23
Figure 13: Research publications on materials for L-PBF (from [42])	24
Figure 14: Classification of residual stresses into three length scales (adapted from [90]) ...	27
Figure 15: Effects of RS in L-PBF Parts. a) reduced fatigue properties, b) distortion upon removal, and c) potential failure in the process (from [90]).....	29
Figure 16: Thermal Gradient Mechanism (a) and constrained contraction effect (b) in L-PBF process (from [95]).....	30
Figure 17: Development of residual stress due to solid contraction (from [44]).....	31
Figure 18: Simplified Theoretical Model of the L-PBF Process [46]	31
Figure 19: Inter-layer thermal boundary effect on the microstructure of an L-PBF 316L part (from [97])	34
Figure 20: Stress distribution obtained via the contour method where Z is the build direction (from [103]).....	35

Figure 21: MTS3000 RESTAN (REsidual STress ANalyzer) system by SINT Technology positioned on the construction platform with the samples (from [108]).....	37
Figure 22: Residual stress hole-drilling measuring device (from [109]).....	38
Figure 23: T-Shaped cantilever deformation method proposed by Zaeh and Branner (from [95]).....	39
Figure 24: BCM proposed by Kruth et al. [111] in which the curvature of the part is measured (a) before and (b) after removal from the base plate	39
Figure 25: Schematic of the neutron diffraction method (from [108])	42
Figure 26: In-situ measurement system for strain and temperature evolution by Van Belle [47]	44
Figure 27: Experimental arrangement for measuring the developed strains in the substrate by Shiomi et al. [45]	44
Figure 28: Strain Increment in model and base plate by removal of the top layer (from [45])	45
Figure 29: Experimental set-up for in-situ distortion measurements using a DVRT proposed by Dumbar et al. [48]	45
Figure 30: The Force Transducer Device (FTD), developed by Robinson [from 119] for in-situ measurements.	46
Figure 31: Temperature distribution during laser sintering of powdered INOX 316L stainless steel: Region 1 is the melt isotherm, 1450 °C. (from [123])	47
Figure 32: Schematic of the heat transfer conditions during L-PBF process (from [124]).....	48
Figure 33: Simulation schematic of L-PBF proposed by Fu and Guo (from [148])	50
Figure 34: Final temperature and residual stress distribution for interlayer effect simulation (from [95])	51
Figure 35: Process parameters that affect residual stress formation in L-PBF (adapted from [90]).....	52
Figure 36: Functionality of input factors and output parameters for the L-PBF process (adapted from [149])	53
Figure 37: Process window of L-PBF zones for Ti-6Al-4V (from [150])	54
Figure 38: Formation of layer single track in L-PBF, where: 1 - Laser Beam; 2 - Single Track Bead; 3- Loose Powder Material Layer; 4- Base or Previous Layer; l - Melt Pool; m - Track Width; n- Powder Consolidation Area[149]	55

Figure 39: SEM showing the balling effect of single scan tracks occurred while using lower laser powers (70-110 W), while the scan tracks are continuous for higher laser power (150-190 W) (from [156])	56
Figure 40: Schematic of the patterns of heat flow in a thin wall sample when the melt pool is (1) in the middle of the top edge and (2) when it is at the side edge of a thin wall plate (from [102])	57
Figure 41: Schematic of four different scanning strategies used in the L-PBF process (from [165])	59
Figure 42: Schematic representation of the Island scan strategy (from [59])	60
Figure 43: Sector size and orientation of used scan strategy by Yasa and Evren (from [167])	61
Figure 44: Treatment strategy classification according to laser treatment type in L-PBF (from [149])	62
Figure 45: a) Renishaw AM250 L-PBF machine and b) inside view from the build chamber..	67
Figure 46: Renishaw AM250 laser beam profile	67
Figure 47: Focal point at datum plane (from [169])	68
Figure 48: Schematic of a Renishaw AM250 L-PBF system	69
Figure 49: Definition of a layer through the intersection between the 3D STL model and a slicing plane (from [2])	73
Figure 50: Description of scan strategies used in L-PBF (adapted from [169])	73
Figure 51: Schematic of the laser scanning point exposure and hatch distance (adapted from [169])	74
Figure 52: Schematic of scanning parameters used in the L-PBF process	74
Figure 53: Melt pool characteristics for laser-powder interaction for single beads	78
Figure 54: Geometry of tensile test specimens (dimensions in mm)	79
Figure 55: DIC Setup for part deformation measurements (top and bottom left). FTD sample with speckles with white and black paint to the surface of the part (bottom right).	80
Figure 56: Loads registered by each load cell based on 5kg increments of load: (a) before calibration; and, (b) after calibration	83
Figure 57: FTD substrate design for in-situ measurements	84
Figure 58: Single array load cell FTD1	85
Figure 59: Cross-section of the FTD1 assembly	86
Figure 60: FTD 14 load cell arrangement for a rectangular part geometry (measurements are in mm)	87

Figure 61: FTD2 for in-situ measurements in the L-PBF process	87
Figure 62: Cross-section of the FTD2 assembly	88
Figure 63: Schematic of the square build geometry for the FTD2 (measurements in mm) ...	89
Figure 64: Loads registered by each load cell for FTD2 based on 5kg increments of load:) before calibration (top); and, after calibration (bottom)	90
Figure 65: FTD setup into the Renishaw AM250 L-PBF machine	91
Figure 66: CAD of the substrate used for the modified FTD used for in-situ measurements.	92
Figure 67: Load cell wiring fed through the overflow compartment into the InstruNet data loggers.....	92
Figure 68: Load cell wiring arrangement into three InstruNet100i for data acquisition	93
Figure 69: Process of a part being built on the Renishaw AM250 machine with the use of the FTD	94
Figure 70: Lattice structure used for the pyramid section	98
Figure 71: Scan strategies tested for the rectangular part geometry on the FTD1. (a) Stripe scan strategy with 67° rotation, (b) Stripe scan strategy with all X scan vectors, (c) Stripe scan strategy with all Y scan vectors, (d) meander scan strategy with 67° rotation, and (e) Chessboard scan strategy with 67° rotation.....	100
Figure 72: Schematic of the rectangular based where 12 single beads are scanned on the top surface (measurements are in mm) showing the width, height and depth measurements made for a single bead (bottom right). Parameters used for the single beads are shown in Table 13	103
Figure 73: FTD2 In-situ measurement results from sample S1 (see Table 8) built with: laser power 200W, Stripe scan strategy and solid pyramids section	107
Figure 74: Surface profile showing the curl effect from the measured forces for Figure 68 at the end of the build for sample S1 (see Table 8 for more details)	107
Figure 75: Contour plots of measured forces at layers (a) 10, (b) 50 and (c) 100 for a square sample (S1), shown in Figure 73. Using a Stripe scan strategy and a 30µm layer thickness (see Table 8 for more details).	108
Figure 76: Comparison of the sum of the absolute resultant force of the corner and centre load cells per layer for Sample S1 built using the Stripe scan strategy with a 30µm layer thickness.....	109
Figure 77: Effect of laser power and support structure on forces induced during the build process using a Stripe Scan Strategy. See Table 8 and Table 9 for details of specimens.....	110

Figure 78: Contour plots of force at the end of each build for square samples S1 to S6 with the use of Stripe scan strategy and a laser power variation from 200 W to 160 W. Using a solid base (S1-S3) and lattice structure base (S4-S6). See Table 8 for further details.....	111
Figure 79: Density results and micrographs from Samples S1, S2 and S3, built using different levels of laser power shown in Table 8.....	112
Figure 80: In-situ measurements for a rectangular part built on the FTD1 with a Stripe scan strategy for specimen S7, see Table 10 for details	114
Figure 81: Curl-up of specimen S7 (see Table 10) following release from the build platform as previously studied by Thomas [170] in his thesis work	114
Figure 82: Comparison of measured forces for the front and back rows of the FTD1 for a rectangular part for Sample S7. More details can be seen in Table 8	115
Figure 83: Results from In-situ force measurements using FTD1 for a rectangular part using three scan strategies: Rotating 67° per layer (Sample S7), Stripe all-X (Sample S8) and all-Y scan strategies (Sample S9)	115
Figure 84: Contour plots of force at the end of each build for rectangular samples S7, S8 and S9 shown in Figure 79 using (a) Stripe 67° rotation scan strategy, (b) scan vector with all X orientation, and (c) scan vector in all y orientation. See Table 7 for further details.....	116
Figure 85: Development of forces in each layer for different scan strategies for Samples S7, S8 and S9, see Table 10 for details.....	117
Figure 86: In-situ Measurements of the sum of the measured forces (N) per layer for rectangular parts built with the Stripe (S7), Chessboard (S10), and Meander strategies (S11) and a layer thickness of 30 µm, see Table 10 for details.	118
Figure 87: Contour plots of force at the end of each build for rectangular samples S7, S10 and S11, using a 30 µm layer thickness and different scan strategies (a) Stripe (b) Chessboard, and (c) Meander. See Table 10 for details.....	119
Figure 88: Sum of absolute measured forces for the first 15 layers of the rectangular part built using the Stripe (S7), Chessboard (S10) and Meander (S11) scan strategies with a layer thickness of 30 µm, see Table 10 for details.	120
Figure 89: In-situ Measurements Resultant Forces (N) per Layer. Comparison of Stripe S12, Chessboard S13 and Meander S14 scan strategies used to build square parts with 30 µm layer thickness showing the sum of the absolute forces registered from FTD2. See Table 10 for details.....	122

Figure 90: Contour plots of force at the end of each build for square samples S12, S13 and S14. Samples built using a 30 μm layer thickness and different scan strategies (a) Stripe, (b) Chessboard and (c) Meander. See Table 7 for details.	123
Figure 91: Sum of absolute values measured in the first 15 layers of squared parts built using Meander, Stripe and Chessboard scan strategies with 30 μm layer thickness. See Figure 89 for complete build and Table 10 for details of the parts and build parameters.	124
Figure 92: Sum of absolute values measured in squared parts built using Stripe (S15) and Meander (S16) scan strategies with 60 μm layer thickness. See Table 10 for details of the build parameters.	125
Figure 93: Contour plots of force at the end of each build for square samples S15 and S16 built using a 60 μm layer thickness and different scan strategies (a) Stripe and (b) Meander. See Table 7 for details.	125
Figure 94: Effect of layer thickness on residual forces for (a) Stripe and (b) Meander scan strategies. See Table 10 for further details.	126
Figure 95: Comparison of build height among the different scan strategies and layer thickness for the squared samples.	127
Figure 96: Sequence for the part removal from the FTD1 for DIC measurements for part deformation	128
Figure 97: Results from DIC measurements for out of plane distortion when the bolts are removed from the FTD1 in the sequence shown in Figure 88 for Sample 7 (see Table 10) for details. Note that no data was collected when the final set of bolts were removed.	128
Figure 98: DIC measurements of part deformation after removal for different scan strategies and layer thicknesses for Ti-6Al-4V square samples (S12-16), see Table 10 for details	130
Figure 99: In-situ measurements of the forces developed for a square part built using the Stripe scan strategy using Inconel 625. Data for Sample S17, see Table 11 for details.	132
Figure 100: Comparison of the sum of measured forces for the Stripe and Meander strategies using Inconel 625 to build square samples (Samples 17 and 18), see Table 11 for details. .	132
Figure 101: Contour plots of force at the end of each build for Samples S17 and S18 built using a 60 μm layer thickness and different scan strategies a) stripe and b) Meander. See Table 11 for details.	133
Figure 102: In-situ measurements of the sum of the forces for square parts built with Stripe scan strategy in various materials. Data for samples S15, S18, S19 and S20 shown, see Table 10 and Table 11 for details.	134

Figure 103: Contour plots of force at the end of each build, from Figure 102, for square parts using a 60 μm layer thickness and different metal powders (Samples S15, S17, S19 and S20). See Table 10 and Table 11 for details.....	134
Figure 104: Dilatometer curve for the longitudinal direction of 18% Maraging steel from -196 $^{\circ}\text{C}$ to annealing temperature (adapted from Kranzlein [184]).....	135
Figure 105: In-situ Measurements of forces developed for Sample S20 built in Maraging Steel with the Stripe Scan Strategy, see Table 11 for details.	136
Figure 106: Contour plots of force from Figure 101, (a) at the end of the build at layer 100 and (b) after the part cools down for squared Sample (S20) built using Maraging steel and using the Stripe scan strategy. See Table 11 for details.....	136
Figure 107: DIC Measurements of out of plane displacement (top) (positive towards the laser) and along diagonal (bottom) in Sample S20 built using the Stripe strategy and using Maraging steel, see Table 11 for further details.....	137
Figure 108: Results from the in-situ measurements for a square part built with a Stripe strategy in Maraging steel with the inert gas atmosphere of Nitrogen. Data is shown for Sample S21, and further details are given in Table 11.....	138
Figure 109: Contour plots of force at the end of each build for square parts before cooling down using Maraging steel with a variation of the inert gas using Argon (S20) and Nitrogen (S21) gas. Samples built using the Stripe scan strategy and a 60 μm layer thickness. See Table 11 for details.	138
Figure 110: Comparison of the Sum of forces measured in square parts built using Maraging steel using N_2 and Ar as the inert gas atmosphere. Data is shown for parts S20, S21 and S22. For which further details can be found in Table 11.....	139
Figure 111: Contour plots of force after the part cools down from Figure 106, for square parts built using Maraging steel Samples S20, S21 and S22. Samples built using a 60 μm layer thickness and different scan strategies a) and b) Stripe and c) Meander. See Table 11 for details.	140
Figure 112: Effect on the part deformation after removal of the inert gas atmosphere for Maraging Steel samples showing DIC results (top) and displacement along a diagonal (bottom) using data from samples S20 and S21 built using the Stripe Scan Strategy, for further details see Table 11.	141
Figure 113: Effect on the part deformation after removal for square parts built using Maraging Steel and the Meander scan strategy showing DIC results (top) and displacement along a diagonal (bottom) for sample S22, see Table 11 for further details.....	142

Figure 114: In-situ measurements for forces in the sample build with Stripe strategy in Inconel 625 with an Inert Atmosphere of Nitrogen. Data for sample S23 Table 11 for details.....	143
Figure 115: Out of Plane displacement from DIC (left) and micrographs showing porosity and relative density (right) for square parts (S18, and S23) built using the Stripe scan strategy from Inconel 625 metal powder using N ₂ and Ar as the inert gas. See Table 11 for more details.	143
Figure 116: Contour plots of force at the end of each build for square samples S24, S25 and S26. Samples built using the Stripe scan strategy and a 60 μm layer thickness with a variation of point distance from 60 μm to 80 μm. See Table 12 for details.	144
Figure 117: In-situ measurements of resultant forces developed in samples S24, S25 and S26 with variation in point distance (PD) built using Stripe strategy using Inconel 625 metal. Details for the square parts can be found in Table 12.	145
Figure 118: Bulk density as a function of volumetric energy density in square parts built using Stripe scan strategy.	145
Figure 119: Micrographs showing porosity on a function of point distance in density cubes parts built using Stripe scan strategy in Inconel 625 metal. Details for relative density and volumetric energy density are shown and further details can be found in Table 12	146
Figure 120: Out of plane displacement map from DIC for square parts with different point distances built using stripe scan strategy in Inconel 625 as detailed in Table 12; together with numerical results (Top).....	147
Figure 121: Tensile stress results from samples with different point distance, see Table 12 for more details.	148
Figure 122: Alicona Infinite Focus image of the surface for a single bead of Ti-6Al4V built with no powder (No.12 in Table 18) (top) and for the single bead (No.12 in Table 19) with powder (bottom), see Table 13 for more details.....	149
Figure 123: Optical Micrograph (top) for a single bead of Ti-6Al4V built with powder (No.12 in Table 19) and the corresponding height across the marked section (bottom) from which the height of the bead was evaluated.	150
Figure 124: Optical Micrograph (top) for a single bead of Ti-6Al4V built with no powder (No.12 in Table 18) and the corresponding height across the marked section (bottom) from which the height of the bead was evaluated.	150
Figure 125: Cross-section of samples showing the melt pool geometry of single beads built using Ti-6Al-4V without powder and with different laser power (vertically) and for exposure times of 40 μs (left), 50 μs (middle) and 100 μs (right). The details of the beads are described in Table 13.....	153

Figure 126: Cross-section samples showing the melt pool geometry of single beads built using Ti-6Al-4V with powder and with different laser power (vertically) and for exposure times of 40 μs (left), 50 μs (middle) and 100 μs (right). The details of the beads are described in Table 13.	154
Figure 127: Comparison of measurements results shown in Table 20 from the height, width and depth of single beads built using Ti-6Al-4V with one 30 μm layer of powder with different laser power and exposure times, see Table 13 for more details.	155
Figure 128: Comparison of measurements results shown in Table 21 from the height, width and depth of single beads built using Ti-6Al-4V with one 30 μm layer of powder with different laser power and exposure times, see Table 13 for more details.	156
Figure 129: SEM images showing the melt pool geometry for single beads built using Ti-6Al-4V with powder and different laser power and for exposure times of 40 μs (left) 50 μs (middle) and 100 μs (right). The details of the beads are shown in Table 19.	157
Figure 130: SEM images showing the melt pool geometry for single beads built without powder and different laser power and for exposure times of 40 μs (left) 50 μs (middle) and 100 μs (right). The details of the beads are shown in Table 19.	158
Figure 131: Cross-section samples showing the melt pool geometry of single beads built using Inconel 625 and built without powder and with different laser power (vertically) and for exposure times of 40 μs (left), 50 μs (middle) and 100 μs (right). The details of the beads are described in Table 13.	160
Figure 132: Cross-section samples showing the melt pool geometry of single beads built using Inconel 625 and built with powder and with different laser power (vertically) and for exposure times of 40 μs (left), 50 μs (middle) and 100 μs (right). The details of the beads are described in Table 13.	161
Figure 133: Cross-section samples showing the melt pool geometry of single beads built using Maraging steel and built without powder and with different laser power (vertically) and for exposure times of 40 μs (left), 50 μs (middle) and 100 μs (right). The details of the beads are described in Table 13.	162
Figure 134: Cross-section samples showing the melt pool geometry of single beads built using Maraging steel and built with powder and with different laser power (vertically) and for exposure times of 40 μs (left), 50 μs (middle) and 100 μs (right). The details of the beads are described in Table 13.	163
Figure 135: Cross-section samples showing the melt pool geometry of single beads built using Maraging steel with Nitrogen as Inert gas; built without powder and with different laser power	

(vertically) and for exposure times of 40 μs (left), 50 μs (middle) and 100 μs (right). The details of the beads are described in Table 13.	164
Figure 136: Cross-section samples showing the melt pool geometry of single beads built using Maraging steel with Nitrogen as Inert gas; built with powder and with different laser power (vertically) and for exposure times of 40 μs (left), 50 μs (middle) and 100 μs	165
Figure 137: Comparison of measurements results shown in Table 22 from the height, width and depth of single beads built using one 60 μm layer of powder with a laser power of 200 W and an exposure time of 100 μs using different metal powders, see Table 13 for more details.	167
Figure 138: Comparison of measurements results shown in Table 23 from the height, width and depth of single beads built without powder with a laser power of 200 W and exposure time of 100 μs using different metal powders, see Table 13 for more details.	167
Figure 139: Absolute total measured force (N) from in-situ measurements for a square part in Ti-6Al-4V as a function of laser power (W), from samples S1, S2 and S3, shown in Figure 73.	173
Figure 140: Relationship of measured force to material properties: yield strength, thermal conductivity, ultimate tensile strength and thermal expansion for the different metal powders tested.	174
Figure 141: Dimensional part geometry change due to the phase transformation for Maraging steel.	175
Figure 142: SEM image showing the microstructure of the melt pool boundary from (left) sample with Argon gas (S20) and (right) from sample using Maraging steel with Nitrogen gas (S21) inert atmosphere.	176
Figure 143: Schematic of the formation process of microstructure in the Maraging steel during L-PBF (from [173])	177
Figure 144: Total measured force vs Energy density from samples with a point distance (PD) variation	178
Figure 145: SEM images of the melt pool characteristics with energy input variation from 51.94 J/mm^3 (top left), 57.72 J/mm^3 (top right), and 115.44 J/mm^3 (bottom) for Ti-6Al-4V samples showing porosity in the sample due to lack of fusion (top left), dense melt pool heat conduction (top right) and keyhole porosity (bottom).	178
Figure 146: Design of FTD3 for higher temperatures and greater load capacity.	181
Figure 147: Cross-section of the FTD3.	182
Figure 148: Part geometry for In-situ residual force measurements for the FTD3	182

Figure 149: Scan strategies to achieve a lower thermal gradient to be used in the FTD3.... 183

Tables

Table 1: Residual stress measuring techniques (adapted from [92, 105]).....	36
Table 2: Ti-6Al-4V ELI-0406 alloy material properties	65
Table 3: Inconel 625-0404 alloy material properties.....	65
Table 4: Inconel 718-0405 alloy material properties.....	66
Table 5: Maraging Steel M300 alloy material properties	66
Table 6: Renishaw AM250 Machine Specifications	68
Table 7: In-process measurements used to estimate or infer residual stresses during the L-PBF process	81
Table 8: Build parameters for consideration of the effect the laser power on residual stress	97
Table 9: Lattice structure build parameters	98
Table 10: Build parameters used for Ti-6Al-4V samples built on a Renishaw AM250 machine for a part density greater than 99.9%	100
Table 11: Renishaw AM250 build parameters for Nickel-based superalloys.....	103
Table 12: Parameters with a variation of the point distance for Inconel 625	104
Table 13: Single beads build parameters.....	104
Table 14: Results from the measured forces from the samples with laser power variation S1 to S6.	112
Table 15: Scanning time (in seconds) per layer (L1-L16 for samples S7, S10 and S11) with a rectangular geometry (see Table 10 and Figure 72 for more details)	121
Table 16: Scanning time (in seconds) per layer (L1-L16) for samples with square geometry see Table 10 and Figure 91 for details.	124
Table 17: Results from DIC measurements of square parts after removal.....	129
Table 18: Results from the measurements of the top surface for single beads without powder built using Ti-6Al-4V	152
Table 19: Results from the measurements of the top surface for single beads with powder built using Ti-6Al-4V	152
Table 20: Results from the measurements of height, width and depth for single beads without powder built with different laser power and exposure times (see Table 13) obtained from the micrographic sections from Figure 125.....	155

Table 21: Results from the measurements of height, width and depth for single beads with one 30 μm layer of powder built with different laser power and exposure times obtained from the micrographic sections from Figure 126.....	156
Table 22: Results from the measurements of height, width and depth for single beads with one 60 μm layer of powder built with different laser power and exposure times obtained from the micrographic sections from Figure 132, Figure 134 and Figure 136.	166
Table 23: Results from the measurements of height, width and depth for single beads without powder built with different laser power and exposure times obtained from the micrographic sections from Figure 127, Figure 129, and Figure 131.	166
Table 24: High-temperature load cell availability.....	181

Nomenclature

Roman Symbols

Ed	Energy Density	J/mm ³
P	Laser Power	W
PD	Point Distance	μm
ET	Exposure Time	μs
HD	Hatch Distance	μm
LT	Layer Thickness	μm
SS	Scan Speed	mm/s
T	Temperature	°C
t	Time	s
UTS	Ultimate Tensile Stress	MPa
RS	Residual Stress	MPa

Greek Symbols

λ	Wavelength	nm
α _y	Yield Stress	MPa
ρ	Density	gcm ⁻³
α'	Martensite	-
γ	Austenite	-
		-

Acronyms

AM	Additive Manufacturing
L-PBF	Laser Powder Bed Fusion
PBF	Powder Bed Fusion
SLA	Stereo Lithography
SLM	Selective Laser Melting
SLS	Selective Laser Sintering
STL	Stereolithography
EBM	Electron Beam Melting
FDM	Fused Deposition Modelling
RP	Rapid Prototyping
CAD	Computer Aided Design
DIC	Digital Image Correlation
FTD	Force Transducer Device
FEM	Finite Element Modelling
DIC	Digital Image Correlation
UV	Ultra Violet
DfAM	Design for Additive Manufacturing
DMLS	Direct Metal Laser Sintering
TGM	Thermal Gradient Mechanism

1 Introduction

Additive Manufacturing (AM) is defined by the ISO/ASTM 52900 [1] as “the process of joining materials to make objects from 3D model data, usually layer upon layer, as opposed to subtractive manufacturing methodologies”. AM techniques produce objects directly from a 3D computer-aided design (CAD) model, which allows the production of more complex geometries than traditional manufacturing methods without the need for additional tooling, reducing manufacturing steps and material waste [2-4]. AM emerged in the 1980s [5, 6] from the term rapid prototyping (RP) with the development of Stereo Lithography Apparatus (SLA), patented by Charles Hull in 1986 [7], which polymerised photosensitive resins bonding thin layers of solid material layer by layer using ultra-violet light [8]. AM has experienced significant growth over the past 30 years; different AM techniques have developed to produce ready to use parts from a wide range of materials (i.e. polymers, ceramics or metals) by consolidating layers in different ways. Some processes use thermal energy from lasers or electron beams directed by optics for melting metallic powders, and others use inkjet-type printing heads to spray binder or solvent onto ceramic or polymer powders. Some AM processes include Fused Deposition Modelling (FDM), Electron Beam Melting (EBM), Selective Laser Sintering (SLS) and Selective Laser Melting (SLM) [2, 3, 9]. Although AM systems produce parts by using different processes i.e. sintering, fusing or polymerisation of materials, each technique has the same principle of producing a final component from the CAD model by the addition of layer upon layer until the 3D part is complete. The implementation of new technologies into the different AM processes have significantly improved the quality of the finished parts and allowed AM to evolve from producing prototypes to fabricating ready to use components by employing new materials, improvements in process parameters and the freedom of design.

Some AM technologies allow the production of nearly full density parts of complex geometries that are difficult to produce with traditional methods, which can reduce production costs by the optimisation of material used and generating less waste. AM parts may be designed and manufactured in ways that would not be possible using traditional methods (e.g. mould casting) allowing the optimization of new designs keeping or even improving the properties of the finished part compared to traditional manufacturing processes. Over recent years, industries such as automotive, aerospace, medical, dental and construction have started to adopt AM processes as their method of manufacturing [10-12]. However, the variations in part quality and mechanical properties of the components due to inadequate dimensional

tolerance, presence of defects, surface roughness and residual stresses, among others, limit its use in high-value applications. While much progress has been made in the development of AM processes the various problems involved from the different AM techniques pose multiple challenges for AM technologies in the desire to produce functional parts, such as improving part quality, lowering production costs, increasing production speed and utilizing new materials [13]. Overcoming these challenges involves the use of computer simulations, post processing tests and in process experimental approaches to assess the accuracy of AM parts.

One of the primary markets for AM is manufacturing metal components. The metal systems and metal powder materials market was worth \$905M in 2016 and is expecting to be worth \$6.6 billion by 2026 [14]. One of the most widely used AM techniques used for the production of high-density metal parts, is Powder Bed Fusion (PBF), it is defined by the ISO/ASTM 52900 [1] as the “additive manufacturing process in which thermal energy selectively fuses regions of a powder bed”. PBF allows the manufacture of metal components of complex geometries directly from a CAD model, selectively melting thin layers of metal powder layer by layer using a scanning energy source. The PBF process includes the following commonly used 3D printing techniques: direct metal laser sintering (DMLS), electron beam melting (EBM), selective heat sintering (SHS), selective laser sintering (SLS) and selective laser melting (SLM).

The two main components of metal AM process are the type of raw material input and the energy source used to consolidate or form the part (see Figure 1). There are different AM processes capable of producing near-net-shape metal components and these can be classified in three major categories; (1) powder bed systems, (2) powder feed systems, and (3) wire feed systems [15]. One of the most widely used and researched methods for metal AM is powder bed fusion (PBF). Two of the most important PBF processes are Electron Beam Melting (EBM) and Laser powder bed fusion (L-PBF), due to their advantages in producing complex functional metallic components rapidly and cost-effectively, and their increasing use for industrial applications in the aerospace and biomedical fields. EBM, commercialised by Arcam, is a PBF process, which uses an electron beam as the heat source to melt metal powder materials in a high vacuum chamber with a typical layer thickness of 100 μm [16]. A key characteristic of EBM is that the powder bed is preheated significantly to reduce the temperature gradient reducing the development of residual stresses compared to L-PBF; however, as the EBM process is more complex and due to the single patent, L-PBF processes have the largest share of the PBF market (82% of the PFB market in 2016) [17].

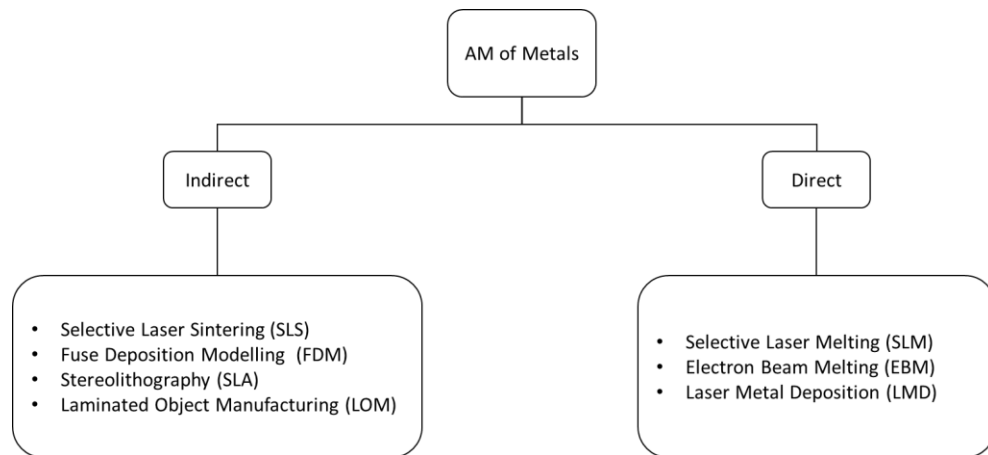


Figure 1: Classification of metal AM processes (adapted from [18])

The focus of this thesis lies within the selective laser melting (SLM) process, also known as laser powder bed fusion (L-PBF). The additive manufacturing technology Selective Laser Melting (SLM) [5], is defined by the ISO/ASTM 52900 [1] as the “powder bed fusion process used to produce objects from powdered materials using one or more lasers to selectively fuse or melt the particles at the surface, layer upon layer, in an enclosed chamber”. SLM emerged in the late 1980s and early 1990s [19] by Dr M. Fockle and Dr D. Schwarze and was a development from the SLS process by raising the temperature of the powder to above its melting point and was patented in 1998 as “SLS at Melting Temperature” [20]. SLS compared to SLM binds powder materials via solid-state sintering or melting of binding agents, resulting in parts with high porosity and low strength. Post-processing is needed to improve the properties of SLS finished parts, such as heat treatment and material infiltration, taking additional time. In the SLM process, the material is completely melted by the use of a high-intensity laser eliminating the need for the binder materials and post-processing required for SLS. The SLM process enables the production of individual metal parts of nearly 100% density relative to cast parts and complex geometries matching the mechanical properties of parts conventionally manufactured without the need for tooling or pre-production costs.

Figure 2 illustrates the operating principle of the L-PBF process. First, the 3D-CAD model is converted into a STereolithography (STL) file, which is defined by the ISO/ASTM 52900 [1] as “a file format for model data describing the surface geometry of an object as a tessellation of triangles used to communicate 3D geometries to machines in order to build physical parts”. The STL file is processed by machine specific software to slice the STL file and generate the data for individual layers, and then the file is transferred into the L-PBF machine. Subsequently,

a defined thin layer of the metal powder material with a spherical grain structure from 10–45 μm (see Figure 3) is deposited and evenly distributed over a substrate in the build chamber. Since the metal powder is the raw material used to produce L-PBF parts powder characteristics, such as spherical particle shape, particle size distribution, close packing of particles and good flow, are very important to achieve a consistent powder dosing through the build process. The two main methods used to create spherical particles for AM metal powder are gas atomisation and plasma atomisation [21-23].

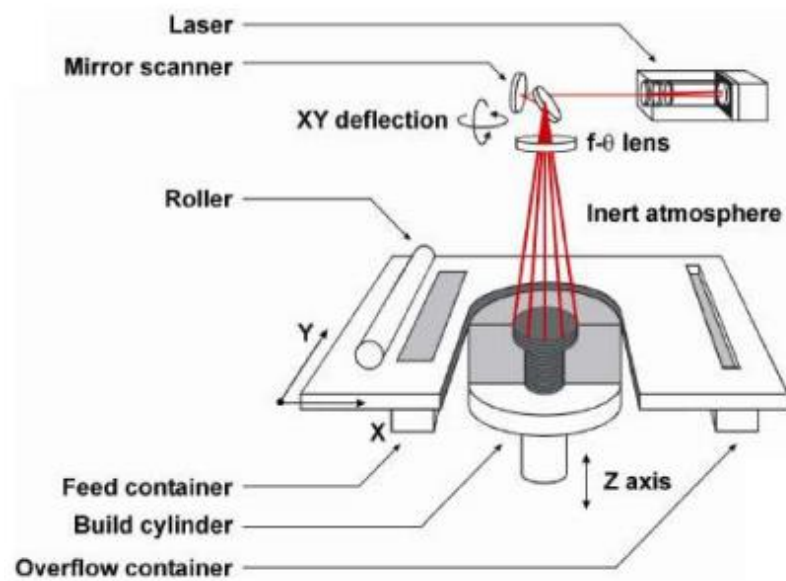


Figure 2: Operating principle of the Laser Powder Bed Fusion (L-PBF) process (from [9])

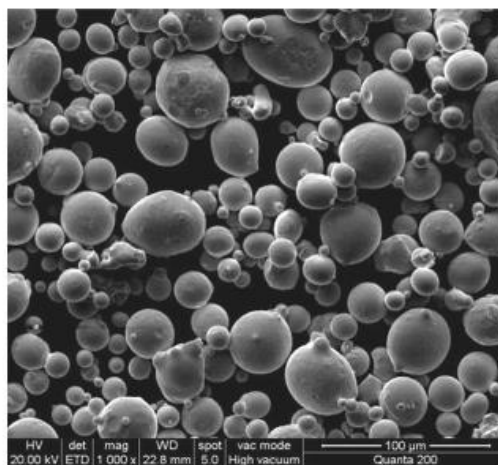


Figure 3: SEM micrograph of the CoCr-01 alloy powder (from [24])

After the powder is spread over the build platform, a single or multiple high-power laser beam selectively melts the desired part geometry using predefined scanning parameters. The geometric information of individual layers is transmitted by the laser beam to the powder bed; where the regions to contain solid material are scanned under an inert atmosphere, commonly, Argon or Nitrogen to avoid oxidation, causing a solid layer of the piece to be produced. During production, the laser executes a scanning or filling strategy. The strategies associated with the laser path are characterized by the length, direction, and separation (point and hatch spacing) of neighbouring scan vectors. After the scanned layer is completed, the build platform is lowered by a defined layer thickness, and the process is repeated until the functional 3D part is finished. When the part is complete, the unfused powder is sieved and can be reused for future builds. Since standard metallic powders are used, which melt completely, the part has a density of approximately of the cast material, thus assuring mechanical properties that match or even exceed those of conventionally manufactured parts [9]. Different materials are available with this technology, such as steel, titanium, aluminium, cobalt-chromium and nickel alloys, among others.

In order to achieve a successfully finished part through the L-PBF process, an optimum design for AM (DfAM) must be achieved by the use of CAD preparation software to select the best orientation and support strategy for each build. Several software packages for solid modelling using CAD have been developed since 2011 allowing the optimisation of both DfAM and material properties for L-PBF processes; as well as the design of complex lattice structures that optimize reductions in material and weight, making the process more cost-effective [25].

AM manufacturing of metal components has expanded extensively in the last three decades within AM techniques such as L-PBF and EBM. The benefits from the freedom of design in metal components to produce ready to use parts of complex geometries have gained significant interest in research and have been adopted by a large number of industries for prototyping and manufacturing purposes. Metal AM technologies could revolutionise many sectors of manufacturing by reducing component lead time, production costs, material waste, energy usage, and carbon footprint [26]. AM of metals is opening up new possibilities for low-cost manufacturing and novel designs that cannot be made using current technologies, state of the art in AM PBF has improved from a rapid-prototyping to production technology.

1.1 Applications of L-PBF

Parts produced through PBF can match or exceed the mechanical properties of parts conventionally manufactured [27], making it widely used as a manufacturing process by industries such as aerospace, automotive and medical engineering [14]. The aerospace and automotive industries continue to find new applications for L-PBF, which offers potentially significant benefits from the manufacture of lightweight parts with unique geometries capable of decreasing material waste and energy consumption [28].

PBF includes the following commonly used 3D printing techniques: direct metal laser sintering (DMLS), electron beam melting (EBM), selective heat sintering (SHS) and laser powder bed fusion (L-PBF). L-PBF and EBM processes being the most important in the metal industry due to the accuracy of the finished part and the wide range of metal powders alloys currently developed for these processes. EBM is very similar to L-PBF but differs in the source of the energy used for melting the powder; EBM uses an electron beam to deliver the melting energy while L-PBF uses laser energy to melt the material. Of these two PBF processes, L-PBF represents the majority of industrial and academic applications [29, 30], this could be due to the more straightforward process of L-PBF technology over EBM and the fact that there is currently only one manufacturer for EBM machines [31], Arcam AB recently acquired by General Electric (GE) [32].

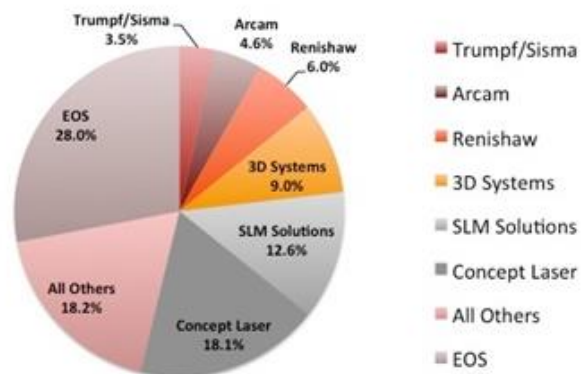


Figure 4: Metal Additive Manufacturing (AM) leading companies (from [14])

Many firms have a share of the L-PBF market and are distributed as shown in Figure 4. The German company, EOS (Electro Optical System), leads with 28% of the 2016 market. Recently,

GE has invested over \$1.4 billion in the acquisition of Arcam AB and SLM Solutions Group AG enabling the company to develop GE Additive, creating new services and applications across the company, and gaining 346 patents in powder metals alone [32]. There is wide interest in future investment in AM technologies to accelerate market adoption due to the potential benefits of metal AM to both the economy and environment. Among many incentives to invest in AM technologies, one of the main advantages has been creating lighter parts through the freedom of design. Which, gives the ability to produce complex geometries allowing the reduction of the part count in an assembly by combining different parts produced using traditional manufacturing methods into a single component. Reducing the part count reduces the weight of the aircraft by eliminating assembly components such as bolts, welds or other interfaces used to attach parts [33].

GE Aviation has adopted metal AM into their process on a significant scale; an example is the use of 3D printed nozzles used in the LEAP-1C jet engine (see Figure 5), which is used as a power plant for the Boeing 737 MAX and Airbus A320neo [34]. The use of the 3D printed nozzles led to a 15% reduction in fuel consumption and CO₂ emissions versus current engines, a 50% cut in NO_x emissions, compliance with the most stringent noise standards and it has been approved by the Federal Aviation Administration (FAA) and the European Aviation Safety Association (EASA) [34]. GE Aviation has also tested a 35% additive manufactured inclusion of metal AM components into an Advanced Turboprop Engine (ATP), which is set to power the all-new Cessna Denali single-engine aircraft and reduced the final weight by enabling the reduction of part numbers. The use of AM also enabled additional freedom in the design of the aircraft, which led to reductions in fuel consumption and CO₂ emissions [35]. GE's ATP uses more additive parts than any production engine in aviation history and reduces 855 subtractive manufactured parts into twelve Additive Manufactured components reducing by 5% the ATP's weight while contributing a 1% improvement in specific fuel consumption. The AM parts include sumps, bearing housings, frames, exhaust case, combustor liner, heat exchangers and stationary flow path components [35]. In 2015 Rolls -Royce announced that it would flight-test a 3D printed titanium structure that measured 1.5m in diameter and 0.5m-thick and was claimed to be the largest 3D printed component to power an aircraft. The front bearing housing contained 48 aerofoils and was manufactured using Arcam's electron beam melting technology [36]. As PBF has already been proven to reduce material waste, fuel emissions, and lead times in other aerospace projects, this component was suggested by Rolls-Royce to cut manufacturing lead time by 30%.

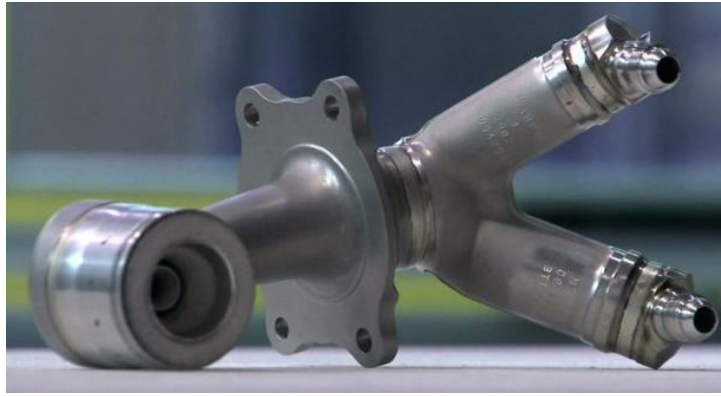


Figure 5: 3D Printer engine fuel nozzle used for the LEAP-1C jet engine [34]

In addition to the aerospace sector, metal AM technology is accelerating industrial development in other sectors such as the automotive industry from printing prototypes to ready-to-use parts. The French sports car manufacturer Bugatti started using AM technology in 2014 with the design and production of a biconically optimised differential housing for the front axle (Figure 6). More recently, Bugatti successfully tested a large 3D printed brake calliper built on an SLM 500 system in Ti-6Al-4V and achieved a tensile strength of 1,250 N/mm² and a material density over 99.7%. BMW Group achieved the first cost-effective series production of a metal AM component in the commercial automotive market with the use of an optimised fixture for the folding mechanism of the BMW i8 Roadster. The optimised AM fixture, produced using a novel printing technique, is ten times stiffer than the plastic injection moulded counterpart and was 44% lighter in AlSi10Mg [37].



Figure 6: Comparison of front axle differential using traditional manufacturing vs metal 3D printed part [33]

Governments, especially in the United States of America (USA) and United Kingdom (UK), are supporting AM technologies development by founding research together with leading AM companies. The U.S Army through the Army Research Laboratory (ARL) has signed a \$15 million contract with 3D Systems to develop a metal 3D printer that can produce large parts. ARL has invested in AM for two decades, producing custom tools and refurbishing worn parts. Still, the aim is to implement this metal printing platform for the manufacture of long-lasting, durable components. The build area of the printer is aimed to be around 1000 x 1000 x 600 mm, while it will be able to print parts with a wall thickness of 100 μ m and layer thickness of 30 μ m [38]. Sigma Components received £140,000 from the UK government through the National Aerospace Technology Exploitation Programme, which it is using to work with Rolls Royce to 3D print lightweight pipe end-fittings. Also in 2015, the UK government invested £154 million in four 3D printing research projects, to explore new technologies and drive research with the aim of keeping the UK competitive on the world stage by creating lighter, greener and more fuel-efficient aircraft and reducing CO₂ emissions by 75% by 2050 compared to levels in 2000 [36, 39].

Over the past two decades, continuous advances have pushed forward the concept of using AM in support of the surgical treatment of conditions ranging from arthritis of the hip or knee to ablation of malignant tumours of the head and neck [40]. Significant advances in applications and materials have led to metal AM playing a key role in shaping the way surgery is performed today. The anatomy of each patient is unique and complex, which creates an opportunity to produce patient-specific implants, such as cranial plates, using AM. Custom-shaped titanium implants can be fabricated at exactly the right size and shape, either parametrically scaled to fit the patient or even produced directly from a computer tomography (CT) scan of the original bone to be replaced or from a symmetrical healthy bone [41]. The use of AM parts in medicine can contribute to reducing the length of operations, which reduces the risk to patients and the costs of surgery. Prosthetics and orthotics were relatively early adopters of the AM. Customised surgical instruments and direct AM-fabricated implants are expected to continue to expand into many other anatomical areas and surgical specialities [25].

The common materials used in L-PBF are stainless steel, pure titanium and titanium alloys (such as Ti-6Al-4V), aluminium casting alloys, nickel-based superalloys (Inconel 718, Inconel 625 and Maraging steel), and cobalt-chromium alloys. Steel and other iron-based materials have been the leading materials for L-PBF due to their early start in the field from 1993.

Titanium-based metals have attracted much interest due to their application in high value-added industries such as aerospace, due to its lightweight, and medicine due to its good biocompatibility. Nickel alloys are widely used for aero applications as the base for high-temperature superalloys [42]. Research in novel materials has increased in recent years, and the range of alloys available for use in L-PBF has expanded as new technologies and applications emerge [18]. An essential aspect of the research prior to the implementation of new materials are the tests and evaluations that have to be made in order to find the right process parameters to accomplish the desired part quality. Since, a final component produced by L-PBF must meet the desired specifications for chemistry, surface roughness, damage tolerance, fatigue, strength, and part deformation. Many of these material properties are influenced by the residual stresses induced in the part during manufacture; and, hence the in-situ measurement of the forces induced during manufacture is a key driver for the work presented in this thesis.

1.2 Motivation

L-PBF allows the production of more accurate metal parts than any other AM process and with a density of approximately 100% relative to cast parts, assuring mechanical properties that match or even improve those of conventionally manufactured parts [9, 43, 44]. However, the large thermal gradients in the process lead to the development of residual stresses that remain in the final component after manufacture. Residual stresses must be considered from the early stages of the L-PBF process, i.e. part design, because they can have a significant impact on the final component reducing the mechanical properties of the manufactured part and generating critical part deformation. When high residual stresses develop during the building process, they can cause the build process to fail due to a collision between the part and the wiper in the L-PBF machine.

Residual stresses can also reduce the life of the finished part through its influence on fracture toughness and fatigue crack growth [45]. Therefore, it is essential to understand the development of residual strains in the process in order to control or reduce them. The two main processes of residual stress development in L-PBF are the Thermal Gradient Mechanism (TGM) and the constrained shrinkage of material on cooling [46]. The TGM creates tensile stress in the top surface as the laser melts the powder and partially melts the previously

deposited layers. As the solid material heats up, it starts to expand; however, it is constrained by the surrounding material causing compression in the top layer and tension in the surrounding material. Subsequently, as the top layer cools down, the previously solidified layer to which it is fused restrains it from shrinking inducing tension in the new layer and compression in the surrounding material.

Previous studies have demonstrated that the parameters used for the build process have a significant effect on the development of residual stresses within the part, i.e. the scan strategies, laser power, layer thickness and exposure time among others [42, 43]. Currently, different techniques are used to measure residual stress after the build process is completed, either destructive methods (hole-drilling and contour method) or non-destructive methods (x-ray diffraction and neutron diffraction). The acquisition of measurements of the deformation of the part during the L-PBF process is difficult because manufacturing must be conducted in a chamber containing an inert atmosphere and a new layer of powder has to be spread across the part at regular intervals. Limited research has been reported on the analysis of the stresses as they develop during the process [45, 47, 48]. Nevertheless, measurements have shown that there is an interlayer effect on the development of residual strains in the process [48]; however, the focus was on a single material and a single measuring point. Therefore, there is a lack of understanding of the effect of different process parameters and material properties on the development of residual stresses during the L-PBF process.

There are several challenges to fully understanding the residual stresses developed in the L-PBF process and the effect that the processing parameters and metal properties have on the interlayer effects while the part is being built. To understand the effect that the different scan strategies have on the melting of subsequent layers of the part for different metal powders during the building process, much higher fidelity measurements are required. A measuring technique proposed by Robinson [49], consists of an in-process device with multiple measurement points across the substrate, was used in this thesis while parts were built to determine the effect of the process parameters and the material properties on residual stress. The better understanding of the development of residual stresses in the L-PBF process will help to reduce the development of residual stress in the final component eliminating the need for post-processing heat treatments.

In the current literature, there is a lack of detailed understanding of the process-material property relationship in the L-PBF process and the effect on the residual stress developed during the building process. The properties of each metal powder and alloy are different;

therefore, the laser-material interaction and melt pool characteristics will not be the same for each metal powder. In order to produce nearly completely dense parts, different process parameters are used for each metal alloy and are likely to induce different residual stresses; hence, an investigation of these stresses needs to be conducted to understand the effect of metal properties on the development of residual stresses in the L-PBF process. Thus, although the industry has grown significantly over the last three decades, many opportunities remain for improving the state of the art.

1.3 Aims and Objectives

The aim of this investigation is to understand the complex evolution of residual stresses in the L-PBF process through the use of in-situ measurements and to understand the effect of the process-material relationships on residual stresses. During the development of this PhD, the following objectives were addressed:

1. To conduct a literature review of PBF processes, residual stress development in L-PBF, in-situ measurement and current understanding of residual stress.
2. To investigate the generation of residual stresses in the L-PBF process through the use of a Force Transducer Device (FTD) to explore how residual stresses originate and evolve during the manufacturing process using different metal powders.
3. To explore and identify the key parameters in the build process that result in the formation of residual stresses through in-situ measurements and investigate the effect of the material properties on the development of residual stress.
4. To investigate a correlation from the in-situ measurements, process parameters and material properties in the development of residual stresses in the L-PBF process.

1.4 Experimental Plan

Based on the research objectives outlined, a proposed flow chart with the experimental plan is shown in Figure 7. This project was part of a collaboration involving the University of Liverpool and Renishaw Plc working together on the €4m EU funded ENCOMPASS project with the EU's Research and Innovation Programme under the grant agreement No 723833 (<https://encompass-am.eu/>, <https://cordis.europa.eu/project/id/723833>). The ENCOMPASS project aimed to create a fully digital integrated design decision support (IDDS) system to cover the whole manufacturing chain for the laser powder bed fusion (L-PBF) process encompassing all individual processes within it. The ENCOMPASS project included 9 other partners, besides Renishaw and the University of Liverpool. Due to the collaboration within the ENCOMPASS project, the machine and powder choices were strongly directed by Renishaw due to their investment and support in the form of the L-PBF machines allocated to this project. Therefore, the experimental work was conducted in two phases, the first stage was conducted using Ti-6Al-4V due to the interest of collaborators in this particular material and the machine and powder assigned for the project. When the collaboration with the Encompass project ended the assigned machine was sold, and a second phase was conducted using different metal powders and different machines. This second phase allowed to the investigation into determining the effect of different material properties using three nickel-based alloys: Inconel 625, Inconel 718 and Maraging steel. Experimental work was performed using a novel device for in-process measurements to study the effect of a variety of processing parameters and using different metal powders to better understand residual stress generation during the L-PBF process. Combining these many elements together provided a better understanding of the development of residual stresses in the L-PBFP that could eventually provide a method to reduce and control the development of residual stresses and the distortion of manufactured parts.

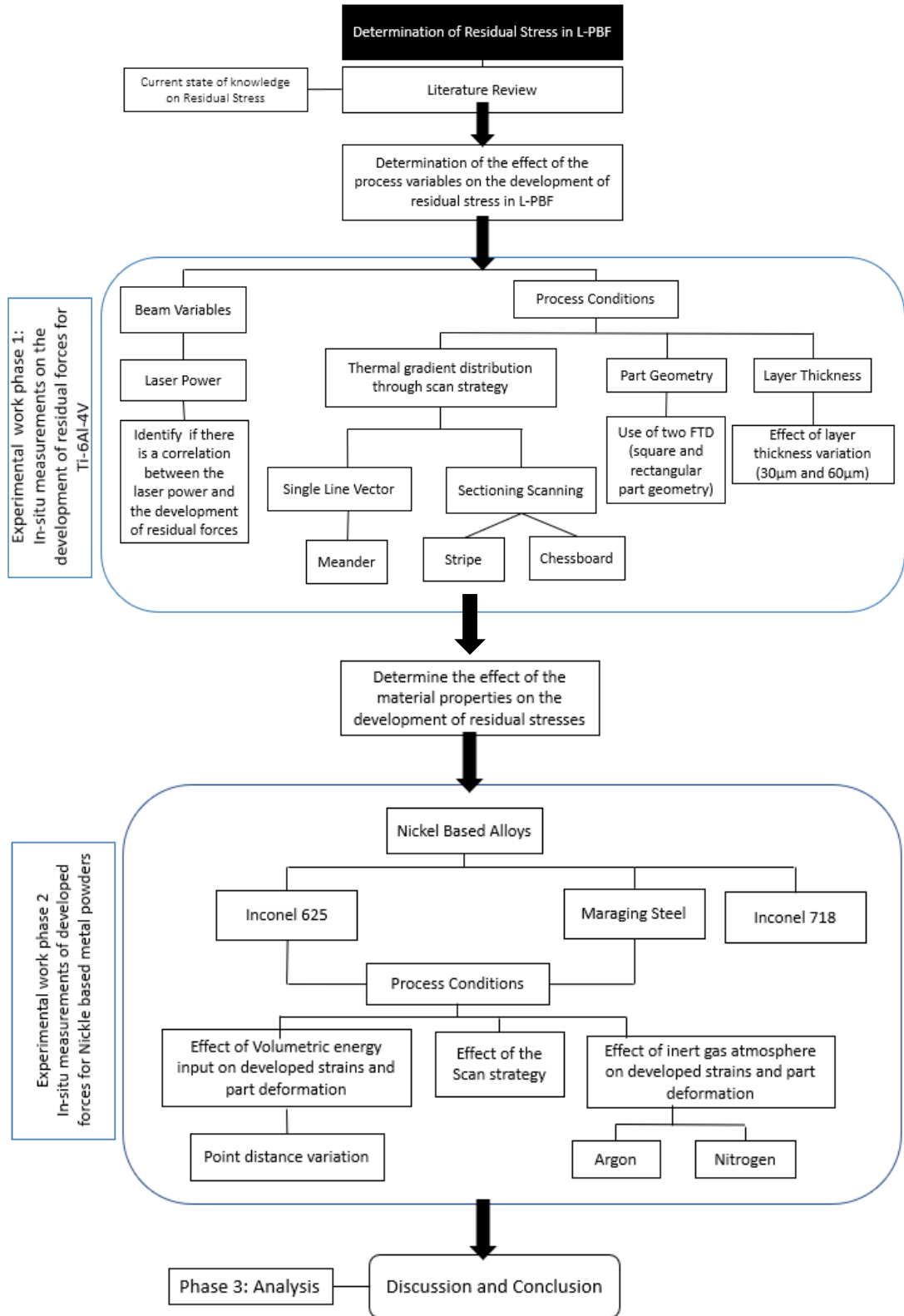


Figure 7: Experimental plan flow chart Phase 1 using Ti-6Al-4V and Phase 2 using Nickel based alloys

1.5 Thesis Structure

The structure of this thesis is outlined below:

- **Chapter 2: Literature Review**

In this chapter, a literature review is reported, which identifies the current state of knowledge of residual stress development in the laser powder bed fusion (L-PBF) process. First, a general review of the history of additive manufacturing and PBF process is presented, followed by an overview of the development of residual stress in L-PBF. The different techniques used to measure and predict residual stresses are discussed. Finally, the effects of the process parameters and the material properties on the development of residual stresses and part deformation in L-PBF parts are reviewed.

- **Chapter 3: Materials and Methods**

This chapter gives an overview of the materials and methods used during this investigation. It describes the equipment and software used and the different techniques for the analysis of the results.

- **Chapter 4: Experimental Results**

In this chapter, the results from the experimental work performed during the investigation are presented. Three modes of experimental work were used: in-situ measurements using a force transducer device; post-build measurement of the part distortion using digital image correlation; and post-build microscopy to examine the morphology of the melt pool. The development of residual forces in L-PBF have been studied based on in-situ measurements with the use of a Force Transducer Device (FTD). Modifications to an existing residual stress dynamometer were performed for the FTD to permit its use in a Renishaw AM250 system. The effect on residual forces induced in the L-PBF process by different process parameters, i.e. laser power, scan speed, layer thickness and scan strategy, are reported for different metal powders: Ti-6Al-4V, Inconel 625, Inconel 718 and Maraging300 steel.

The effect of the material properties and processing parameters for different metal powders on the deformation of the final part were measured using digital image correlation (DIC) and are presented in this chapter. The results from a microscopic analysis of the melt pool characteristics for a single track with powder and no powder are reported. In addition, the results of experiments to investigate the effect of laser speed, power and hatch distance on the characteristics of the melt pool are described.

- **Chapter 5: Discussion**

In this chapter, a discussion of the reliability and significance of the results obtained in the investigation is presented. The findings are compared to those reported previously in the literature, and a revised design for the FTD is proposed.

- **Chapter 6: Conclusions**

In this chapter, the conclusions obtained from this research work are summarized along with recommendations for future work.

1.6 List of publications

- **R. Magana-Carranza, J. Robinson, I. Ashton, P. Fox, C. Sutcliffe, E.A. Patterson. A Novel Device for In-situ Force Measurements during L-PBF, 2020 (accepted).**
 - This paper describes the design and manufacture of the FTD and its first use as a novel device for in-situ measurements during the L-PBF process, which are included in this thesis in Section 3.5.5. The paper describes the results and analysis from the in-situ measurements of the forces developed in the L-PBF process for a square sample built using Inconel 625 and using the FTD, shown in Figure 99.
- **R. Magana-Carranza, C. Sutcliffe, E.A. Patterson. The effect of processing parameters and material properties on residual forces in L-PBF, 2020 (submitted, under review).**
 - This paper is based on the results and analysis of the effect of process parameters and material properties on the developed residual forces in the L-PBF process. This paper includes the results and analysis from the experimental work for the study of the use of different scan strategies and layer thickness (Section 3.62) in the L-PBF process. The study of the effect of the energy density is presented, as well as a comparison of the developed forces and part deformation using different the metal alloys (Section 4.2.2).

2 Literature Review

This chapter presents a literature review covering the relevant published research and the current state of knowledge. The review starts with the history of Additive Manufacturing (AM) covering the different AM techniques and the development of Powder Bed Fusion (PBF) for metal components from prototyping to producing ready-to-use parts. The development of residual stresses in L-PBF is then reviewed, followed by the techniques used to measure residual stresses and the results from previous experiments reported in the literature. Finally, the chapter is concluded with a consideration of the effect of the process parameters and material properties on residual stresses in the L-PBF process.

2.1 Background of Additive Manufacturing (AM) and Powder Bed Fusion (PBF)

Additive manufacturing (AM) emerged from the term rapid prototyping (RP) and is defined as the process of joining materials to make objects using 3D model data, layer upon layer employing thin cross-sections of the part [4, 19]. The 3D CAD model is broken into 2D cross-sections of finite thickness; the thinner each layer is, the closer the final part will be to the original geometry [6, 50]. AM processes include different techniques using different materials (Figure 8); however, all of these technologies employ the same principle, the transformation of a geometric CAD model into a physical model produced layer by layer. The main advantage of AM processes is the freedom they give to the designer to utilize complex geometries not possible by traditional manufacturing methods; without requiring planning of process sequences or specific equipment for handling materials, or the need of any additional tooling.

AM first emerged in 1987 with Stereolithography (SL) [2, 7] from 3D Systems, a process that solidifies thin layers of ultraviolet (UV) light-sensitive liquid polymer using a laser (see Figure 9a). In 1988, 3D Systems and Ciba-Geigy partnered in SL materials development and commercialised the first generation of acrylate resins. DuPont's Somos stereolithography machine and materials were developed the same year. In 1991, three AM technologies were commercialised, including fused deposition modelling (FDM) from Stratasys, solid ground curing (SGC) from Cubital, and laminated object manufacturing (LOM) from Helisys (see Figure

9b). FDM extrudes thermoplastic materials in filament form to produce parts layer by layer (see Figure 9c). SGC is a photo-polymer-based additive manufacturing technology used for producing models, prototypes, patterns, and production parts, in which the production of the layer geometry is carried out by means of a high-powered UV lamp through a mask. LOM is a rapid prototyping system in which layers of adhesive-coated paper, plastic, or metal laminates are successively glued together and cut to shape with a knife or laser cutter [19].

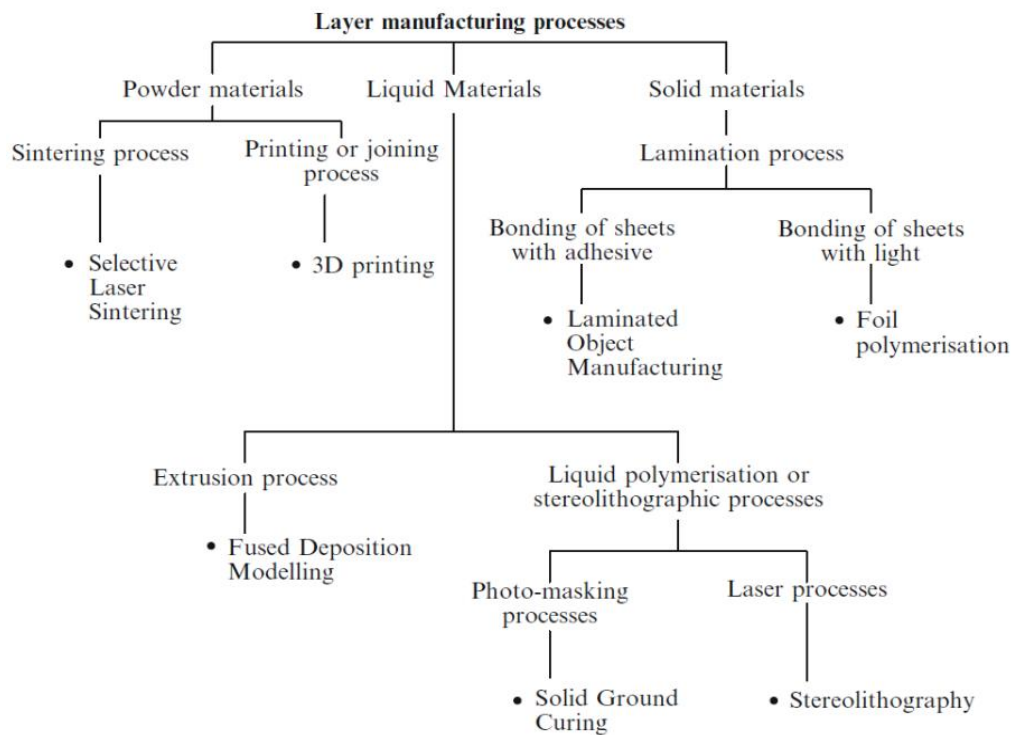


Figure 8: Classification of Additive Manufacturing Technologies (from [2])

Selective laser sintering (SLS) from DTM (now a part of 3D Systems) and the Soliform stereolithography system from Teijin Seiki became available in 1992 (see Figure 9d). In 1993, Soligen commercialised direct shell production casting (DSPC) and was patented by Massachusetts Institute of Technology (MIT). Using an inkjet mechanism, DSPC deposited liquid binder onto the ceramic powder to form shells for use in the investment casting process. At around the same time, the stereolithography QuickCast build style was introduced, which consisted of producing investment-casting patterns that are mostly hollow, making it possible to burn them out without fracturing the ceramic shell. In the mid-90s, Stratasys introduced the Genisys machine, which used an extrusion process similar to FDM but based on technology developed at IBM's Watson Research Center. While 3D Systems sold its first 3D printer (Actua 2100), using a technology that deposits wax material layer-by-layer using an

inkjet printing mechanism; and, Z Corp. launched its Z402 3D printer, primarily for concept modelling. Based on MIT's inkjet printing (3DP) technology, the ballistic particle manufacturing (BPM) process deposited wax materials using an inkjet print head. In 1997, AeroMer was founded and developed a laser additive manufacturing (LAM) that used a high-powered laser and powdered titanium alloys. By the late '90s, 3D Systems introduced a faster and less expensive version of the Actua 2100 called the ThermoJet. In addition, in 1999, Rödgers began to sell its controlled metal build-up (CMB) machine, mainly based on technology developed at the Fraunhofer Institute for Production Technology. At around the same time, Fockele & Schwarze of Germany introduced its steel powder-based selective laser melting system [51].

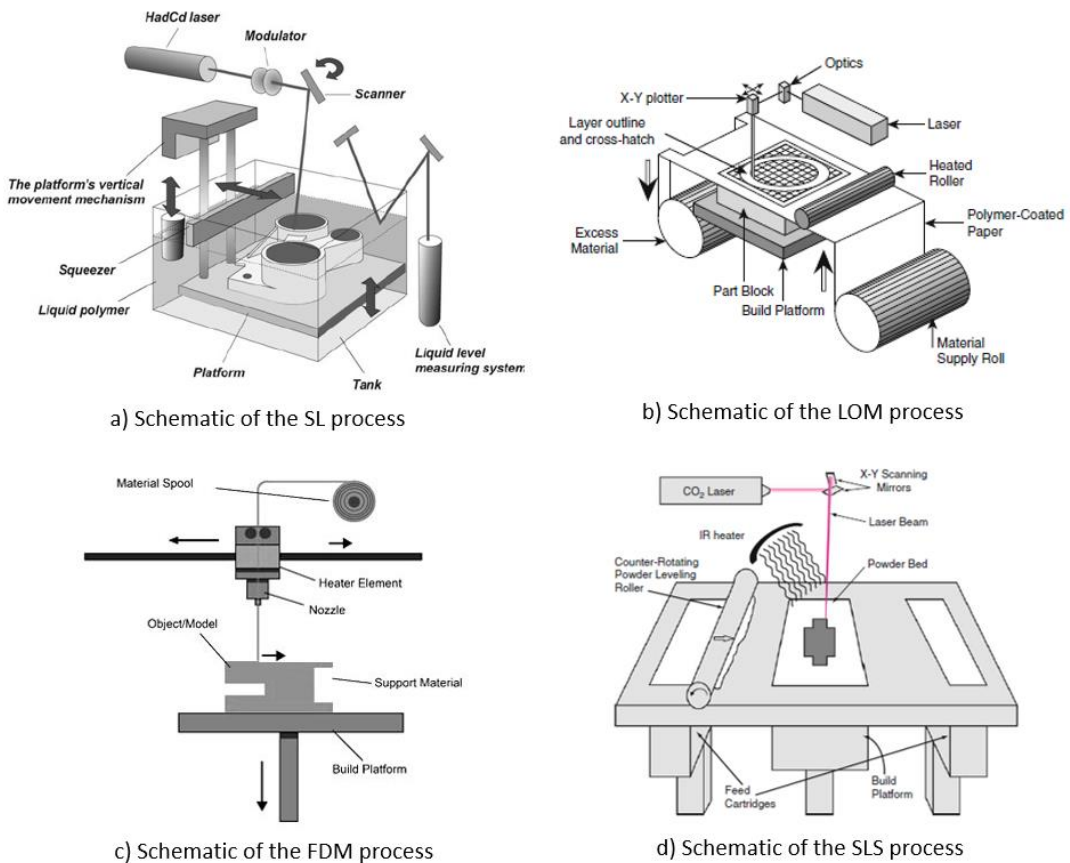


Figure 9: Schematic principles from the different AM processes: a) Stereolithography (SL) process (from [52]), b) Laminated Object Manufacturing (LOM) process (from [53]), c) Fused Deposition Modelling FDM (from [54]) and d) Selective Laser Sintering (SLS) process (from [55])

In 2000, several new technologies were introduced: Object Geometries of Israel announced Quadra, a 3D inkjet printer that deposited and hardened photopolymer using 1,536 nozzles and a UV light source. Sanders Prototype (now Solidscape) introduced PatternMaster, a

machine designed to produce precision wax patterns. Precision Optical Manufacturing (POM) announced direct metal deposition (DMD), a laser-cladding process that produces and repairs parts using metal powder. Z Corp. introduced its Z402C machine, the world's first commercially available multi-colour 3D printer.

In 2001, EOS announced its DirectSteel 20-V1, a steel-based powder consisting of particles 20 microns in size, which produced metal parts with 20 microns layer thickness. Also, the company introduced EOSINT 380, a laser-sintering machine with speed improvements. Concept Laser GmbH introduced a new system that combined laser sintering, laser marking, and laser machining; the machine used an yttrium-aluminium-garnet (YAG) laser and stainless-steel powder to produce nearly fully dense parts. In 2003, EOS introduced the EOSINT M 270 direct laser metal sintering machine, which used a fibre laser. In the same year, Trumpf, a German company, introduced its TruForm LF which used a 250-watt laser and a fibre optic cable to direct light onto a bed of pure powder metal. In November 2005, MCP Tooling Technologies (now MTT Technologies Group) introduced the SLM Realizer 100 Selective laser-melting machine. During this period, Voxeljet Technology GmbH of Germany introduced a large powder-based system machine VX800 which uses 3DP technology originally developed at MIT and commercialised by Z Corp. In 2008 MTT released a larger selective laser-melting machine, the SLM 250-300. This machine offered a 250 mm x 250 mm x 300 mm build volume with automated powder handling and recycling. In May 2009, EOS sold its first EOSINT P 800 laser-sintering machine for processing PEEK and other high-temperature materials [51].

Qualification and certification have been repeatedly identified as a challenge to widespread adoption of AM structurally critical components; the current process is too costly and takes too long. Hence, alternative means are needed to accelerate the qualification and certification of the AM processes [15]. More recent developments in the L-PBF process are the development of multi-laser or quad-laser machines. The quad-laser machines have four lasers operating simultaneously to enhance the AM capability. The quad-laser system reduces the production times significantly by working with four laser beams to manufacture a part. Multiple lasers can be used to increase build rates in L-PBF by either having the lasers operating independently on separate parts or cooperating on single components. Using a quad-laser configuration is particularly effective, as it can increase build rates by 90% over twin-laser configurations [56]. Machines like the SLM Solutions' SLM500 achieving build rates up to 171 cm³ in a 500 mm x 280 mm x 365 mm build chamber using lasers with power ratings

between 800 W and 2.8 kW. The system also offers an automated closed-loop material supply, recovery and sieving to minimise operator handling of the metal powder. The SLM500 was the first quad-laser machine introduced to the market in 2013 [56] (see Figure 10 [57,58]).

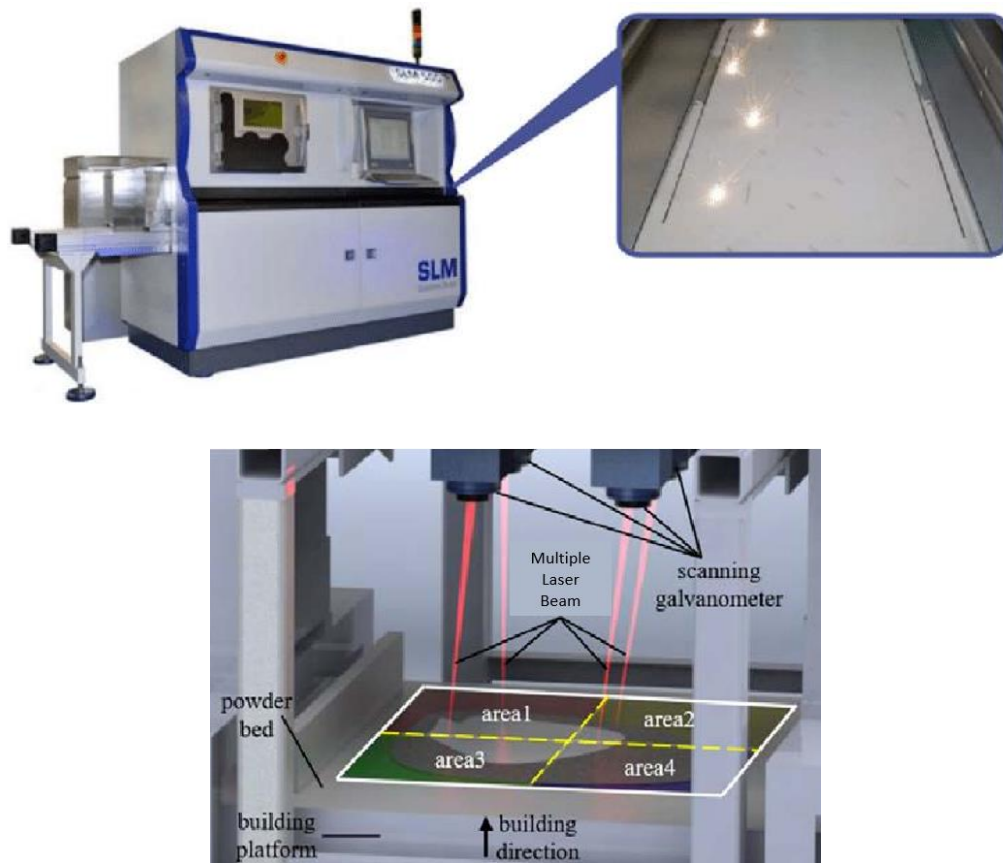


Figure 10: SLM 500HL machine multi-laser technology and schematic of the multi laser system (from [57] and [58])

AM technologies fabricate models by fusing, sintering or polymerising materials in predetermined layers [10]. It makes it possible to manufacture complex geometries including internal part details that are difficult to manufacture using machining and moulding processes because the process does not require a predetermined tool path, draft angles and undercuts. Layers in AM are formed by slicing CAD data by converting files into STL format [1]. The STL file developed by 3D Systems Inc. is a representation of a 3D model by a number of three-sided planar facets (triangles), each facet defining part of the external surface of the object [2]. Layer thickness depends upon many parameters, including the machine being used and ranges from 10 μm up to 200 μm . Layers in AM are built up on top of a previously deposited layer, as shown in Figure 11. After a layer is processed, the work platform is moved down by a single layer thickness in the Z direction, and a fresh material layer is created in a number of different ways depending on the technique being used, i.e. in a powder-based system, the

powder is spread using a roller or wiper, and in other systems, the material is deposited through a nozzle. Different software such as VISCAM RP, MAGICS, Ansys, Simufact Additive, QuantAM, and Netfabb are available to position and orient parts in the build platform to maximise the number of parts per build. Additionally, they allow the creation of support structures to separate the part from the bed, to support overhanging structures, to avoid part failures due to induced residual stresses and to reduce part deformation during the build process.

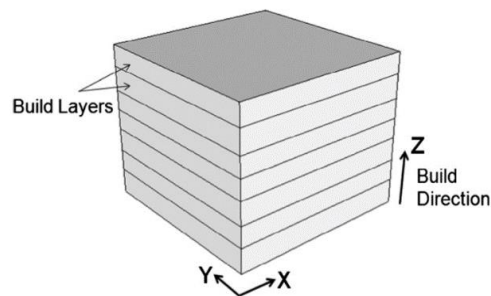


Figure 11: Definitions of the axes and planes discussed with respect to the build layers (from [59])

A large number of additive processes are now available [13]. AM systems are classified in terms of the energy source or the material feedstock. Some methods melt or soften material to produce the layers [60, 61], i.e., Selective Laser Melting (SLM) or Direct Metal Laser Sintering (DMLS), Selective Laser Sintering (SLS), Fused Deposition Modelling (FDM); while others cure liquid materials using different sophisticated technologies, i.e., Stereolithography (SLA). With Laminated Object Manufacturing (LOM), thin layers of paper, polymer or metal are cut to shape and joined together [62] (see Figure 9).

Over the last three decades, the impact of AM has continued to grow, with the new materials and advances in system developments [11, 13, 25, 63]. Many sectors of industry from all sectors have realised the potential of using these types of processes to develop their products, enabling cost savings, new optimised designs, and new products and processes [32-35, 40, 56]. Several industries, such as biomedical and aerospace are adopting AM as their main method of manufacture [9, 14]. As the development of AM technologies continues to grow across the world work on the international standardisation of processes and materials has progressed to support the large-scale industrialization of the technology and the potential demand for products [13]. A proposed timeline of the past, present, and potential future developments of AM applications by Tromans [64] can be seen in Figure 12.

AM applications timeline

This timeline lays out past, present and potential future AM developments and applications.

(courtesy of Graham Tromans)

1988-1994	rapid prototyping
1994	rapid casting
1995	rapid tooling
2001	AM for automotive
2004	aerospace (polymers)
2005	medical (polymer jigs and guides)
2009	medical implants (metals)
2011	aerospace (metals)
2013-2016	nano-manufacturing
2013-2017	architecture
2013-2018	biomedical implants
2013-2022	in situ bio-manufacturing
2013-2032	full body organs

Figure 12: AM applications timeline (from [64])

There is still potential growth in AM technologies as demonstrated by Bourell et al. [65] who published a roadmap for AM based on a workshop attended by 65 key people in AM, that identifies important aspects of AM which need to be further developed to achieve significant benefits in terms of affordability, maintainability, reliability, rapidity and functionality. These developments included:

- **Design:** Produce a new foundation for computer-aided design systems to overcome the limitations of existing solid modelling in representing complex geometries and multiple materials.
- **Process modelling and control:** Create closed-loop and adaptive control systems with feedforward and feedback capabilities. Control system algorithms based on predictive models of the system response to process changes. Produce new sensors that can operate in build chamber environments.
- **Material, process and machines:** Develop screening methodologies to answer the question as to why some materials are processable by AM, and some are not. Develop and identify sustainable (green) materials, including, recyclable, reusable, and biodegradable materials.
- **Biomedical applications:** Create design and modelling methods for customised implants and medical devices. Develop viable Bio-AM (BAM) processes for fabrication of “smart scaffolds” and for construction of 3D biological and tissue models using living biologics.

- **Energy and sustainability applications:** Develop equitable indicators for measuring sustainability in AM processes and products. Identify sustainable engineering materials for AM processes.

2.2 Materials in L-PBF and their Applications

There is a wide range of engineering materials that are processable through L-PBF [6, 12, 15, 42]. Most of the research has focused on Iron, Titanium, and Nickel-based alloys, due to their widespread application and their competitive process costs [42], as shown in Figure 13. Developments in new technology have allowed for improvements in process parameters in L-PBF, e.g., higher laser power, which has enabled research on many other metals, such as Aluminium, Copper, Magnesium, 17-4PH Stainless Steel and Tungsten [3, 63]. A particularly novel application of the L-PBF process involves the manufacture of open-cellular structures with pre-selected elastic modulus or stiffness (E) for aerospace structural components, complex heat exchangers and orthopaedic implants tailored to eliminate bone stress shielding by reducing E for high-modulus metals by more than an order of magnitude [3].

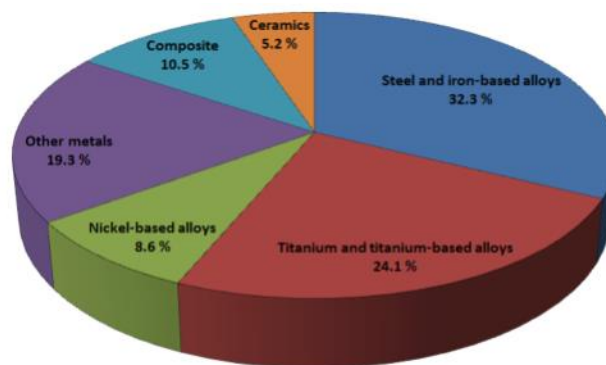


Figure 13: Research publications on materials for L-PBF (from [42])

2.2.1 Steel and Iron-based Alloys

Iron-based alloys have been investigated since 1993 [66] and are the most commonly used in L-PBF due to their competitive price and that they are readily processable. Research in steel has increased significantly due to the advantage of producing porous structures that allow the reduction of the material's relative density allowing the production of lightweight components while retaining the high strength properties of the material. This means that besides the design freedom given by AM, additional material savings and weight reductions can be achieved. Most of the research publications on L-PBF for ferrous metals are based on

316L Stainless Steel; however, it was only in 2010 that Tolosa et al. [67] achieved a 99.9% relative density in L-PBF samples. Different variants of steel have also been investigated, including Maraging300 steel [68-70] and 17-4 PH [71, 72]. Steel is often used in industry due to its strength; L-PBF steel parts have been shown to be stronger compared to their cast counterparts [27, 67]. This could be attributed to the L-PBF process, where a very small amount of material is melted, and rapid solidification takes place, resulting in a more uniform microstructure throughout the part.

There is a wide range of applications of L-PBF using steel materials due to their key properties, such as strength, ductility and biocompatibility [34-36]. Some important applications of steel components in L-PBF include heat exchangers where the freedom of design in L-PBF allows the production of conformal cooling channels used in injection moulding. Garcia et al. [73], used metal-AM to produce a mould incorporating spiral conformal cooling channels for injection moulding parts which improved part quality and cycle time. Wong et al. [74], investigated the potential applications of L-PBF to heat transfer applications with the use of novel geometries and lightweight structures in steel 316L and Aluminium 6061 components. Steel AM produced parts are also used for medical and dental applications. Kruth et al. [75], described a biocompatible metal framework for dental prostheses produced from L-PBF 316 stainless steel and Ti-6Al-4V and demonstrated that the use of L-PBF for the fabrication of the complex framework was viable without the need of manual intervention and with less pre-or post-processing. Li et al. [76] studied the design of structures with a gradient of porosity produced in 316 steel using L-PBF by varying the scan speed and this enhanced tissue growth in biocompatible implants.

2.2.2 Titanium and Titanium Alloys

Titanium in the liquid state is highly reactive and sensitive to Oxygen, making it difficult to be processed by conventional methods. Almost all research has focused on commercially pure Titanium (CpTi) and Ti-6Al-4V (Ti64). It is possible to achieve parts with a high relative density in Titanium (99.5%) [77] and Ti-6Al-4V (99.98%) [16, 78] using the L-PBF process. L-PBF produced Titanium and Ti-6Al-4V parts show similar or superior strength to their cast counterparts (UTS = 654 MPa and UTS = 1250 MPa respectively) [16, 27, 78]. Koike et al. [16] performed a comparison of AM produced samples of small dental implant products using Ti-6Al-4V ELI to cast specimens. The specimens were fabricated using electron beam melting (EBM) and laser melting systems (SLM). The samples manufactured using SLM and EBM had much finer α - β lamellar structures compared to the cast samples. Grindability was found to

be comparable to those of wrought and cast Ti-6Al-4V ELI specimens, and, both EBM and SLM processing exhibited harder samples than the cast counterparts.

The interest in Titanium and its alloys has largely been due to the potential application in the medical sector because of its good biocompatibility. Porous Titanium structures with mechanical and biomedical properties close to those of the human bone are possible with L-PBF scan strategies [79-81]. Mullen et al. [82] designed a novel porous titanium structure with a unit cell approach for the purpose of bone in-growth and applicable to the production of orthopaedic devices in commercially pure titanium (CpTi). Murr et al. [83] studied the mechanical and microstructural behaviour of Ti-6Al-4V during EBM and L-PBF, which can produce a wide range of crystallographic phases for biomedical applications, that are difficult to produce with traditional methods. Vandenbroucke and Kruth [78] examined the production of specific frameworks for complex dental prostheses using L-PBF to efficiently manufacture parts in Ti-6Al-4V and Co-Cr-Mo with appropriate mechanical and chemical properties. The use of L-PBF for medical and dental applications has strong economic potential because it allows the manufacture of multiple unique parts in a single production run and enables mass customisation [18].

2.2.3 Nickel-based Superalloys

Nickel-based superalloys are typically used in high-temperature applications such as aircraft and automotive engines. Nickel alloys investigated for use in the L-PBF process include Inconel 625, Inconel 718, Chrome and Hastelloy X among others. Nickel-based alloy parts fabricated by L-PBF have achieved nearly 100%, (99.98% Inconel 718) density relative to cast parts and had higher ultimate tensile strength (UTS) compared to their cast counterparts [84].

Due to their excellent corrosion resistance high-temperature strength, fatigue resistance, wear resistance, and good weldability, Nickel superalloys, like Inconel 718, have been used for high-temperature applications up to about 700 °C [85]. Combined with the advantages of L-PBF, such as freedom of design, engine components can be made with complex internal structures to increase cooling efficiency or to reduce weight, reducing fuel consumption and CO₂ emissions. The turbine blades, which are thin-wall parts with complex channels inside, were produced using L-PBF from Inconel 718 and Cobalt Chrome alloy by Concept Laser [74]. Inconel 718 has been tested in applications for aircraft engines, including swirlers in combustion chambers, repair patches and turbocharger rotors [18]. Since 2016, Airbus Safran Launchers pursue a comprehensive approach to the development of L-PBF processing for Inconel 718 injectors for liquid rocket engines [86].

2.3 Development of Residual Stress in L-PFB

L-PBF involves the heating and melting of powder material with a laser beam and the rapid solidification and cooling of the melted material to form the desired component. The unique rapid heating-cooling thermal cycle of AM leads to residual stress in the produced part which affect the microstructure of the produced samples [27]. Residual Stresses (RS) are defined as stresses that remain inside a material when it has reached equilibrium with its environment after manufacturing, heating or other alterations and results whenever a material undergoes non-uniform plastic deformation [87-89]. From the measurement perspective, residual stresses can be classified by the length scale in which they operate and are divided into three characteristic length scales [89]. A schematic of the types of residual stress is shown in Figure 14.

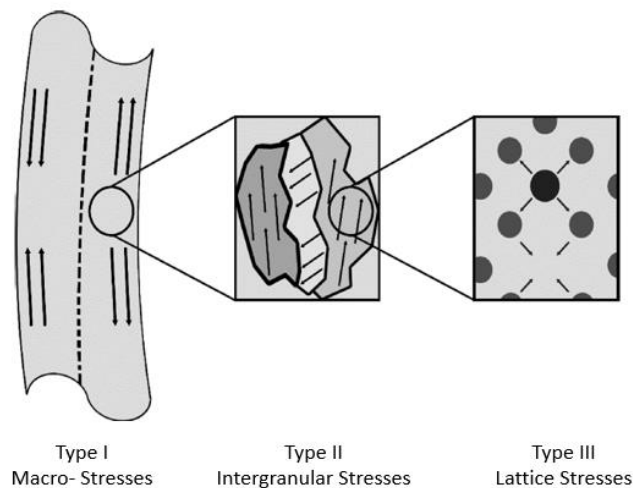


Figure 14: Classification of residual stresses into three length scales (adapted from [90])

Type I residual stresses are macro stresses that act on the scale of the component's geometry and may cause global distortion. These types of stresses are those mainly discussed in the literature regarding AM components. They arise from the non-uniform plastic deformation at the part scale and directly affect the fatigue properties of the material and are the main cause of distortion during or after production. Type II residual stresses are micro-stresses acting at the scale of individual grains; these tend to arise due to local microstructural effects, e.g. differences in slip behaviour from grain to grain. Type III residual stresses are at the atomic scale, arising from heterogeneous behaviour; this might arise from line defect (dislocations) or point defects, such as arise from radiation damage or doping with atoms of different size [89, 91].

Due to the thermal cycle of L-PBF and the locally concentrated energy input, global residual stresses (Type I) develop in the part during the process and can lead to geometry distortion. Thermally generated residual stresses are often the consequence of non-uniform heating or cooling operations. Coupled with the material constraints in the bulk of a large component, this can lead to severe thermal gradients and the development of significant internal stresses. Residual stresses that arise in the part as it is being produced in the L-PBF process can be critical to performance and should be considered in the design of a component. In any free-standing body, the equilibrium of stresses must be maintained, which means that the presence of a tensile residual stress in the component will be balanced by a compressive stress elsewhere in the body. Tensile residual stresses in the surface of a component are generally undesirable since they can contribute to, and are often the major cause of, fatigue failure, quench cracking and stress corrosion cracking [92].

Residual stress imposes some serious limitations on the practical use of the final component by reducing its mechanical properties (e.g. ultimate tensile strength, yield strength). A schematic representation of crack propagation due to residual stresses induced during an L-PBF process is shown in Figure 15a. Leuders et al. [93], concluded that internal residual stresses were primarily responsible for worsening crack propagation, thereby reducing fatigue life. The distribution of residual stresses in L-PBF parts has also been found to result in anisotropic fatigue properties.

Residual stresses may also reduce the part quality by affecting geometric tolerances. These stresses can cause warping and, in extreme cases, can cause the part to pull away from its supports, or even to crack [28]. The metal base plate on which the parts are built constrains part distortion during printing; hence, when the part is removed from the base plate, the constrained stresses are released causing a permanent part deformation as shown in Figure 15b. Large residual stresses exceeding the yield strength will result in plastic deformation and/or micro-cracks in the parts that could lead to failure of the production process as a consequence of the interaction of the part with the powder recoater, as illustrated in Figure 15c. Moreover, large residual stresses can limit the strength of the parts compared to a stress-free state [94]. Therefore, it is critical to understand the development of residual stresses in the process.

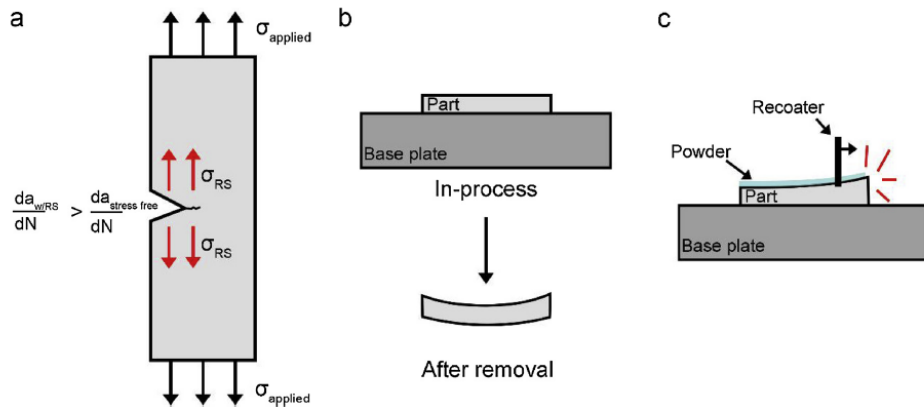


Figure 15: Effects of RS in L-PBF Parts. a) reduced fatigue properties, b) distortion upon removal, and c) potential failure in the process [from [90]].

The two major contributors to the development of residual stress within the L-PBF process are the Thermal Gradient Mechanism (TGM) and the contraction caused by the cooling of the new solid material [46].

2.3.1 Thermal Gradient Mechanism

Large thermal gradients occur around the laser spot and rapid heating of the upper layer and with slow heat conduction, results in a steep temperature gradient. In the absence of mechanical constraints, the expansion of the top layer causes bending the part away from the laser beam, as shown in Figure 16(a). Elastic compressive strains are introduced since the underlying material is at a lower temperature and restricts the expansion of the hotter top layer; and, when the material's yield strength is reached, the top layer will be plastically compressed in the heated zone. During the cooling stage when the source is removed, the plastically compressed upper layers start shrinking when cooling down but the shrinkage is partially restrained by the plastic strain formed in the heating stage. Finally, tensile residual stress is formed in the heated zone, which is balanced by compressive stress in a zone surrounding it that induces bending towards the laser beam, as shown in Figure 16a.

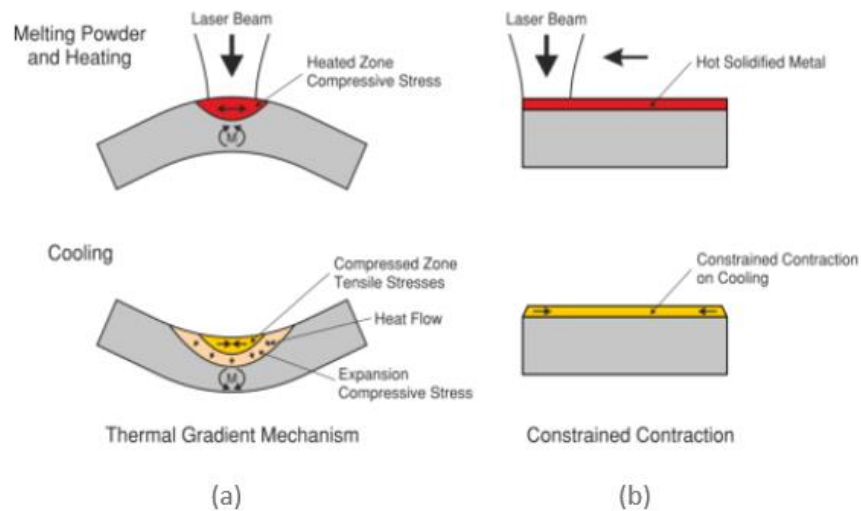


Figure 16: Thermal Gradient Mechanism (a) and constrained contraction effect (b) in L-PBF process (from [95])

2.3.2 Thermal Contraction

Thermal contraction is another explanation for the development of residual stresses in L-PBF, due to the process of building in layers. During the L-PBF process, when a new layer is added and heated far above the temperature of the underlying part, the new layer of material will first expand uniformly. This expansion of the top layer will be restricted by the much cooler underlying part, resulting in the development of compressive stresses in the new layer, and tensile stresses in the underlying part. A schematic of the thermal contraction is shown in Figure 16b. When the heat source is removed, the new layer will cool at enormous cooling rates of the order of $10^3 - 10^8$ K/s [96], contracting at a greater rate than the cooled part beneath, thus resulting in tensile stresses in the new layer and compressive stresses in the part below. The thermal gradient mechanism (TGM) is based on localised heating and cooling, whereas the thermal contraction is based on global heating and cooling.

2.3.3 Theoretical Model

A theoretical model was proposed by Shiomi et al. [45] to calculate the residual stress in an L-PBF part built on a base plate. When the first layer is added on the base plate, it is cooled down from the melting point and shrinks. Since the shrinkage strain is much greater than the elastic strain for the yield stress, the residual stress of the new layer is considered to be equal to the yield stress Y . The proposed model by Shiomi et al. [45] is shown in Figure 17.

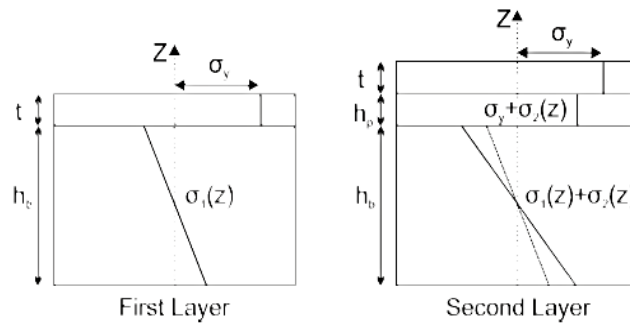


Figure 17: Development of residual stress due to solid contraction (from [44])

The strain ϵ created by the cooling of the part can be calculated with the material's coefficient of thermal expansion (CTE) α and the variation in temperature ΔT , as shown in Equation 1.

$$\epsilon = \alpha \Delta T \quad (1)$$

The yield strength is, however, related to the temperature of the material. The yield stress at higher temperatures is lower; therefore, the required temperature change to yield the material at higher temperatures will be smaller.

A simplified theoretical model proposed by Mercelis and Kruth [46], described in Figure 18, was developed to calculate the residual stress in L-PBF samples assuming that a part is being built on top of a base plate with height h_b . The part built so far has a height h_p and the layer thickness t .

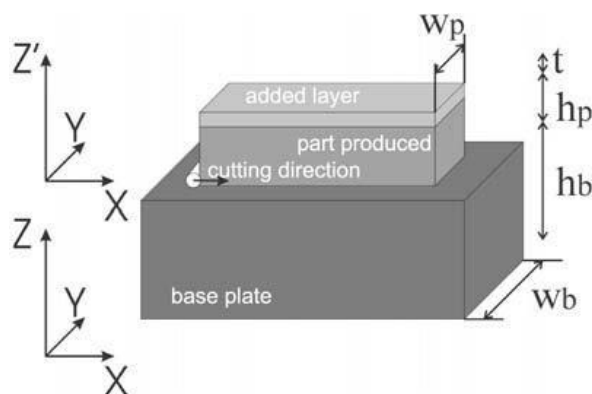


Figure 18: Simplified Theoretical Model of the L-PBF Process [46]

This simple theoretical model assumes that:

- The base plate and the part being built are at room temperature.
- The upper layer induces stress due to its shrinkage ($\alpha\Delta T$); the tensile stress is equal to the material's yield strength σ (since a strain of $\alpha\Delta T$ would result in a much larger stress than the yield strength).
- The stress σ_{xx} is independent of the Y coordinate. i.e. the variation of the normal stress across the width of the part is neglected.
- The general beam theory is valid.
- No external forces are applied to the combination of the base-plate and part.

The sum of the stresses normal to the build plane must be zero for static equilibrium to exist. At each instant, the equilibrium of both forces Equation (2) and moments Equation (3) need to be obeyed since no forces are acting on the system:

$$\int \sigma_{xx}(z)dz = 0 \tag{2}$$

$$\int \sigma_{xx}(z)zdz = 0 \tag{3}$$

Where z is the vertical build direction and σ_{xx} is the in-plane stress. To complete the calculations, Shiomi et al. [45] and Mercelis and Kruth [46], assumed linearity of the strain field with respect to the layer height. The assumptions used for these models reduce the accuracy of the prediction of residual stresses compared to the actual L-PBF process due to the fact that the material's properties are dependent on the temperature. The assumption that no external forces are applied is also a limitation given that there are forces from the supports and substrate until removal of the part from the substrate. Despite these limitations, this model could be helpful for prediction residual stresses and making comparisons with other methods, including FEA simulations.

The mechanisms described by Shiomi et al. [45] and Mercielis and Kruth [46] give some insight into the development of residual stress in the L-PBF process. However, the development of residual stresses is more complicated because each layer is heated uniformly in the single tracks exposed to the laser causing each track to heat and cool independently. When a layer is added to the base plate, it induces a compressive stress in the upper part of the base plate and tensile stress in the lower part. When successive layers are added on top, each layer induces further stresses in the base plate, but also in the already solidified layers; thus, changing the tensile stresses present in the previous layers and eventually resulting in compressive stresses in the underlying layers, and hence the in-plane residual stresses are more significant than the normal (z-direction) stresses [46]. This effect was confirmed by Liu et al. [97], who investigated the origin of residual stress in terms of the thermal gradient mechanism for 316L L-PBF parts by measuring stresses along the vertical and horizontal directions by X-ray diffraction and demonstrated that the residual stress distribution and its evolution in the vertical (z) direction are significantly affected by the subsequent thermal cycling (STC).

In terms of the microstructural effects, when a high-energy laser irradiates the molten pool, the temperature gradient between the bottom of the molten pool and the surface provides a driving force for the growth of the grain. Due to the fast solidification and cooling rates when the laser beam moves out of the molten pool, the crystal development of austenite is significantly restricted due to there being insufficient time for the grain growth. In L-PBF, when a subsequent layer is deposited over the underlying layer, the temperature in the previously solidified layer has already decreased, which leads to a uniform heating and cooling process between the adjacent layers. This thermal boundary effect changes the cooling and solidification processes as well as the microstructural evolution as can be seen in Figure 19 and the stresses concentrated at the bottom of the part connecting to the base plate result in a tensile stress [97].

Stress in an L-PBF part is built up locally by the thermal shrinkage of the solidified melt pool and is larger in the direction of a scan track than perpendicular to it. The shrinkage is impeded in the horizontal direction by the solid material below, causing horizontal tensile stresses at the top surface of L-PBF produced parts. These horizontal stresses exert a tensile force which would cause the part to curl up if it were not anchored to the base plate. Because the part is anchored, curl up is avoided but vertical tensile stresses are introduced at the sides, while compressive stresses exist in all directions in the centre of the part [98].

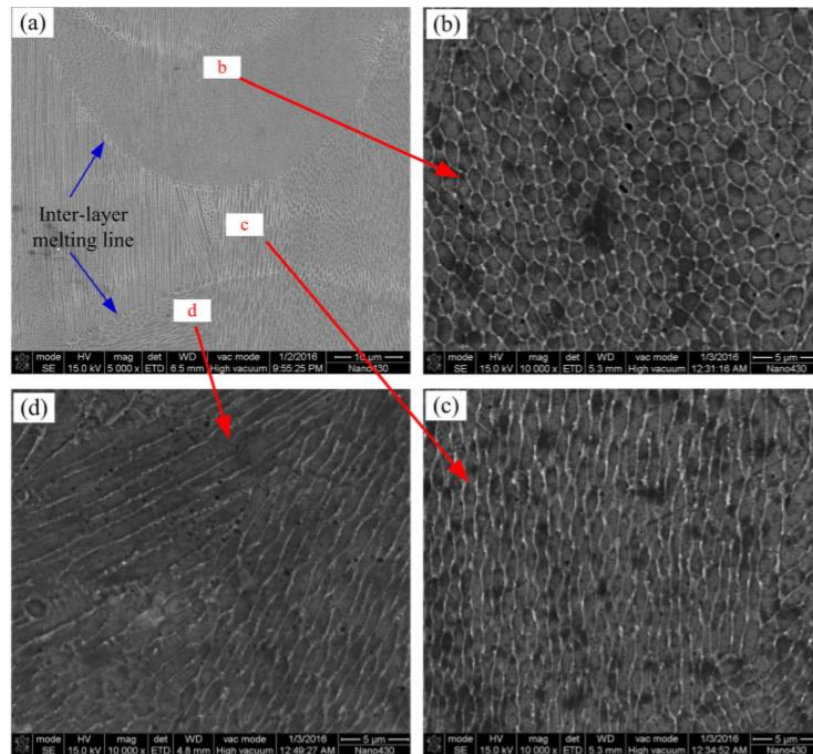


Figure 19: Inter-layer thermal boundary effect on the microstructure of an L-PBF 316L part (from [97])

The layer-by-layer additive process results in residual stress magnitude and orientation being highly dependent on the process parameters (e.g. laser power, scan strategy, scan speed and layer thickness), material properties and part geometry. It has been shown that due to the high and localised energy of the laser beam, the magnitude of the resulting stresses in the L-PBF process are generally large, approaching the material's yield strength [46]. The stresses in the longitudinal direction (σ_{xx}) of the beam motion are typically much higher than those in the transverse direction (σ_{yy}), i.e. perpendicular to the path due to the contraction of the heated material being more severely constrained in the direction of the laser path [99]. The maximum tensile stresses in the transverse direction have been found to be approximately half those in the scanning direction [100].

Many researchers have confirmed through experiment and modelling that the top and the bottom of parts are generally in tension, while the middle section is in compressive stress. Moat et al. [101], used neutron diffraction and the contour method to map the stress field inside a thin wall. Results from both methods coincided and showed that the overall stress state in the part, while still attached to the base plate, were compressive in the centre and tensile along the side and top surfaces. Rangaswamy et al. [102], also used neutron diffraction and the contour method on 3-D solid structures. They found that residual stresses were large in the vertical direction and smaller in the horizontal plane. The stress maps showed that

mainly vertical stresses were present, which were compressive in the centre and tensile along the outer surfaces. Vranken et al. [103] showed from 2-D residual stress plots obtained using the contour method that the stress field in a sample, produced using L-PBF, were compressive stresses in the centre and tensile stresses near the top and bottom edges, as can be seen in Figure 20.

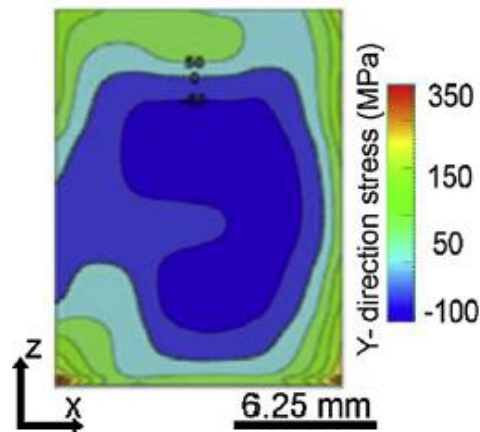


Figure 20: Stress distribution obtained via the contour method where Z is the build direction (from [103])

Based on similar findings, Denlinger et al. [104] developed a three-dimensional finite element model (FEM) and used a thermomechanical analysis to gain an insight into the accumulation of residual stresses in multi-layer builds. Results from the FEM showed that the newly deposited layers experienced high levels of tension (above the yield strength), while layers beneath were forced into compression.

2.4 Measurement Techniques of Residual Stress in L-PBF

Residual stresses induced in the L-PBF manufacturing process can reduce the mechanical properties of the final component. Due to the strong anisotropy associated with the build direction in the L-PBFP process, significant differences have been found in the mechanical performances of L-PBF parts [27]. Therefore, identifying the source of residual stress is essential; once residual stresses are identified, further studies can be conducted to determine ways to reduce or control the development of residual stresses during the L-PBF process. There are many techniques for measuring residual stresses in metals, and they can be classified as either destructive or non-destructive [92]. A wide variety of existing residual stress measurement techniques have been applied by researchers to measure residual

stresses in L-PBF components. These methods of stress analysis vary in terms of technique, resolution and accuracy. Table 1 gives an overview of the most common techniques.

Table 1: Residual stress measuring techniques (adapted from [92, 105])

Technique	Penetration	Resolution	Accuracy	Comments
Hole Drilling (distortion caused by stress relaxation)	1.2 x hole diameter	50 -100 μm depth	± 50 MPa, limited by reduced sensitivity with increasing depth	Destructive. Quick and simple. Low cost. Measures in-plane RS type I.
Curvature / Contour (distortion as stress arise or relax)	0.1 - 0.5 of thickness	0.05 of thickness; no lateral resolution	Limited by minimum measurable curvature	Destructive. Stress not uniquely determined unless used incrementally. Medium cost. Measures RS type I.
X-ray Diffraction (atomic strain gauge)	Near-surface <1 mm (with layer removal)	1mm laterally; 20 μm depth	± 20 MPa, limited by non-linearity or surface condition	Non-destructive only as a surface technique. Sensitive to surface preparation. Portable systems Measures macro and micro RS. Peak shifts: types 1, 2; peak widths: type II, III. High cost.
Neutron Diffraction (atomic strain gauge)	Volumetric	500 μm	$\pm 50 \times 10$, limited by counting statistics and reliability of stress-free references	Non-destructive. Excellent penetration & resolution 3D maps; low data acquisition rate. Macro and micro RS. Microstructure sensitive, Measures RS types I, II, III. High cost.

2.4.1 Destructive and Non-destructive Methods

Destructive methods rely on the monitoring of changes in the distortion of the component when removing material to allow the stresses relaxation. The regions of a sample containing residual stress will relax into a different shape when the stresses are released, providing data for the back-calculation of residual stress.

2.4.1.1 Hole drilling

Hole drilling is one of the most widely used techniques for measuring residual stress as it is relatively simple, quick and low cost. Equipment can be laboratory-based or portable, and the technique that can be applied to L-PBF produced parts in a wide range of metals. The principle of the technique involves drilling a small hole into a component containing residual stresses at the centre of a strain gauge rosette which is used to measure the locally relieved surface strains. The hole drilling method is described by an ASTM standard test method ASTM E 837-13 [106]. Due to the high sensitivity of the method, many factors must be considered such as the position of the strain gauge rosette, the size of the hole and the levels of residual stress

to be measured. This method is only valid for uniform residual stresses that should not exceed 60% of the yield strength of the material or errors can arise due to localised yielding. The surface roughness may also affect the quality of strain gauge attachment, which would reduce the accuracy of the strains recorded. Material may, therefore, need to be removed before the gauges are bonded to the surface, but this would inherently change the levels of residual stress, as the removal of material would allow stresses to be relaxed.

The hole-drilling method has been successfully applied to studying the residual stresses in components manufactured by L-PBF in different materials [107-109]. Knowles et al. [107], used the hole drilling method to evaluate residual stress within L-PBF Ti-6Al-4V specimens, where the residual stresses were found to be exceedingly high and in some areas approached and exceeded the yield strength of the material. Salmi et al. [108] used an MTS3000 REsidual STress ANalyzer (RESTAN), which is a system manufactured by SINT Technology based on the hole drilling method to measure the residual stresses of the samples (see Figure 21). The technique involves drilling a small hole into a component containing residual stresses at the centre of a strain gauge rosette which is used to measure the locally relieved surface strains. Measurements were taken for AISi10Mg parts and compared the residual stresses in samples after building and after stress relieving using shot-peening treatments. The outcomes of the study showed the presence, on the as-built components, of high tensile stresses that the usual post-processing operations were not able to minimise. Casavola et al. [109], successfully measured residual stresses for a set of components in AISI 18 Maraging steel employing the strain gauge hole drilling method using a strain gauge rosette with three radial grids, as shown in Figure 22, and showed that the stress magnitude decreased in the inner layers.



Figure 21: MTS3000 RESTAN (REsidual STress ANalyzer) system by SINT Technology positioned on the construction platform with the samples (from [108]).

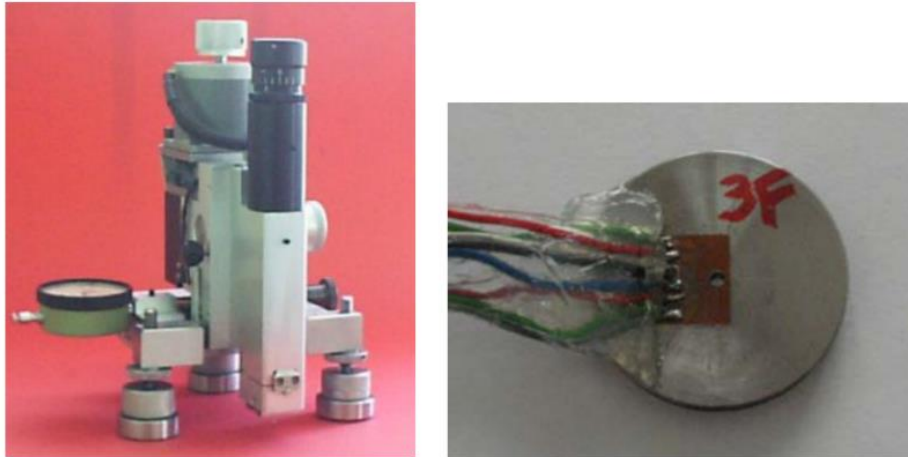


Figure 22: Residual stress hole-drilling measuring device (from [109])

2.4.1.2 Curvature Method

Curvature measurements are frequently used to determine the stresses within coatings and layers. The deposition of a layer can induce stresses which cause the substrate to curve. The resultant changes in the curvature during deposition make it possible to calculate the stress as a function of the thickness of the deposited layer. The curvature can be measured with contact methods (i.e. strain gauges) or without direct contact (i.e. digital image correlation, laser scanning). The Stoney Equation (4) [110] is often used to relate the deflection to the stress:

$$\sigma = -\frac{4}{3} E \frac{h^2}{l^2} \frac{dg}{dh} \quad (4)$$

Where, g is the deflection of a thin beam of length (l) and stiffness (E), and σ is the stress along the beam of thickness (h). Using a similar concept, Zaeh and Branner [95] proposed a method to measure the deformation of a T-shaped cantilever when releasing the residual stresses developed through the L-PBF process after the part is detached from the supports using a wire-cutting EDM as shown in Figure 23. The results of their investigation showed that deformation in the negative vertical direction occurred when the residual stresses in the parts were released. In addition, the results showed that the use of different parameters in the process affected the deformation of the part after removal, i.e. using a smaller layer thickness

caused larger part deformation, scan strategies using only X-vectors caused more deformation than Y-vectors, and heating the substrate at higher temperatures reduced the deformation of the part.

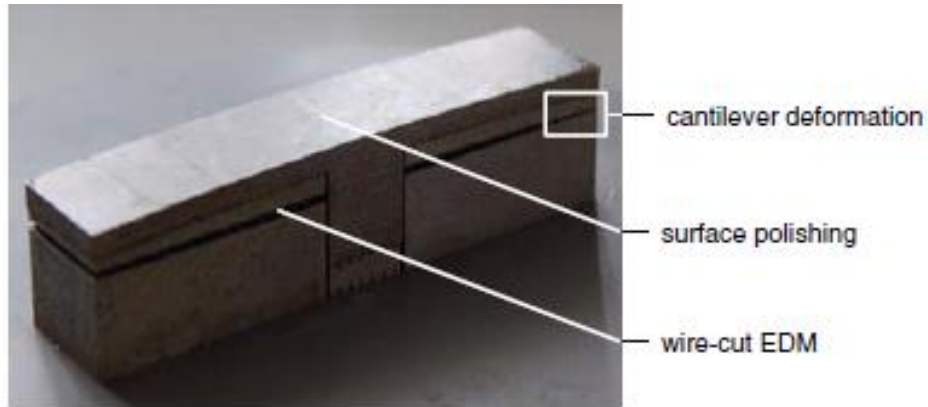


Figure 23: T-Shaped cantilever deformation method proposed by Zaeh and Branner (from [95])

Using the same approach, Kruth et al. [111], proposed the bridge curvature method (BCM) to compare the effect of different parameters in the L-PBF process on the development of thermal stresses. The method consists of measuring the deformation of a bridge-like part after removal from the base plate, as shown in Figure 24. This method has been adapted by other researchers [112, 113], whose results agreed with Kruth's experimental results in that shorter scan vectors and a rotation angle between the layers reduced residual stresses and part deformation.

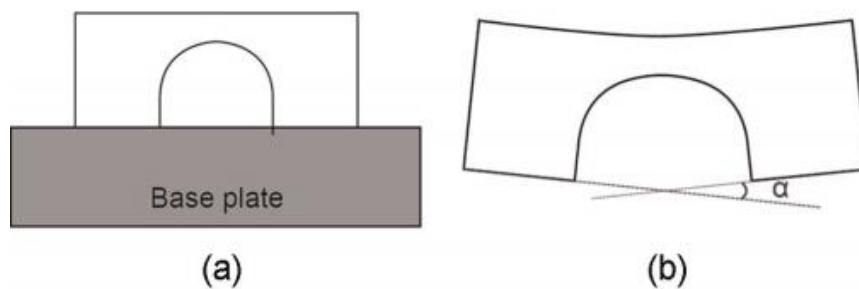


Figure 24: BCM proposed by Kruth et al. [111] in which the curvature of the part is measured (a) before and (b) after removal from the base plate

2.4.1.3 *The contour method*

The contour method is a powerful method for measuring residual stresses. This method involves cutting a planar surface through a part containing residual stress. The cut releases the residual stresses across the plane and the newly exposed surface responds by deforming [114]. By measuring the out-of-plane deformations, it is possible to determine the original residual stresses across the cut through the use of the finite element (FE) method. This is achieved by imposing displacement boundary conditions on the cut surface of the FE models that are equal and opposite to the measured deflections. The contour method requires a very accurate planar section to be cut through the stressed material; for this reason, electrical discharge machining (EDM) is typically used. Vrancken et al. [103] used the contour method together with a finite element model (FEM) to measure residual stresses in L-PBF components, where the normal stresses obtained are assumed equal to the stresses needed to return the part to a flat surface.

2.4.1.4 *X-ray diffraction*

X-ray diffraction relies on elastic deformations within a polycrystalline material to measure internal strains in a material. The deformation causes changes in the spacing of the lattice planes from their stress-free value to a new value that corresponds to the magnitude of the applied stress. This new spacing will be the same in any similarly oriented planes, with respect to the applied stress and the crystal lattice; therefore, the lattice spacing effectively acts as a very small strain gauge. During a measurement, the specimen is irradiated with high energy X-rays that penetrate the surface, the crystal planes diffract some of these X-rays, according to Bragg's law (5) and a detector, which moves around the specimen to detect the angular positions where diffracted X-rays are located, records the intensity of these rays at a function of angular position [115].

$$\lambda n = 2d \sin \theta \quad (5)$$

Where λ is the wavelength of the incident radiation, d is the interplanar spacing and, θ the Bragg angle, which is the angle that the incident beam makes with the diffracting plane. In the case of a stress-free material, the interplanar spacing d , for a particular reflection (hkl), is constant from one crystallite to another. When the material is deformed elastically, the lattice spacing of the crystallites change from their stress-free values and cause a shift in the Bragg angle. The strain calculated from this shift is termed the lattice strain. The lattice strain will depend upon the orientation of the reflecting group of crystallites with respect to the direction of stress [115]. Since the penetrating power of X-rays used for diffraction is small,

surface preparation is very important, and the surface must be smooth to avoid incorrect readings from the X-rays. This can be achieved by surface grinding, followed by mechanical polishing.

The X-ray method has been used by many researchers to measure residual stress in L-PBF components [97, 103, 115]. Liu et al. [97] studied the effect of the process parameters in L-PBF by X-ray measurements along with the vertical and horizontal directions. The influences of subsequent thermal cycling, energy input and scanning track length were investigated and the results showed that residual stresses parallel to the scanning direction are much larger than that perpendicular to the scanning direction. Lower energy input and shorter line lengths induced smaller residual stresses in the L-PBF parts. The method has also been used by Vrancken et al. [116], who concluded that the direction of the largest stress on the top surface coincides with the direction of its scan vector for all tested materials (Ti-6Al-4V, AlSi10Mg, Inconel 718, Maraging steel and 316L).

2.4.1.5 Neutron Diffraction

Neutron diffraction is a non-destructive method that relies on elastic deformations within a polycrystalline material that causes changes in the spacing of the lattice planes from their stress-free value. Measurements are carried out in much the same way as in X-ray diffraction, with a detector moving around the sample, locating the positions of the high intensity diffracted beams. The most significant advantage that neutrons have over X-rays is their large penetration depths, which makes them capable of measuring at near-surface depths of around 0.2 mm down to bulk measurements of up to 100 mm in aluminium or 25 mm in steel. Figure 25 shows a schematic of the neutron diffraction process, which is representative of the other diffraction methods.

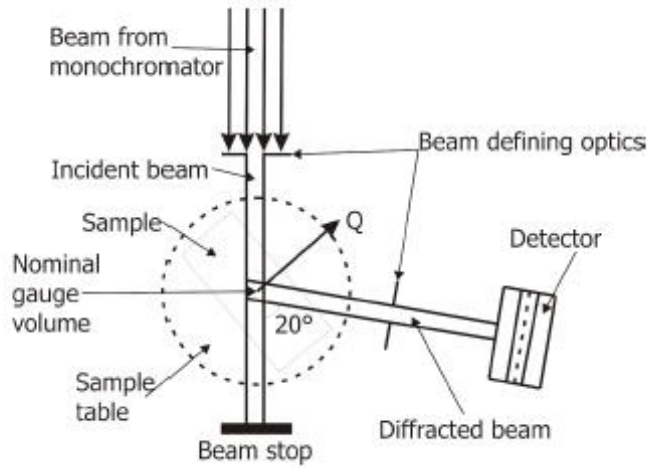


Figure 25: Schematic of the neutron diffraction method (from [108])

With high spatial resolution, neutron diffraction can provide complete three-dimensional strain maps of components [92, 117]. The neutron diffraction technique for making strain measurements makes use of Bragg's law (Equation 6) to relate the neutron wavelength (λ), the measured angle of diffraction (θ) and the lattice spacing (d) of the lattice planes identified by Miller indices (hkl)

$$\lambda n = 2d_{hkl} \sin \theta_{hkl} \quad (6)$$

The elastic lattice strain at a particular location is derived from the change in the experimental lattice spacing with respect to an appropriate stress-free reference lattice spacing d_{hkl}^0 , as follows (Equation 7),

$$\varepsilon_{hkl} = \frac{d_{hkl} - d_{hkl}^0}{d_{hkl}^0} \quad (7)$$

Three orthogonal elastic stress components (i.e. σ_x, σ_y and σ_z), directed along the geometrical axes (X, Y, Z), may be calculated from three measured components of elastic strain ($\varepsilon_x, \varepsilon_y, \varepsilon_z$) using Hooke's Law, which is written for the component σ_x as (Equation 8),

$$\sigma_x = \frac{E_{hkl}((1 - V_{hkl})\varepsilon_x + V_{hkl}\varepsilon_y + V_{hkl}\varepsilon_z)}{(1 + V_{hkl})(1 - 2V_{hkl})} \quad (8)$$

Where, E_{hkl} is the diffraction elastic constant analogous to Young's modulus and V_{hkl} is analogous to Poisson's ratio. Diffraction elastic constants relate the elastic lattice strain in the direction normal to the (hkl) plane used in the diffraction measurement, to the macroscopic stress field [102].

Among many researchers, Rangaswamy et al. [102] applied this method to study the development of residual stress of LENS® SS 316L and Inconel 718 samples. The results showed that the residual stress at the centre of the samples is compressive and tensile at the edges of the parts. The magnitudes of the residual stresses exceeded 40-50% of the nominal yield strength of the material. Anderson et al. [99] used neutron diffraction to determine the distribution of residual stress in Ti-6Al-4V samples produced by L-PBF. They concluded that increasing the layer thickness reduced the stress gradients in the part and that the use of alternated scan vectors gave a more homogenous stress field.

Furthermore, Sochalski-Kolbus et al. [118] using neutron diffraction compared the residual stress distribution of Inconel 718 samples produced by EBM and DLMS, where DMLS samples exhibited higher residual stress levels compared to the EBM samples, most likely due to the powder-preheating step used in the EBM process.

2.4.2 In-process Measurements of Residual Stress in PBF

Understanding the development of residual stress in the building process is needed to control residual stresses in L-PBF [42]. Some more specific techniques for making residual stress measurements during the L-PBF process have been developed. Researchers have developed in-situ measurement techniques using strain gauges, laser displacement sensors (LDS) and differential variable transducer (DVRT) [45, 47, 48, 119].

Some researchers have used strain gauges attached to the base plate to measure the changes in strain during the building process with the addition of each new layer [45, 47]. Van Belle et al. [47] studied the development of residual stresses by measuring the variation in strains and temperature during the fusion and consolidation of new layers. A rosette strain gauge and a k-type thermocouple were attached to the bottom of a support structure, which was clamped onto the moving bed of the L-PBF machine, as shown in Figure 26. The strains and

temperature variation were recorded during the manufacturing process for Maraging steel samples.

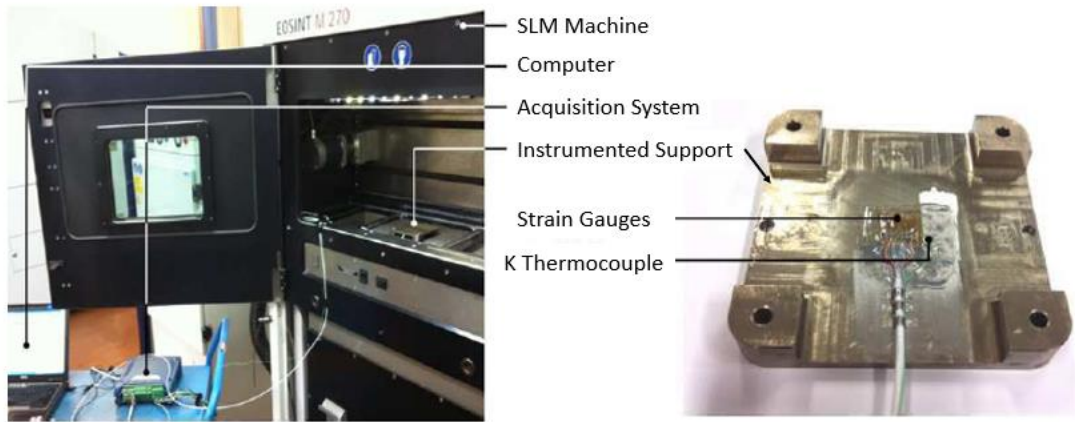


Figure 26: In-situ measurement system for strain and temperature evolution by Van Belle [47]

Shiomi et al. [45] studied the thermal distortion in the L-PBF process for Chrome-Molybdenum steel samples. Measurements were taken using two strain gauges attached at the centre of the base plate that measured the strains parallel and perpendicular to the laser scan. A schematic of the setup used by Shiomi is shown in Figure 27.

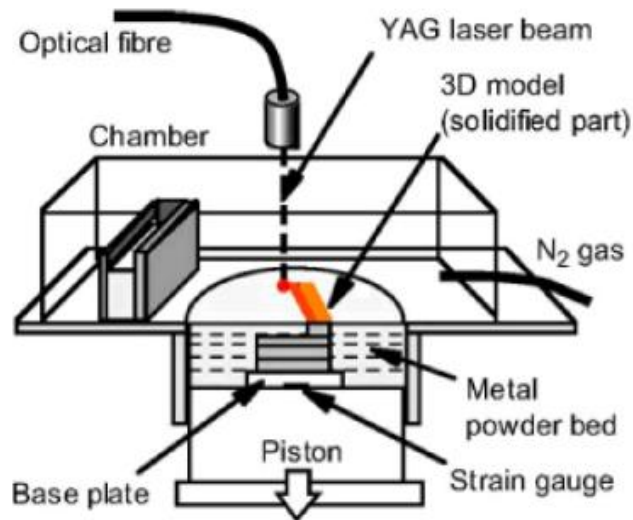


Figure 27: Experimental arrangement for measuring the developed strains in the substrate by Shiomi et al. [45]

In both studies, the calculated strain difference per layer ($\Delta\epsilon$) was used to estimate the residual stress and was based on the layer removal method (Figure 28).

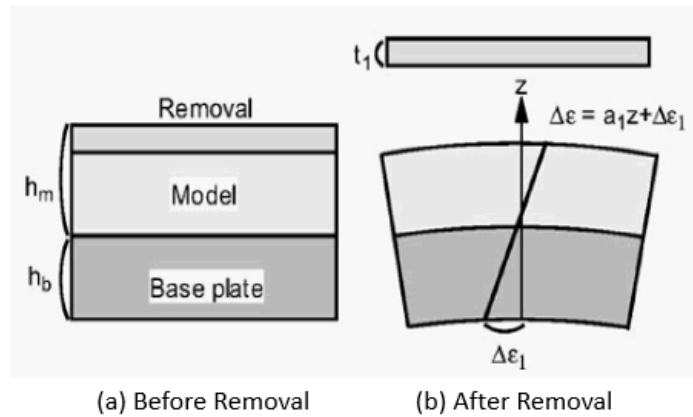


Figure 28: Strain Increment in model and base plate by removal of the top layer (from [45])

Other studies have used displacement sensors for in-process analysis instead of strain gauges, including differential variable reluctance transducers (DVRT) [48] and laser displacement sensors (LDS) [120]. Dumbar et al. [48] developed an enclosed system for in-situ measurements of temperature and distortion from underneath the part. Distortion measurements were completed using a differential variable transducer (DVRT) displacement sensor, connected to a DEMOD-DC to convert displacement into voltage. The voltages were measured by a voltage data acquisition (DAQ) system, and temperature measurements were completed using a K-type thermocouple. A substrate attached to the top of the enclosed system was used as a build plate, as shown in Figure 29.

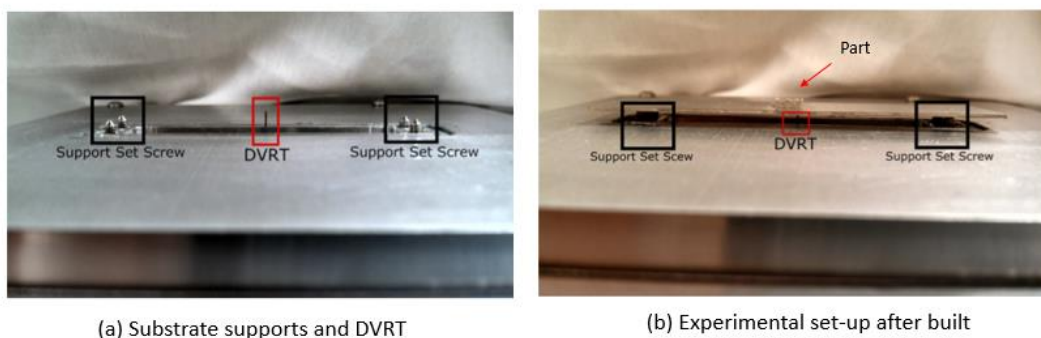


Figure 29: Experimental set-up for in-situ distortion measurements using a DVRT proposed by Dumbar et al. [48]

The distortion in this study is considered as an analogue of residual stress. Results from the in-situ measurements for Inconel 718 samples, showed a distortion cycle during the L-PBF process resulting in a final distortion in the Z direction caused by the thermal gradient mechanism (TGM). Using a constant scan strategy increased distortion by 37.6% as compared with a rotating scan pattern. A similar study was performed by Denlinger et al. [120], who analysed the effect on the inter-layer dwell times on distortion and residual stress in Ti-6Al-4V and Inconel 625. In-situ measurements of distortion in the substrate were taken with a laser displacement sensor (LDS). A substrate was clamped from one end, and the LDS was placed at the free end of the substrate to capture the bowing distortion mode of the sample in the z-direction. Results showed that increasing dwell time, to allow additional cooling during the deposition process, reduced distortion for the Inconel 625 samples; whereas the opposite occurred for the Ti-6Al-4V samples.

Robinson et al. [119] studied residual strains developed during the L-PBF process with the use of a Force Transducer Device (FTD) (see Figure 30). Their FTD consisted of a specially enclosed substrate holding an arrangement of load cells that allowed the building of two different part geometries and measurement of the forces developed. The load cells were connected to Titanium pegs that work as the build platform and registered the developed strains while the part is being built. Their results showed the primary stresses to be in the scanning direction and by using shorter scans, the strains developed were lower than with unidirectional long scans. The use of a higher laser power increased the residual stress in the component.



Figure 30: The Force Transducer Device (FTD), developed by Robinson [from 119] for in-situ measurements.

Some other non-disruptive methods have been developed for in-situ measurements by using optical monitoring systems. Smurov et al. [122] analysed the thermal processes during selective laser melting of a layer of INOX 316L metal powder using an Infra-Red (IR) camera. The laser interaction parameters, specifically the power, scan rate, and heated spot diameter, corresponded to typical operating windows for the L-PBF processes. The temperature of the

surface of the melt pool of the metal powder during the L-PBF process was determined with the infrared camera. A schematic of the temperature distribution during the laser sintering of powdered INOX 316L stainless steel is shown in Figure 31. Results illustrate the effect of the scan rate and laser power on the geometry of the melt zone. Another study was developed by Rodriguez et al. [123] investigated the absolute surface temperatures using in-situ IR imaging of the melted or solid surfaces layer-by-layer during fabrication within an EBM system. The thermal camera was synchronised with the system's signal voltages for three synchronised events (pre-heating, melting, and raking) to capture images automatically. A calibration procedure was established to acquire absolute temperature values from the IR images to determine the solid material's emissivity and the reflected temperature or mean radiant temperature of the build chamber. Verification of the data was performed using a thermocouple embedded during fabrication that showed a 3.77% difference in temperature. The thermal model developed can be extended to other PBF processes to improve thermal monitoring and control of the fabrication process.

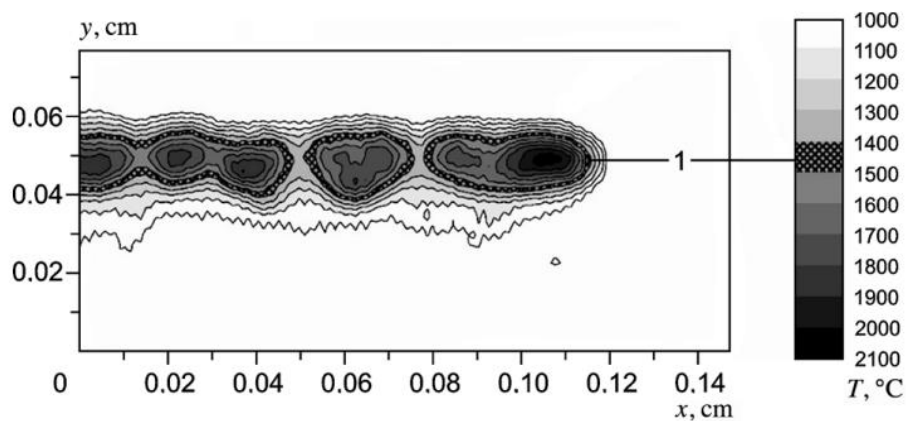


Figure 31: Temperature distribution during laser sintering of powdered INOX 316L stainless steel: Region 1 is the melt isotherm, 1450 °C. (from [123])

2.5 Methods to Model and Predict Residual Stress in PBF

The measurement methods described previously are often used to validate Finite Element (FE) models. FE models are then used to predict the development of residual stresses in a build for different process parameters or part geometries. FE models have been developed to simulate the L-PBF process to identify the best process parameters in order to reduce or control residual stresses. FE models are not only used to predict residual stresses, but they can also be suitable for the development of new scan strategies and to develop the optimum parameters for new materials thus reducing the need for costly experimental work. FE models

together with experimental methods have been widely used to study and understand residual stresses in the L-PBF process and other AM technologies; therefore, it is important to understand and review the FEA models developed in the literature.

L-PBF is a very complex process that involves the production of components formed from the addition of hundreds or thousands of individual layers that range from 20 μm to 100 μm in thickness; in addition, each layer is melted non-uniformly by a moving laser beam resulting in complex patterns of heat transfer. Therefore, a precise representation of the L-PBF process using an FE model requires an enormous computational expense and time. In order to reduce the computational expense and to develop accurate FE models, some studies have focused their models only on understanding the thermal cycles developed in each single scan [124-130]. This provides an insight into the flow of matter and energy in the laser melting process but ignores the multi-layer effects. At the same time, other researchers have extended their studies into the prediction of the residual stresses that develop in the whole process, resulting in good comparisons with experimental results [131-144].

Most of the studies are similar in the consideration of the thermal effects; Figure 32 shows a schematic of the factors considered in modelling the heat transfer in a thermal model (i.e. heat conduction theory, initial and boundaries conditions). The laser scans the powder bed according to a defined scanning pattern, resulting in the powder undergoing state and phase changes from solid to liquid and then back to solid when cooling. Considering the temperatures and phase conditions, temperature-dependent material properties are also required for accurate results. The FE model involves information from the material properties such as the coefficients of thermal expansion, conductivity, yield strength, density, elastic modulus and the specific latent heat.

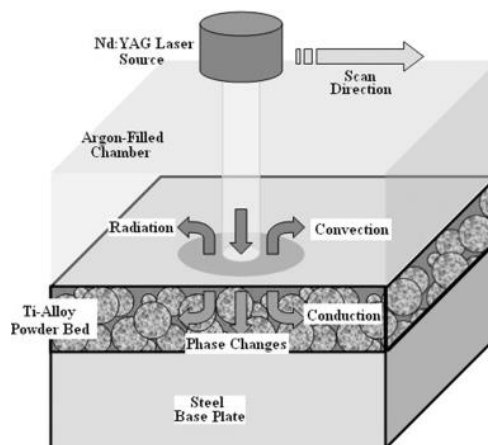


Figure 32: Schematic of the heat transfer conditions during L-PBF process (from [124])

The heat transfer is usually modelled using Fourier's theory for heat conduction [145]. To describe the governing heat conduction (9) was used by Carslaw and Jeager [146].

$$k \left(\frac{\delta^2 T}{\delta x^2} + \frac{\delta^2 T}{\delta y^2} + \frac{\delta^2 T}{\delta z^2} \right) + q = \rho c \frac{\delta T}{\delta t} \quad (9)$$

Where k is conductivity coefficient, T is temperature, ρ is density, c is heat capacity coefficient, and q the internal heat generation.

The initial conditions and boundary conditions can be described by Equations (10) and (11).

$$T(x, y, z, 0) = T_0 \quad (10)$$

$$-k \left(\frac{\delta T}{\delta z} \right) = \epsilon_{\theta} \sigma (T^4 - T_e^4) + h(T - T_e) \quad (11)$$

Where, T_0 the initial temperature, T_e the free stream temperature, ϵ_{θ} the emissivity, σ the Stefan-Boltzman constant, and h the convective heat transfer coefficient.

The parameters modelled vary among the different studies, due to the costs and time implications for the simulations. The heat transfer into the part can be modelled as originating from an area of constant temperature [147] or as a distribution of heat flux [95]; and the volume of irradiated material is often increased to reduce computational expenses. Another common strategy to reduce computational costs has been to group a large number of thin layers into a small number of much thicker layers, because this allows faster residual stress and distortion calculations but reduces the level of precision. Fu and Guo [148] developed an FE model to simulate the multi-layer deposition of Ti-6Al-4V in L-PBF. A physics-based layer build-up approach coupled with a surface moving heat flux was incorporated into the model. The melt pool shape and dimensions were predicted and experimentally validated. The temperature gradient and thermal history in the multi-layer build-up process were also obtained, as shown in Figure 33.

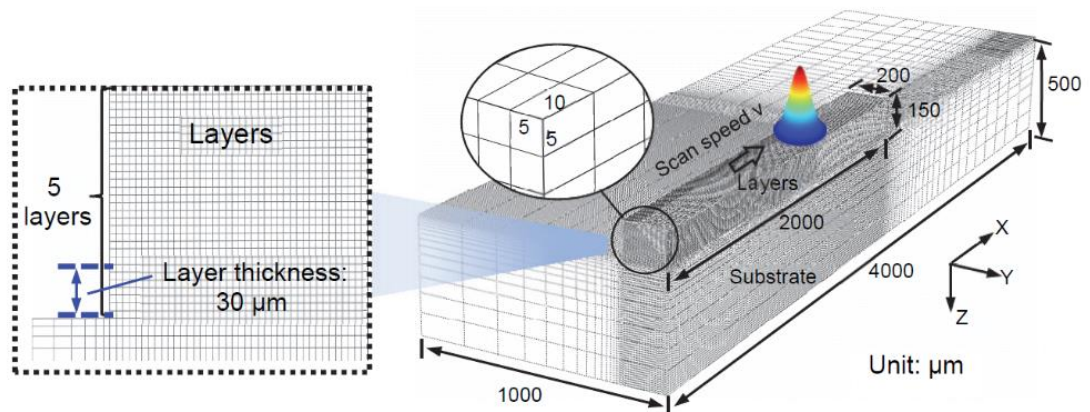


Figure 33: Simulation schematic of L-PBF proposed by Fu and Guo (from [148])

Another approach used to model the multilayer effect and final part deformation is to ignore the laser motion within layers; Zaeh and Branner [95] developed an FE model of a T-shape cantilever based on their experimental work. To reduce calculation times the simulation was performed by grouping 20 real layers of 50 μm into a single layer of 1 mm, and every layer was charged with 200 W power for a period of time of 20 ms followed by a cooling period of 4 s. The layers were heated uniformly, thus reducing computational time while still allowing multilayer effects and in-plane residual stresses to be estimated. The residual stresses predicted by Zaehe and Branner are shown in Figure 34. The results show a stress of about 490 N/mm^2 within the cantilever while the measurements from neutron diffraction exhibited a maximum of 435 N/mm^2 . The simulation results shown are close to those in the experimental work and could be improved by reducing the layer thickness for a more realistic approach.

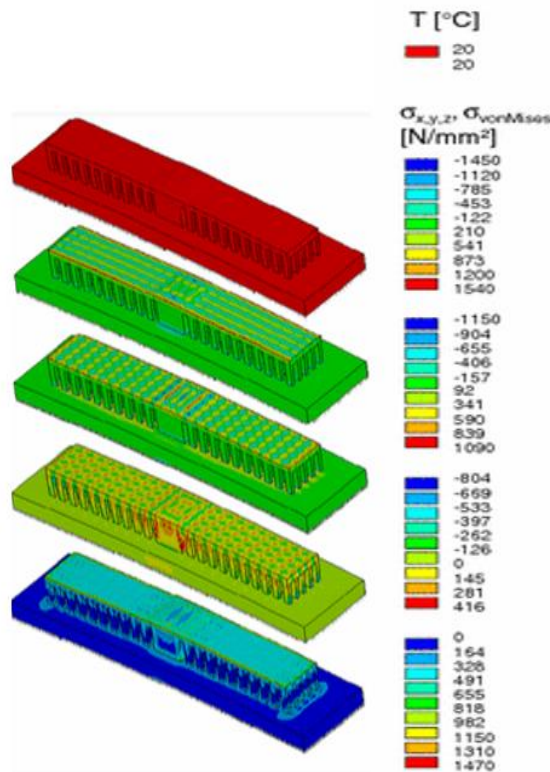


Figure 34: Final temperature and residual stress distribution for interlayer effect simulation (from [95])

There are a large number of simplifications performed in the modelling of the L-PBF process in order to reduce the computational costs; however, good correlations to experimental work have been achieved. FE models have helped to understand and predict the development of residual stresses and part deformation in the L-PBF process. Several commercial software packages have been developed for specific AM processes to allow predictions of residual stress and part deformation; these include, Ansys, 3DSIM and Simufact Additive. The use of these software packages enables the analysis of the use of different process parameters in different materials to select the optimum part orientation and support structures to achieve a successful build with the lowest residual stress level.

2.6 Process dependence on Residual Stress

According to the literature, many process variables in L-PBF affect the development of residual stress. From a combination of experimental analysis and FEM simulations performed in the literature, it is clear that changing the process variables has a significant impact on the resulting residual stresses and part deformation for the built part. Bartlett and Li [90]

categorised the most prevalent process parameters discussed in the literature in three main groups: scanning strategy, beam variables and process conditions, as shown in Figure 35.

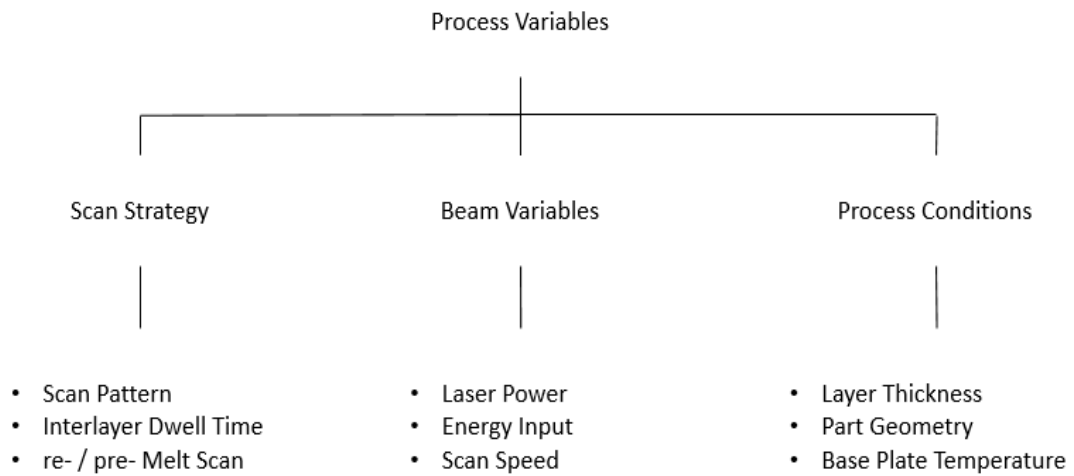


Figure 35: Process parameters that affect residual stress formation in L-PBF (adapted from [90])

L-PBF, as in other AM process, has a wide range of input factors and output parameters affecting the functionality of the final component. Input factors to be considered include laser power, scanning speed, scanning interval, scanning strategy, layer thickness and metal powder physical properties. The output parameters which determine the functionality of the part and are measurable, include tensile strength and part density [149]. A schematic of functionality input factors and output parameters for the L-PBF process is shown in Figure 36. The main input parameters for the L-PBF process and their effect on residual stresses as reported in the literature are reviewed in this section.

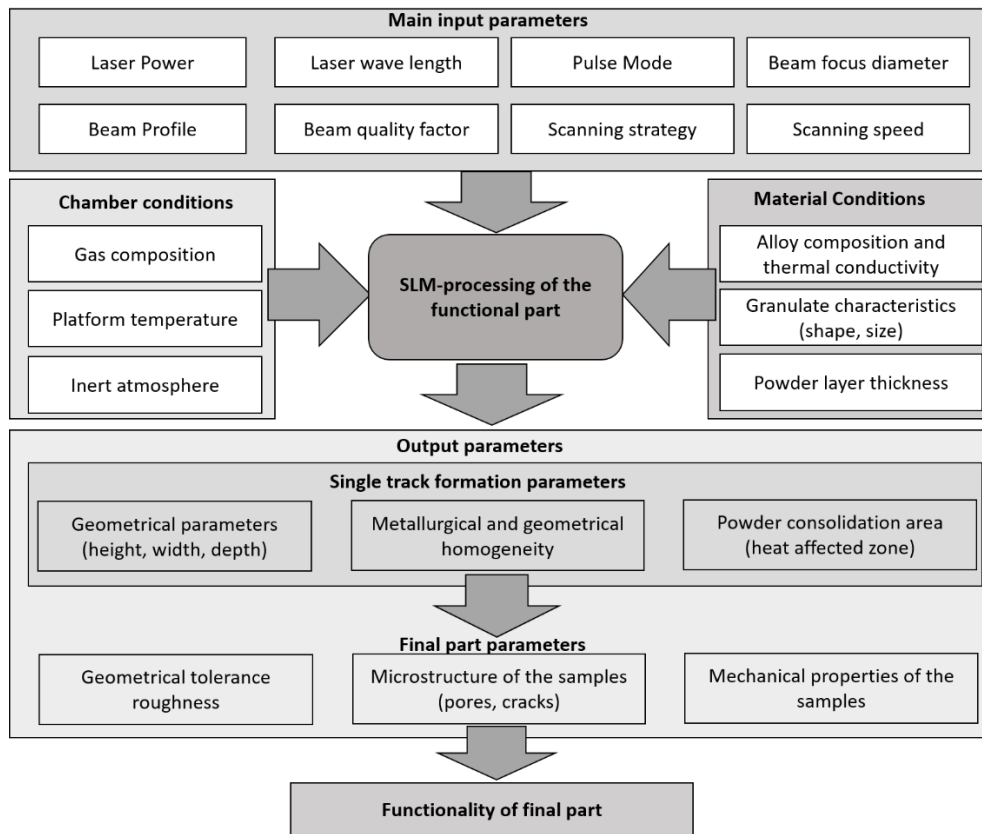


Figure 36: Functionality of input factors and output parameters for the L-PBF process (adapted from [149])

2.6.1 Process Parameters and Material Properties

Since the foremost objective in L-PBF is to produce components with comparable density to cast material, sufficient heat input to melt a certain amount of material is required. Therefore, the process parameters need to be appropriate for each type of metal powder which requires using the correct processing parameters, e.g. laser power and exposure time. When plotting the power and speed of the laser beam as a function of one another, the graph can be divided into four zones, as shown in Figure 37. The combinations of power and speed in zone I result in parts of comparable density to cast material, while high power and lower speed in zone II result in 'over melting' and lower power and high speed in zone III result in lack of fusion. While for zone OH with high power and very low scan speeds leads to significant thermal deformation in the part [150]. A combination of high power and lower scan speed can result in the generation of keyholes due to the excessive heat supply.

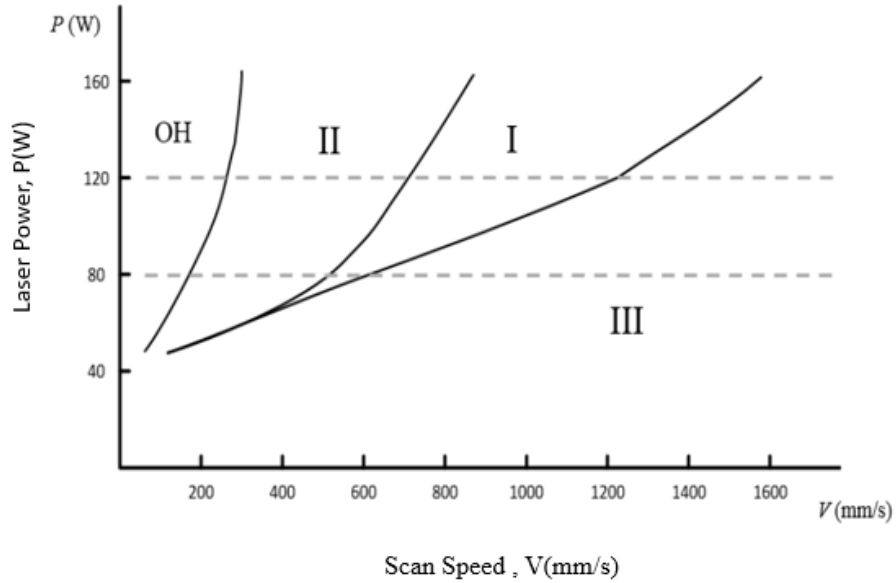


Figure 37: Process window of L-PBF zones for Ti-6Al-4V (from [150])

Process parameters such as laser power, scan speed, point distance, hatch spacing and layer thickness are adjusted for each specific material to assure the powder is completely melted and fused to the neighbouring melt vector and with the previous layers. Not using the correct parameters corresponding to the specific material properties, could lead to the formation of material defects during the process, such as keyhole porosity [151] and lack-of fusion (LoF) [152] defects. The process parameters and the laser-material interaction will be discussed in more detail further in this thesis. It is known that the thermal conditions and cooling rates affect the development of residual stress in the L-PBF process. The parameters for the energy input laser power and scan speed are the primary variables that alter the energy input in the process. The volumetric energy density ED (J/mm^3) is defined as the average energy applied per volume of material was calculated from the formula defined in (Equations (12) and (13)) [153].

$$ED = \frac{P}{SS * HD * LT} \quad (12)$$

$$SS = \frac{PD}{ET} \quad (13)$$

Where, P is laser power (W), SS scan speed (mm/s) defined from Equation (13), PD point distance (μm) over ET exposure time (μs), HD is hatch spacing (mm), and LT is layer thickness

(mm). Simons et al. [154] reported significant higher residual stresses in 316 L-PBF samples when the energy density was increased from 43 J/mm^3 to 71 J/mm^3 . Since components with lower energy density have higher porosity, there are no fixed connections to the surrounding tracks and the residual stresses can be reduced. Yadroitsev et al. [155] in a single-track deposition study reported laser power to be the most important factor in determining the residual stress development in the L-PBF process and in being a critical factor in reducing porosity in the produced samples.

Each cross-section of a part manufactured by L-PBF is produced as a result of laser melting of sections of the powder surface. A schematic of the formation of a melt pool is shown in Figure 38, and is controlled by the scanning parameters, laser power, exposure time, point distance, hatch distance, and layer thickness. The laser beam melts the powder particles, and with each pass, an extended molten pool is formed. Tensile forces below the surface can cause track fragmentation, which is one of the L-PBF problems known as balling-effect [149, 156]. Manvatkar and DebRoy [157] found that lowering the laser power reduced the melt pool size and the heat transfer to surrounding material, which resulted in higher cooling rates [157]. Higher laser power has been reported to result in lower part deformation [158]; while reducing the exposure time or scan speed leads to lower temperature gradients, lower cooling rates and reduces residual stress developed [157, 159, 160]. The limit on the point distance is determined by the ability to produce a continuous melt track because reducing the point distance too much results in a bigger melt pool and a balling effect. In contrast, increasing the point distance too much results in a broken melt track without a proper melting that can generate porosity or delamination.

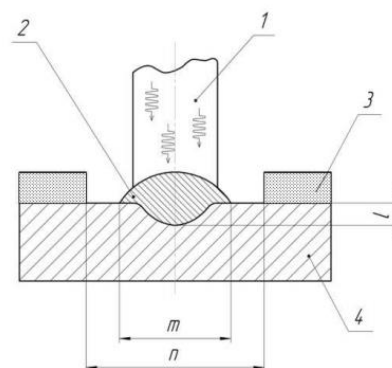


Figure 38: Formation of layer single track in L-PBF, where: 1 - Laser Beam; 2 - Single Track Bead; 3- Loose Powder Material Layer; 4- Base or Previous Layer; l - Melt Pool; m - Track Width; n- Powder Consolidation Area[149]

Ruidi et al. [156] showed that the balling characteristics are also strongly influenced by laser powers (Figure 39). At lower laser power of 70–100 W, the scan tracks were discontinuous combined with having balling initiation. On increasing the laser power to 150–190 W, the scan tracks became continuous without the presence of any balling initiation as seen in Figure 39. Therefore, the high laser power can provide enough input energy, favouring the wetting and spreading of molten pool similar to the influence of scan speed on balling initiation. Zhirnov et al. [149] suggested that properties of the final part depend upon the properties of each track and separate layer as well as on the bond between them. Their experimental results showed that L-PBF has a threshold nature, where, in some areas, the laser melt is continuous and, in other areas, it is unstable where the tracks are not continuous. Instabilities occurred at low scanning speeds in the form of deviations and defects as well as at extremely high speeds where balling effects occurred. Therefore, the size of the melt pool is important in preventing the formation of balling and instability in order to produce a successful layer by layer build.

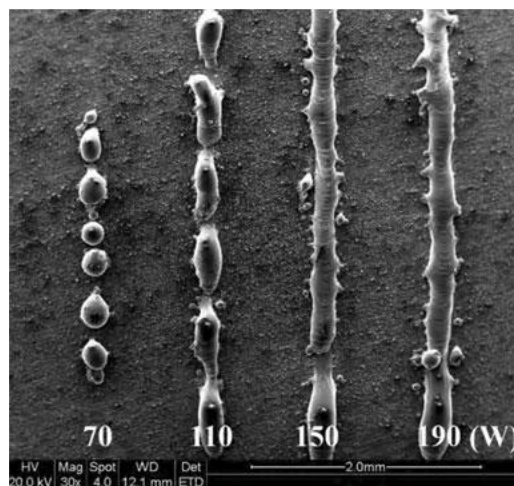


Figure 39: SEM showing the balling effect of single scan tracks occurred while using lower laser powers (70-110 W), while the scan tracks are continuous for higher laser power (150-190 W) (from [156])

Melt pool characteristics, such as geometry and dimensions, provide significant information that is helpful for the determination of process parameters for new materials, and machine set-up or model calibration. Single beads can be easily fabricated and analysed for melt pool characterisation, significantly reducing time and cost compared to conventional optimisation methods based on more expensive experimentation [161, 162].

The use of different metal powders and scanning parameters change how residual stresses are developed in the L-PBF process. The thermal conductivity of materials is especially

important as it determines the temperature gradient during cooling. Conductivity is not, however, the only property that affects the thermal gradient. The length of an L-PBF part and the moment of inertia affect the magnitude of the residual stresses [29]. According to Casavola et al. [109], circular specimens warp less as opposed to components where the geometrical dimensions have greater relative variation. Their work also concluded that for the same diameter, thicker specimens have lower stresses as opposed to thinner specimens. Rangaswamy et al. [102] showed that the geometry of the sample has an important effect on the development of residual stresses, because, the thermal expansion is not the same at the centre and corners of a part. As the laser deposits material away from the edge, the pattern of heat flow is roughly circular in and near the melt pool as shown schematically in Figure 40, however, at an edge, the heat flow is localized and the energy dissipates further into the previous layers.

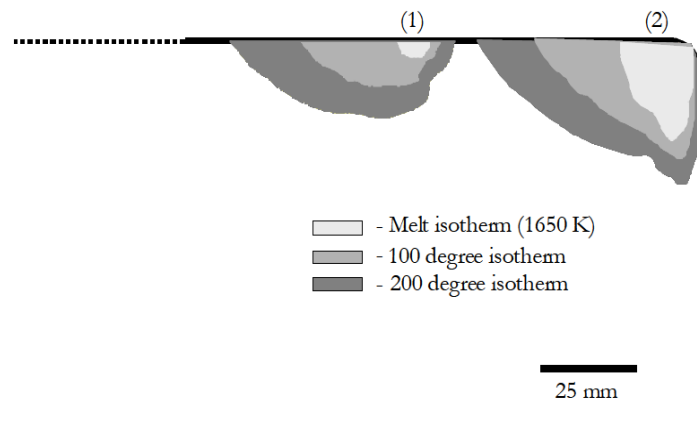


Figure 40: Schematic of the patterns of heat flow in a thin wall sample when the melt pool is (1) in the middle of the top edge and (2) when it is at the side edge of a thin wall plate (from [102]).

Material properties also have significant implications in the thermal contraction mechanism. Materials inherently have different coefficients of thermal expansion; hence the deformation generated from the constrained contraction will also differ. This process is also dependent on the temperature difference between the already solidified and the newly formed layers, which could be affected by the layer thickness. The absorption capacity of the powder layer depends not only upon the powder's physical-chemical properties but also on its granulometry (particle size and shape) and bulk density. When the metal powder is in its solid-state, the material properties are affected mainly by the via thermal conductivity (k), and when the metal powder is melted, it is necessary to consider the ratio of the thermal conductivity and area (k/A) [109].

The geometry of the parts also has a significant consequence on the magnitude and orientation of residual stresses. The part geometry has an effect on the heat transfer within the part and this, in turn, affects the temperature gradient and thus the magnitude and orientation of the residual stresses. The effect of the geometry influences not just the heat transfer during the build, but also the local temperature gradient surrounding the melt pool. If the part is melted with vectors that traverse the full width of the part, the time between consecutive vectors coming back to the same point will be different for different widths. Therefore, the temperature of adjacent vectors will also differ; this means, a higher thermal gradient and thus greater residual stress in parts with long scans in comparison to short scans. When alternating the scan strategies layer by layer, the part temperature will be more homogeneous; this is one of the reasons why it has been proposed in the literature that alternating the scanning strategies in each layer is a way to reduce the residual stresses [48, 49]. The heat transfer is not only dependent on the geometry, but also on the surroundings such as the supports structures used in the build, which can act as conduction paths, and therefore affect the stress [119]. In addition, an experimental analysis done by Casavola et al. [163] using the hole drilling method, suggested that the development of residual stress in an L-PBF component is influenced by the positioning of the part on the build plate and by the thickness of the part, with the lowest stress value occurring at the central position of the build plate and the thickest specimen.

2.6.2 Scanning Parameters

The scanning strategy determines the distribution of energy in each layer. The variation of the scan vector lengths, the sequence and direction of scan vectors and the rotation of the consecutive layers alters the way heat is supplied to the powder bed and affects the properties of the finished part. Vasinonta et al. [164] proposed that different scanning parameters should be used at the edge and at the centre of the part as the heat transfer conditions will be different at the edges of the slice compared to the centre of the layer. At the edges, there is a reduced number of heat transfer paths, which causes the edges to be hotter than the centre. Therefore, a greater temperature gradient will be apparent at the edges, which causes the development of compressive stresses in the centre of the part, and tensile stresses at the edges.

Previous studies in the literature have reported that the residual stresses in a component is affected by the scan strategy used to expose the metal powder in each layer to the laser beam. The scan strategy consists of two main parts: the scan parameters or parameter set (laser

power, scan speed, scan spacing and layer thickness) and the scan pattern (laser path). A number of different scan patterns have been developed in order to improve the efficiency of the L-PBF process. Jhabvala et al. [165] suggested four major scanning strategies to control the temperature gradient inside the part in the L-PBF process. A schematic of the scan strategies is shown in Figure 41.

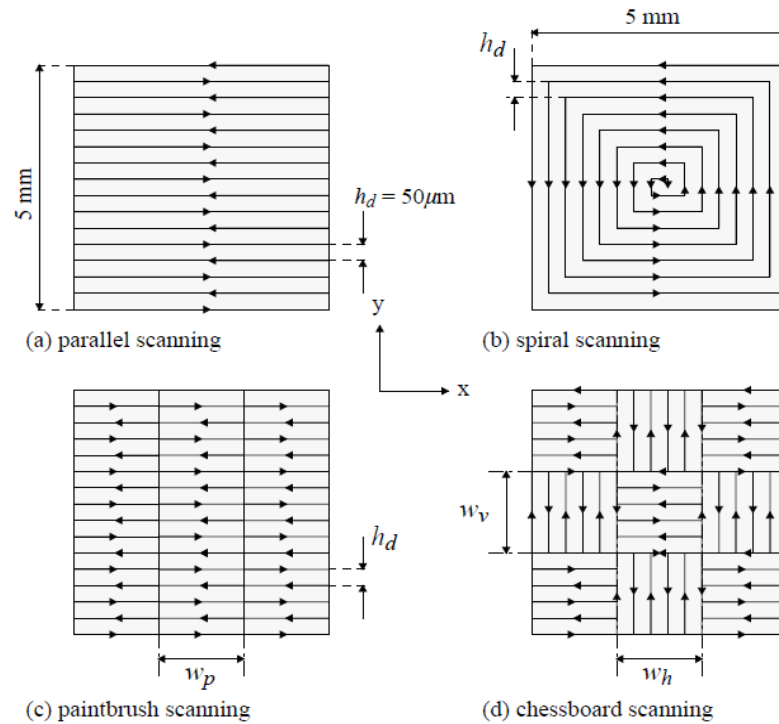


Figure 41: Schematic of four different scanning strategies used in the L-PBF process (from [165])

Parallel scanning is the most common strategy and consists of parallel scan vectors in each with the layer of the part, either all in the same direction, back and forth, or the scan vectors rotate 90° between each layer to form an alternating pattern. Spiral scanning consists of a continuous exposure path rotating from the centre out or from the outside to the centre. Paintbrush scanning consists of splitting the part into columns reducing the length of the scan vectors. Chessboard scanning or island scanning, shown in Figure 42, consists of splitting the part surface into small chessboard squares and parallel scanning each square in a random direction, thus reducing the scan vectors length. These scanning strategies are designed to minimise the thermal influence of previously scanned sectors on the next scanned vector.

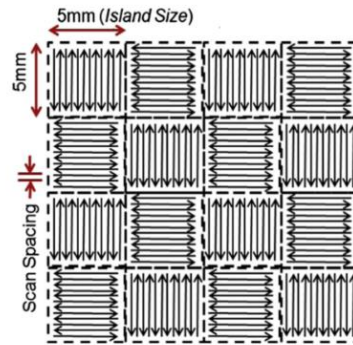


Figure 42: Schematic representation of the Island scan strategy (from [59])

Mercelis and Kruth [91] suggested that the exposure strategy has a significant influence on the residual stress levels developed during the process. Results from their experimental work showed that the stresses are larger perpendicular to the scan direction than along the scan direction. A subdivision of the surface into smaller parts resulted in a lower maximum stress value and equally large stresses in the X and Y direction. Heating of the substrate plate resulted in a reduction of the residual stress level since the temperature gradients were reduced. When the part was removed from the base plate, it contained much lower stress levels than when attached to the base plate, but suffered from deformation during the part removal because, when the part is detached from the substrate, its constraints were released causing uniform shrinkage and bending [94]. The stress distribution in the part, consisted of a zone of tensile stresses just below the upper surface, a large zone of compressive stress in the centre and tensile stresses at the bottom. The magnitude of the stresses depended on the part height and the stiffness and thickness of the base plate. Before the part removal, a greater build height resulted in a lower stress level in the base plate and a more uniform stress level in the part; therefore, the use of a thick base plate resulted in less deformation due to part removal compared to a thin base plate [91, 111, 166].

In an investigation of sectoral scanning or island scanning, Yasa and Evren [167] concluded that sectoral scanning reduced residual stresses compared to common scan strategies, especially when the orientation of the scan tracks was set at 45° to the x-direction as shown in Figure 43. The sector size did not have any significant impact on the residual stresses. The scan spacing between successive scan tracks was found to be optimal at 62% of the spot size when other process parameters were constant (a scan speed of 300 mm/s, a laser power of 100 W and a spot size of 180 μm). Very low scan spacing resulted in excessive energy intensity into the powder material resulting in irregular and large pores. In contrast, very high scan spacing factors resulted in un-molten regions between tracks resulting in aligned and

excessive porosity. With similar results, Zaeh and Branner [95] used of the cantilever method and neutron diffraction to obtain similar results and concluded that the use of island scanning is preferred over long scanning vectors.

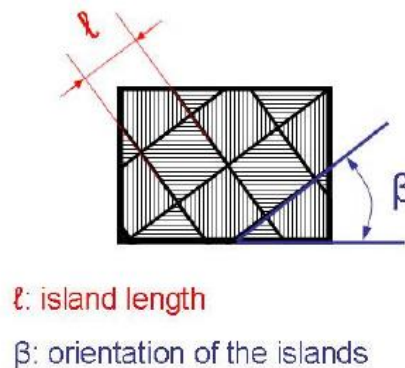


Figure 43: Sector size and orientation of used scan strategy by Yasa and Evren (from [167])

Robinson et al. [49] performed an experimental analysis by building sample blocks with different scanning strategies. Using the hole drilling method, they found that scanning direction, scan vector length and the part geometry had important effects on residual stresses. The direction and magnitudes of the residual stresses were found to be very dependent on the scanning strategy used, with unidirectional scans generating the largest stresses. The use of hatch rotations, other than alternating 90° , showed little benefit in lowering the magnitude of residual stresses; but could lead to a more uniform distribution.

Bo et al. [168] in an experiment using a helix scan strategy and a progressive scan strategy concluded that helix scan strategy was more suitable for complex parts resulting in lower maximum deformations. Jhabvala and Boillat [165] investigated the spiral scan strategy and found that it reduced the temperature gradient within a layer compared to parallel scan vectors.

Carter et al. [59] investigated the effects of the use of different scan strategies and suggested that ideally, the optimum scan strategy should be calculated using a layer by layer approach taking into account the part geometry and even adjusting the fundamental parameters of laser power and scan speed. Manufacturers of L-PBF commercial equipment have made many different laser scanning strategies available, and a classification of these strategies is shown in Figure 44.

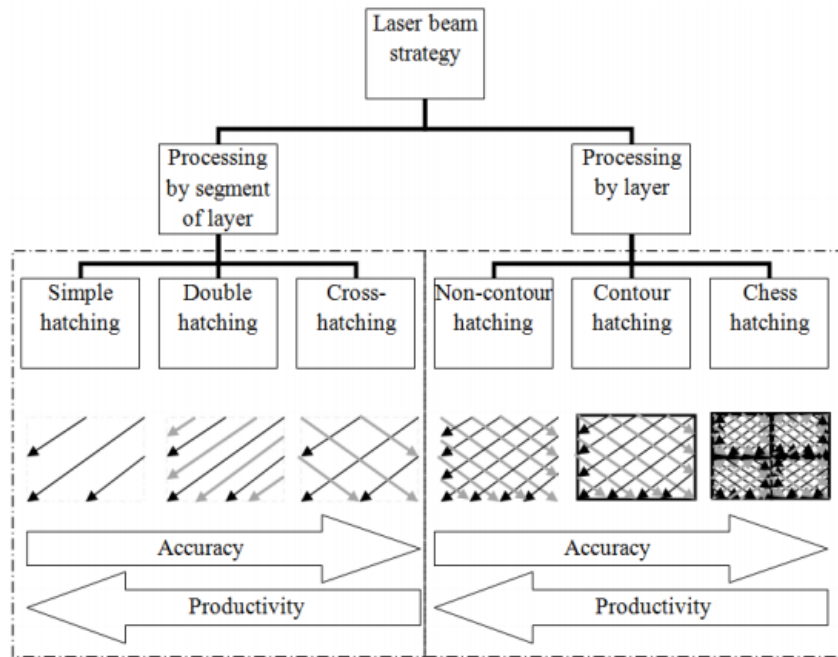


Figure 44: Treatment strategy classification according to laser treatment type in L-PBF (from [149])

2.7 Knowledge Gap in Literature

Laser-Power Bed Fusion (L-PBF) is well-established as an additive-manufacturing process with a history of innovation in machine design culminating recently in multi-laser machines that also include automated, closed-loop material supply, recovery and sieving. A wide range of materials have been investigated, and specialised build strategies developed to permit the production of parts for an ever-increasing number of industrial sectors, including aerospace, automotive and biomedical. However, residual stresses induced in the parts remain an issue for laser powder bed fusion because these stresses can influence the mechanical performance of a part both in terms of decreased functionality due to distortion and of reduced service life due to fatigue and fracture. Two main mechanisms have become popular as explanations of the formation of residual stresses during the L-PBF process, namely the thermal contraction and thermal gradient mechanism. However, despite extensive efforts, our understanding of the mechanism of residual stress formation during L-PBF are limited, and this severely impairs our ability to reliably predict or control residual stresses. This lack of understanding arises partly from the large choice of build parameters available for controlling the building of a part; and partly, from the difficulty in evaluating residual stresses at an appropriate spatial resolution either during or after the build process. There is a significant body of work describing the influence of many build parameters, based on both experimentation and

simulation studies; however, this body of work does not provide a comprehensive or systematic knowledge of these influences and instead provides information about trends, which inhibits the development of optimum build strategies. Residual stresses cannot be evaluated directly and have been inferred from measurements of deformation and strain using point sensors in-situ and after the build process using either destructive techniques, such as hole drilling and the contour method, or non-destructive techniques, such as x-ray and neutron diffraction. However, none of these techniques provides detailed information about the distribution of residual stresses induced during the build process which Carter et al. [59] have proposed will vary both spatially and temporally as each layer is added to a part. Hence, knowledge of the variation of the residual stress, during the build process at an appropriate level of resolution and as each layer is added, would appear to be essential to creating reliable simulations of the process and, hence or otherwise, devising optimum build strategies. Recently in the manufacturing group in the University of Liverpool, Robinson [119] developed a force transducer device (FTD) that provides real-time, in-situ data describing the forces exerted on the baseplate in an L-PBF machine during the build process. Hence, in this study, following a review of the relevant literature (objective #1), the FTD has been selected to explore the evolution of residual stress during the build process (objective #2) and to investigate the influence of a number of key build parameters on the evolution of residual stress in selected materials (objective #3). The use of different metal powders allowed the investigation of the effect of the metal powers on the development of residual stresses (objective #4). The experience gained from this investigation has been used to propose a revised design of the FTD capable of working at higher temperatures and loads. The FTD, as its name implies, provided measurements of the forces generated on the base plate during the L-PBF process from which residual stress can be inferred. Overall, these components of the study are designed to provide new knowledge about the evolution and final state of residual stresses developed during L-PBF by using the latest in-situ measurements technology to provide time-varying data such as each layer is added. The methods employed and results obtained are described in the next chapters.

3 Materials and Methods

This chapter details the materials and methods used during this investigation, including the manufacturing equipment used for the production of the L-PBF samples and details the different metal powders that were studied to evaluate the effect of the material properties on residual stress. In this chapter, a description of the different measurement techniques and software packages used for the analysis of the results is also presented.

3.1 Materials Used

This section presents an overview of the materials used in the experimental work described in this thesis. L-PBF samples were built in different metal powders to evaluate the residual forces developed in the L-PBF process and the part deformation after removal. The materials used for the experimental work are widely used in L-PBF by different industries [13, 18, 25]. For the Encompass project, a study of the effect of residual forces was done in Ti-6Al-4V (Phase 1). After the completion of the Encompass project (Phase 2), and due to the interest and machine availability provided by the sponsor Renishaw, the effect of the material properties on the development of residual forces was investigated using: Inconel 625, Inconel 718 and Maraging steel.

3.1.1 Ti-6Al-4V ELI-0406 Alloy

Ti-6Al-4V ELI-0406 alloy comprises a mass fraction of up to 90% Titanium alloyed with Aluminium up to 6.75% and Vanadium up to 4.5%. Powder supplied by Renishaw for AM has a particle size of 15-45 μm . Ti-6Al-4V has excellent specific strength (strength to weight ratio) which makes it ideal for load-saving structures where weight is an important factor. It has good corrosion resistance, and it is biocompatible, leading to it being widely used for surgical and dental applications. It has good osseointegration properties, low thermal expansion and conductivity. Its material properties specifications are shown in Table 2. Further details of its material specifications can be found in the material data sheet in Appendix A1.

Table 2: Ti-6Al-4V ELI-0406 alloy material properties

Density	4.42 g/cm ³
Thermal conductivity	6 W/mK to 8 W/mK
Melting range	1635 °C 1665 °C
Coefficient of Thermal Expansion	$8 \times 10^{-6} k^{-1}$ to $9 \times 10^{-6} k^{-1}$
Particle size distribution	15-45 μ m

3.1.2 Inconel 625-0404 Alloy

Inconel 625-0404 alloy comprises Nickel alloyed with Chromium of mass fraction up to 23% and Molybdenum up to 10%, along with other minor elements. Powder supplied by Renishaw for AM has a particle size distribution of 15-45 μ m. Inconel 625 has a wide range of applications in industry, particularly where good tensile, creep, rupture strength, very high corrosion and oxidation resistance at high temperatures is required. Its material properties specifications are shown in Table 3. Further details of its material specifications can be found in the material data sheet in Appendix A1.

Table 3: Inconel 625-0404 alloy material properties

Density	8.44 g/cm ³
Thermal conductivity	9.2 W/mK to 10.7 W/mK
Melting range	1290 °C 1350 °C
Coefficient of Thermal Expansion	$12.8 \times 10^{-6} k^{-1}$
Particle size distribution	15-45 μ m

3.1.3 Inconel 718-0405 Alloy

Inconel 718-0405 alloy comprises a mass fraction up to 55% Nickel alloyed with Iron to 21% and Chromium up to 21%, along with other minor elements. Powder supplied by Renishaw for AM has a particle size distribution of 15-45 μ m. Inconel 718 has a wide range of applications in industry and is particularly suitable for applications where good tensile creep and rupture strength are required. Properties of this material include high strength, excellent corrosion resistance and a working temperature between -250 °C and 650 °C. Its excellent welding characteristics and resistance to cracking makes it an ideal material for AM. Its material properties are shown in Table 4. Further details of its material specifications can be found in the material data sheet in Appendix A1.

Table 4: Inconel 718-0405 alloy material properties

Density	8.19 g/cm ³
Thermal conductivity	6 W/mK to 12 W/mK
Melting range	1260 °C 1336 °C
Coefficient of Thermal Expansion	12 µm/mK to 16 µm/mK
Particle size distribution	15-45 µm

3.1.4 Maraging Steel M300.

In Maraging Steel M300, Nickel is the main alloying element with up to 19% mass fraction, with Cobalt up to 10%, Molybdenum up to 5.2% and Titanium up to 1.2% as secondary intermetallic alloys. This metal alloy has a martensitic crystal structure and is strengthened by ageing at approximately 500 °C. This ultra-low Carbon alloy has very high strength and hardness properties delivered from precipitation of intermetallic compounds. It is widely used in mould and die tooling due to its high strength, high hardness, wear resistance, and good machinability. Its material properties are shown in Table 5. Further details of its material specifications can be found in the material data sheet in appendix A4.

Table 5: Maraging Steel M300 alloy material properties

Density	8.1 g/cm ³
Thermal conductivity	142.2 W/mK at 20 °C, 21.0 W/mK at 600 °C, 28.6 W/mK at 1300 °C
Melting point	1413 °C
Coefficient of Thermal Expansion	$10.3 \cdot 10^{-6} \text{ K}^{-1}$
Particle size distribution	15-45 µm

3.2 Manufacturing Equipment

All experiments were carried out on a Renishaw AM250 (Renishaw, UK) L-PBF machine (Figure 45) at Renishaw PLC facilities in Stone, Staffordshire UK. The Renishaw AM250 is an industrial 3D printer which uses the typical Selective Laser Melting (SLM) 3D printing technology, designed for the production of components with high precision and surface quality. From the beginning of the project, the Renishaw AM250 - W44 was assigned by the sponsor, Renishaw in collaboration with the Encompass project, to study the effect of residual strain in Ti-6Al-4V (Phase 1). After the completion of the Encompass project (Phase 2) in order to compare the development of residual stresses in different metal powders experimental work with different materials was carried out using: Inconel 625, Inconel 718 and Maraging steel.

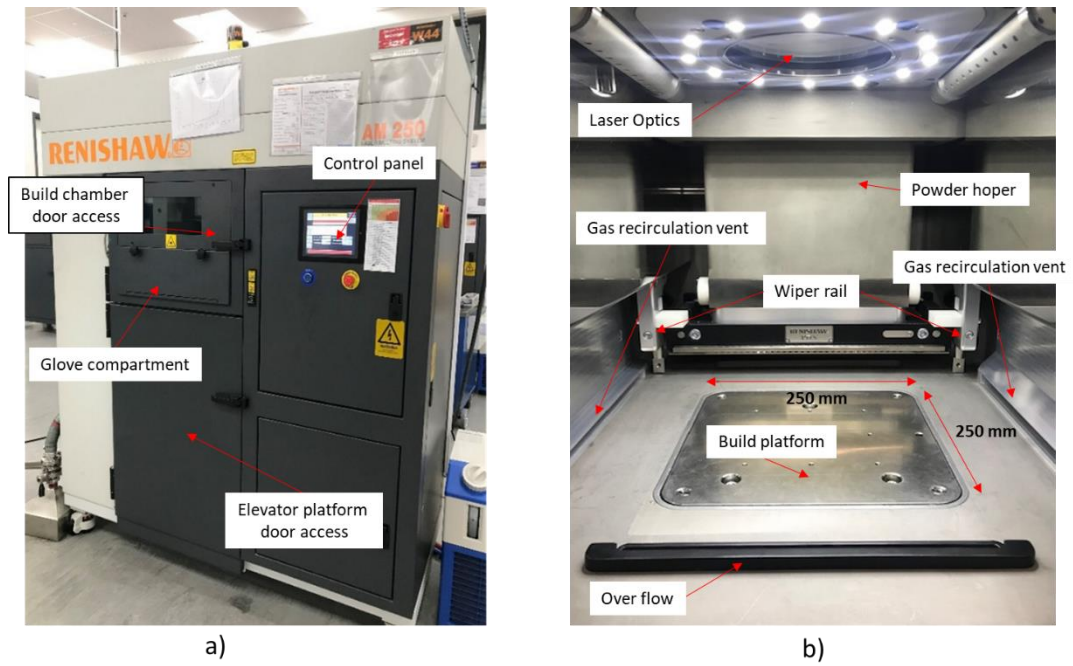


Figure 45: a) Renishaw AM250 L-PBF machine and b) inside view from the build chamber

The Renishaw AM250 operates with an R4 RedPOWER (SPI Lasers, UK) laser which is a modulated ytterbium fibre laser with a maximum power output of 200 W and an output wavelength of $\lambda=1070$ nm. The laser beam at its focal point has a Gaussian profile with a $1/e^2$ diameter of approximately 70 μm , as shown in Figure 46. The machine specifications are shown in Table 6.

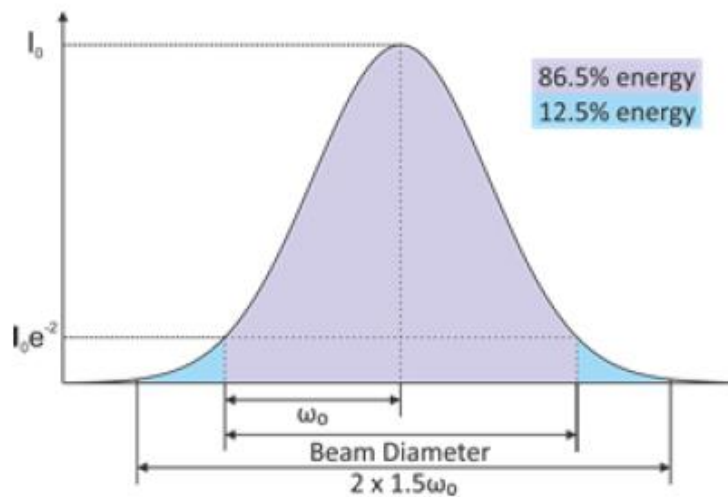
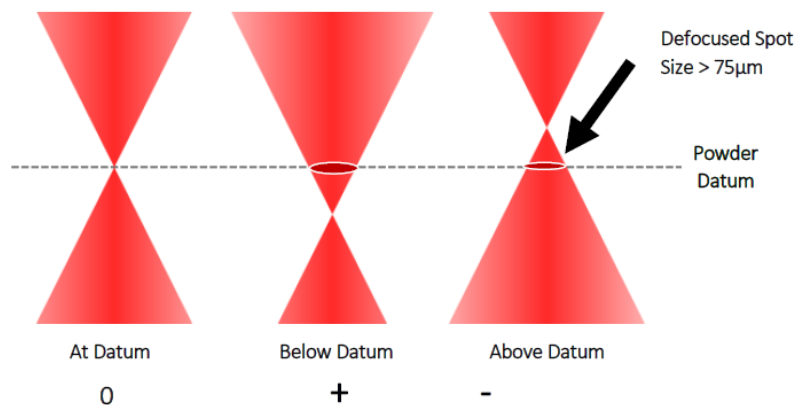


Figure 46: Renishaw AM250 laser beam profile

Table 6: Renishaw AM250 Machine Specifications

Machine	Build Volume [mm]	Laser Power [W]	F-theta focal length [mm]	Nominal Focus Diameter [μm]
Renishaw AM250	250 X 250 X 300	200 W IPG	250	70

The Rayleigh length for the focal point is around 2 mm long, which gives a ± 1 mm tolerance with which the focus spot can be achieved. The optical system consists of a Galilean beam expander formed of three lenses within a bespoke linear guide system. The beam is directed by two galvanometer scanning mirrors which steer the beam through an f-theta objective lens that adjusts the focal length to a flat field thus keeping the spot size the same across the powder bed. The diameter of the spot can be adjusted by moving the objective lens along the beam direction. A positive value will move the focal point below the datum, and a negative value will bring the focal point above the datum line, as described in Figure 47.

*Figure 47: Focal point at datum plane (from [169])*

The Renishaw AM250 machine operates with a protective overpressure Argon gas atmosphere. Oxygen is removed from the machine by a vacuum system and refilled with Argon gas, which gives an Oxygen content within the build chamber of less than 0.1 %. A gas recirculation system flows over the build area to blow vapour and spatter away from the powder bed to avoid contamination. The vapour flows through gas vents, and spatters are trapped by a filter. The system operates with a safe change filter for the removal of nanoparticles, which are formed from the condensation of the metal vaporised during the process, and which are pyrophoric due to their high surface area to volume ratio. The safe filter keeps the spatters out of contact with Oxygen, thus evading potential hazards. The build platform

dimensions are of 250 mm x 250 mm x 300 mm. The dosing system consists of a fixed hopper for powder loading, and the defined amount of powder to be dosed is triggered by a wiper system. Each dose is evenly distributed across the building platform by a silicone recoater (see Figure 45b).

3.2.1 Manufacturing Process

The following steps outline the process that is involved in the manufacture of a part by L-PBF irrespective of the machine used. A schematic of the L-PBF machine can be seen in Figure 48:

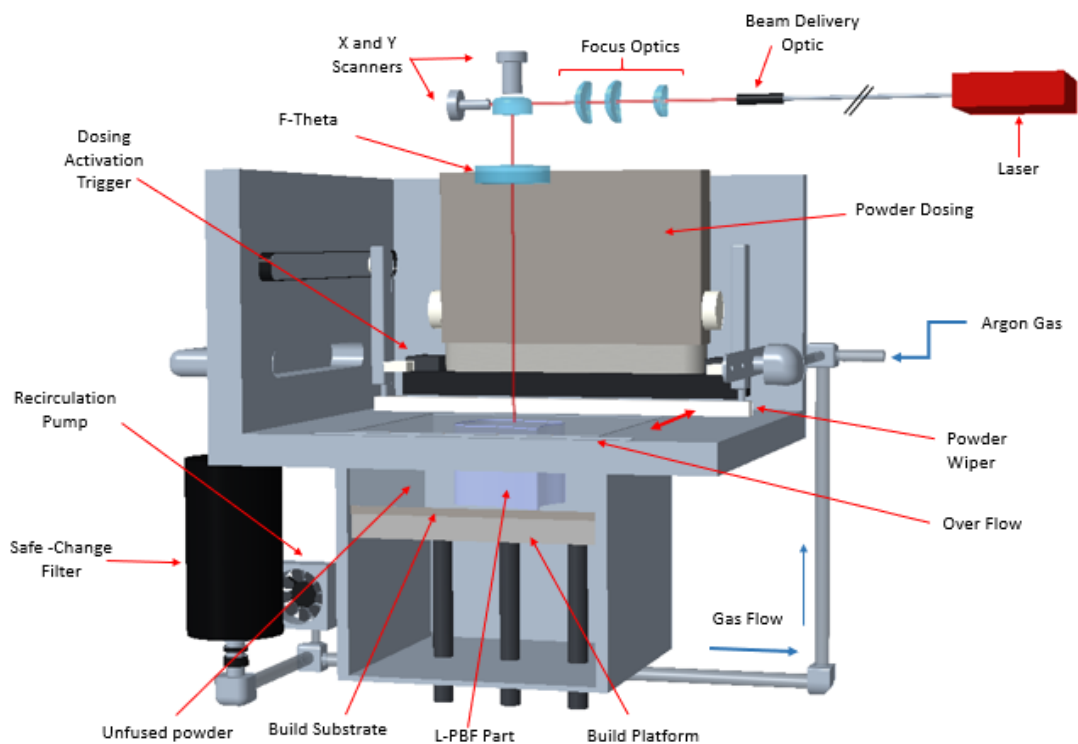


Figure 48: Schematic of a Renishaw AM250 L-PBF system

A build file (.MTT format) is loaded into the L-PBF machine. The file is prepared using QuantAM software (Renishaw, UK) to customise the material profile based on the metal powder, build parameters (i.e., scan strategies, layer thickness, scan speed) and allowing for the creation of additional supports when needed. The .MTT files are converted directly from an .STL file [1, 170] which are standardised files for AM technologies and divide the 3D parts into 2D triangles.

A flat substrate of similar material to the metal powder is securely fastened to the build platform of the L-PBF machine. To ensure the flatness of the substrate, the thickness of the substrate is measured at each corner with a digital calliper, and the average is input into the machine to provide a datum for positioning the laser. Then, the substrate is securely attached

to the build platform by aligning the four bolt holes on the substrate to the ones on the build platform. Once the holes are aligned, the bolts are inserted and must be tightened with an Allen key so that the substrate is secured firmly to the build platform and to avoid any movement of the substrate during the building process, as well to ensure that the bolt head does not protrude above the substrate to avoid any interactions with the wiper.

The height of the recoated blade must be calibrated so it can deposit an evenly distributed layer of powder. The space between the recoater blade and the substrate is measured across the entire building surface using a 50 μm gauge. Setting the proper wiper height ensures that the melted powder will properly fuse to the substrate on the first layer and that the powder will be evenly distributed across every layer during the build process.

L-PBF process is performed within an inert gas atmosphere to reduce the rate of oxide formation on the melted metal and for safety reasons by keeping the process chemically inactive relative to reactive gases that exist in the air (i.e. O_2 and CO_2). Renishaw uses Argon as inert gas for the building environment of its additive manufacturing systems. In order to create an inert atmosphere inside the chamber, first, a vacuum is created by removing all the Oxygen from the chamber. Then, the Oxygen levels are dropped further by purging the chamber with Argon gas until the Oxygen level falls below 0.1% (<1000 ppm). The Argon gas pressure in the machine must be kept between 7-15 mBAR to prevent air from leaking into the chamber. The Argon gas is recirculated through the machine with a recirculating pump, and gas flows over the build area to blow away vapour and spatter to avoid contamination of the part. The gas flow also carries highly reactive nanoparticles into the safe change filter to be neutralized. This condensed material is highly flammable and can immediately ignite when exposed to air. Therefore, after the build is completed, the safe change filter is completely sealed by closing the top and bottom knobs before being removed from the machine keeping the spatters out of contact with Oxygen. Then, the safe filter change is carefully filled with water to neutralise the condensed nanoparticles attached to the filter during the build process.

For powder dosing during the building process, the metal powder (typically with a spherical size particle between 15-60 μm) is stored in a hopper, where the minimum level for completing the build must be kept avoid from running out during the build. The characteristics for AM metal powder, such as spherical particle shape, close packing of particles and good flow, are fundamental to achieving a consistent powder dosing through the build process. A single dose of powder is released from the hopper by the recoating mechanism triggered by the wiper arm and is spread uniformly by a silicone wiper over the whole area of the substrate.

To ensure the build platform is completely covered on each layer, the quantity of powder to be dosed must be defined for each build and can vary depending on the layer thickness. Any excess powder drops into the front and back overflow compartments to be sieved and reused in future builds.

The laser is scanned over the metal powder to melt and fuse the metal powder particles together and to the previous layers to form the desired parts. The laser operates by using point exposures; each point is given an XY coordinate position along with pre-set parameters to avoid porosity: point distance (mm), exposure time (μm) and power (W).

After the geometry is scanned, the build platform moves down by the chosen layer thickness, and the process of powder deposition and laser exposure is repeated until the desired part(s) has been manufactured.

To remove the part from the machine, the build platform is raised to the maximum top position, and the unfused powder is carefully removed from around the part by slowly raising the substrate and sweeping the excess powder into the overflow compartment by hand using brushes. Once all the powder is swept away, the substrate is removed from the chamber.

The part is removed from the base plate by the use of a wire-cutting system. A wire Electro Discharge Machine (wire EDM) [171] is commonly used for L-PBF part removal due to its high precision and because it can have a cutting path or kerf as small as 0.021 mm (0.83 mils) using \varnothing 0.02 mm (0.79 mils) wire. The wire EDM process is achieved by creating an electrical discharge between a thin single-strand metal wire, usually brass, which is fed through the workpiece, submerged in a tank of dielectric fluid, typically deionized water, in order to control the sparking process from shorting out [171]. Because wire EDM does not require high cutting forces for removal of material no change in the mechanical properties of a material is expected. However, the part can distort due to the residual stress-relief in the machining process. Wire EDM was used for this experimental work to cut off the FTD part from the machined pegs in order to re-use the machined pegs for future builds. After the part is wire cut from the base plate additional cleaning of the part to remove any loose powder is done using an ultrasonic bath and parts are rinsed with ethanol or deionised water. Once the part is completely cleaned and any excess powder removed, post-processes are performed which might include, machining, polishing and or heat treatments.

The unfused powder is sieved with a 56 μm mesh screen and ultrasonic deblending for 10 minutes in order to remove any large particles or sintered globules ejected from the melt pool.

All the powder from the overflow bottles must be sieved before it can be reused for future builds to remove any contaminated powder that could affect future builds. Once the powder is sieved, the cleaned powder is deposited into clean bottles and fed into the L-PBF machine for reuse.

3.2.2 Scanning Parameters

A 3D CAD solid geometry can be created in a variety of solid modelling software such as Creo (PTC, USA). To create the data that is required to build the part, the geometry information must be converted into a standardised file format; the current accepted standard file is Stereolithography (STL) [1]. This file contains an unstructured set of triangles each with a vector normal to the surface that points to the outside of the part. These triangles form an interconnected surface that is used as an approximation to the surface of the part (see Figure 49). The accuracy and resolution of this representation are dependent on the number of triangles and the levels of curvature of the original surfaces. The STL file is then sliced into 2-dimensional layers with a particular layer thickness. For L-PBF, this layer thickness generally ranges between 20 μm and 100 μm . To convert these outlines into a solid structure the whole bounded area must be exposed to the laser. Scan vectors are generated that will fill the 2D slices; these define the path that the laser will follow in each layer. Hatching is the process by which the 2D slices are converted into a toolpath or scan lines. There are a variety of hatch types used in L-PBF and described in the literature; the three scan strategies used for this experimental work are Meander, Stripe and Chessboard, which are described in Figure 50. The selected scan strategies for the experimental work were the strategies used by Renishaw for their commercially manufactured parts. These scan strategies were selected as part of the investigation as they cover the principal variations in scan strategies generally used in the L-PBF process [160]: Meander, single line vector, and two types of sectional scanning Stripe and Chessboard.

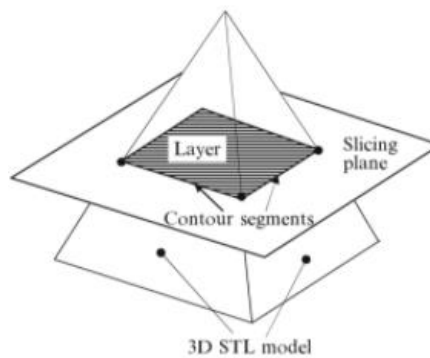


Figure 49: Definition of a layer through the intersection between the 3D STL model and a slicing plane (from [2])




Scan Strategy	Layout	Description
Meander		Straight line vector path from each side of the border. The beam passes to the preceding tracks in quick successions at the top and bottom hand corners.
Stripes		The area within the border is split into stripes 5mm and a meander technique is used within each stripe which allows more consistent temperature. Stripe offset is used to overlap stripes to prevent porosity
Chessboard		Layer is divided into square fields 5mm^2 , like a chessboard. Each field is rotated by 90° . Field offset is used to overlap stripes to prevent porosity

Figure 50: Description of scan strategies used in L-PBF (adapted from [169])

The distance between the hatch lines is defined in the material file as the hatch distance. Hatch lines are subdivided into a series of points. Instead of running continuously, the laser operates by using discrete point exposures. Each exposure creates a melt pool of metal, which takes the form of a 3D Gaussian curve. A representation of the point distance and hatch lines are shown in Figure 51.

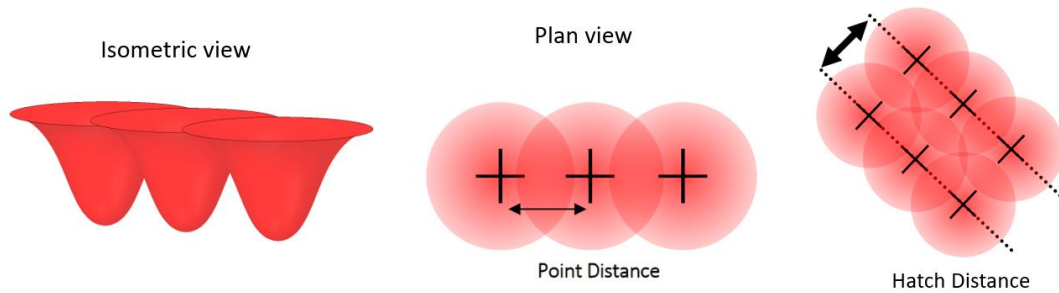


Figure 51: Schematic of the laser scanning point exposure and hatch distance (adapted from [169])

The key parameters for the laser scanning process are:

- **Power (W):** dictates the intensity of the laser beam
- **Exposure time (μs):** length of time the laser will be on for each point.
- **Point distance (mm):** the distance between the centres of each successive melt pool
- **Hatch distance (μm):** the distance between the lines of point exposures.

It is important to select the correct hatch distance in order to produce nearly completely solid components; hatch lines need to overlap in order to completely melt all the powder within the part geometry and to reduce the porosity in the part. A schematic of the parameters for each scan layer is shown in Figure 52.

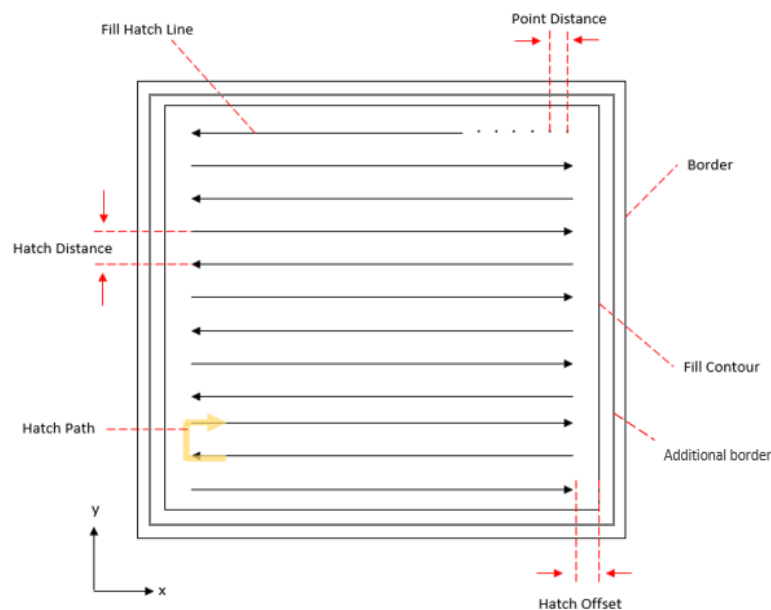


Figure 52: Schematic of scanning parameters used in the L-PBF process

3.3 Software Packages

Different software packages were used throughout the investigation with a variety of applications and capabilities. These applications include the creation of 3D CAD models, design and manipulation, data acquisition, programming and simulation.

3.3.1 **Creo 5.0 (PTC, USA)**

Creo Parametric, formerly known as Pro/ENGINEER, is a design software for solid modelling. This software was used to design all the L-PBF samples tested for the experimental work. This software was also used to design modifications to the FTD and to develop a proposed new design of FTD. This software was used due to compatibility with prior work and because it provides the tools needed for the design of L-PBF samples; as well as the option to easily convert files into .STL format for the L-PBF process.

3.3.2 **QuantAM 4.1.0.76 (Renishaw, UK)**

QuantAM is the data preparation software for Renishaw AM machines. Its function includes slicing of the imported .STL file. This software was used to prepare the L-PBF build files, set the part orientation and location in the build platform. The software allows the production of additional supports when needed. This software was used to select the filling hatch strategy and to set the material file for the metal to be used which assigned the process parameters. This software is an integral part of the Renishaw product and is supplied with the Renishaw AM250 machine used for the experimental.

3.3.3 **ImageJ/FIJI 1.48 (National Institute of Health, US)**

ImageJ is a Java-based program developed at the National Institutes of Health and the Laboratory for Optical and Computational Instrumentation. The software allows the analysis of microscopy samples and the analysis of image structures. FIJI is an image processing tool-kit and was used for the majority of the image analysis and processing development within the project. This software was used due to its availability and capability to measure dimensions in microscope images of the melt pool.

3.3.4 **InstruNet World Plus v3.7 (GW Instruments, US)**

InstruNet World Plus is a data acquisition software. It enables one to digitise, plot, control, analyse and save to disk analogue to digital (A/D), digital to analogue (D/A), and digital input or output (I/O) data from InstruNet hardware. The software was used for data acquisition during the in-situ measurements during the L-PBF process. This software was used due to its

availability and compatibility with InstruNet boxes to which the load cells and thermocouples were connected.

3.3.5 Abaqus Student Edition 2017 (Dassault Systèmes, France)

Abaqus is a Finite Element Analysis (FEA) package that runs from either a command line or a GUI interface. The GUI function allows both pre-processing, solving and post-processing functions. The main use of this software was to simulate the experimental results from the in-situ measurements for part deformation and residual stress developed in the process. This software was used as it is provided by the University of Liverpool. It contained the functions needed for the simulation, i.e. the spring element mechanism required to simulate the load cell in the FEA analysis used for the part deformation analysis of the sample.

3.3.6 ExaSIM v2.2 (Ansys Inc., US)

An Ansys software exaSIM, developed by 3DSIM, is a simulation software that can help machine operators and designers using additive manufacturing to develop parts and to identify residual stress, distortion and build failure. The software allows the simulation of part deformation and stresses after removal for different materials and PBF machines. This software was used as it was provided as part of a collaboration with 3DSIM during the project.

3.3.7 Conform Surfaces 1.2 (University of Liverpool, UK)

This software was developed at the University of Liverpool [119]. It includes the algorithms for creating conformal surfaces, surface modifications and structure analysis. This software was used because of the capabilities of the software to design porous structures from a solid CAD model.

3.4 Measurement Equipment

The following section details the measurement equipment used in the experimental work.

3.4.1 Image Correlation System Q-400 (Dantec Dynamics, DNK)

The Digital 3D Image Correlation System Q-400 is an optical measuring device for full-field, non-contact and three-dimensional measurement of shape, displacements and strains on components and structures made from almost any material. A multi-camera system was used to measure the part deformation of the samples after removal from the building platform.

3.4.2 Instron® 5984 tensile testing machine (Instron, USA)

The Instron 5984 is a dual compressive and tensile testing machine fitted with a 100kN load cell controlled by the Bluehill software (Instron, USA). This testing equipment allowed compression or tensile loading of material samples to establish their strength and stiffness.

3.4.3 SEM JOEL JSM 7001f (Joel Ltd, U.K.)

The JOEL JSM-7001F is a field emission Scanning Electron Microscope (SEM). This machine was used for Scanning Electron (SE) imaging and Energy-Dispersive X-ray (EDX) analysis, as it has an Oxford Instruments INCA X-act EDX detector. The SEM was used to capture images for the analysis of the melt pool geometry and melt pool boundaries of the L-PBF samples.

3.4.4 SmartScope® ZIP 300 (OGP, UK)

SmartScope ZIP® 300 is a fast, accurate metrology system offering a combination of hardware performance, optical capability, and ease-of-use to fully characterise parts automatically in a single setup. It is composed of a rigid cast iron base that ensures stability and metrological accuracy. As a multisensor machine, SmartScope ZIP 300 is available with contact and non-contact probes, including the unique switchable TTL (through-the-lens) laser, which was used for the determination of the density of the samples.

3.5 Measurement Methods

This section details the measurement methods and the protocols followed during testing.

3.5.1 Melt pool and Microstructure Analysis

In order to measure the melt pool characteristics for the single bead-tracks, the specimens were first sectioned through the middle of the part to reveal the melt pool depth of single tracks. The sections were vacuum mounted in a low viscosity epoxy resin (Eposet, Metprep Ltd, UK). The mounted specimens were polished down to a surface integrity of 10 µm using standard metallographic techniques. Fine chemical polishing was accomplished using a "Metaserv Auto-pol" machine (Metallurgical Services Ltd, UK), operating at 150 rpm, on a short-napped cotton substrate. Samples were washed with a mild detergent solution, rinsing initially with distilled water and finally with ethanol and dried in a stream of hot air. The melt pool characteristics were then analysed under a microscope; measuring melt pool dimensions, i.e. width, height and depth. A schematic of the dimensions acquired for the melt pool analysis is shown in Figure 53. A light optical microscope (LOM) and Scanning Electron Microscopy (SEM) machine were used for imaging and analysis. The JOEL JSM 7001f machine was used

for SE imaging and EDX analysis, as it has an Oxford Instruments INCA X-act EDX detector. The EDX detector system provided a chemical analysis of the samples which provided accurate data at the micro- and nanoscales. The SE and EDX images helped to reveal the melt pool formation which is difficult to detect by using a standard microscope. Accelerating voltage can be selected in the range of 0-40 kV and different accelerating voltages were used depending on the requirement for the microstructure analysis.

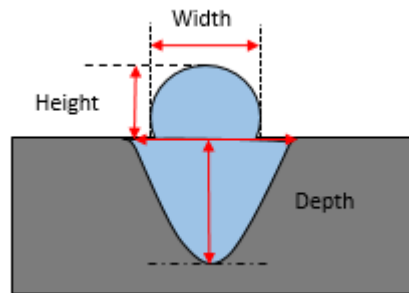


Figure 53: Melt pool characteristics for laser-powder interaction for single beads

3.5.2 Relative Density of Solids

In order to assess their relative density, the samples were first sectioned through the centre of the part, removing any molten material that could be attached at the surface of the part which could affect the density measurements. The samples were vacuum mounted in a low viscosity epoxy resin (Eposet, Metprep Ltd, UK). To facilitate a rapid and consistent production of specimens the mounted samples were automatically polished using a Buehler Automet™ 250 grinder polisher (Buehler, USA) to 20 nm surface finish with the use of noncrystallising Colloidal Silica, following standard procedures for each metal. After polishing, the samples were washed with a mild detergent solution, rinsing initially with distilled water and finally with ethanol, prior to drying in a stream of hot air. The density of the samples was then measured using the SmartScope® ZIP 300 optical CMM. The samples were mounted and fixed into the sample holder, and optical density testing was carried out on 10 mm x 10 mm x 10 mm blocks. For porosity analysis twenty images of each cube were taken, stitched together, a threshold applied to generate binary images, and the pixels counted to reveal the metallurgical porosity of the specimens; this method was able to detect pores greater than 14 µm in diameter.

3.5.3 Tensile Testing

Tensile test specimens of the geometry shown in Figure 54 were fabricated parallel to the build direction of the machine (Z-axis). Tensile tests were performed on an Instron 5984 tensile testing machine equipped with a UKAS calibrated 100 kN load cell and an Instron® extensometer (Instron, USA), with the experiments being logged and controlled using the Bluehill® 3.76 software (Instron, USA). Tests were conducted using strain rates of 0.005 min⁻¹ (start to yield point) and 0.05 min⁻¹ (yield point to failure). The strain rates were defined by Renishaw as for following their standardised procedure.

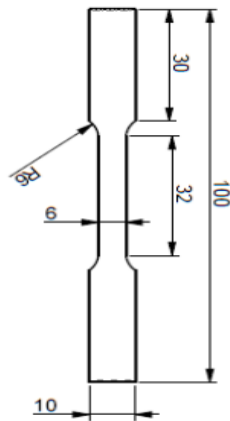


Figure 54: Geometry of tensile test specimens (dimensions in mm)

3.5.4 Part Deformation after Removal

The residual stresses developed during the building process in L-PBF parts are released when the part is detached from the base plate. The amount of deformation occurring on release is related to the distribution of residual stresses in the part. A non-contact measuring system, Digital Image Correlation (DIC), was used to measure the part deformation of the L-PBF samples after removal from the FTD. Digital Image Correlation (DIC) is a 3D, full-field, non-contact optical technique for measuring contour, deformation, vibration and strain in almost any material. The setup used consisted of a Digital Image Correlation System (DIC) (Q-400 DIC – Dantec Dynamics GmbH, Ulm, Germany) fitted with a pair of CCD cameras with matching 50mm lenses. The basic operation of DIC consists of tracking a speckle pattern in reference and deformed images; therefore, a speckle pattern must be applied to the sample. The pattern must cover the area of interest, therefore, to measure the out of plane displacement in the build direction of the part, the FTD samples were prepared for analysis by adding a speckle pattern on the top surface. First, as a background, the surface of the part was completely painted with white spray paint. After the paint was completely dry, speckle pattern

in the form of dots of black paint was sprayed into the surface. To make sure that the Force Transducer Device (FTD) was stationary while the bolts attaching the part were being released, the FTD was clamped into a flat surface. Measurements for the part deformation were recorded as the stresses were relieved when the bolts that attached the build to the load cells were removed one by one from the back of the device. A schematic of the DIC set-up for measurement of the part deformation is shown in Figure 55.

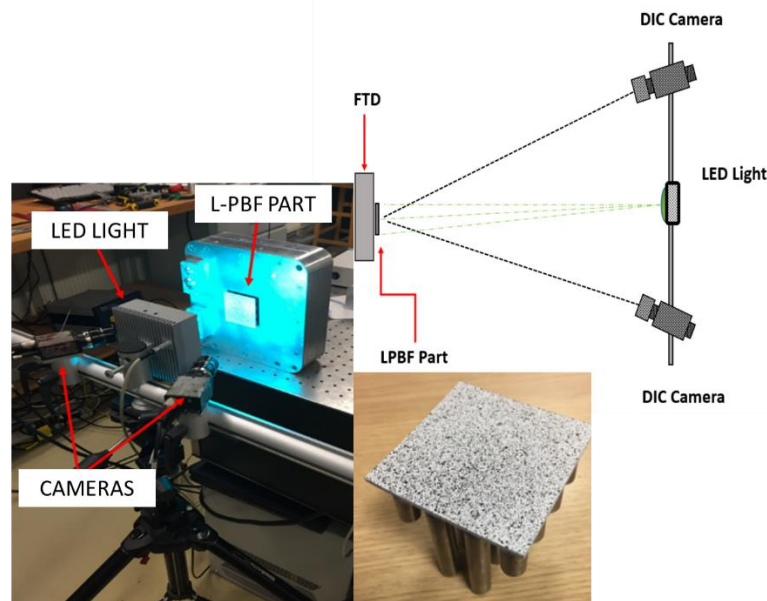


Figure 55: DIC Setup for part deformation measurements (top and bottom left). FTD sample with speckles with white and black paint to the surface of the part (bottom right).

3.5.5 In-situ Measurements of Strains Developed in L-PFB

The literature shows that residual stresses arise in the L-PBF process due to the high energy input and the rapid changes in temperature during the building process [59, 132, 141]. Some research has been done on the development of residual stress during the L-PBF process through in-situ measurements from the build plate [45, 47, 48, 119], but there is still not a clear understanding of how residual stress develops in the actual part during the L-PBF process. It is difficult to measure residual stresses in-situ with most measurement techniques due to the fact that the part is completely surrounded by powder obscuring all but the top layer of the part. A comparison among the in-process measurements reported in the literature to estimate or infer residual stresses during the L-PBF process is shown in Table 7. Shiomi et al. [44], and Van Belle et al. [49], used strain gauges located under the base plate to measure the strain variation per layer during the L-PBF process. Dumber et al. [50] measured the base plate

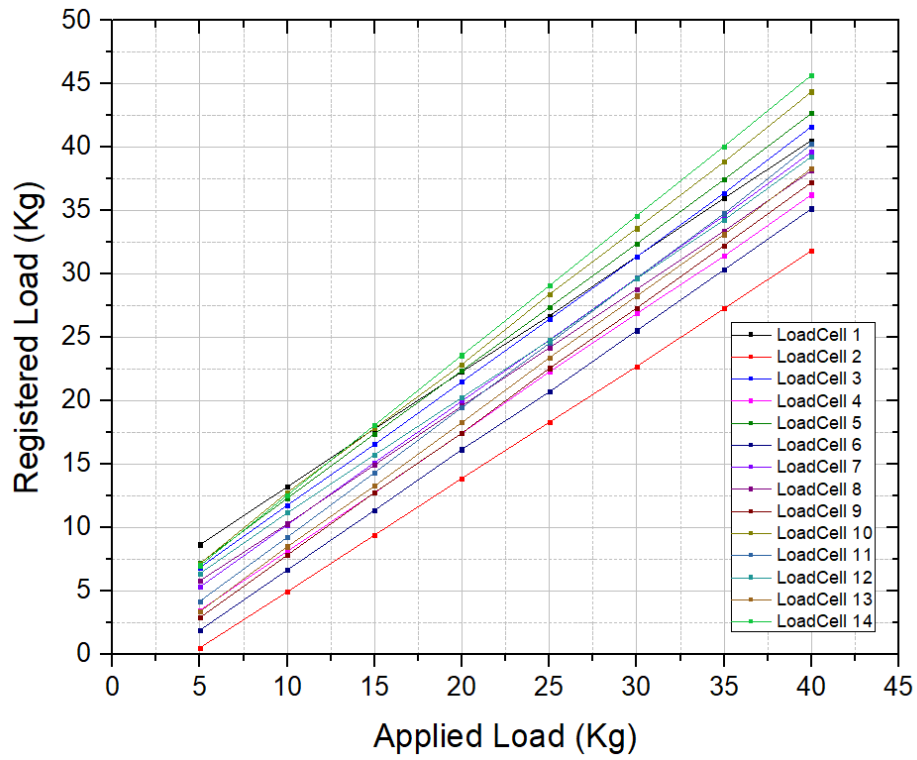
distortion during the process, and Robinson [119] manufactured a Force Transducer Device (FTD) to measure the forces developed while the part is being built. As many measuring methods were available, it was necessary to select the one that would be most advantageous to the research objectives. While Shiomi's, Van Belle's and Dumbar's proposed methods are limited to providing information at the base plate and at a single point, Robinson's multiple load cell arrangements allow measuring the developed forces directly from the sample and measurements are taken at different positions on the part. The method proposed by Robinson [119] gives a good opportunity to understand the evolution of the residual stresses during the process at different sections in the part geometry tested; therefore, this novel measurement technique was used for the measurements of in-situ residual stress presented in this thesis. This section describes the design of the FTD.

Table 7: In-process measurements used to estimate or infer residual stresses during the L-PBF process

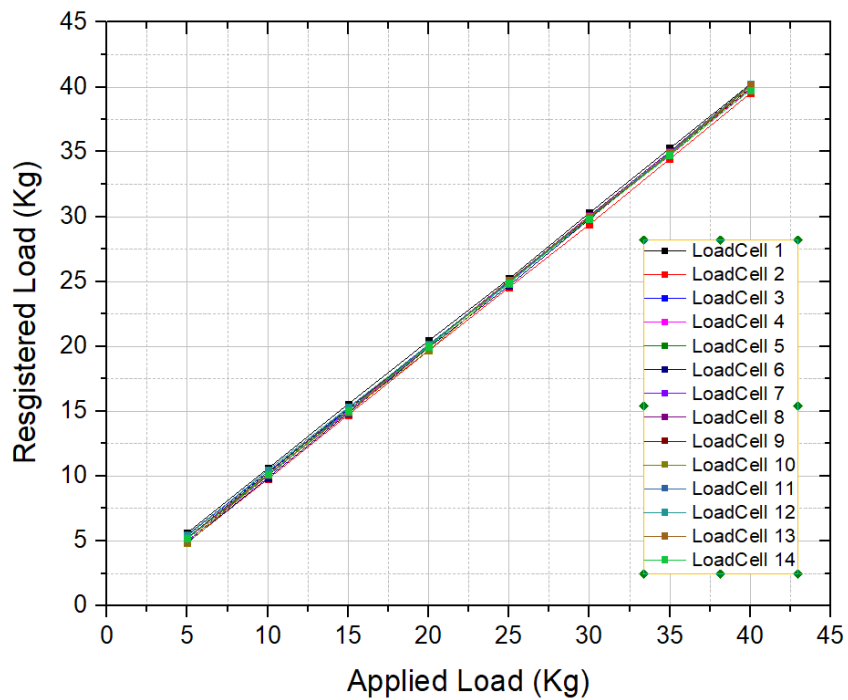
Reference	Method / Measurements	Position	Pros	Cons
Shiomi et al. [45] Van Belle et al. [47]	Strain Gauge / Strain	Base Plate	- Measures strain changes on the platform with the addition of new layers	- Measurements are taken from the baseplate and not from the build - Single point measurement
Dumbar et al. [48]	DVTR / Distortion	Base Plate	- Measurements of the direct distortion of the base plate during the build process	- Measurements are taken from the baseplate and not from the build - Single point measurement
Robinson [119]	Load Cell / Force	Support	- Multiple point measurements of force developed during the building process - Easy to set-up for multiple L-PBF machines	- Limited by force and temperature - Lack of in-process measurement of the temperature of the part

In-situ measurements of strains developed during the L-PBF process were performed using strain gauge binocular load cells ± 50 kg (RobotShop, UK), with an operating temperature range of -20 °C to 55 °C, an output rate of 2.0 ± 0.15 (MV/V), and a temperature sensitivity (%RO/°C) of 0.0016. The strain-gauge configuration is based on a Wheatstone bridge for measuring bending strains and such that they are insensitive to movements, meaning that if the built part is not perfectly aligned on the load cell, then the effect on the recorded load is insignificant. Strain gauges produce a voltage differential and must be read by a high-resolution analogue-to-digital converter. The load cells were connected to 16 channel InstruNet i100 (Omega, USA) data acquisition (DAQ) system with a read-back accuracy of ± 3 mV, at a sample rate of 3.122 s/sec/ch and 100,000 points/scan.

The load cells were calibrated, to ensure that the readings taken were accurate, by adding known weights to each load cell in increments of 5 kg up to a maximum of 40 kg. The real load and the measured load were then plotted against each other, and the gradient of the line of best fit was taken as the scaling factor. The scaling factor for each load cell was input into the InstruNet World Plus software (Omega, USA) and the loading process was repeated to ensure the scaling was accurate. The results from the calibration are shown in Figure 56, as distributions of the differences between the applied load and the registered load from each of the 14 load cells after the calibration. The temperature of the system was measured using K-type thermocouples (TC) which were attached to one of the load cells at each FTD. Due to the reduced space in the overflow compartment and the available channels on the InstruNet data loggers no more than one thermocouple could be attached into the device. Therefore, it was assumed that all of the load cells would be at approximately the same temperature, assuming that the heat distribution was similar across the surface of the part. The build process was halted when the thermocouples registered a temperature exceeding the operating range of the load cell.



(a)



(b)

Figure 56: Loads registered by each load cell based on 5kg increments of load: (a) before calibration; and, (b) after calibration

3.5.5.1 Single Array Force Transducer Device (FTD1) for Rectangular Part

In order to measure the development of residual forces at different points in the build, a preliminary design of Force Transducer Device (FTD) was used. The design consisted of a single array of 14 binocular load cells on a rectangular grid (32 mm x 112 mm) and allowed the measurement of the forces developed during unidirectional scanning patterns.

In order to avoid modifications to the machine and for easy setup and removal after use, the FTD was designed on a 250 mm x 250 mm aluminium monocoque chassis which is the size of a standard substrate, as shown in Figure 57. This allowed the FTD to be fitted directly into standard L-PFB machines without the need for modifications.

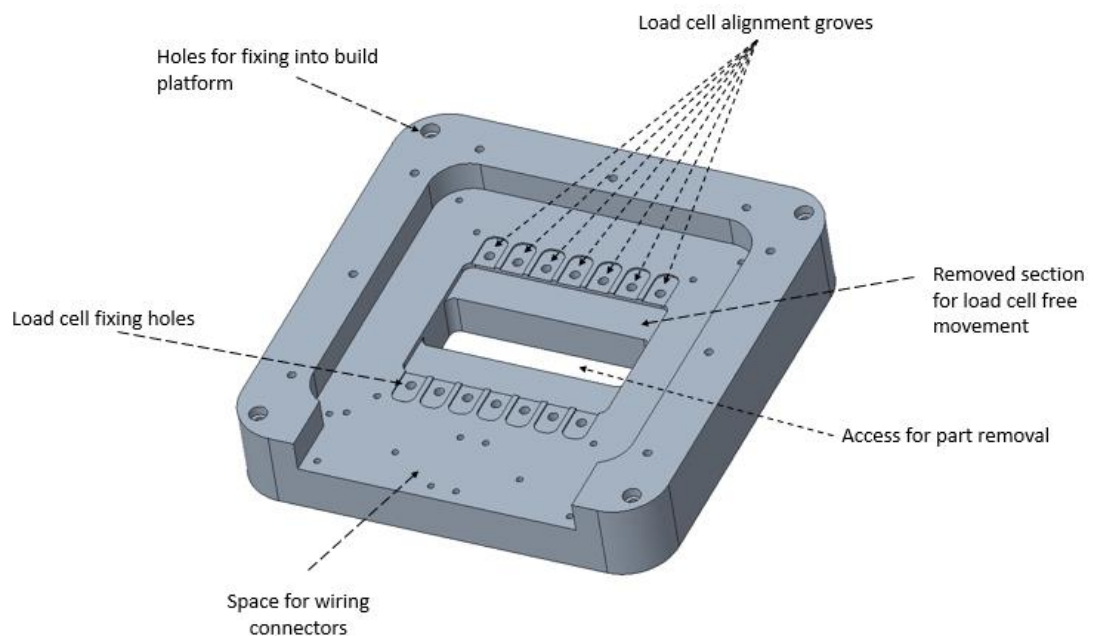


Figure 57: FTD substrate design for in-situ measurements

To ensure the correct positioning of the load cells in the substrate, 14 groves were machined for the alignment; below the load cells, an area was cut-out to ensure that the movement of the load cells was not restricted during the build. An additional slot at the front of the substrate was created as a wire exit. To maintain the inert gas atmosphere inside the building chamber, the load cells wiring was connected to two push-pull sealed connectors (LEMO, UK). The removable sealed connectors allowed the wiring harness to pass through the overflow compartment. The wiring was fitted through a flange, and a cable gland was used to seal the

wire exit to maintain the inert atmosphere inside the machine. The push-pull connectors made the FTD easy to remove after each build for powder cleaning.

To create a build platform, 10 mm diameter pegs were bolted onto the free end of each load cell, as shown in Figure 58. The material of the pegs was changed according to the metal powder being used for each build (Titanium pegs for the Ti-6Al-44V samples and steel pegs for the Nickel based metal alloys). An access slot in the centre of the substrate was machined, allowing access to remove the pegs once the build was completed without the need to remove the load cells from the FTD after each build.

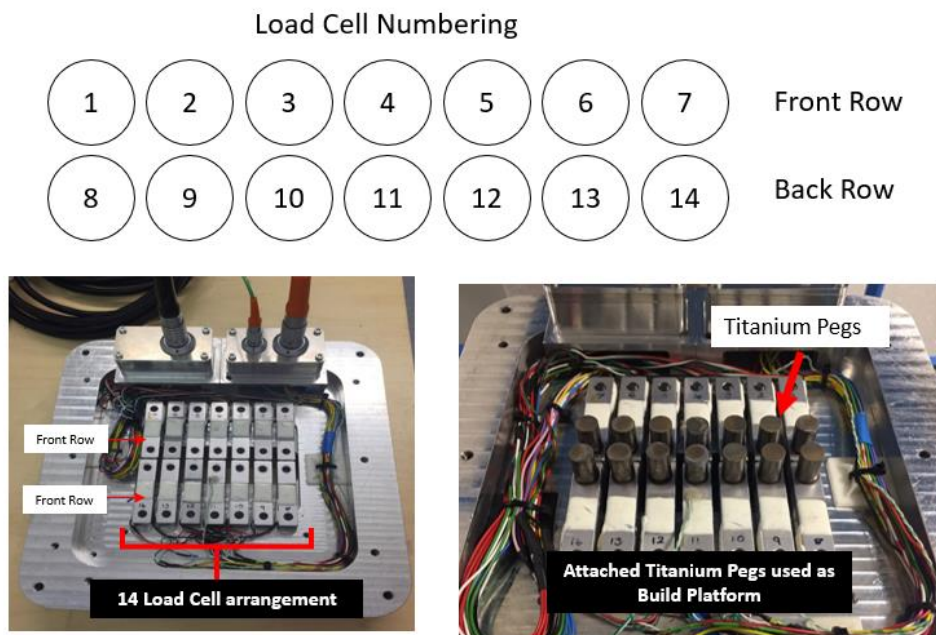


Figure 58: Single array load cell FTD1

It is important that no powder could access the inside of the FTD. To prevent powder ingressing into the load cell, the FTD was fully sealed by adding two 5 mm thick substrates separated by a 0.5 mm thick laser-cut silicone membrane. The holes in the silicone membrane were 8mm in diameter resulting in a tight fit around the 10 mm pegs, providing an effective seal of the load cell volume while allowing free transmission of loads through to the load cells. The substrates are held firmly in place with 11 M5 countersunk screws ensuring that there was no movement between the substrates, while the countersunk screwing maintained a planar upper surface to avoid wiper interaction during the process. A cross-section of the assembly of the FTD1 is shown in Figure 59.

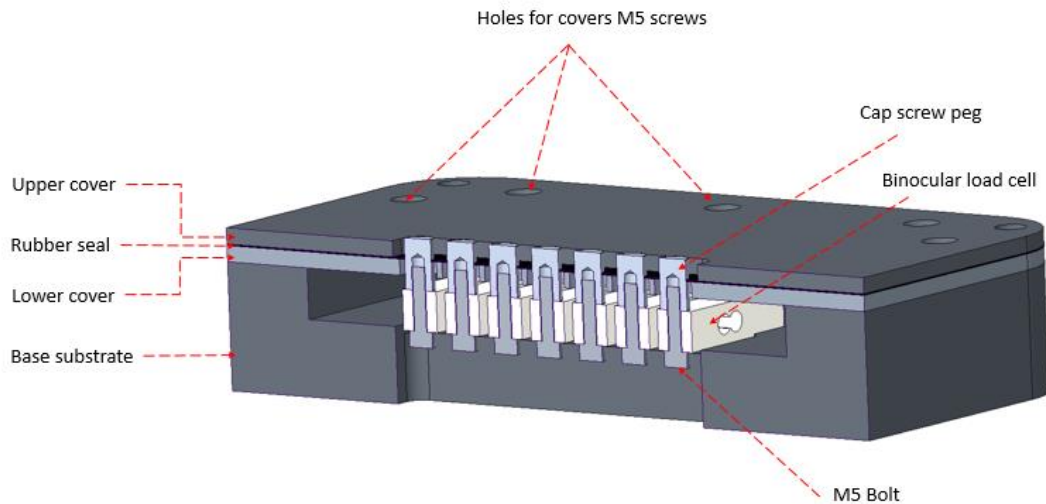


Figure 59: Cross-section of the FTD1 assembly

The use of commercial load cells limits both the maximum temperature and the force that the system can withstand. To ensure that the load cells did not exceed their maximum working temperature, a k-type thermocouple was attached to measure the temperature of the loadcell during the building process. Due to the reduced space in the overflow compartment and the available channels in the InstruNet data loggers no more than one thermocouple could be attached into the device. Therefore, a k-thermocouple was attached to load cell 11 which is located in the centre of the part, this gave an insight of the heat transferred from the part to the load cell, and it was assumed that the heat transfer was similar for the rest of the load cells. If the temperature was close to the limit the build was paused until the temperature of the load cell was reduced before continuing with the build. The build was stopped manually before any of the load cells reached their maximum workable load of 50 kg. The load increment of the load cells, as well as the temperature, were monitored from the InstruNet Plus software which registered the load increment during the build. The FTD1 arrangement measured the development of strains for a 32 mm x 112 mm part. In order to have a solid flat surface prior to connecting each of the load cells for the in-situ measurements a pyramidal section starting from an 8 mm diameter circle, which extended into 16 mm x 16 mm squares, was built up from the metal pegs as shown in Figure 60. The dimensions of the manufactured sample are shown in Figure 60. The height of the part for each build was dependant on the developed strains as the build had to be stopped when any of the load cells reached 50 kg.

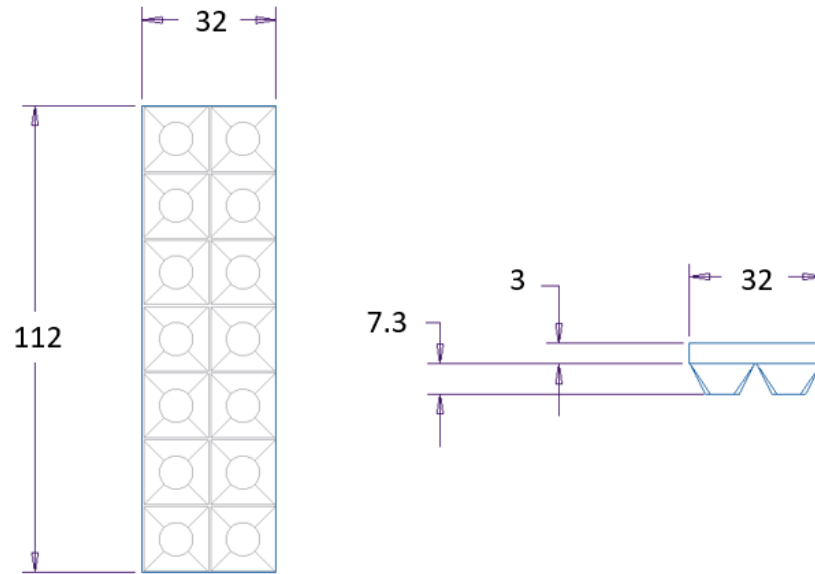


Figure 60: FTD 14 load cell arrangement for a rectangular part geometry (measurements are in mm)

3.5.5.2 4x4 Array Force Transducer Device (FTD2) for square Part

The single array FTD allowed the forces developed by unidirectional scan vectors to be evaluated during the L-PFB process. A second FTD with a 4x4 arrangement was used to measure the effect of alternate scan strategies. The second FTD consisted of 16 Micro Load Cells 0-50 kg (Robot Shop, UK), with a maximum load capacity of 50 kg and a maximum overload of 60 kg, and an operating temperature of -20 °C to 55 °C. The load cells were arranged in two separate substrates, one above the other, as shown in Figure 61. Each of the substrates having eight load cells arranged, such that, the bottom-level load cells measured the forces from the central two columns, and the top-level measured the forces from the outside columns.

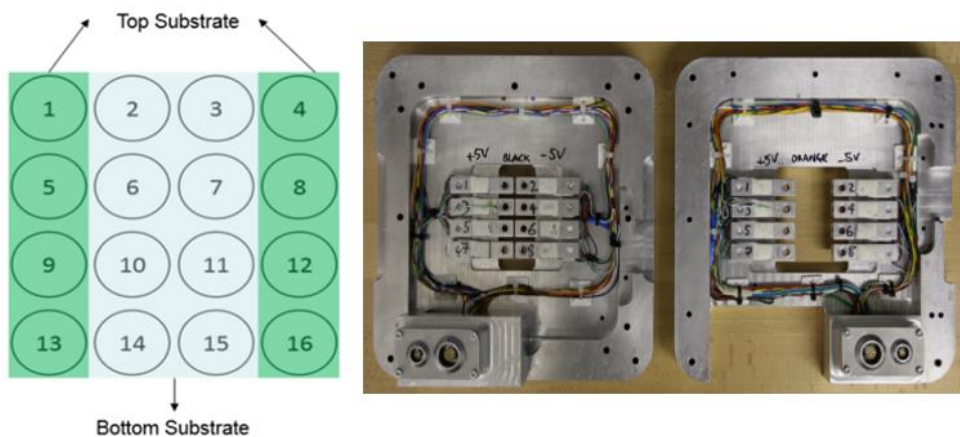


Figure 61: FTD2 for in-situ measurements in the L-PBF process

Similar to the previous FTD, to prevent powder from ingressing into the load cell area, the FTD was fully sealed by adding two 5 mm thick substrates separated by a 0.5 mm thick laser-cut silicone membrane. The holes in the silicone membrane were 8 mm in diameter resulting in a tight fit around the 10 mm pegs, providing an effective seal for the load cell volume while allowing free transmission of loads through to the load cells. The substrates were held firmly in place with 14 M5 countersunk screws ensuring that there was no movement between the substrates and maintaining a planar upper surface to avoid wiper interaction during the process. A cross-section of the assembly of the FTD2 is shown in Figure 62.

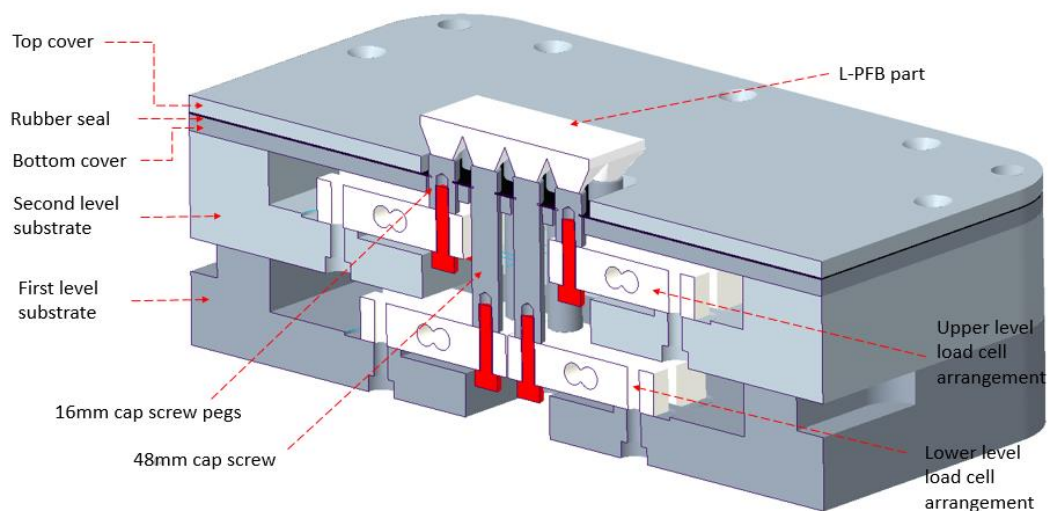


Figure 62: Cross-section of the FTD2 assembly

Cylindrical pegs 10 mm in diameter were attached to each load cell which created a build platform. The material of the pegs was changed depending on the metal powder used for each build (Titanium pegs for the Ti-6Al-44V samples and steel pegs for other materials alloys). The pegs for the bottom section were 48 mm long while the pegs for the top section were 16 mm long, as shown in Figure 62. In order to avoid exceeding the allowable temperature of the load cells, two K-type thermocouples were attached one to a load cell in each level substrate (load cells 5 and 6). Only two thermocouples were used to reduce the wiring thickness and due to the limited capacity of the InstruNet logger channels, and it was assumed that the temperature was similar along the whole of the part. The load cells and thermocouples were connected into three 100i InstruNet data logger boxes (Omega, USA). The InstruNet logger amplified the signal and measured the differential voltage in order to determine the residual forces developed at different stages of the built process. In-situ measurements during the L-PFB process were registered at a sample rate of 3.122 s/sec/ch and 100,000 points/scan. A schematic of the part geometry for in-situ measurements is shown in Figure 63.

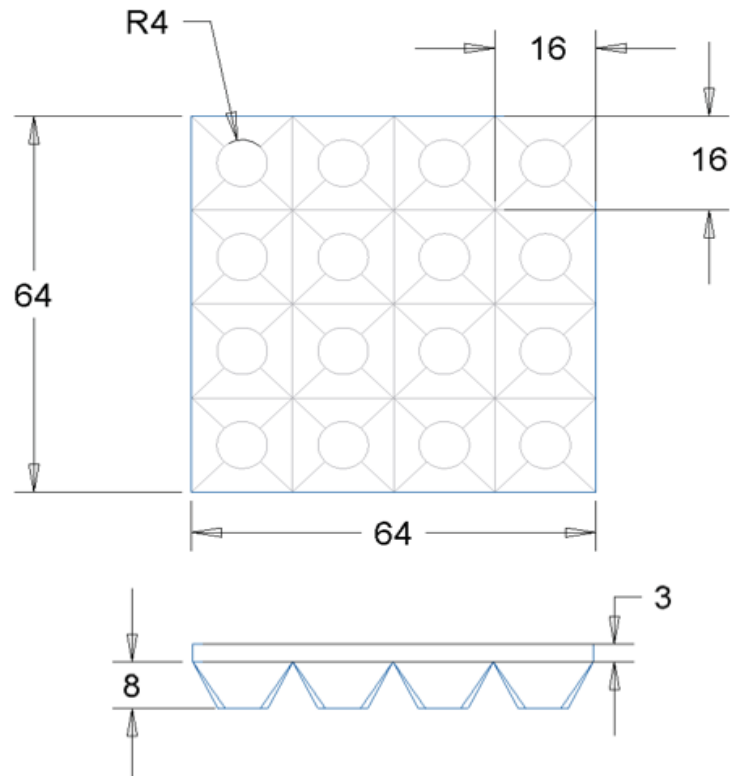


Figure 63: Schematic of the square build geometry for the FTD2 (measurements in mm)

Following the same procedure as for the previous FTD, each of the load cells was calibrated to ensure an accurate reading by adding known loads to each load cell in increments of 5 kg up to a maximum of 45 kg. The real load and the measured load were then plotted against each other, and the gradient of the line of best fit was taken as the scaling factor. This scaling factor was input into the InstruNet plus software (Omega, USA), and the process was repeated to ensure the scaling had been accurate. The results from the calibration are shown in Figure 64, with a standard deviation of 0.222 kg for the distribution of the differences between the applied load and the registered load from each of the 16 load cells after the calibration.

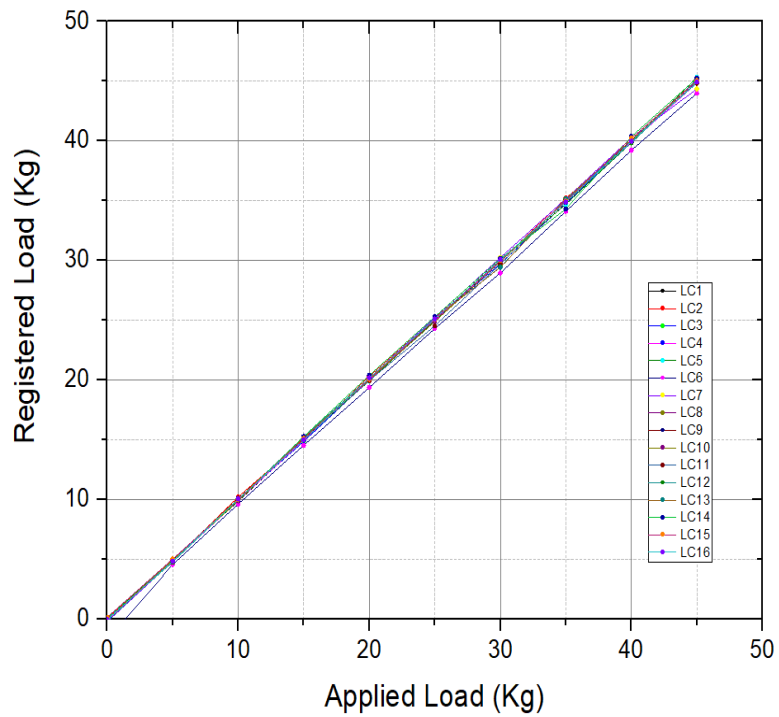
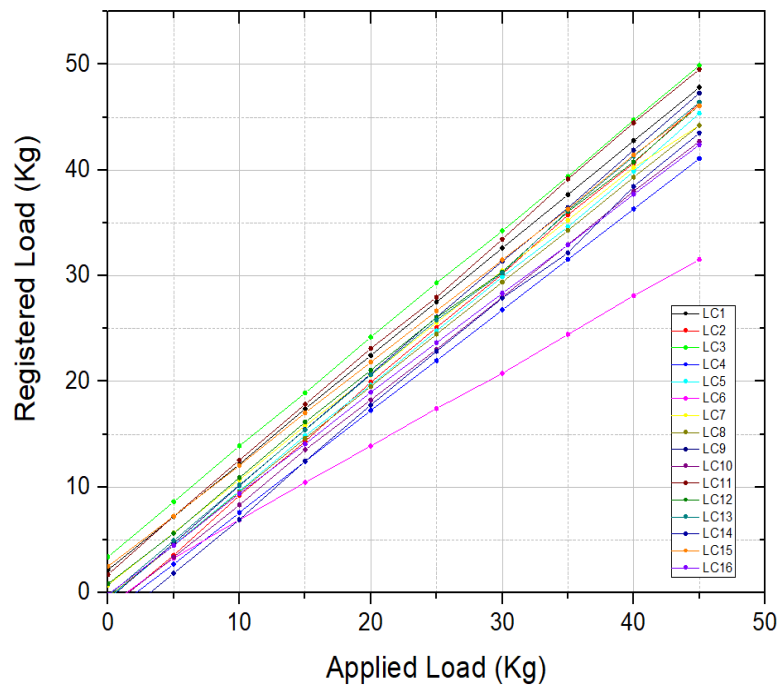
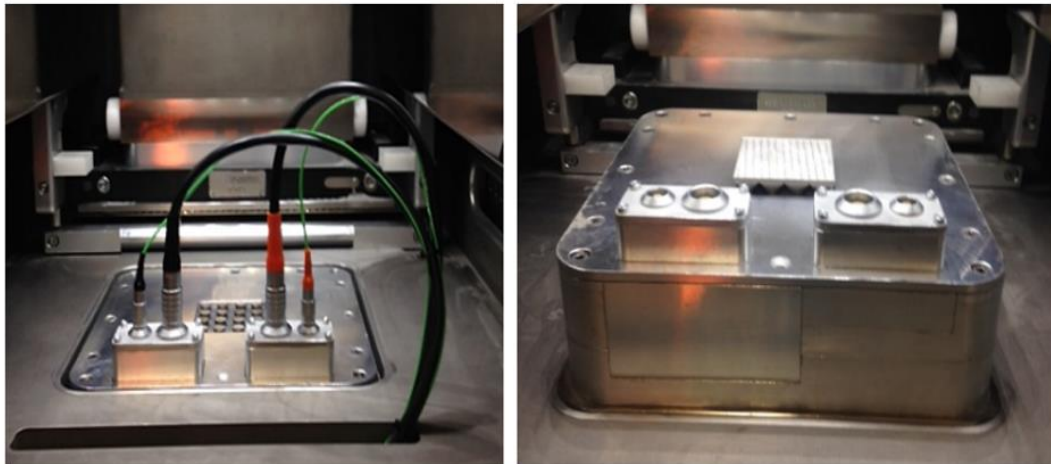


Figure 64: Loads registered by each load cell for FTD2 based on 5kg increments of load:) before calibration (top); and, after calibration (bottom)

3.5.5.3 Modifications to the Force Transducer Device (FTD)

This section will detail the modifications made to the previously manufactured FTDs to allow their use in a Renishaw AM250 machine. The force transducer devices were originally manufactured to carry out experimental work on a Realizer SLM250 machine and were designed to be set up as a regular base plate. The build plate platform for the Realizer SLM250 machine and the Renishaw AM250 are of the same dimensions (250 mm x 250 mm), which allowed the device to be used on the Renishaw AM250 and to be attached as a regular substrate into the build platform without needing any machine or process modifications. A schematic of the setup is shown in Figure 65; where the FTD is attached securely into the build platform as a regular substrate.



(a) The FTD was mounted as regular substrate into the build platform. The wires were fed thru the overflow.

(b) The use of sealed removable connectors allowed and easy setup and removal of the FTD from the machine.

Figure 65: FTD setup into the Renishaw AM250 L-PBF machine

The wiring for the load cells and the K-thermocouples, on the Realizer SLM250 machine, were fed through the glove compartment and properly sealed keeping the inert gas atmosphere required for the L-PFB process. Due to the design of the Renishaw AM250, the wires could not be fed in the same way as in the Realizer SLM250 machine. Therefore, it was decided to feed the wires through the front overflow. Due to the small size of the compartment in the front overflow, for the wiring to fit through the overflow compartment and for ease of set-up and removal, the load cell wiring was connected to a 36-pin Push-Pull Self-Latching Connector (LEMO, UK) as shown in Figure 66. An enclosed section at the front of the FTD was added for the wiring from the load cells and the K-Thermocouples to be attached to the sealed pin connectors and, thus to prevent powder from ingressing into the FTD load cell space.

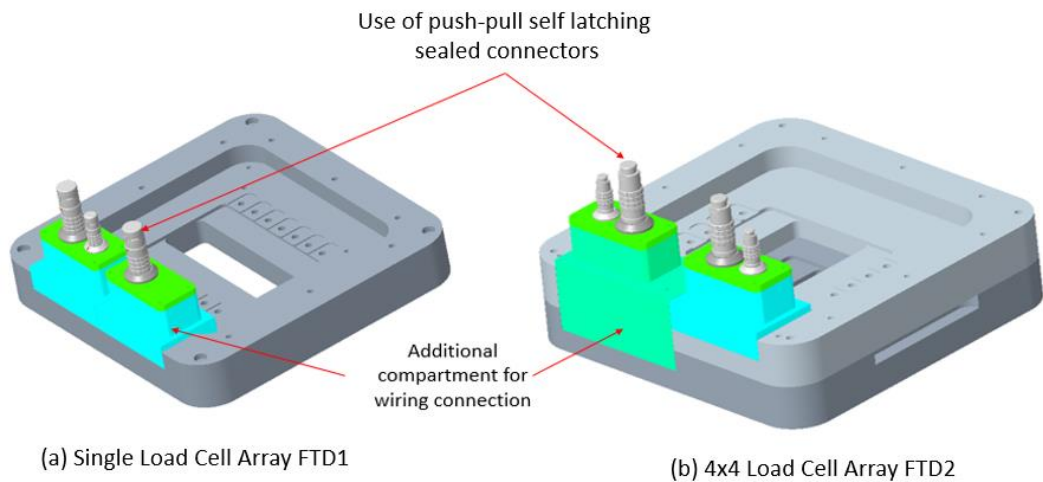


Figure 66: CAD of the substrate used for the modified FTD used for in-situ measurements

The FTD cables were fitted through the overflow compartment of the machine, as shown in Figure 67. To avoid any interaction with the recoating wiper and the FTD connectors, the maximum forward position of the wiper was reduced from 320 mm to 230 mm; therefore, no powder went through the overflow compartment during the building process. The wires were fitted through a flange where a cable gland was used to seal the wire exit to assure standard vacuum and pressure parameters needed on the machine for operation. The other end of the wires were connected into the InstruNet data loggers for data acquisition, as shown in Figure 68.

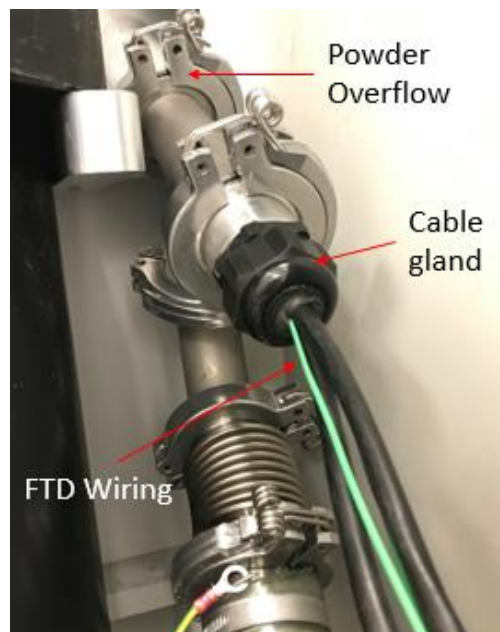
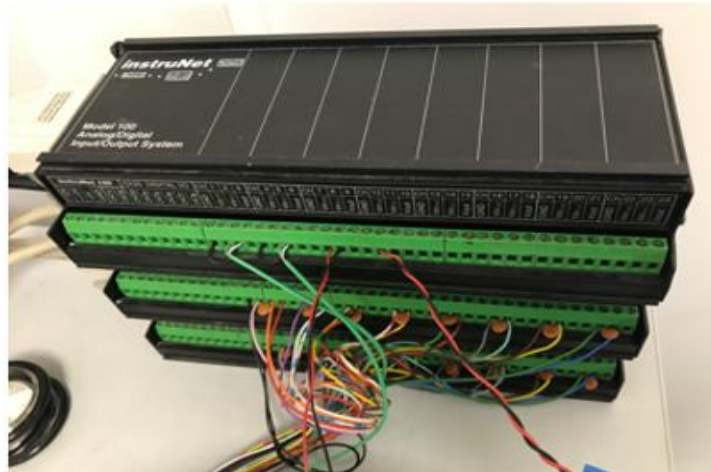


Figure 67: Load cell wiring fed through the overflow compartment into the InstruNet data loggers



LOADCELL WIRING ARRANGEMENT FOR INSTRUNET 100															
Ch	1	2	3	Ch	4	5	6	Ch	7	8	9	Ch	10	11	12
GND	Vin(+)	Vin(-)	Vout	GND	Vin(+)	Vin(-)	Vout	GND	Vin(+)	Vin(-)	Vout	GND	Vin(+)	Vin(-)	Vout
	S1+	S1-	+5V		S2+	S2-	-5V		S3+	S3-			S4+	S4-	
Black	Pink	Orange	Red	Violet	White/Blue	White		Yellow/Blue	Red/Black			White/Red	Yellow/Red		
	LOADCELL 1				LOADCELL 2				LOADCELL 3				LOADCELL 4		
Ch	13	14	15	Ch	16	17	18	Ch	19	20	21	Ch	22	23	24
GND	Vin(+)	Vin(-)	Vout	GND	Vin(+)	Vin(-)	Vout	GND	Vin(+)	Vin(-)	Vout	GND	Vin(+)	Vin(-)	Vout
	S5+	S5-			S6+	S6-			S7+	S7-			S8+	S8-	
	Green/Red	Red/Blue		Grey	Turquoise			Brown	Yellow			Green	Blue		
	LOADCELL 5				LOADCELL 6				LOADCELL 7				LOADCELL 8		

Figure 68: Load cell wiring arrangement into three InstruNet100i for data acquisition

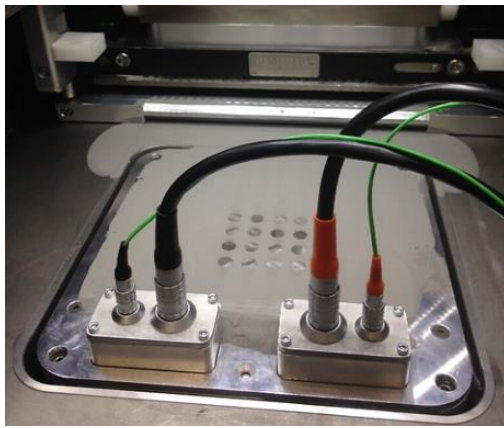
3.5.5.4 Steps for in-situ measurements:

The following steps were performed for each build with the FTD (see

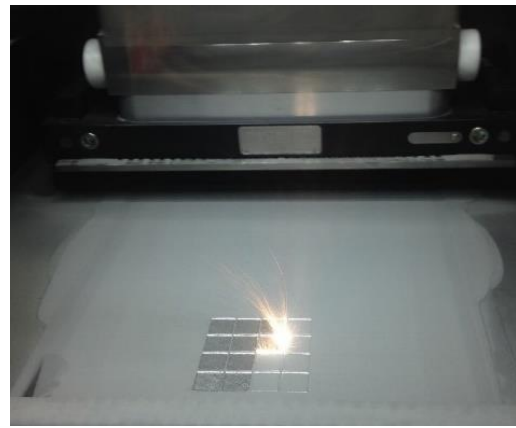
Figure 69):

1. The FTD was attached to the build platform of the L-PBF machine as a regular base plate. The wiper-recoater's maximum front position was adjusted to stop just before reaching the FTD wire section (from 320 mm to 230 mm).
2. Prior to the build, a first dose of powder was spread to assure all the pegs were aligned and that the powder was spread evenly over all of the top section of each of the pegs. As a first stage of the build, solid inverted pyramid structures were built onto the cylindrical pegs from an 8mm circle, which extended into 16 mm x 16 mm squares, until just before they start connecting each other.

3. A second section was built-on top of the inverted pyramid structures, which connected them and each load cell together. The load cells registered the forces developed with each newly deposited layer. The build was stopped once the force reached the maximum working capacity of any load cell of 50 kg.
4. The machine was cleaned, following the standard de-build procedures and the FTD was removed from L-PFB the machine.
5. The L-PBF part was removed from the FTD for post-process measurements of part deformation using the DIC system.



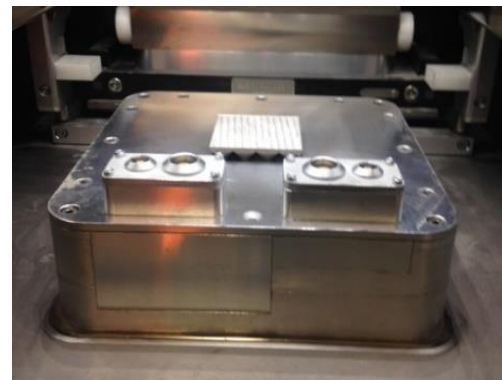
(1)



(2)



(3)



(4)



(5)

Figure 69: Process of a part being built on the Renishaw AM250 machine with the use of the FTD

3.6 Experimental Arrangements

The aim of this investigation is to understand the complex evolution of residual stresses in the L-PBF process through the use of in-situ measurements and to understand the effect of the process-material relationships on residual stress. The experimental requirements came from both the research objectives and the previous knowledge from the literature review. The great complexity from the L-PBF process lies in the extensive amount of parameters involved in the process and their interactions which are influenced by the thermal, physical and mechanical properties of the metal powders used. Three groups of influential parameters are well-known from the literature: scan parameters which are defined by the machine operator, material parameters which are fixed by the choice of metal powders used, and the machine parameters, fixed by the type of machine, such as the laser properties.

The experimental work for this thesis was divided in two sections due to machine availability to perform the experimental work. The first phase consisted of the study of different aspects of the interaction of the Ti-6Al-4V powder with the L-PBFP process. A first study was preformed to determine the in-process distribution and magnitude of the residual forces developed during the L-PBF process, after which the influence of several process parameters was investigated, in particular the laser power, scan speed, and layer thickness. For the second phase, the general behaviour of various materials (Inconel 635, Inconel 718 and Maraging steel) during the L-PBF process was investigated, both in terms of the developed microstructure as well as the material specific response to the process parameters and the residual stresses. Through examination of the literature, the studied processing parameters were in this thesis were determined to be the most influential to the residual stress development in both magnitude and orientation. The fist parameter studied was the laser power (W), it is defined as the applied laser energy per unit time. Laser power is one of the primary variables which alter the energy input in the L-PBF process and plays an important role in determining residual stress magnitude [173]. Next, the scan strategy was considered as it defines the residual stress distribution. The scan strategy largely indicates what will occur in the part as it defines the motion of the laser bean and the properties of the melt pool. The build parameters used for each scan strategy tested were based on those specified by Renishaw to achieve a 99% density and were then modified to explore the influence of the build parameters. The modification of the process parameters, i.e. laser power could affect part density, therefore the effect of the energy density on residual stress was further

investigated through the variation of the scan speed. Finally, the effect of the material properties on residual stresses were studied.

Previous studies in the literature suggest that the relationship among certain process parameters and residual stress magnitude can be material dependent [120, 166]. The phase transformation that occurs in certain materials can act to counter the shrinkage and the stress distribution during the L-PBF process, therefore it is important to understand the relationship of the material properties and the processing parameters on the residual stresses in the L-PBF process. All samples were produced using a Renishaw AM250 machine previously described in Section 3.2 and the in-process residual forces were measured by the use of the FTD previously described in Section 3.5.5.

3.6.1 Effect of the Processing Parameters on Residual Stress and Part Deformation using Ti-6Al-4V

3.6.1.1 *Effect of the Laser Power*

In order to investigate if there is a correlation between the laser power and the forces induced in the process, the laser power was varied, while keeping the rest of the process parameters constant. Samples were built using Ti-6Al-4V due to the machine allocated by the sponsor for the Encompass project. The maximum power of the laser for the Renishaw AM250 is 200 W; therefore, the laser power was lowered by 10% and 20% to 180 W and 160 W. This variation on laser power was chosen in order to see a clear effect on the variation of the energy input, which previous studies in the literature suggest was the most important factor to influence the residual stress development and the effect of the part density [173] which was studied further on this chapter. All samples were produced with an identical scanning strategy and layer thickness. The Stripe scan strategy, described in Section 3.2.2 was chosen as this is the most commonly used scan strategy in Renishaw's commercial builds. Using the parameters described in Table 8, where S1 are Renishaw's recommended parameters for building a part with a relative density greater than 99.9% and using a rotation of 67° per layer because previous studies have shown that rotating scan strategy in each layer reduces the levels of residual stress [49]. The use of a 67° rotation between each layer was used to ensure that it is many layers before the scanning direction is exactly repeated. All parts were 64 mm x 64 mm with the geometry as described in section 3.5.5.2 built on the FTD2. In order to start the force measurements for all the samples under the same conditions, the inverted pyramid structures were built using a Stripe scan strategy and using Renishaw's recommended parameters in

Table 8 which produced a part with a density nearly equivalent to a cast part. All the processing parameters described in Table 8 are subject to be changed by the user from the material file (.CVS) and can be input into the build from the QuantAM software. However, in order to achieve a part with a density greater than 99.5%, the material files should be carefully selected according to the metal alloy being used.

Table 8: Build parameters for consideration of the effect the laser power on residual stress

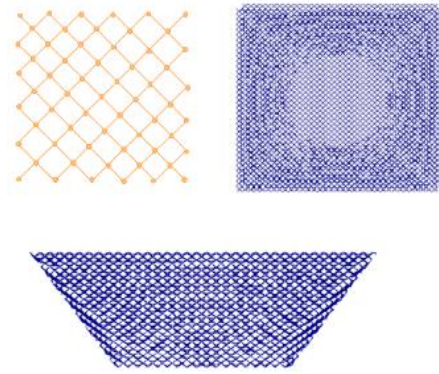
Sample	Pyramid Section	Laser Power (W)	Layer Thickness (μm)	Exposure Time (μs)	Point Distance (μm)	Scan Strategy
S1	Solid Structure	200	30	50	55	Stripe / 67° rotation
S2	Solid Structure	180	30	50	55	Stripe / 67° rotation
S3	Solid Structure	160	30	50	55	Stripe / 67° rotation
S4	Lattice Structure	200	30	50	55	Stripe / 67° rotation
S5	Lattice Structure	180	30	50	55	Stripe / 67° rotation
S6	Lattice Structure	160	30	50	55	Stripe / 67° rotation

Lattice Support Structures

The use of commercial load cells limited the force and temperature allowable in the system; therefore, in an attempt to reduce the heat transferred to the load cells and allow building for a longer period of time without reaching the maximum workable temperature; three additional samples were built using the parameters described in Table 8 for the square section, but with the inverse pyramid section built using a lattice structure as shown in Figure 70. The lattice structure will reduce the heat transferred from the build into the load cells. The lattice structure was generated using Boolean clipping, generated with the use of the Conformal Surfaces software (Liverpool University, UK) with a unit size cell of 450 μm . The parameters for the lattice structure used for the connector pillars are shown in Table 9.

Table 9: Lattice structure build parameters

Lattice Structure Parameters for Pyramid Section	
Unit Cell Size	450 μm
Laser Power	200 W
Layer Thickness	30 μm
Exposure Time	50 μm

*Figure 70: Lattice structure used for the pyramid section*

Since the load cells used in the FTD are capable of working up to 55° Celsius and a load of 50 kg, the machine was stopped at each build before the registered forces by the InstruNet loggers reached the maximum load capacity. The building process is described in Section 3.5.5.

3.6.1.2 Effect of the Scan Strategy and Layer Thickness

Previous literature suggests that dividing the scan vector into short scan vectors reduces the residual stresses developed in the part [91, 97, 137, 174]. This occurs both due to the reduction in the length of scan vectors and as a result of the rotation of the orientation of the scan vectors in each layer [48, 49]. In order to study the effect of altering the scan strategy with sectoral scan vectors, a first set of samples were tested using the Stripe scan strategy with a scanning orientation that was rotated 67° per layer, with all stripes-oriented vectors in the Y direction and with all stripes-oriented vectors in the X direction as shown in Figure 71, and using the single array FTD with the rectangular part geometry. This was followed by an analysis to determine the effect of the three scan strategies used by Renishaw, i.e. Meander, Stripe and Chessboard (previously described in Section 3.2.2) on the residual forces and part deformation. Additional samples with the Stripe, Meander and Chessboard scan strategies were built on the FTD2 with a square part geometry, to determine the effect of the scan strategies and layer thickness on residual forces developed with a different part geometry. The use of these scan strategies allowed a comparison of the use of single-line vectors and sectioning scan vectors. The parameters used for each scan strategy were based on those specified by Renishaw to achieve a relative density greater than 99.8% and were then modified to explore the influence of the build parameters (Table 10). The parameters to produce samples with a relative density higher than 99.8 for each scan strategy are defined independently and are highly dependent on the single vectors geometry. The hatch distance

(HD) and point distance (PD) for the laser scan vectors is critical, and have been found to determine the level of porosity and the level of surface roughness within a part, therefore they have to be defined specifically for each scan strategy depending on the geometry of the scan vectors (length and direction). If the hatch spacing is greater than the track width, this results in unfused powder between tracks. On the contrary, reducing the hatch spacing has a variety of issues: increased build time, over heating in small regions, and increased susceptibility of porosity due to the effect of keyholes [142]. Keyhole pores are a particular type of pore defect in the L-PBF process, which form when excess energy is imparted by the laser to the melt pool. These pores act as stress concentrators and have a negative effect on the mechanical properties. Overheating during changes in laser scan velocity, such as at laser turn points, leads to increased evaporation of metal from the surface causing a deep keyhole depression to form. The keyhole depression is unstable and can collapse to trap gas in the pores within the part [142]. The lengths of the scan vectors differ among the scan strategies; therefore, the parameters vary among the scan strategies tested for the 30 μm samples, in the case of Stripe and Chessboard as the scan vectors are sectioned in smaller segments. Therefore, an overlap between the fields is needed to prevent porosity reducing the point distance but increasing the hatch distance. As for the Meander's parameters to prevent porosity, by using single line vectors from side to side, a shorter hatch distance for the scan vectors is used. Finally, to determine the effect of the layer thickness, samples were built with an increment in the layer thicknesses from 30 μm to 60 μm . In previous studies, Renishaw had determined that the Chessboard scan strategy produces more defects per unit area of the part than the Stripe and Meander scan strategies, due to the high concentration of heat induced at the border of each check board. For the Chessboard scan strategy, due to an acceleration of the laser at the border area of each of the squares, a higher heat concentration is induced to the part; the concentrated heat in a particular area induces more defects in the part, such as keyhole porosity. Therefore, Renishaw had previously determined that the Chessboard scan strategy with a layer thickness of 60 μm was not suitable; therefore, the layer thickness was only studied for the Stripe and the Meander scan strategies by changing the layer thickness from 30 μm to 60 μm . The scanning strategies test cases are shown in Table 10.

Table 10: Build parameters used for Ti-6Al-4V samples built on a Renishaw AM250 machine for a part density greater than 99.9%

		Material Ti-6Al-4V					
Sample Number	Part Geometry	Scan Strategy	Laser Power (W)	Layer Thickness (μm)	Point Distance (μm)	Exposure Time (μs)	Hatch Distance (mm)
S7	Rectangular	Stripe	200	30	55	50	0.105
S8		Stripe All X	200	30	55	50	0.105
S9		Stripe All Y	200	30	55	50	0.105
S10		Chessboard	200	30	55	50	0.105
S11		Meander	200	30	75	50	0.065
S12	Square	Stripe	200	30	55	50	0.105
S13		Chessboard	200	30	55	50	0.105
S14		Meander	200	30	75	50	0.065
S15		Stripe	200	60	60	70	0.095
S16		Meander	200	60	60	70	0.095

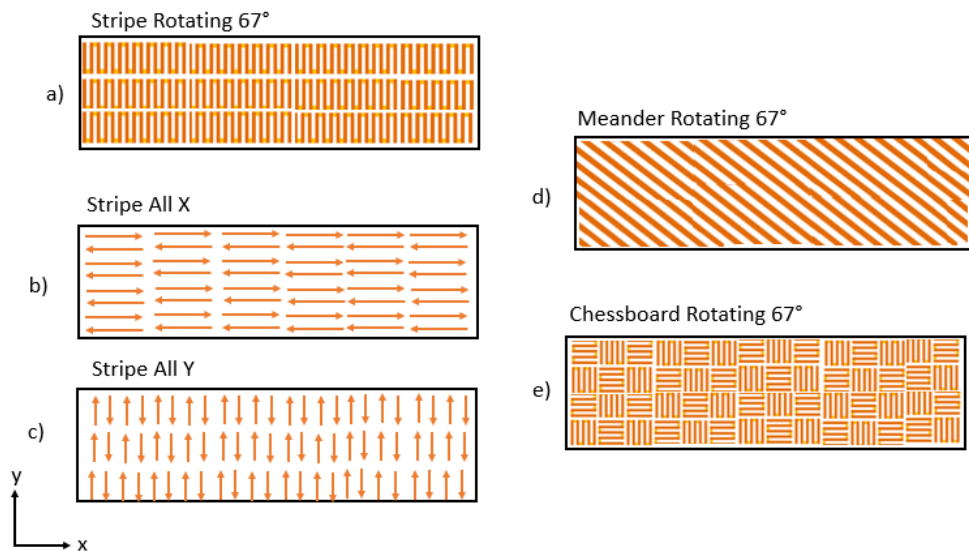


Figure 71: Scan strategies tested for the rectangular part geometry on the FTD1. (a) Stripe scan strategy with 67° rotation, (b) Stripe scan strategy with all X scan vectors, (c) Stripe scan strategy with all Y scan vectors, (d) meander scan strategy with 67° rotation, and (e) Chessboard scan strategy with 67° rotation.

3.6.2 Effect of the Material Properties and Processing Parameters using Nickel-based Alloys

Samples were manufactured using different metal powders in order to determine the developed forces through the L-PBF process. The build parameters used are shown in Table 11, which were previously defined by Renishaw to create parts with a density greater than 99.9%.

3.6.2.1 *Effect of the scan strategy*

In order to compare if the results from the previous section built from the use of the Stripe scan strategy and the Meander scan strategy, built using Ti-6Al-4V, was an effect of the scan strategy rather than of the metal powder. As it was previously defined by Renishaw the Chessboard scan strategy produces more defects per unit area to the part than the Stripe and the Meander scan strategies and is not suitable to be used with a 60 μm layer thickness. Therefore, the layer thickness was only studied for Stripe and Meander scan strategies by doubling the layer thickness from 30 μm to 60 μm . Two samples (S17 and S18) were built using Inconel 625 and a 60 μm layer thickness using the Meander and the Stripe scan strategies; additional samples were built using Maraging steel using the Stripe and Meander strategies (S21 and S22) using the parameters described in Table 11. This allowed comparison of the effect of the scan strategies on different metal powders and see if the difference was an effect of the scan strategy rather than of the metal alloy.

3.6.2.2 *Effect of the Metal Alloy*

In order to compare the effect of the metal properties on the developed forces during the process, samples were built in four different metal powders Ti-6Al-4V, Inconel 625, Inconel 718, Maraging Steel. All samples were built using Stripe scan strategy and the build parameters previously defined by Renishaw to create parts with a density greater than 99.9% for each metal alloy, as described in Table 11. To reduce the building time all samples were built using a layer thickness of 60 μm .

3.6.2.3 *Effect of the Inert Gas*

Previously manufactured parts from Renishaw had shown a variation in the measurements between samples built with Nitrogen instead of Argon gas as the inert atmosphere. Therefore, samples were manufactured with Nitrogen to explore the effect on the forces using the FTD measurements. Two samples using Maraging steel were built varying the inert gas atmosphere in the machine between Argon (Ar) and Nitrogen (N_2). An additional sample with Inconel 625 was built with Nitrogen (N_2) inert gas atmosphere, in order to see if this was solely an effect for the Maraging steel. The samples were built using Stripe scan strategy and the

build parameters previously defined by Renishaw to create parts with a relative density greater than 99.9% for each metal alloy, as described in Table 11.

3.6.2.4 *Effect of the Energy Density*

Previous literature shows a known dependency of the developed residual stresses on the thermal condition. In order to study the effect of the energy input during the build process and the effects of the part density, three samples were built using Inconel 625 only, due to machine availability, increasing the point distance from 60 μm to 70 μm and 80 μm , while keeping the rest of the parameters constant. This study investigated the effect of the energy density on residual stress in regards to the volumetric energy input. The parameters used for each build are shown in Table 12. All samples were built using the same scan strategy i.e. Stripe with a rotation of 67° per layer. Samples were built in this material due to machine availability.

3.6.3 **Melt Pool Characteristics**

Depending upon heat condition of the powder bed, the melt pool of laser melting metallic powder exhibits a varied size and morphology, even if the identical scanning parameters are used. It is known that the base plate or a solid metal provides high thermal conduction for fusion energy to be dissipated, while the powder bed heat conduction is much lower than that of solid metals due that gas-filled pores may reduce the thermal conductivity [175]. Thus, the characteristics of the melt pool on a powder bed without any prior layers will have different properties than those developed with a previous powder bed, and this could give significant information for the development of FEA models. Therefore, single tracks were performed under two conditions; one set was built with a previous 30 μm layer thickness of metal powder, and a second set directly over the support part with no previous disposed layer of powder. In collaboration with 3DSIM (Ansys) single bead samples were built using different metal powders Ti-6Al-4V, Inconel 625 and Maraging steel where single beads were built varying the laser power (W) and exposure time (μs), as shown in Table 13. The parameters used for the development of the single beads were defined in collaboration with 3DSIM (Ansys) based on their requirements for the calibration of their simulation software. The samples were cross-sectioned, and measurements were taken 4 mm apart from the centre of the part, as shown in Figure 72.

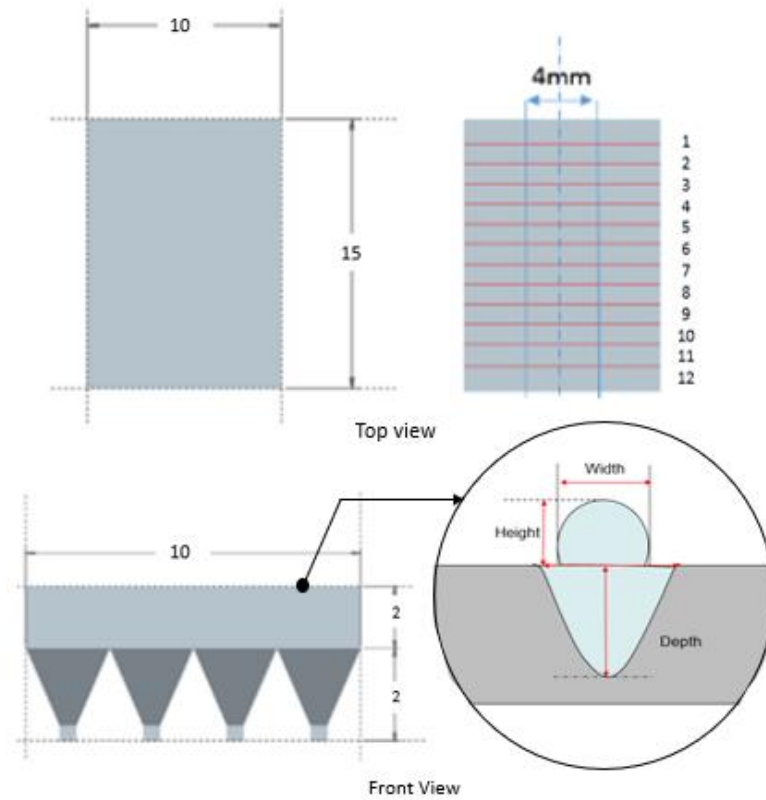


Figure 72: Schematic of the rectangular base where 12 single beads are scanned on the top surface (measurements are in mm) showing the width, height and depth measurements made for a single bead (bottom right). Parameters used for the single beads are shown in Table 13

Table 11: Renishaw AM250 build parameters for Nickel-based superalloys

Sample Number	Material	Scan Strategy	Laser Power (W)	Layer Thickness (μm)	Point Distance (μm)	Exposure Time (μs)	Hatch Distance (mm)	Inert Gas
S17	Inconel 625	Meander	200	60	60	100	0.14	Ar
S18	Inconel 625	Stripe	200	60	60	100	0.14	Ar
S19	Inconel 718	Stripe	200	60	60	70	0.09	Ar
S20	Maraging Steel	Stripe	200	40	65	80	0.08	Ar
S21	Maraging Steel	Stripe	200	40	65	80	0.08	N ₂
S22	Maraging Steel	Meander	200	40	65	80	0.08	Ar
S23	Inconel 625	Stripe	200	60	60	100	0.14	N ₂

Table 12: Parameters with a variation of the point distance for Inconel 625

Sample	S24	S25	S26
Point Distance (μm)	60	70	80
Energy Density J/mm^3	39.68	34.01	26.76
Scan Strategy	Stripe		
Laser Power (W)	200	200	200
Exposure time (μs)	100	100	100
Hatch Distance (mm)	0.140	0.140	0.140
Layer Thickness (μm)	60	60	60

Table 13: Single beads build parameters

Bead No.	Laser Power (W)	Exposure Time (μs)	Scan Speed (mm/s)	Energy Density (J/mm^3)
SB 1	160	40	1375	36.9408
SB 2	160	50	1100	46.1760
SB 3	160	100	550	92.3520
SB 4	170	40	1375	39.2496
SB 5	170	50	1100	49.0620
SB 6	170	100	550	98.1241
SB 7	180	40	1375	41.5584
SB 8	180	50	1100	51.9480
SB 9	180	100	550	103.8961
SB 10	200	40	1375	46.1760
SB 11	200	50	1100	57.7200
SB 12	200	100	550	115.4401

4 Experimental Results

This chapter presents the results from the experimental work performed on the effect of the processing parameters and material properties on the development of residual forces in the L-PBF process, from which residual stresses were inferred. Results from the out-of-plane measurements of distortion by DIC are also presented in this chapter. In-situ measurements were performed with the use of a Force Transducer Device (FTD). The use and evaluation of these techniques, for residual stress assessment in L-PBF, extends our understanding of how the stresses are developed in different metal powders, providing the necessary knowledge required for the optimisation of the process. The research was performed in four different metal powders and are described in two sections: Ti-6Al-4V and Nickel-based superalloys (Inc625, Inc718 and Maraging Steel).

4.1 Effect of Processing Parameters on Residual Stress and Part Deformation for Ti-6Al-4V

The first phase of the experimental work was performed using Ti-6Al-4V, because as for the machine assigned for the project, the sponsors, Renishaw, were interested in this particular material due to its significant commercial usage in the aerospace industry. The literature review showed that due to the thermal cycles in the L-PBF process, residual stresses develop in the part that can lead to critical distortion. The aim of this section was to understand the effects that process parameters, such as laser power, scan strategy and layer thickness, have on residual stress development for Ti-6Al-4V. Previous literature reported that laser power is the principal factor that defines layer bonding [176], and therefore, it has a large effect in determining the development of residual stresses. To assess the effect of the laser power and in order to determine if there was a correlation between the induced forces and the laser power input, a set of experiments were performed in which the laser power was varied while keeping the rest of the process parameters constant. In order to see a noticeable effect, the laser power was reduced by 10% and 20% from the maximum value of 200 W. Another factor that contributes significantly to the residual stresses is the scan strategy, as it defines the path along which the laser melts the metal powder and this affects the thermal gradients and cooling rates induced in each layer [59, 113, 143, 167]. The effect on the induced forces of the three most commonly used scan strategies: Stripe, Meander and Chessboard, were studied by in-process measurements. Finally, the effect of layer thickness has shown to affect

the residual stress in the L-PBF process [177] by altering the thermal gradients induced in the part; therefore, a study on the effect of the layer thickness on the forces induced and part deformation was conducted.

4.1.1 Effect of the Laser Power

The forces registered while the part was being built were recorded and plotted against time and layer number for each build. The resultant forces developed over time during the building process for sample S1 using 200 W laser power are shown in Figure 73. The results from the in-process measurements show that the edges in the part are in tension or being pulled up, against the build platform (load cells 1, 4, 13 and 16), generating a tensile force in the load cells; while the load cells in the middle are being compressed or pushed towards the build platform (load cells 6, 7, 10 and 11), thus the deformation creates a bending moment in the build, e.g. curl as previously described by Thomas [178]. The curl effect from the forces developed during the process can be seen in Figure 74. This agrees with the literature that the residual stress near the centre of the part tends to be compressive and tensile near the surface area [158, 179] with respect to the build platform; therefore, the stresses would act to make the sample curl relative to the baseplate [46], as it can be seen from the surface plot in Figure 74. Figure 75 shows the contour plot of the force on the load cells at layer 10, layer 50 and layer 100 (when the build was stopped); as it can be seen, the forces are symmetrical and evenly distributed through the part. The tensile forces must balance the compressive forces, and the distribution of forces must be symmetrical. The tensile forces registered at the corners are balanced by the compressive forces registered by the central load cells, and the smaller tensile forces at the centre of the edges parallel to the x-axis are balanced by the smaller compressive forces at the centre of the edges parallel to the y-axis through the build. Therefore, as no additional forces are acting over the FTD the algebraic sum of the forces remains zero, as it can be seen from the red line in Figure 69. The results in Figure 73 are illustrated in three groups, i.e. loads measured in the centre, corners, and edges; hence, to reduce the number of forces on each graph the absolute sum of the forces from each group of load cells has been used in subsequent graphs, e.g. Figure 76.

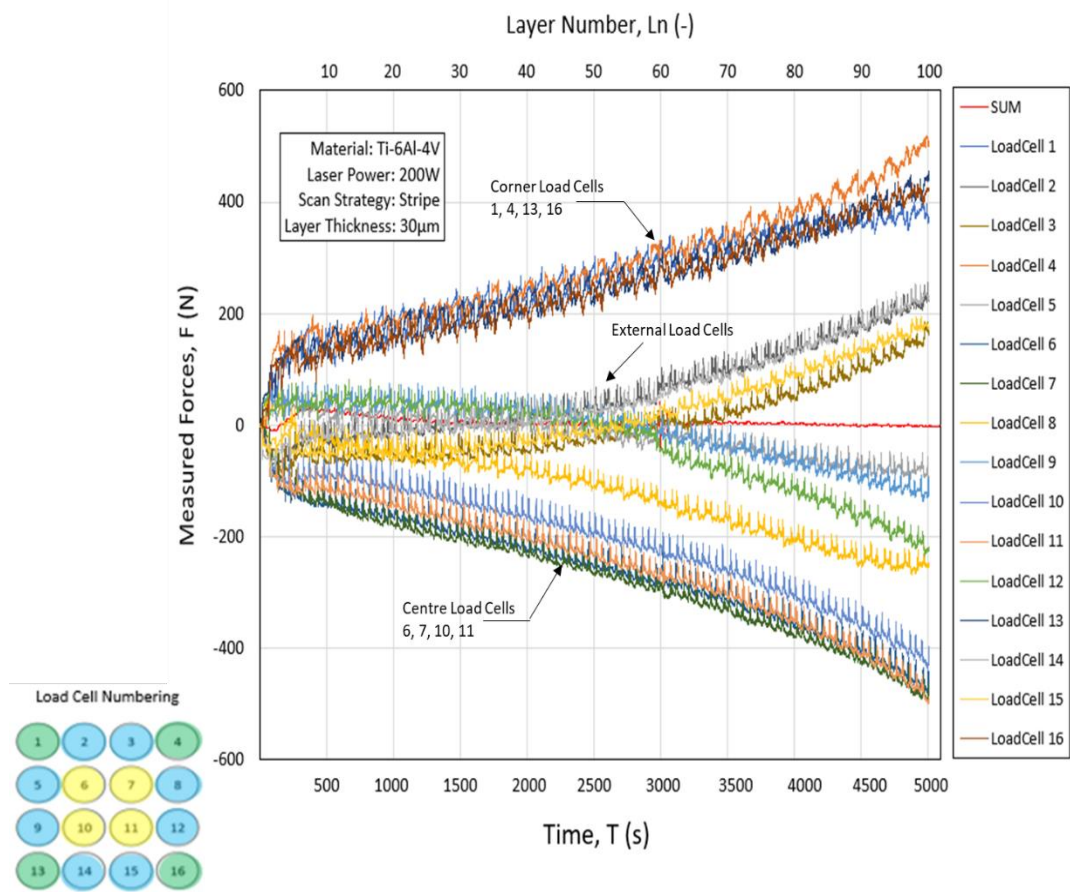


Figure 73: FTD2 In-situ measurement results from sample S1 (see Table 8) built with: laser power 200W, Stripe scan strategy and solid pyramids section

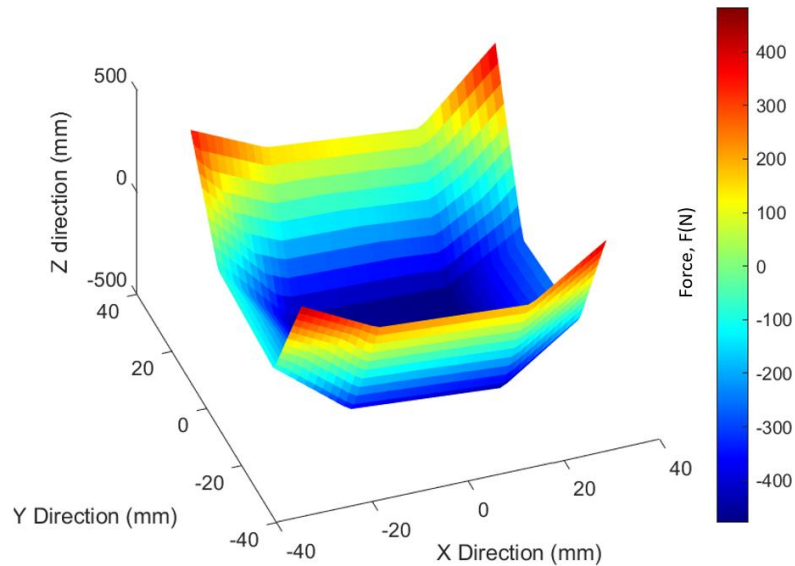


Figure 74: Surface profile showing the curl effect from the measured forces for Figure 68 at the end of the build for sample S1 (see Table 8 for more details)

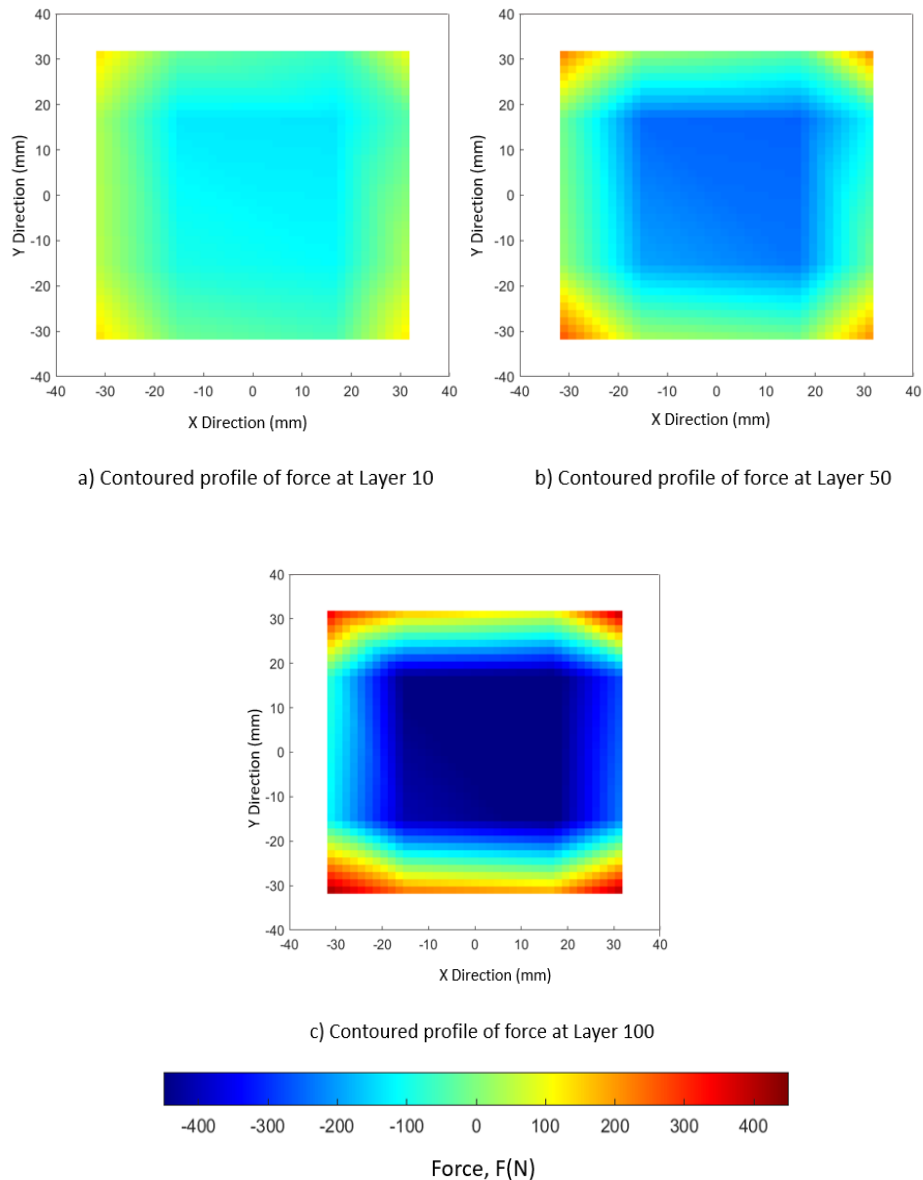


Figure 75: Contour plots of measured forces at layers (a) 10, (b) 50 and (c) 100 for a square sample (S1), shown in Figure 73. Using a Stripe scan strategy and a 30 μ m layer thickness (see Table 8 for more details).

Figure 76 shows the forces measured during the scanning process per layer. Each oscillation represents one layer of the build. When the laser is melting the metal powder, it causes a release of the residual stresses in the part; and an increase in the stresses when the part cools down as the laser beam is moved away and while the metal powder is spread for the next layer. This effect represents the thermal gradient mechanism (TGM), where, as the part is heated up by the laser this will locally relieve some stress and as the laser moves away the part cools down, causing the strain levels to rise due to the constraints of the underlying layers. As the melt pools solidify, the cooling causes the deposited material to shrink, pulling the

supports together generating a strain in the load cells. As can be seen in Figure 76, the development of the forces after the first ten layers of the build seems to follow a linear trend for both the centre and the corner load cells, this agrees with Shiomi et al. [45].

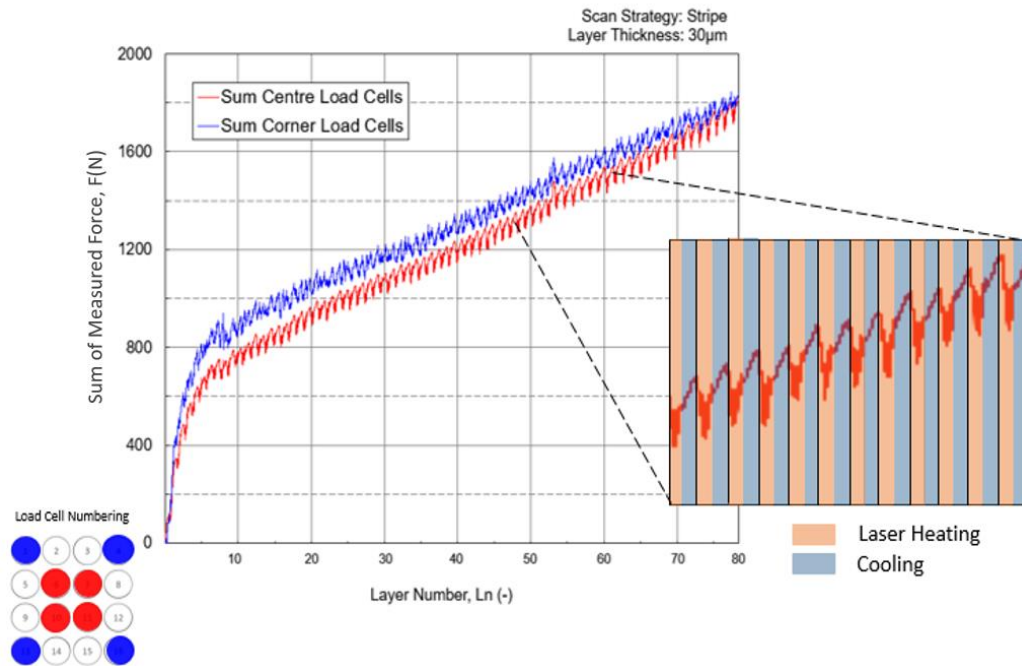


Figure 76: Comparison of the sum of the absolute resultant force of the corner and centre load cells per layer for Sample S1 built using the Stripe scan strategy with a 30µm layer thickness.

The sum of the absolute values for the corner load cells, shown in Figure 76, exhibit a higher strain rate than for the centre load cells, which might be caused by the geometry of the part. This would imply that the stresses generated are not equal across the build, such that the stresses are higher in the corners than in the centre of the part. This could be due to thermal expansion not being the same at the centre as it is in the corners of a part, as described by Rangaswamy et al. [102]. At the corners the heat flow is localised, and the energy dissipates further into the previous layers compared to the centre, which is surrounded by more material, and consequently, the energy dissipates to the sides.

Plots of the sum of the absolute forces from the load cells for the builds with porous and solid supports for the first 55 layers are shown in Figure 77. The results showed that the samples built with a porous structure in the pyramid section registered lower forces than the samples with a solid structure. This could be due to the lattice structure being less dense than the solid structure and absorbing deformation in the structure which is not transferred to the loadcells.

The samples built with 160 W laser power (samples S3 and S6; see Table 14) had a lower initial increment of force in the first layers of the build; this could be due to the melt pool being smaller with less laser power. The samples S3 and S6 failed at layer 55 and layer 61, respectively, due to a lack of bonding between the first layer of the square part and the pyramid section. As the penetration depth of the laser beam is smaller with a lower laser power, the melt pool depth is shorter; therefore, the bonding between the new layer and the previous layer is not as strong as for the higher laser powers, generating less strain into the load cells. In addition to developing insufficient bonding, a shorter penetration depth or melt pool depth could generate porosity in the parts [155].

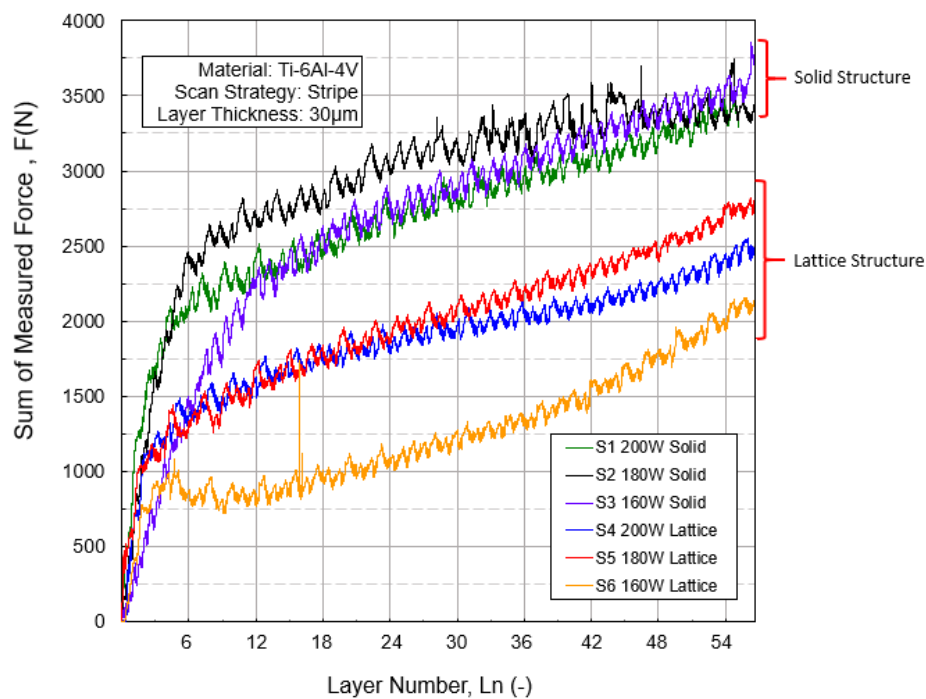


Figure 77: Effect of laser power and support structure on forces induced during the build process using a Stripe Scan Strategy. See Table 8 and Table 9 for details of specimens.

The variation of laser power had an effect on the forces measured using the FTD. For the samples with a laser power of 160 W (S3 and S6), the forces registered in the first layers of the build were much lower than for the samples built using a laser power of 200 W and 180 W; however, the samples with the lower laser power (S3 and S6) failed due to the poor fusion between the pyramid structure and the square section. For the samples with solid pyramid structures, the load cells registered at layer six an absolute sum of force of 1197 N for S3 while 2072 N for S1 and 2172 N for S2. However, later in the build at layer 12, the absolute sum of forces for S1 and S3 levelled up to 2326 N and 2191 N, while for S2 the absolute measured

forces at the same layer were 2677 N. This could be because of the lower laser power (160 W) for sample S3 causing a lower bonding with the previous section, which can lead to a partial release of the residual stresses due to the separation from the pyramid section. And after approximately 12 built layers, a more solid structure is built underneath the top surface levelling the values of residual stress development as suggested by Zyl et al. [180]. Figure 78 shows a contour map of the measured forces at the end of each build for Samples S1 to S5.

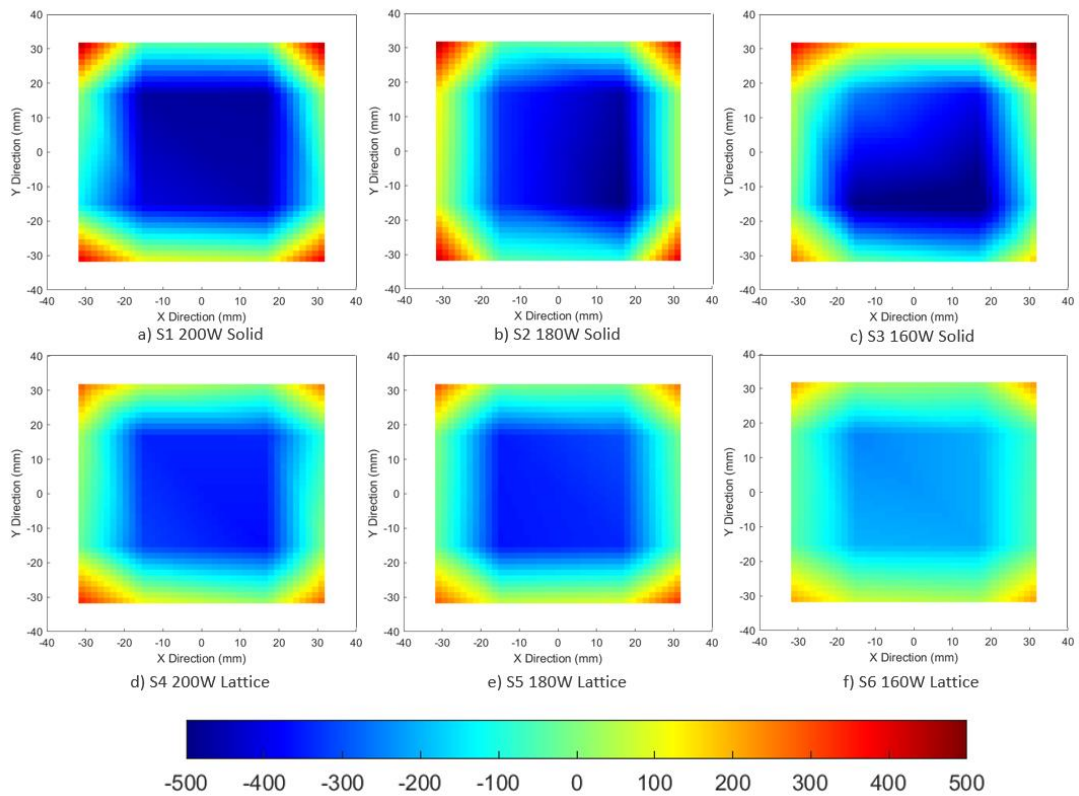


Figure 78: Contour plots of force at the end of each build for square samples S1 to S6 with the use of Stripe scan strategy and a laser power variation from 200 W to 160 W. Using a solid base (S1-S3) and lattice structure base (S4-S6). See Table 8 for further details.

In general, the forces in the sample S1 built with the maximum power of 200 W increased at a more consistent and lower rate than when the laser power was 180 W; thus, allowing the build to reach 74 layers for S1 compared to 67 and 55 for samples S2 and S3 respectively before any of the load cells reached the maximum load of 50 Kg (see Table 14). This agrees with previous literature, where it was reported that lowering the laser power reduced the maximum temperature of the melt pool, and its size, which resulted in higher cooling rates [98, 181].

Table 14: Results from the measured forces from the samples with laser power variation S1 to S6.

	No. Layers (-)	Sum of Measured Force (N)
S1 200W Solid	74	4098
S2 180W Solid	67	4037
S3 160W Solid	55	3607
S4 200W Lattice	68	3031
S5 180W Lattice	66	2856
S6 160W Lattice	61	2135

The size of the melt pool affects the cooling rates. A deeper melt pool has more thermal energy to dissipate and so takes longer to cool and solidify [182]; by lowering and controlling the thermal gradients and cooling rates in the process, residual stress can be mitigated. However, these results are contrary to other work [154], where the increase in energy input increased the residual stress levels. By reducing the laser power, the energy input into the sample is less; thus, more porosity is induced in the sample, as it can be seen from the micrographs of the samples shown in Figure 79. Therefore, the effect of the energy density on residual stress was further studied in this thesis.

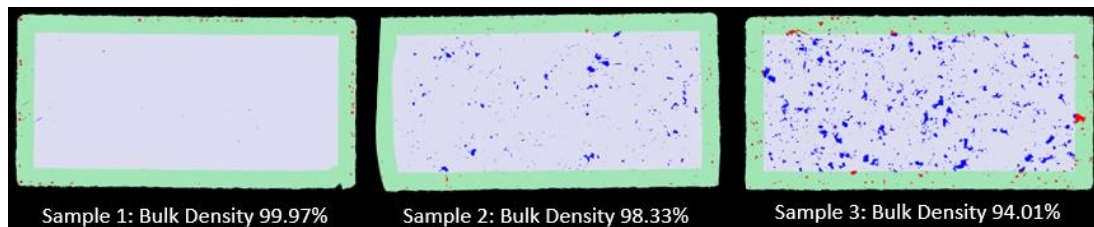


Figure 79: Density results and micrographs from Samples S1, S2 and S3, built using different levels of laser power shown in Table 8

The samples with lattice structure in the pyramids had similar outcomes to those with the solid structures, i.e. samples S4 and S5 built with a laser power of 200 W had the same measured forces in the first layers of the build, whereas, the incremental rate was higher for sample S6 built with 180 W laser power. Sample S6 built with 160 W exhibited much lower forces later in the build and, as for sample S3 the build failed at layer 61.

The samples built with a lattice structure in the inversed pyramid section exhibited lower increments of force as well as lower heat transfer into the load cells (Table 14). However, the results were less consistent between builds due to the lattice structure on the pyramid section of the samples. Therefore, it was decided to use a solid structure for the inversed pyramid section of the samples for all the future experimental work presented in this thesis. These experiments showed that the residual stress depends not only on the process parameters, i.e. laser power but also on the support structures. Imperfections, such as porosity or lack of fusion between layers/supports/substrate, can cause deformation and stress relaxation [180].

4.1.2 Effect of the Scan Strategy and Layer Thickness

According to the literature, the exposure strategy used to fuse the powder layers has a significant influence on the development of residual stress. Some studies suggest that stresses are higher perpendicular to the scan direction than along the scan direction [177, 183], and longer scan vectors develop higher stresses than dividing vectors into shorter length scans [97, 137, 174]. In order to measure the effect of scan strategy on the development of residual stresses, different scan strategies were tested using two different part geometries a rectangular part of 32 mm x 112 mm using the FTD1 and a square part geometry 64 mm x 64 mm using the FTD2, previously described in section 3.5.5. The scan strategies were compared using the parameters needed to produce a sample of nearly 100% density as shown in Table 8. In-situ measurements were recorded through the building process, as described in section 4.1.1. Each build was stopped when any of the load cells reached its maximum allowable force of 50 kg.

In-situ measurements for Rectangular Parts

Results from the in-situ measurements for part S7 are shown in Figure 80. The external corner (load cells 1, 8, 7, and 14) are in tension and are being pulled away from the base plate, while the rest of the structure (load cells 2, 3, 4, 5, 6, 9, 10, 11, 12, and 13) is in compression and is being pushed towards the base plate. Therefore, after the part was detached from the load cells and its strains were released, the part curled away from the build platform as can be seen in Figure 81. This deformation is analysed later in the thesis. The build was stopped at layer 98 at a height of 2.94 mm when load cell 14 approached 50 kg. The forces in the load cells did not increase to a significant extent when the part cooled down after the build was stopped. As shown in the previous samples (Figure 76), the cycle for each layer follows the theory of the thermal gradient mechanism (TGM), i.e. when the laser melts the powder, the stresses are released, and the load cells register lower forces this is followed by a steady increase

when the laser moves away and the melted material solidifies and cools down while the powder is spread for the next layer. Then the process is repeated for each layer.

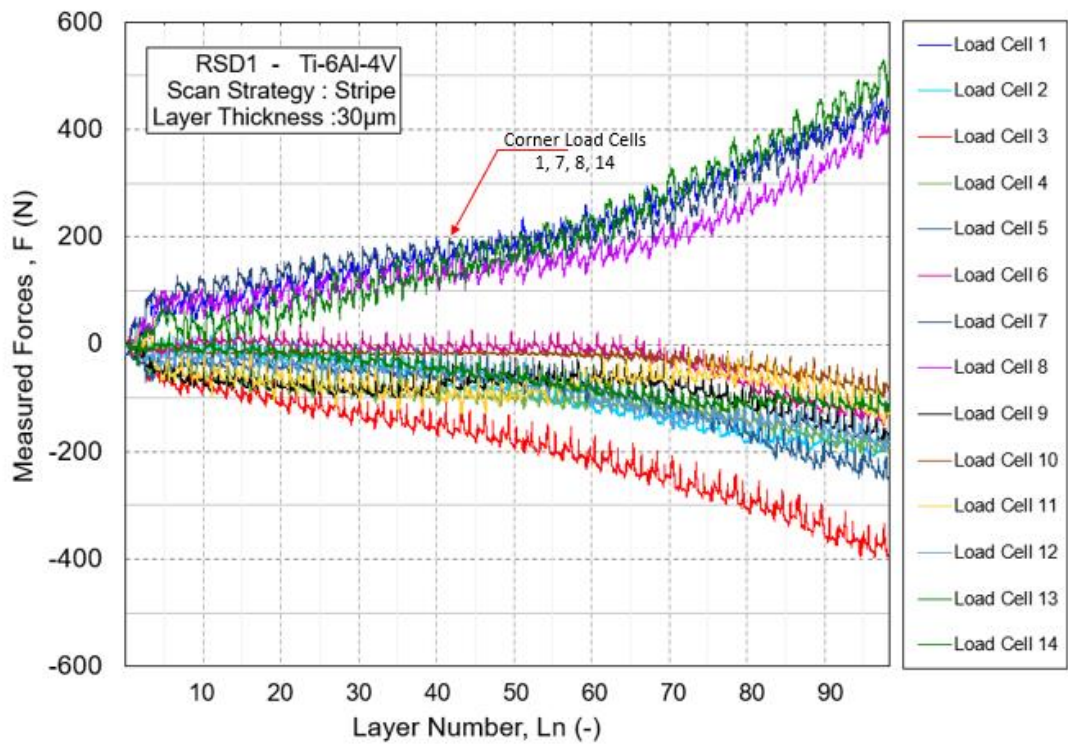


Figure 80: In-situ measurements for a rectangular part built on the FTD1 with a Stripe scan strategy for specimen S7, see Table 10 for details

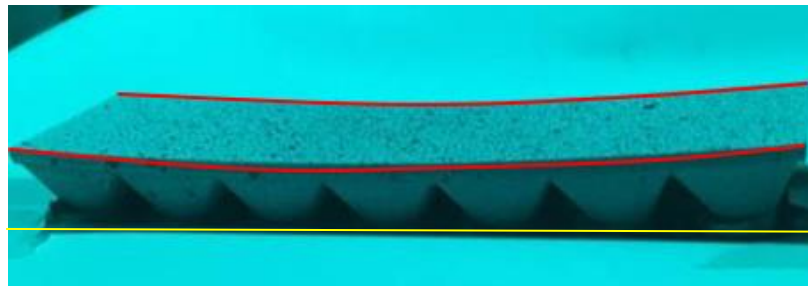


Figure 81: Curl-up of specimen S7 (see Table 10) following release from the build platform as previously studied by Thomas [170] in his thesis work

The sum of the measured forces developed on the front row of load cells (1 to 7) were higher compared to the sum of the forces from the back row (8 to 14), as can be seen in Figure 82.

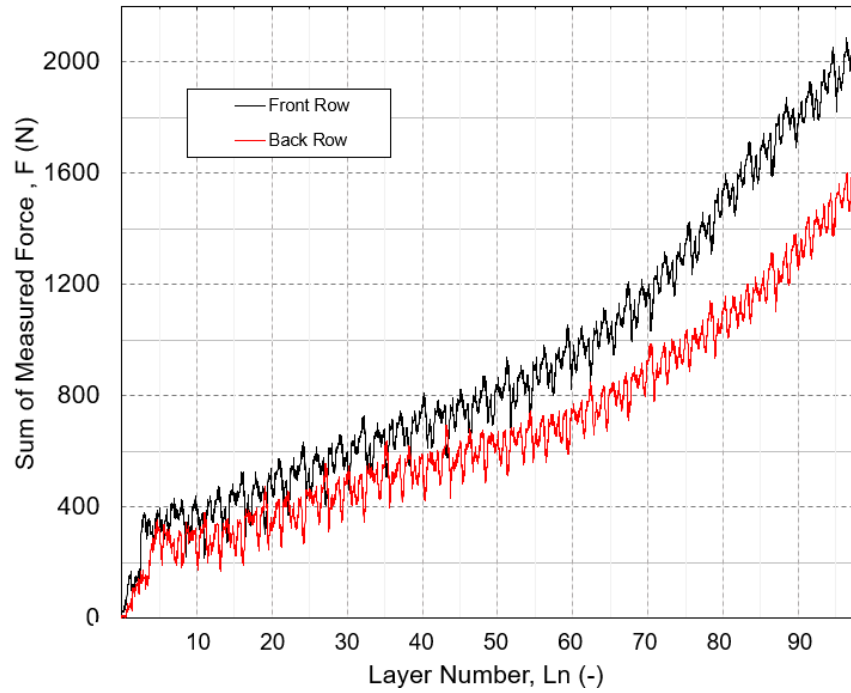


Figure 82: Comparison of measured forces for the front and back rows of the FTD1 for a rectangular part for Sample S7. More details can be seen in Table 8

In order to see the effect of the scanning direction in the development of the forces, two more parts were built, one with all the vectors in the X-direction and one with all the vectors in the Y-direction as shown in Figure 71 b and c. The results from the in-situ measurements are shown in Figure 83.

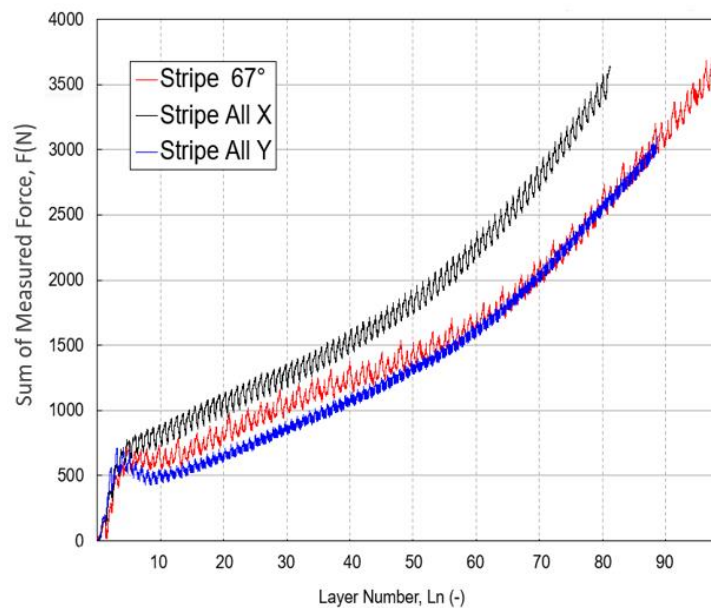


Figure 83: Results from In-situ force measurements using FTD1 for a rectangular part using three scan strategies: Rotating 67° per layer (Sample S7), Stripe all-X (Sample S8) and all-Y scan strategies (Sample S9)

It is clear that the all-X sample (S8) developed much higher forces than the all-Y sample (S9) and the 67° rotating Stripe sample (S7). When the build for the all-X sample S8 was stopped, due to reaching to the maximum load of 50 kg at layer 80, the sum of the forces was 3737 N compared to 2750 N for the all-Y and 2818 N for the stripe rotating 67° build. The length of the rectangular part in the X direction is greater than its width (Y direction); hence, these differences could have arisen because the forces developed parallel to the laser scan orientation were higher than the ones developed perpendicular to the laser scan. This would agree with previous results [49] that suggest that the stress generated normal to the scanning direction are lower than parallel to it. Figure 84 shows a contour plot of the force distribution along the part, as it can be seen the forces in the corners are in tension while the forces at the centre of the part are in compression as from the previous results from the square parts and as previously reported in the literature [158, 179].

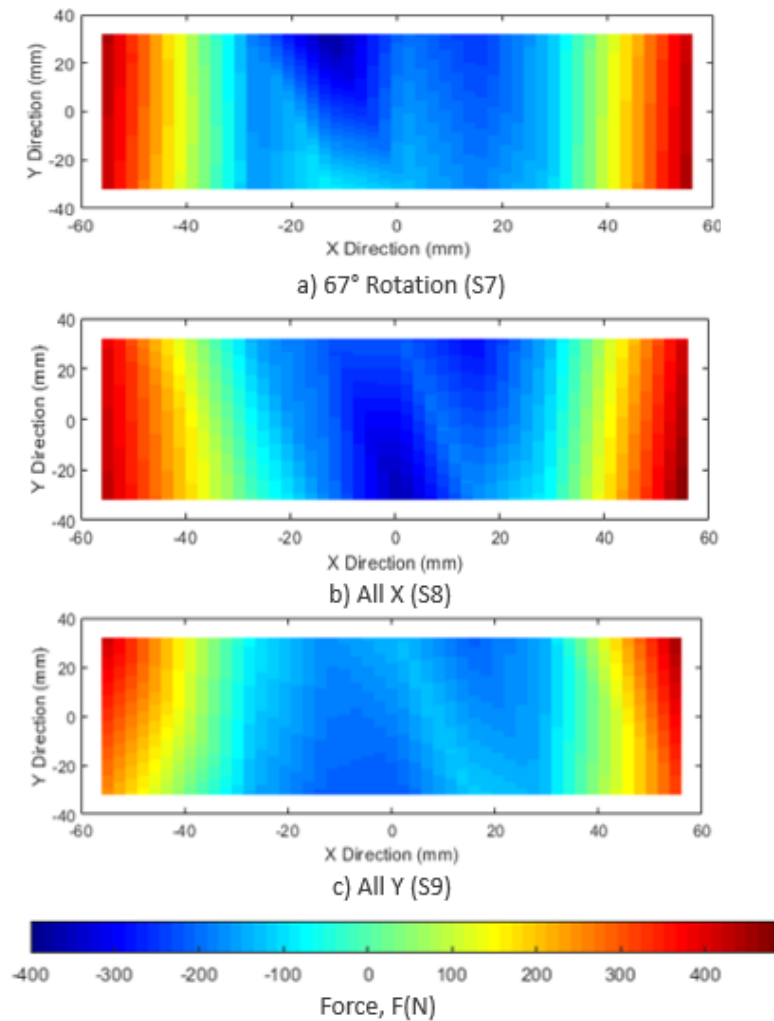


Figure 84: Contour plots of force at the end of each build for rectangular samples S7, S8 and S9 shown in Figure 79 using (a) Stripe 67° rotation scan strategy, (b) scan vector with all X orientation, and (c) scan vector in all y orientation. See Table 7 for further details

A closer look at the development of the forces in each layer for each scan strategy from layer 7 to 12 is shown in Figure 85. Even when the stripe length of each scan vector is the same (5 mm), the orientation of the scanning had an influence on the development of the forces. For the sample S9 with all-Y scan vectors, the forces were much lower and exhibited less variation or amplitude from layer to layer; this could be due to the lower cooling rates. The scanning section is longer in the horizontal direction; therefore, as the laser scans through the whole length of the part, the temperature of the part cools at each location before the laser returns and starts melting the next layer. When the orientation of the scanning vector changes between each layer, it can be seen that there is a higher variation in the forces developed in each layer, due to the fact that the laser starts scanning at different points in each layer. This may contribute to keeping a more constant temperature through the process, especially for more complex part geometries and for parts with more layers. As can be seen in Figure 83, the All Y scanning strategy seems to develop slightly lower forces at the beginning of the build, but later as more layers were added, the forces increase at higher rates until they are equal to those for the rotating scan strategy. The builds had to be stopped due to the limitation of the load cells, but the results could mean that the rotating scan strategy would develop less residual stress if a much higher part was built.

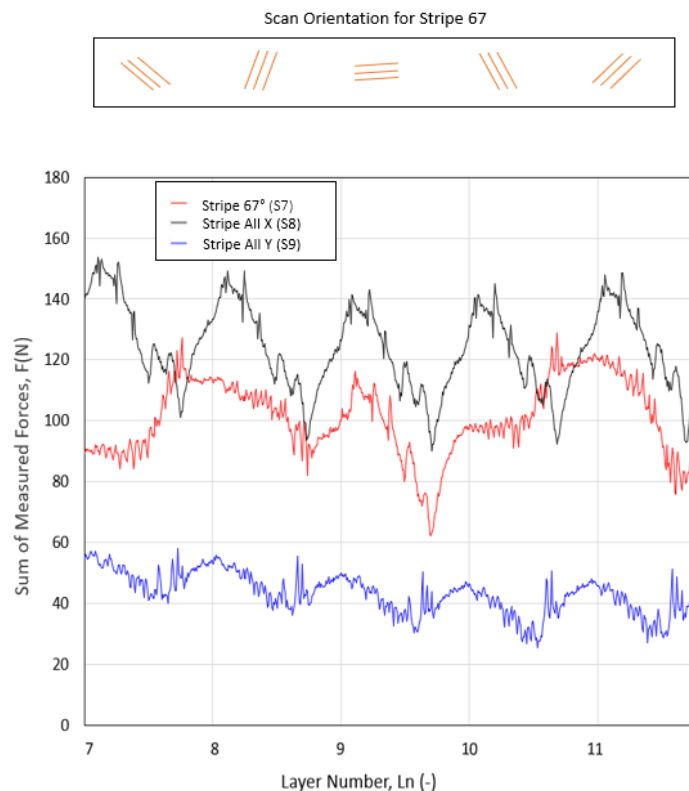


Figure 85: Development of forces in each layer for different scan strategies for Samples S7, S8 and S9, see Table 10 for details.

To further investigate the effect of the scan strategies, samples were built using the Stripe, Chessboard and Meander strategies, samples S7, S10 and S11, respectively. The scan strategies were compared based on the parameters needed to manufacture samples with a relative density greater than 99.9%, as shown in Table 10. The samples were built using the rectangular geometry (samples S7, S10, S11) and the square geometry (samples S12, S13 and S14) on both of the FTDs. Figure 86 shows the sum of the absolute values for the measured forces from the load cells for the builds with Meander, Stripe and Chessboard with the rectangular part geometry samples S7, S10, S11, respectively. The Meander scan strategy developed much lower forces than the Chessboard and Stripe scan strategies. At layer 85 Meander's total force was 1034 N compared to 2638 N for the Stripe and 2473 N for the Chessboard strategies. This allowed a much higher part to be built with the Meander scan strategy before reaching the maximum working force on any of the load cells. The build with the Meander scan strategy was stopped at layer 136, with a height of 4.08 mm. The build with the Chessboard scan strategy was stopped at layer 107, with a height of 3.21 mm, and the build with the Stripe scan strategy was stopped at layer 97, with a height of 2.91 mm, which was almost 30 % less than achieved with Meander scan strategy.

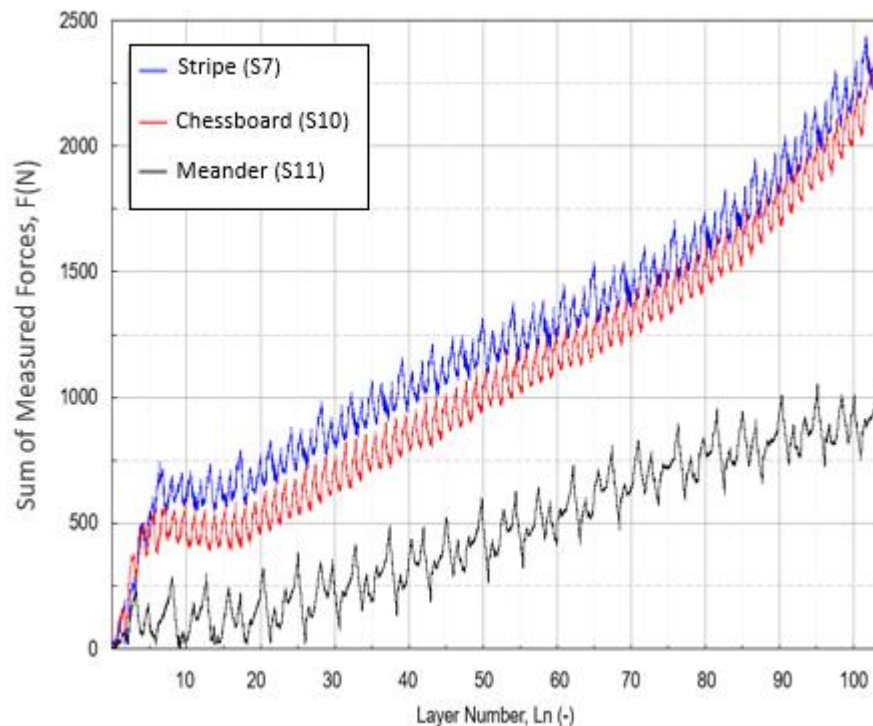


Figure 86: In-situ Measurements of the sum of the measured forces (N) per layer for rectangular parts built with the Stripe (S7), Chessboard (S10), and Meander strategies (S11) and a layer thickness of 30 μm , see Table 10 for details.

Contour plots of force at the end of each build for Samples S7, S10 and S11 are shown in Figure 87. It can be seen that the sample built using the Meander scan strategy with single scan vectors produced much lower forces compared to the Stripe and Chessboard scan strategies, which divide the part geometry into smaller scanning segments. From the samples built using sectioned scanning, Stripe and Chessboard strategy, it can be seen that even that the sum of forces is lower (Figure 86), the sample built using the Chessboard strategy developed higher forces of nearly 500 N at the edges of the part which could lead to higher part deformation; the part deformation is further analysed in this section.

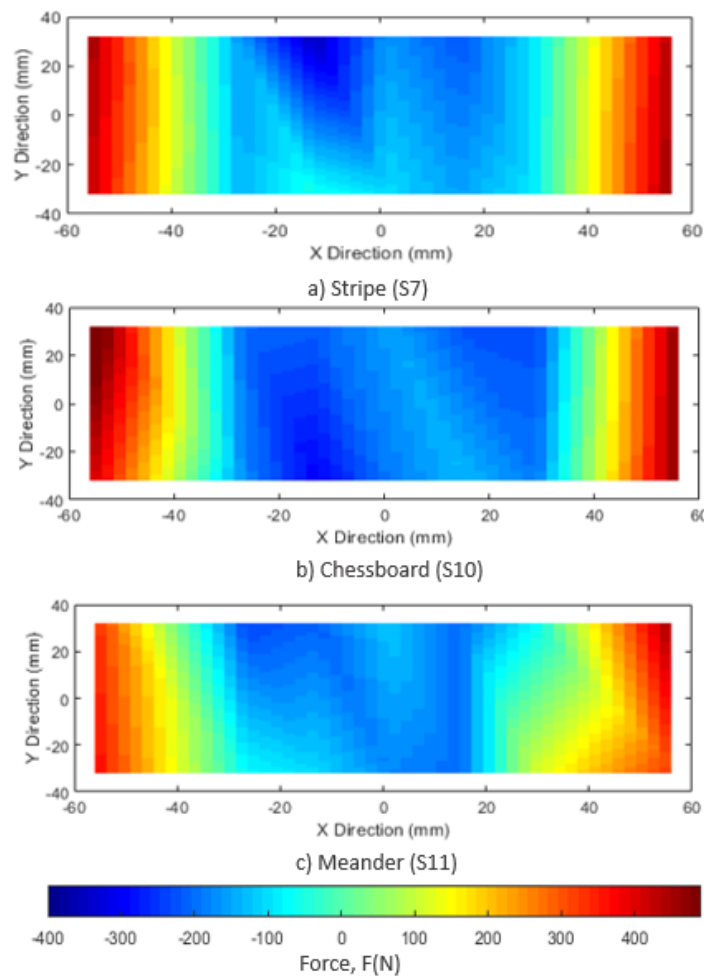


Figure 87: Contour plots of force at the end of each build for rectangular samples S7, S10 and S11, using a 30 μm layer thickness and different scan strategies (a) Stripe (b) Chessboard, and (c) Meander. See Table 10 for details.

From Figure 88, which shows the sum of measured forces for the first 15 layers of the build, it is clear that the Meander scan strategy has a high variation of force from layer to layer compared to the Chessboard and Stripe scan strategies. For the Meander scan strategy, every second layer the forces decrease followed by an increase with the third layer and this reduced

the overall forces in the part. Whereas for the Chessboard and Stripe scan strategies, the increments in forces are approximately constant for each layer, adding up layer after layer. The results imply that the sectioning of the scan vectors gives a more constant temperature during the build. However, the forces measured for a single line vector are much lower compared to the sectioning scans. This could be related to the overlapping of the sectional scanning, which was necessary to avoid porosity in the samples built with Stripe and Chessboard scan strategies; the overlapping means more material is being re-melted, which creates higher thermal gradients in each layer. By reducing the point distance for the Stripe and Chessboard scan strategies, more energy is input into the part, which probably increases the residual forces.

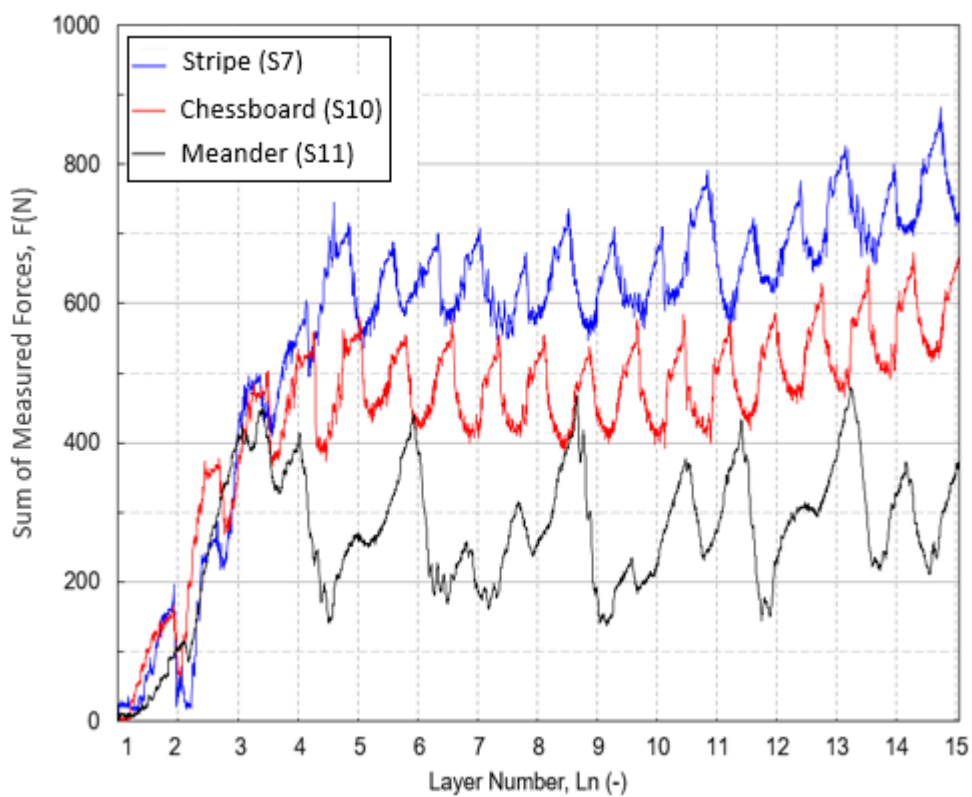


Figure 88: Sum of absolute measured forces for the first 15 layers of the rectangular part built using the Stripe (S7), Chessboard (S10) and Meander (S11) scan strategies with a layer thickness of 30 μm , see Table 10 for details.

In addition to the energy input, the period the laser is on varies with the scan strategies. For the Meander scan strategy, the average time of a scan was 57 seconds per layer, for the Stripe scan strategy the average was 48 seconds and for the Chessboard scan strategy the average was 48 seconds per layer. The Meander scan strategy had a much higher scanning time per layer, and the time between each layer had more variation compared to the other two scan

strategies. This was reflected in the inconsistency of the magnitude of the forces per layer. Table 15 shows the scanning times for the first 15 layers of each build; these times include the time for powder deposition. Previous studies have shown that the interlayer dwelling times have an effect on the development of residual stress [120]. The previous literature suggests that the part geometry also has an effect on the development of residual stresses in the L-PBF process; therefore, in order to see if the effect of dwell time is related to the part geometry, additional samples for each scan strategy were built with a square geometry, and using the FTD2.

Table 15: Scanning time (in seconds) per layer (L1-L16 for samples S7, S10 and S11) with a rectangular geometry (see Table 10 and Figure 72 for more details)

	L1	L2	L3	L4	L5	L6	L7	L8
Stripe (S7)	46.12	46.12	46.12	45.80	45.80	45.80	45.80	45.44
Chessboard (S10)	48.36	48.68	48.68	48.68	48.04	47.72	48.04	48.36
Meander (S11)	60.85	59.25	57.33	57.97	60.53	57.01	57.33	55.41
	L9	L10	L11	L12	L13	L14	L15	L16
Stripe (S7)	45.80	48.36	48.04	48.36	48.04	48.04	49.32	48.04
Chessboard (S10)	48.68	48.36	48.04	48.04	47.72	48.04	47.72	48.04
Meander (S11)	60.21	56.05	56.05	55.41	59.8	58.61	56.37	56.05

In-situ measurements for square parts

Figure 89 shows a comparison among the sum of the forces for 64 mm x 64 mm square parts measured on the FTD2 for each scan strategy (Stripe (S12), Chessboard (S13) and Meander S14), using a layer thickness of 30 μm . As shown in previous results from a rectangular part geometry, the residual stress levels developed in the build vary depending on the scan strategy used. The Meander scan strategy showed the lowest forces, thus enabling a higher part to be built, before reaching maximum working force of any of the load cells. At layer 65, the total force was 1457 N for the Meander scan strategy compared to 2385 N and 2330 N for the Stripe and Chessboard scan strategies respectively.

Figure 89 show the sum of the measured forces for the samples S12, S13 and S14. A contour plot of the measured forces at the end of each build are shown in Figure 90.; S14 manufactured with Meander scan strategy, the build was stopped at layer 129, with a height of 3.87mm. The sample built with the Chessboard scan strategy (S13) was stopped at layer 92 with a height of 2.76 mm. The sample built with the Stripe scan strategy (S12) was stopped

at layer 78 with a height of 2.34 mm. As shown in Figure 89, the Stripe and Chessboard scan strategies showed a faster increased in the measured forces, reducing the part height by 40%, compared to the Meander scan strategy. It is evident from the start of the build, for the Stripe and Chessboard scan strategies, that there is a peak in the force and after the first ten layers, the force increases in an approximately linear manner, as with the previous results for rectangular parts. The differences in the forces measured for the Meander, Stripe and Chessboard scan strategies, could be related to the effect of scan segmentation on the thermal gradient. The Stripe and Chessboard scan tracks were split into 5mm width sections; therefore, to avoid pores in the part, the hatch distance needed to be higher than for the Meander scan strategy, resulting in more overlap between scan vectors and therefore more material being re-melted and higher residual stress. A plot of the measured forces for the first 15 layers of these samples is shown in Figure 91.

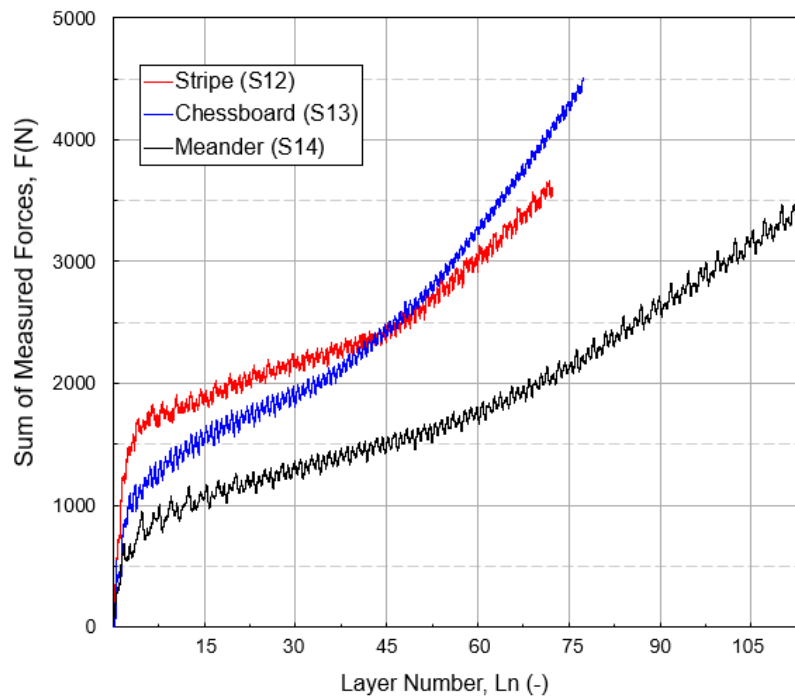


Figure 89: In-situ Measurements Resultant Forces (N) per Layer. Comparison of Stripe S12, Chessboard S13 and Meander S14 scan strategies used to build square parts with $30\ \mu\text{m}$ layer thickness showing the sum of the absolute forces registered from FTD2. See Table 10 for details.

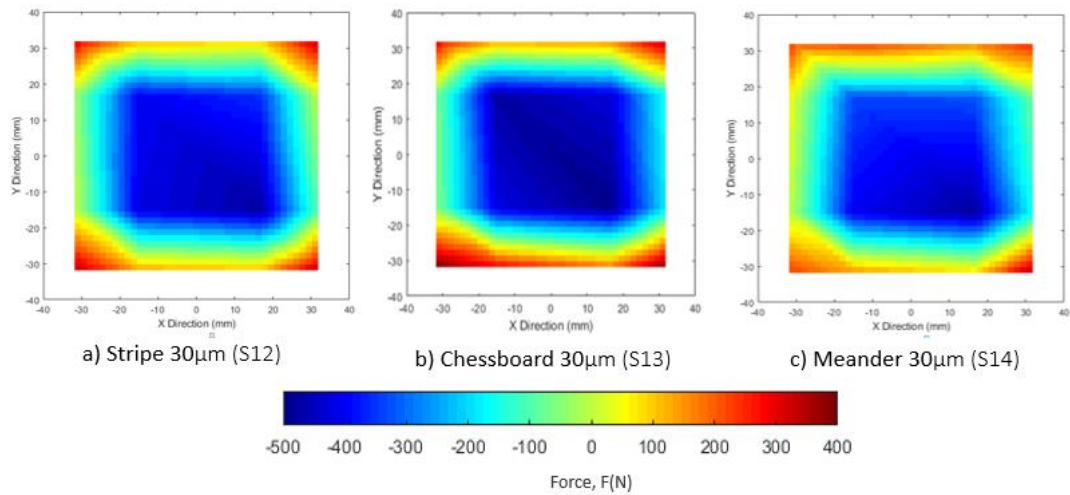


Figure 90: Contour plots of force at the end of each build for square samples S12, S13 and S14. Samples built using a 30 μm layer thickness and different scan strategies (a) Stripe, (b) Chessboard and (c) Meander. See Table 7 for details.

Similar to the rectangular parts, the average scanning time per layer in the square parts was higher for the Meander scan strategy. The scanning times per layer are shown in Table 16, and the Meander scan strategy has more variation than the Stripe and Chessboard scan strategies. However, due to the symmetry of the square part, the variation between layers was not as significant as in the rectangular part for the Meander strategy; nevertheless, it was still more significant compared to Stripe and Chessboard strategies. The average scanning times per layer were 62.29 seconds, 50.01 seconds and 53.79 seconds, for the Meander, Stripe and Chessboard respectively. These results confirm the interlayer effects on the development of residual strains in the L-PBF process; because, as a layer of a part is scanned, the time elapsed from the scanning and powder deposition until the laser heats the same point has been demonstrated to change the forces measured in the Ti-6Al-4V samples, as shown in previous studies [91, 109].

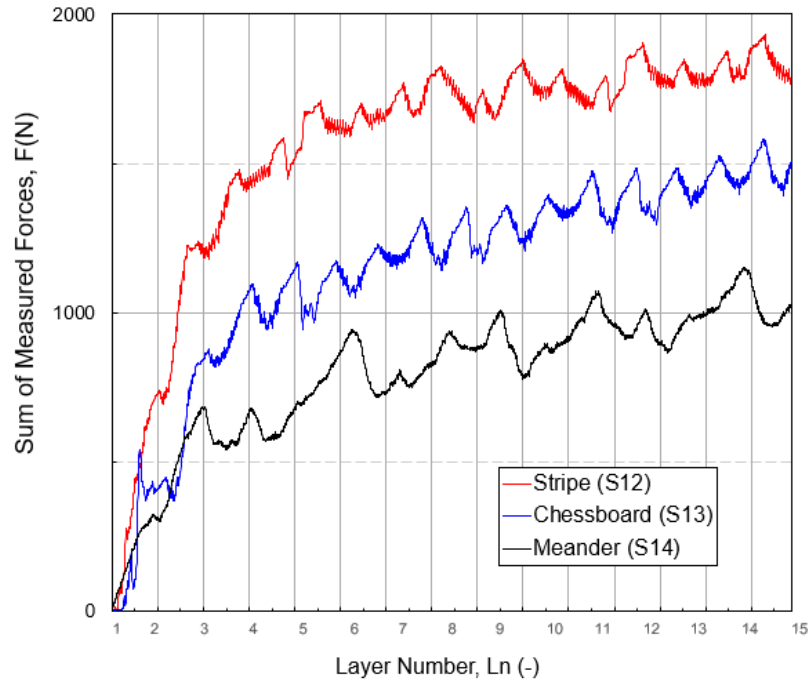


Figure 91: Sum of absolute values measured in the first 15 layers of squared parts built using Meander, Stripe and Chessboard scan strategies with 30 μm layer thickness. See Figure 89 for complete build and Table 10 for details of the parts and build parameters.

Table 16: Scanning time (in seconds) per layer (L1-L16) for samples with square geometry see Table 10 and Figure 91 for details.

	L1	L2	L3	L4	L5	L6	L7	L8
Stripe (S12)	50.93	50.93	50.93	52.21	50.93	51.25	50.93	50.93
Chessboard (S13)	54.45	53.49	53.81	53.81	54.13	53.49	53.81	53.81
Meander (S14)	62.79	61.83	62.79	65.03	61.18	62.47	59.90	64.39
	L9	L10	L11	L12	L13	L14	L15	L16
Stripe (S12)	50.61	50.61	50.93	50.61	51.57	50.93	50.93	50.61
Chessboard (S13)	53.81	53.81	53.81	53.81	53.17	53.81	53.81	53.81
Meander (S14)	60.54	62.79	60.86	64.07	59.90	63.11	62.79	64.07

Effect of the Layer Thickness on Residual Forces

In order to see the effect of the layer thickness on the residual forces, the samples were built using the Stripe and Meander strategies with a layer thickness of 60 μm . As mentioned before the Chessboard scan parameters for a 60 μm layer thickness are not of interest because it is not feasible for larger and more complex part geometries. The results for the forces developed were similar to those for a 30 μm layer thickness and are shown in Figure 92 and Figure 94.

The initial forces developed using the Stripe strategy were much higher than with the Meander strategy. At layer five, the sum of measured forces was of 1000 N for the sample built using the Meander strategy while for the sample built using the Stripe strategy the sum of measured forces at layer five was of 2500 N, over 50% more from the first layers of the build. However, after the first 10 layers the gradient of the plot in Figure 92 are approximately equal and constant for the two scan strategies. The difference in forces at the start of the build allowed a part of 65 layers with a height of 3.9 mm to be built with the Meander scan strategy and only 40 layers with a height of 2.4 mm with the Stripe scan. Contour plots of force at the end of each build for Sampler S15 and S16 are shown in Figure 93.

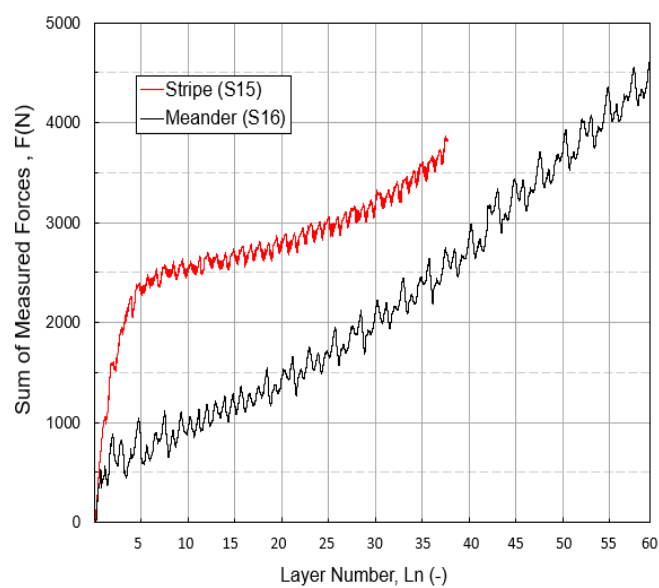


Figure 92: Sum of absolute values measured in squared parts built using Stripe (S15) and Meander (S16) scan strategies with 60 μm layer thickness. See Table 10 for details of the build parameters.

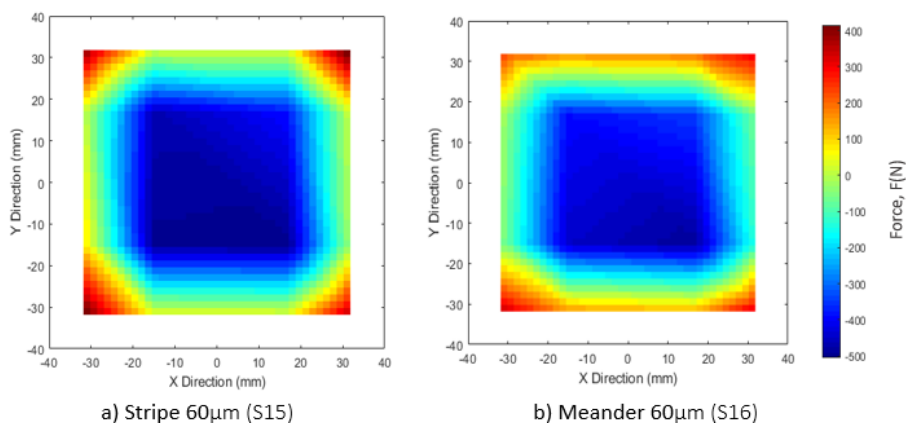
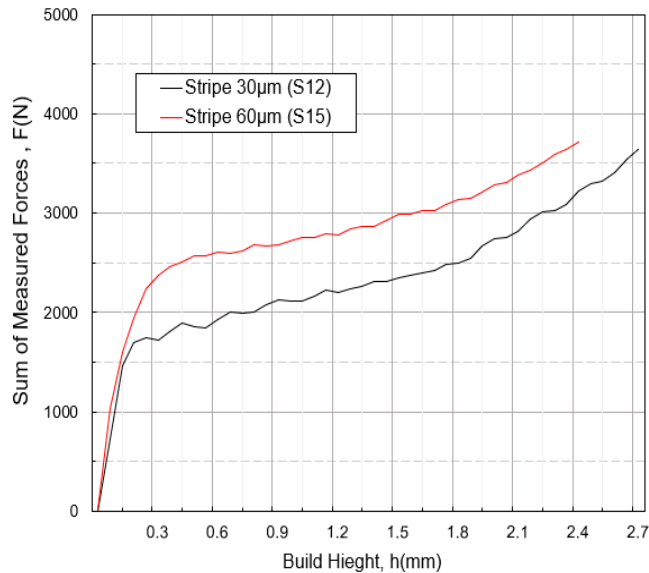
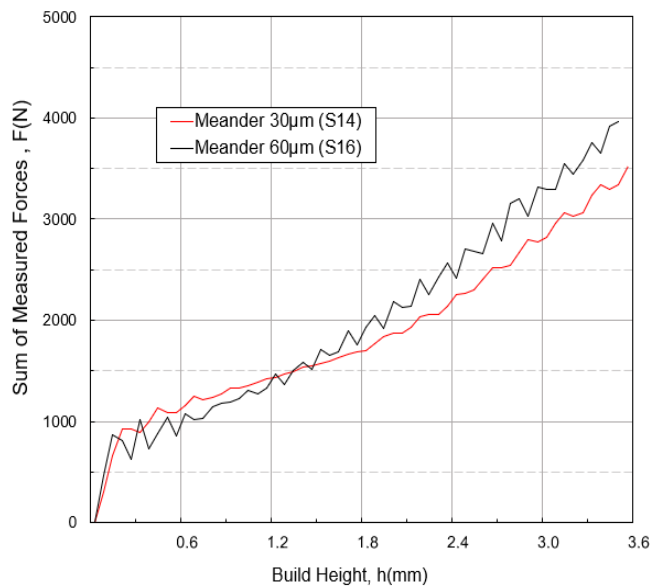


Figure 93: Contour plots of force at the end of each build for square samples S15 and S16 built using a 60 μm layer thickness and different scan strategies (a) Stripe and (b) Meander. See Table 7 for details.

A larger layer thickness requires a larger amount of powder to be melted by the laser beam to induce proper bonding between the newly deposited layer and the previously deposited layers. Thus, different processing parameters were needed to yield the same part density, and this was achieved by increasing the exposure time (ET) and reducing the hatch distance (HD) and point distance (PD) for the 60 μm layer thickness samples.



(a)



(b)

Figure 94: Effect of layer thickness on residual forces for (a) Stripe and (b) Meander scan strategies. See Table 10 for further details.

For the Stripe scan strategy, the increase in exposure time and reduction in point distance reduced the scan speed from 1100 mm/s for a layer thickness of 30 μm to 857 mm/s for a layer thickness of 60 μm . As a result, the volumetric energy density (ED) (J/mm^3) was reduced correspondingly from 57.72 J/mm^3 to 40.93 J/mm^3 . As can be observed in Figure 94(a) induced forces were higher for the 60 μm sample from the start of the build. The total force registered by the load cells at 2.4 mm was 12% higher for the 60 μm layer thickness than for the 30 μm layer thickness corresponding to total forces of 3710 N and 3228 N respectively. For the Meander scan strategy, the increase in exposure time and reduction in point distance reduced the scan speed from 1500 mm/s for a layer thickness of 30 μm to 857 mm/s for a layer thickness of 60 μm . As a result, the volumetric energy density (ED) (J/mm^3) was reduced correspondingly from 68.37 J/mm^3 to 40.93 J/mm^3 . As can be observed in Figure 94(b) the distribution of the induced forces were higher for the 60 μm sample from the start of the build. The total force registered by the load cells at 3.6 mm was approximately 11% higher for the 60 μm layer thickness than for the 30 μm layer thickness corresponding to total forces of 3961 N and 3521 N respectively.

It can be observed in Figure 94 that, for both scan strategies, the induced forces at the maximum height are 11% higher for the thicker layer which is the opposite trend to that expected from the lower energy input and might arise due to the effect of reducing the scan speed. Since, as the scan speed is reduced, the scanning time per layer is reduced which increases the cooling times for the deposited layers and might develop greater residual forces, as previously demonstrated by Denliger [120]. A summary of the build height among the different scan strategies and layer thickness for the square samples is shown in Figure 95.

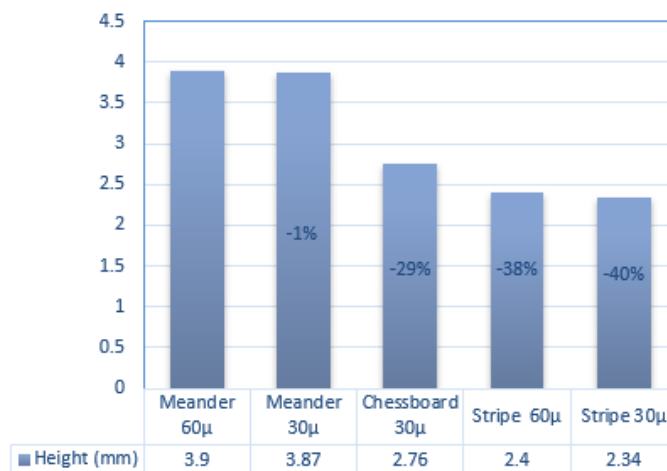


Figure 95: Comparison of build height among the different scan strategies and layer thickness for the squared samples

4.1.3 Analysis of the Part Deformation

When removing the part from the substrate, in this case the FTD, the strains in the part will be released, causing deformation of the part. A non-destructive approach was chosen to measure this part deformation using Digital Image Correlation (DIC) [158]. DIC is a popular and powerful technique for full-field motion, deformation and shape measurement [159]. The deformation of the part after removal was measured using DIC while the bolts were removed in the sequence shown in Figure 96. Figure 97 shows the DIC measurements of the part with no bolts removed (top) where no deformation is registered as the bolts are restraining the part; when the corner bolts have been removed and when the subsequent pair of bolts are removed moving inwards. No data was collected when the final pair of the bolts at the centre of the part were removed because, by this stage they were not restraining any constraint. As expected from the results obtained from the FTD measurements, the corners of the parts curl upwards indicating they were in tension.

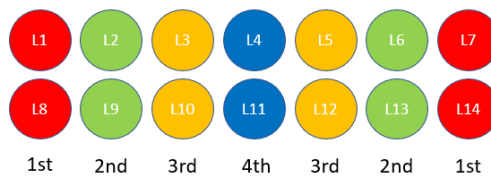


Figure 96: Sequence for the part removal from the FTD1 for DIC measurements for part deformation

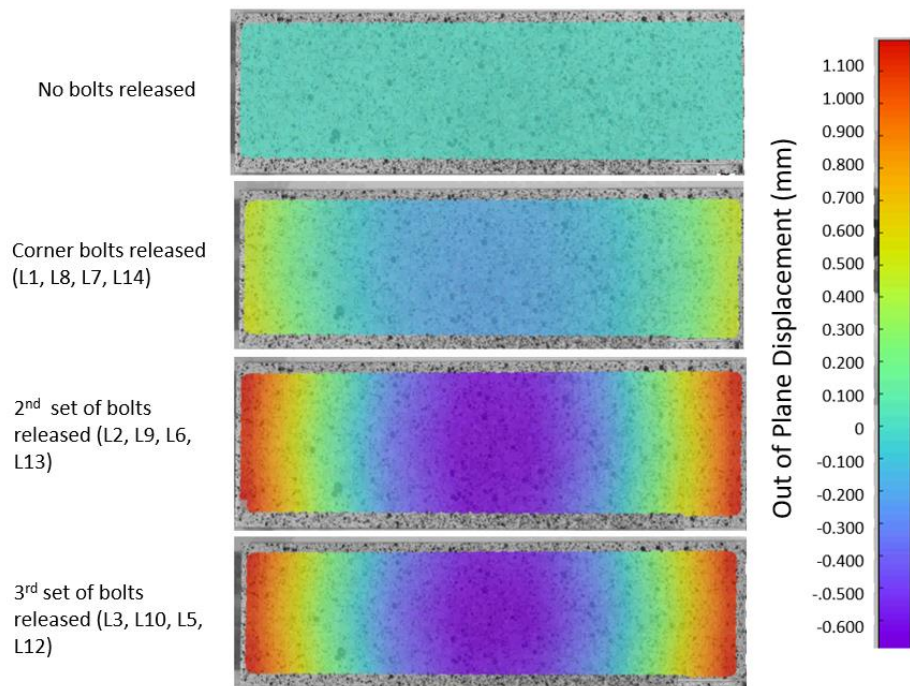


Figure 97: Results from DIC measurements for out of plane distortion when the bolts are removed from the FTD1 in the sequence shown in Figure 88 for Sample 7 (see Table 10) for details. Note that no data was collected when the final set of bolts were removed.

In order to investigate the effect of the scan strategies and layer thickness on the part deformation after the part is released from the build platform, the previously built square samples were measured using the DIC system, and the results are shown in Figure 98. The square parts show the same upwards curl as the rectangular parts but about both axes of symmetry rather than in a single direction. The Meander strategy with a 30 μm layer thickness exhibited the least deformation with an overall part deformation of 0.638 mm. As seen in previous results from the in-situ measurements, the Meander strategy developed lower force increment while the part was being built; thus, less strain was released when the part was detached from the FTD. The meander scan strategy exhibited almost 60% less deformation than the Stripe scan strategy, for which the overall part deformation was 1.209 mm and 1.051 mm for layer thicknesses of 30 μm and 60 μm respectively. While, the layer thickness had almost no effect in the build height results, the DIC measurements show that the parts built with 30 μm layer thickness had approximately 12% less deformation when removed from the load cells compared to the 60 μm layer thickness with the same scan strategy, which was the same % difference in the force developed during the building process. A summary of the results from the DIC measurements are shown in Table 17.

Table 17: Results from DIC measurements of square parts after removal

DIC Results for Deformation on Square Parts					
Scan Strategy	Stripe (S13)	Chessboard (S14)	Meander (S16)	Stripe (S15)	Meander (S17)
Layer Thickness	30 μm	30 μm	30 μm	60 μm	60 μm
Maximum Deformation (towards the laser)	0.657 mm	0.653 mm	0.412 mm	0.753 mm	0.451 mm
Maximum Deformation (against the laser)	-0.394 mm	-0.387 mm	-0.226 mm	-0.456 mm	-0.275 mm
Absolute Deformation	1.051 mm	1.040 mm	0.638 mm	1.209 mm	0.726 mm

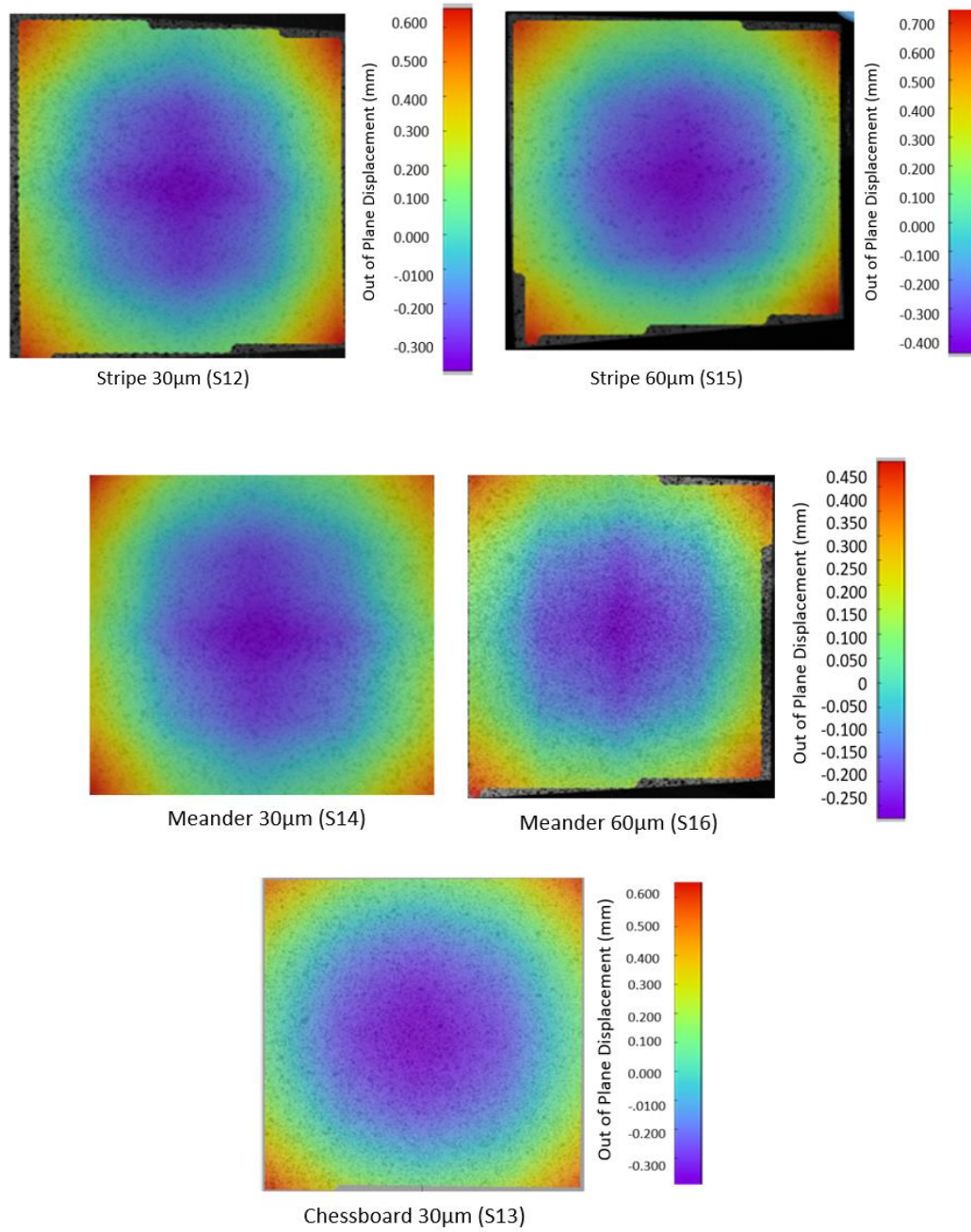


Figure 98: DIC measurements of part deformation after removal for different scan strategies and layer thicknesses for Ti-6Al-4V square samples (S12-16), see Table 10 for details

4.2 In-situ Measurements of Developed Strains in L-PBF for Nickel-based Super Alloys: Inconel 625, Inconel 718 and Maraging Steel

Previous studies suggest that the material properties have an effect on the development of residual stress and can alter the effect of process parameters [90] in the L-PBF process. Therefore, it is important to gain a better understanding of the effect of the material properties on the development of residual stresses in the L-PBF process. In order to determine the effect of the material properties on the development of residual forces, square samples were manufactured, and the FTD2 was used to measure the forces developed when using three different metal powders: Inconel 718, Inconel 625 and Maraging Steel. The effect of the inert gas atmosphere on the forces developed and the part deformation for two metal powders, i.e. Inconel 625 and Maraging steel was also investigated. In addition, in this section, the effect of the volumetric energy input on the development of residual forces is reported for Inconel 625.

4.2.1 Effect of the Scan Strategy

The results from the in-situ measurements of forces developed while the part is built for a square part built using Inconel 625 are shown in Figure 99; the developed forces show similar results as the previously shown for Ti-6Al-4V. The corners of the part are in tension while the centre of the part is in compression. Figure 100 shows a comparison of the sum of the absolute forces for the first 40 layers of the build using the Meander and Stripe strategies with Inconel®625. As shown in the previous section for Ti-6Al-4V, the Meander scan strategy showed a much lower level of force in the building process, allowing the part to reach a height of 3.840 mm compared to the 2.520 mm with the Stripe scan strategy. The processing parameters were the same for both scan strategies (see Table 11), giving the same energy input for both parts of 13003 J per layer. In the first ten layers of the build, the Stripe scan strategy has developed higher forces than the Meander strategy, which is the same found for Ti-6Al-4V. The measured force after the first ten layers of the build was 1600 N and 2500 N respectively for Meander and Stripe scan strategy. While at layer 40, when the build was stopped, the force was 2200 N and 3500 N respectively, i.e. 62% more for the Stripe sample. Contour plots of force at the end of each build for both scan strategies, samples S17 and S18, are shown in Figure 101.

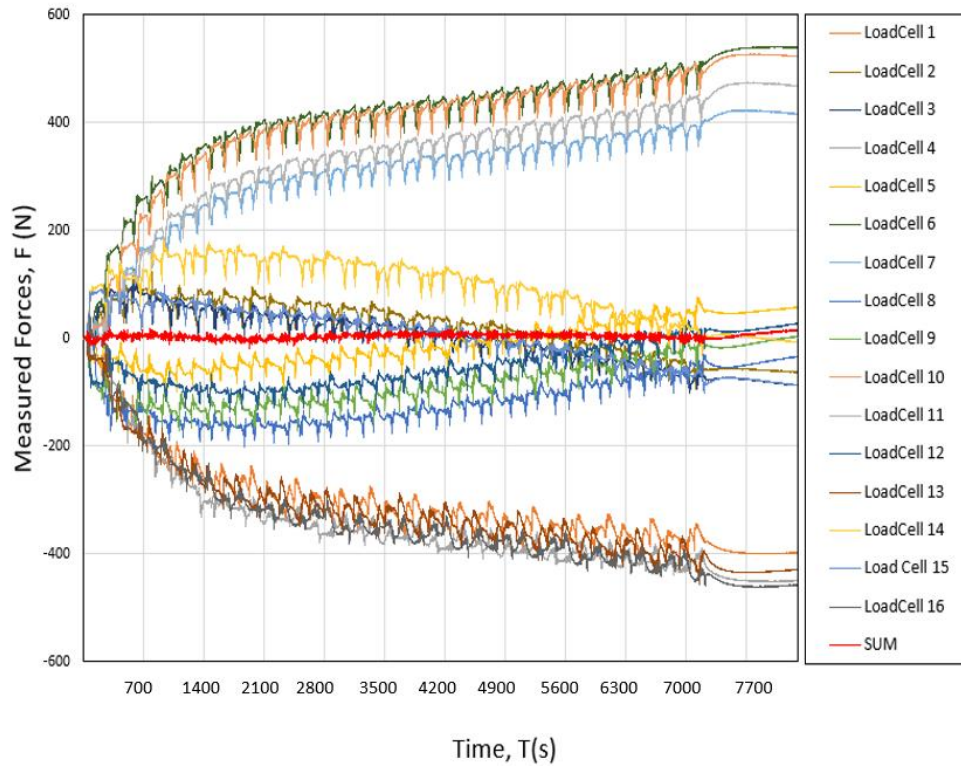


Figure 99: In-situ measurements of the forces developed for a square part built using the Stripe scan strategy using Inconel 625. Data for Sample S17, see Table 11 for details.

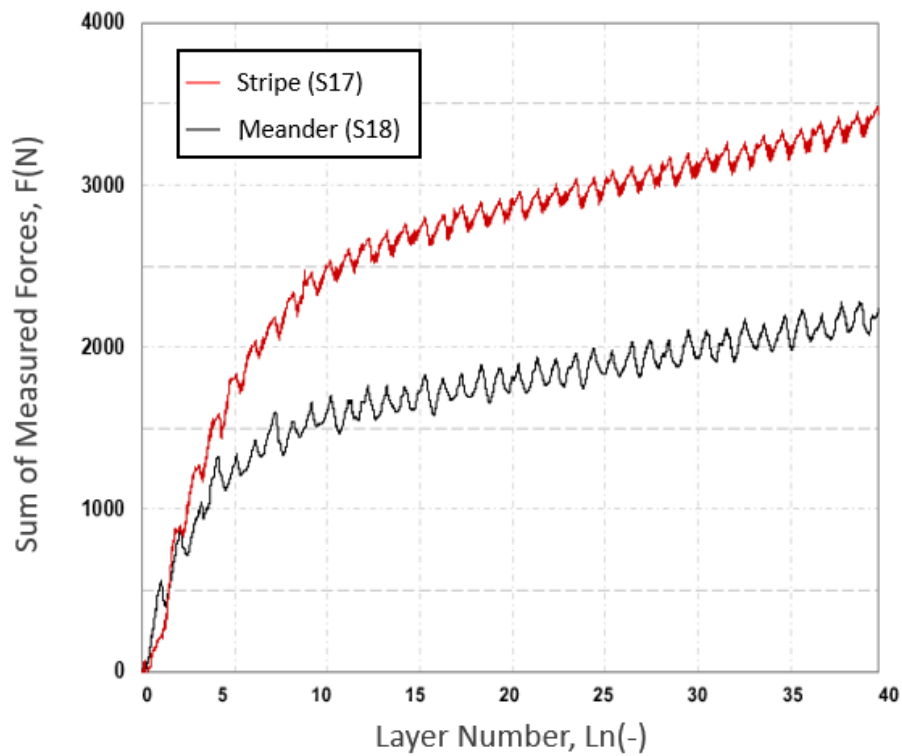


Figure 100: Comparison of the sum of measured forces for the Stripe and Meander strategies using Inconel 625 to build square samples (Samples 17 and 18), see Table 11 for details.

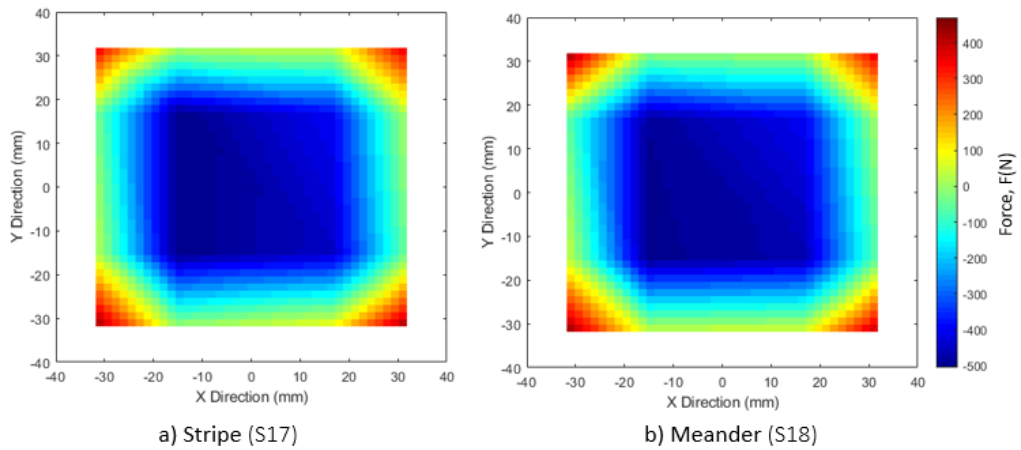


Figure 101: Contour plots of force at the end of each build for Samples S17 and S18 built using a 60 μ m layer thickness and different scan strategies a) stripe and b) Meander. See Table 11 for details.

From layer 10 the gradient in Figure 100 is similar and constant as seen for both scan strategies as was seen previously for Ti-6Al-4V. In both cases, the Meander scan strategy produced lower forces.

4.2.2 Effect of the Metal Alloy

To better understand the effect of the material properties on residual stress, square samples were manufactured to measure the forces developed during the L-PBF, using the processing parameters described in Table 11.

Of the four different materials investigated, the Maraging steel showed the lowest level of force measured during the building process, as shown in Figure 102. From the start of the build, at 0.3 mm, the force induced increased to only 1250 N, which was 50% less than the force developed in the Inconel 718 sample at the same height. The maximum force in the Maraging steel was reached at a build height of approximately 1.2 mm and dropped slightly to 1318 N when the build was finished at a height of 4mm height. This could be due to a phase transformation in the Maraging steel, which might eliminate the residual strains developed during the building process. The rest of the materials exhibited similar behaviour to one another with the maximum permissible force being reached at a build height of about 2.5mm. The maximum resultant force of 3770 N was measured in the Inconel 625 sample. Contour plots of the force at the end of each build are shown in Figure 103, where it is shown that the forces are symmetrically distributed along the X and Y axes for all metal powders; and it is clear that the sample built using Maraging steel show much lower forces developed than the rest of the metal powders tested.

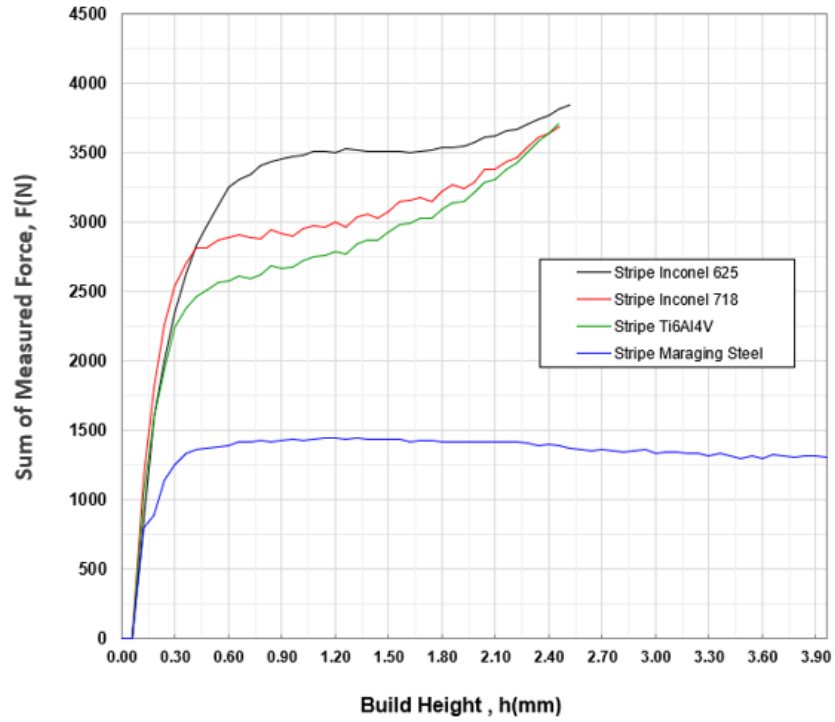


Figure 102: In-situ measurements of the sum of the forces for square parts built with Stripe scan strategy in various materials. Data for samples S15, S18, S19 and S20 shown, see Table 10 and Table 11 for details

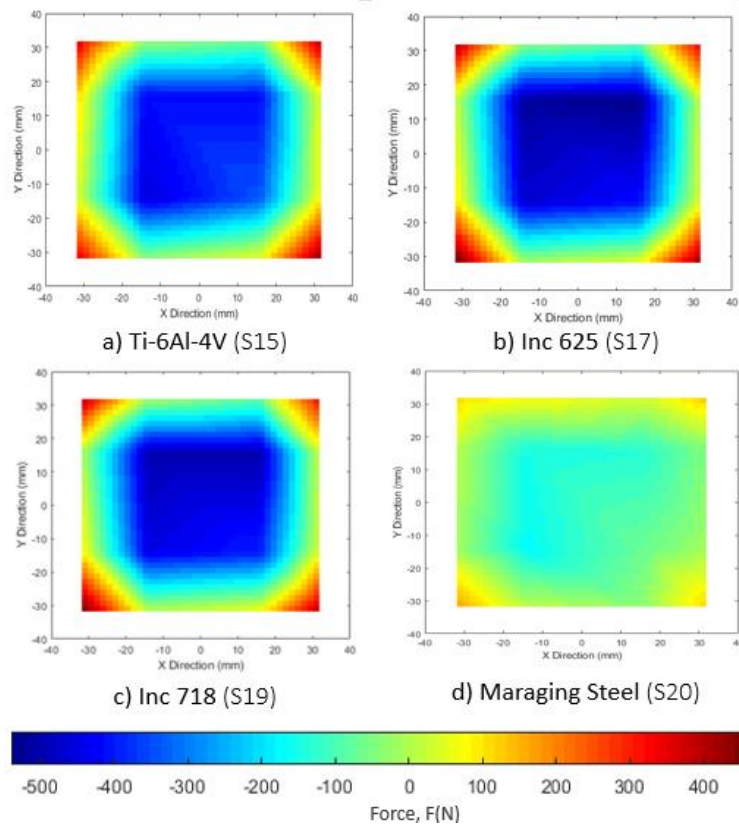


Figure 103: Contour plots of force at the end of each build, from Figure 102, for square parts using a $60\ \mu\text{m}$ layer thickness and different metal powders (Samples S15, S17, S19 and S20). See Table 10 and Table 11 for details.

The residual strains developed for the Maraging steel were very low compared to the rest of the materials using the same scan strategy and remained very constant after the initial stages of the build. This was probably due to an allotropic transformation of martensite to austenite which occurs at low temperatures (see Figure 104) and could have caused a volumetric expansion which would have limited the tensile forces developed during cooling of the part [184]. This is the opposite mechanism to the rest of the materials, when the part cools down, tension occurs in the corner load cells and compression in the centre load cells.

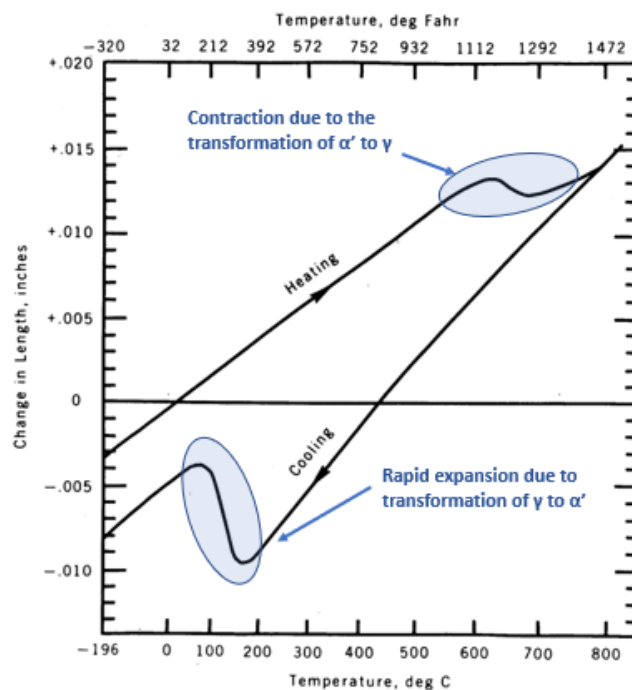


Figure 104: Dilatometer curve for the longitudinal direction of 18% Maraging steel from -196 °C to annealing temperature (adapted from Kranzlein [184])

The resultant forces from the centre and corner load cells for the Maraging steel samples are shown in Figure 105 where it can be seen that after the build is finished and has cooled down, the forces registered by the load cells exhibit the opposite behaviour to that described in the rest of the materials. Instead of slightly increasing during cooling, the forces for the Maraging steel sample reduced as the part cooled down. This behaviour reduced the part deformation when it was released from the base plate, as shown in Figure 107 using the DIC results. As residual levels for the Maraging steel part were 60% less than the developed for the rest of the materials, the part deformation of the sample was very low and the bending of the sample was opposite from the rest of the materials, having a negative bending in reference to the build platform.

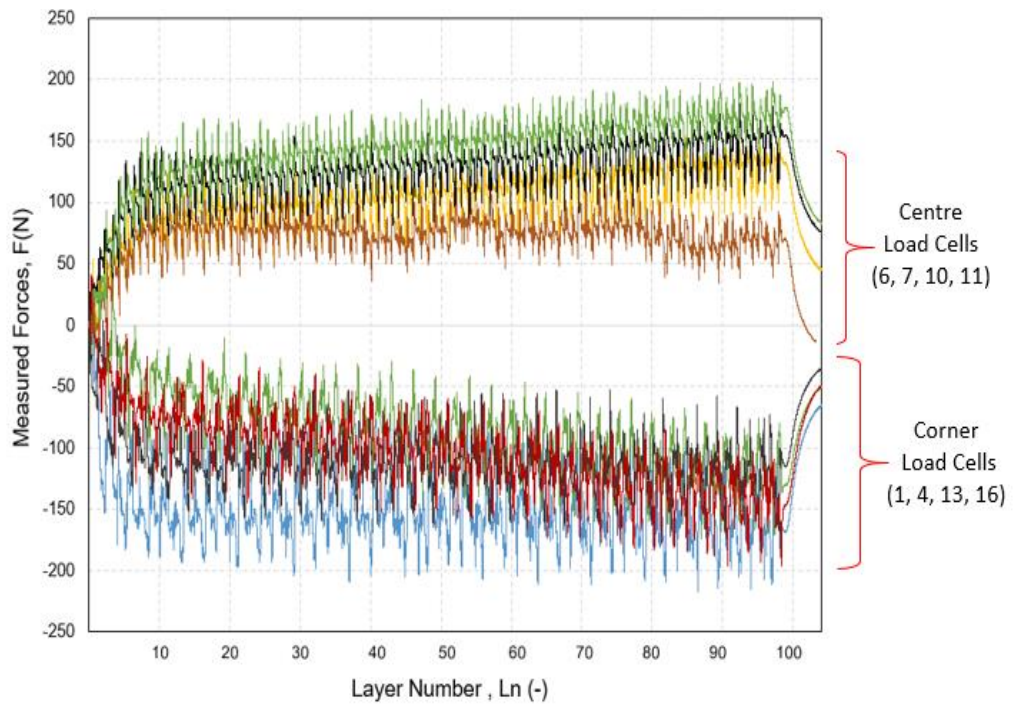


Figure 105: In-situ Measurements of forces developed for Sample S20 built in Maraging Steel with the Stripe Scan Strategy, see Table 11 for details.

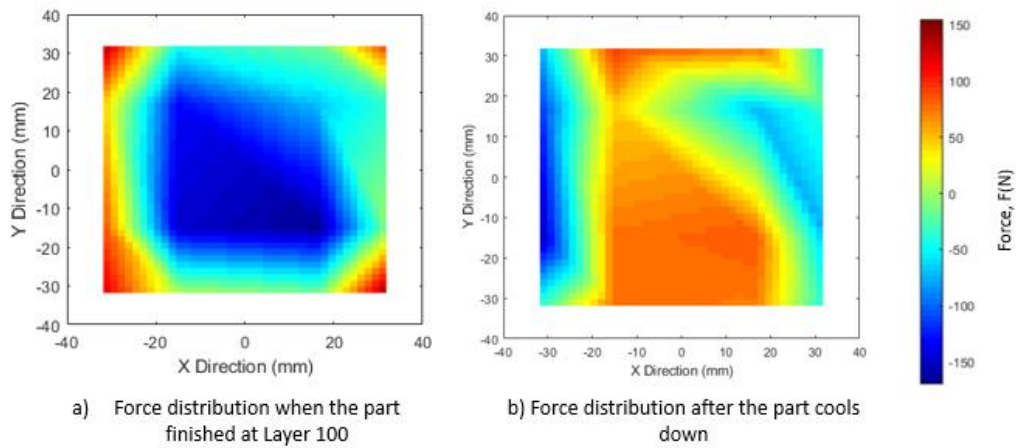


Figure 106: Contour plots of force from Figure 101, (a) at the end of the build at layer 100 and (b) after the part cools down for squared Sample (S20) built using Maraging steel and using the Stripe scan strategy. See Table 11 for details.

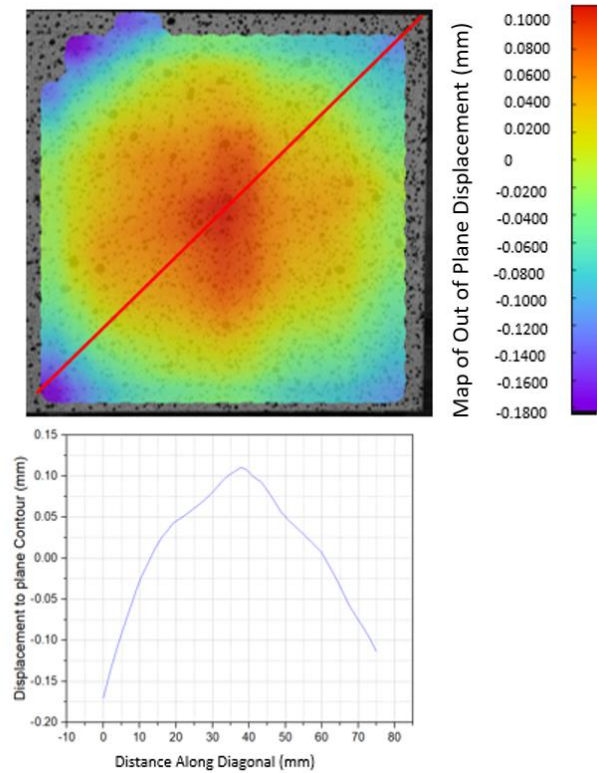


Figure 107: DIC Measurements of out of plane displacement (top) (positive towards the laser) and along diagonal (bottom) in Sample S20 built using the Stripe strategy and using Maraging steel, see Table 11 for further details.

4.2.3 Effect of the Inert Gas Atmosphere

In this experiment, the effect of the inert gas atmosphere on the development of residual forces and the part deformation in Maraging steel was investigated. Renishaw uses Argon gas as inert gas atmosphere and from an observation from Renishaw, that dimensional geometries were affected in samples built using Argon compared to samples built using Nitrogen. Therefore, a study was conducted on the effect of changing the gas as the inert atmosphere from Argon to Nitrogen on the forces developed during the L-PBF process for Maraging steel. Results from the in-situ measurements of the sample built with N_2 as the inert atmosphere are shown in Figure 108; the corners exhibit compressive forces and the centre tensile forces which is opposite to the forces measured in an Argon atmosphere (see Figure 109). Figure 109 show the contour plots of force at the end of each build before the part cools down to room temperature. It is clear how the forces change with the use of different inert gas when the sample is built using Argon the force at the corners is in tension while the centre of the part is in compression, while when using Nitrogen, the corners are in compression while the centre of the part is in tension when the build is stopped before the parts cool down.

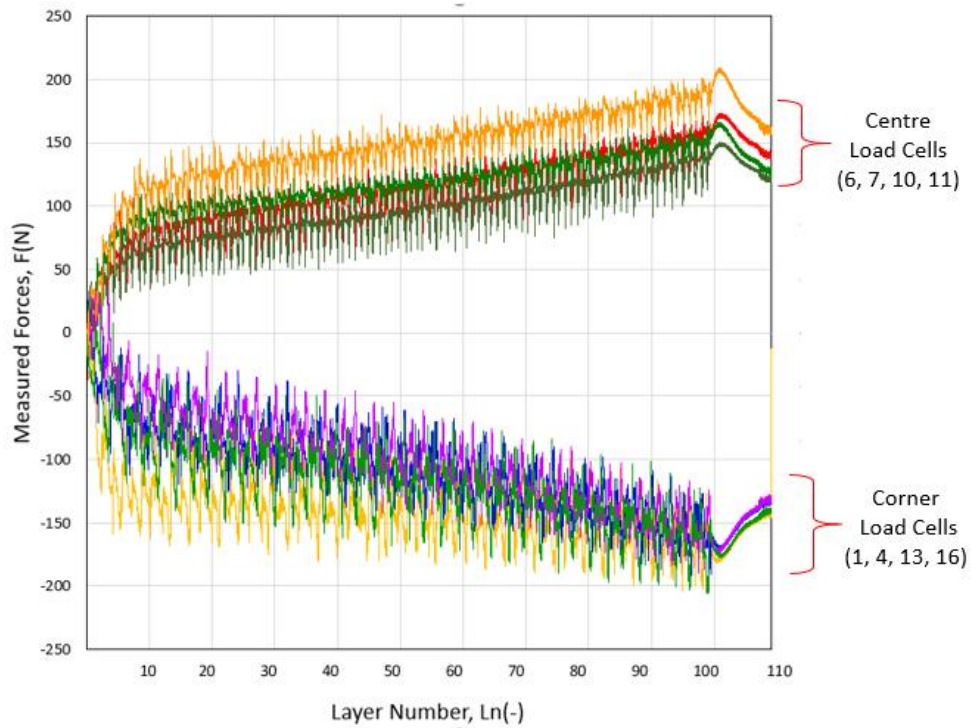


Figure 108: Results from the in-situ measurements for a square part built with a Stripe strategy in Maraging steel with the inert gas atmosphere of Nitrogen. Data is shown for Sample S21, and further details are given in Table 11

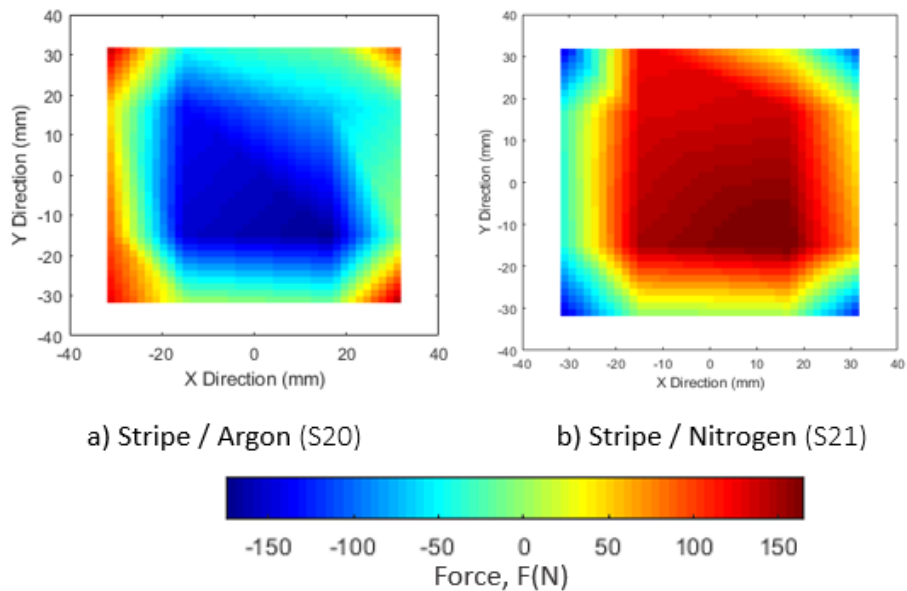


Figure 109: Contour plots of force at the end of each build for square parts before cooling down using Maraging steel with a variation of the inert gas using Argon (S20) and Nitrogen (S21) gas. Samples built using the Stripe scan strategy and a $60\ \mu\text{m}$ layer thickness. See Table 11 for details.

A comparison of the sum of the forces from the samples built in Ar and N₂ atmospheres are shown in Figure 110. It can be seen from the results that forces in the N₂ sample tend to increase slightly with the build height, while the sample built with Ar gas slightly decrease with the build height. The same behaviour was observed with the Meander scan strategy using Ar gas, although the forces were lower than for the Stripe strategy. This could be because the N₂ gas acts as an austenite stabiliser, promoting austenite reversion [84]. After the part cools down the forces are relaxed changing the orientation of the force distribution as shown in the contour plot of Figure 111.



Figure 110: Comparison of the Sum of forces measured in square parts built using Maraging steel using N₂ and Ar as the inert gas atmosphere. Data is shown for parts S20, S21 and S22. For which further details can be found in Table 11.

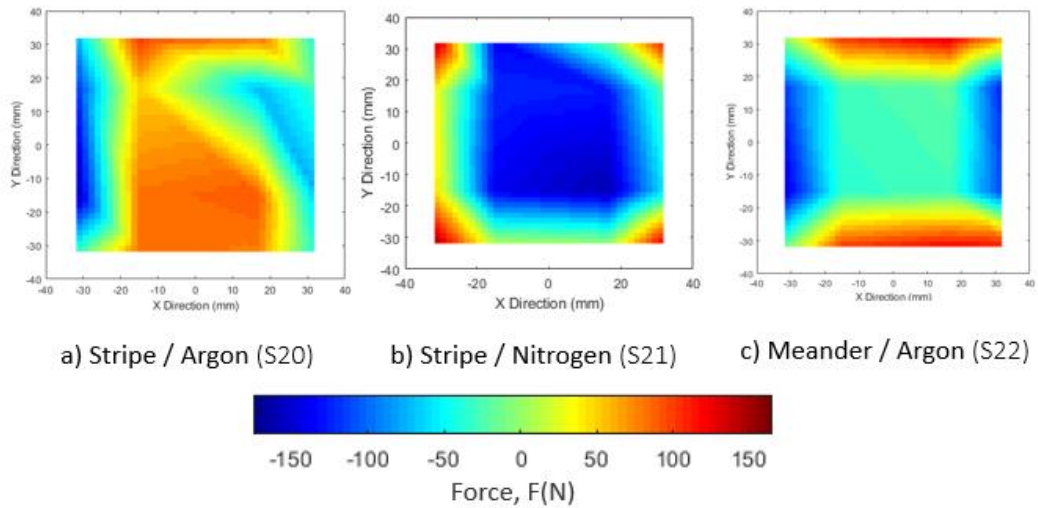
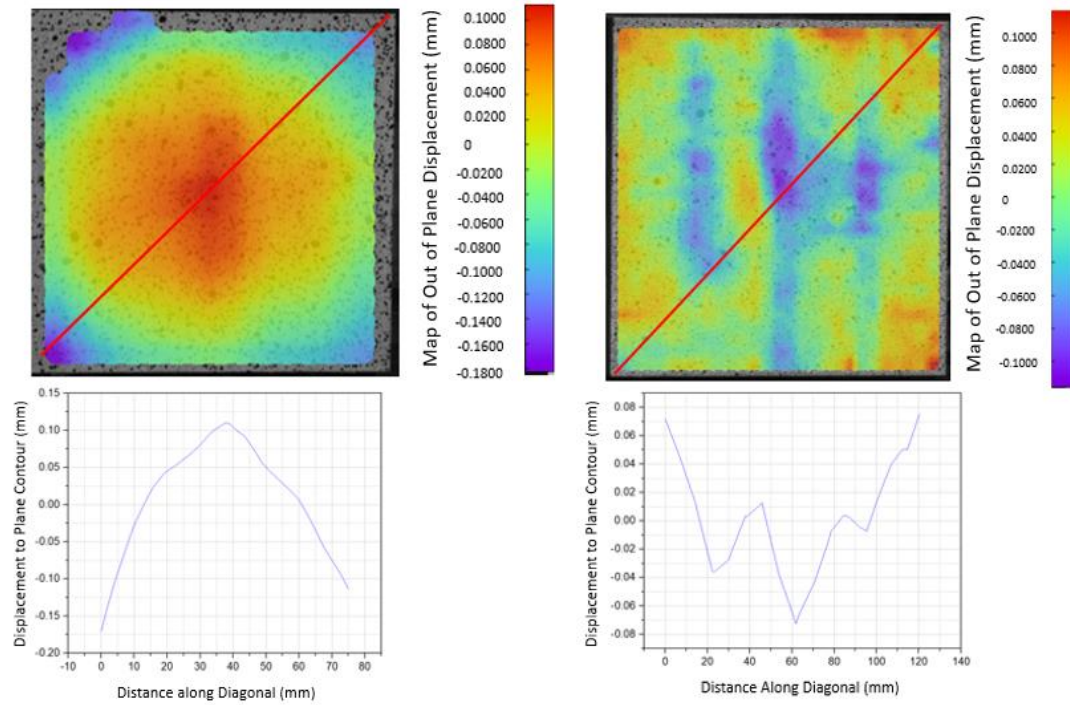


Figure 111: Contour plots of force after the part cools down from Figure 106, for square parts built using Maraging steel Samples S20, S21 and S22. Samples built using a $60\ \mu\text{m}$ layer thickness and different scan strategies a) and b) Stripe and c) Meander. See Table 11 for details.

Analysis of the Part Deformation

A comparison of DIC measurements of part deformation after removal from the base plate for the samples built under Nitrogen and the Argon gas is shown in Figure 112. The results show that the use of a different gas atmosphere has an effect on the part deformation for Maraging steel. For the part built with Argon gas, the centre curls away from the baseplate which is opposite to the behaviours observed in other metals built in an Argon atmosphere. where the corners deform away from the baseplate. However, the part built in the N_2 atmosphere shows the opposite behaviour deformation, as shown in Figure 112.



(a) Sample built using Argon gas (S20)

(b) Sample built using Nitrogen (S21)

Figure 112: Effect on the part deformation after removal of the inert gas atmosphere for Maraging Steel samples showing DIC results (top) and displacement along a diagonal (bottom) using data from samples S20 and S21 built using the Stripe Scan Strategy, for further details see Table 11.

DIC measurements of part deformation after removal from the base confirmed that with the part deformation had the same orientation for both Stripe and Meander strategies in Argon atmosphere, as shown in Figure 113.

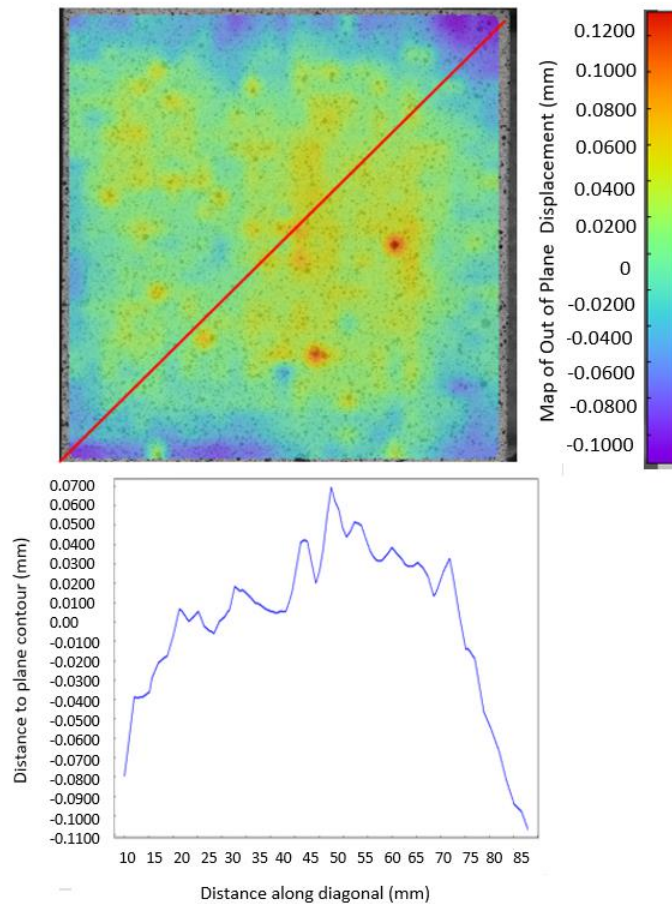


Figure 113: Effect on the part deformation after removal for square parts built using Maraging Steel and the Meander scan strategy showing DIC results (top) and displacement along a diagonal (bottom) for sample S22, see Table 11 for further details.

In order to see if the change in part orientation was an effect of the inert gas rather than the material, an additional sample was built using Inconel 625 (S23) in a Nitrogen inert gas atmosphere, using the parameters shown in Table 11. Results from the in-situ measurements shown in Figure 114 show that after the part was stopped the tendency of the forces did not change as from the Maraging steel sample. As well as the change in inert gas atmosphere from Ar to N₂ did not change the direction of the part deformation for Inconel 625, as shown in Figure 115. However, the N₂ atmosphere reduced the forces developed, allowing 56 layers to be built, which was 27% more than in an Ar atmosphere. The force relaxation when the part cooled down was lower than in the Argon atmosphere, which resulted in lower part deformation.

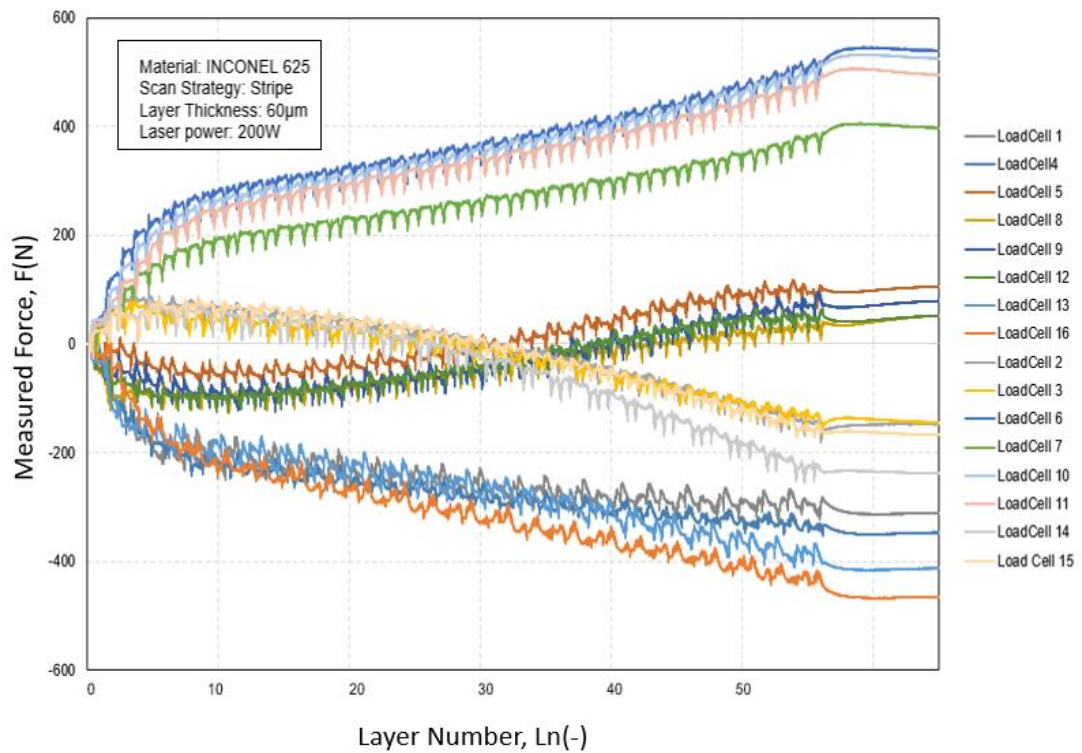


Figure 114: In-situ measurements for forces in the sample build with Stripe strategy in Inconel 625 with an Inert Atmosphere of Nitrogen. Data for sample S23 Table 11 for details.

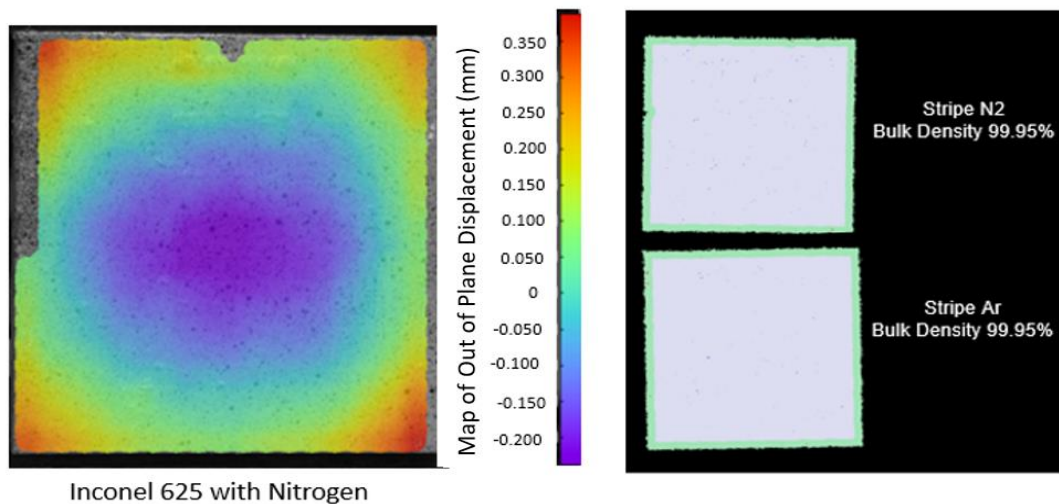


Figure 115: Out of Plane displacement from DIC (left) and micrographs showing porosity and relative density (right) for square parts (S18, and S23) built using the Stripe scan strategy from Inconel 625 metal powder using N_2 and Ar as the inert gas. See Table 11 for more details.

4.2.4 Effect of the Energy Density

In order to see the effect of the energy density on the forces developed during the L-PBF process, three square samples were built using Inconel 625, due to machine availability, increasing the point distance from $60\ \mu\text{m}$ to $70\ \mu\text{m}$ and $80\ \mu\text{m}$, while keeping the rest of the parameters constant (see Table 12).

Results from the variation of the energy density showed that the distribution of the forces changed as the point distance was increased. Figure 116 show the contour plots of force from the variation of the point distance, as it can be seen, higher tensile forces were developed at the edges of the part on the X-axis for the samples built with higher point distance which could generate a higher part deformation after released. However, as it can be seen in Figure 117, the absolute sum of the measured forces developed during the build reduce with increasing point distance. When the point distance was increased in $10\ \mu\text{m}$ increments from $60\ \mu\text{m}$ to $80\ \mu\text{m}$, the scan speed was increased correspondingly from $600\ \text{mm/s}$ to $800\ \text{mm/s}$ in $100\ \text{mm/s}$ increments which decreased in the energy density as shown in Table 12. The bulk density of the samples increased nearly linearly with increasing the energy input [45], see Figure 118. The reduction in energy density resulted in greater porosity due to the lack of fusion of the metal powder particles, and also reduced the density of the part, as shown in Figure 119.

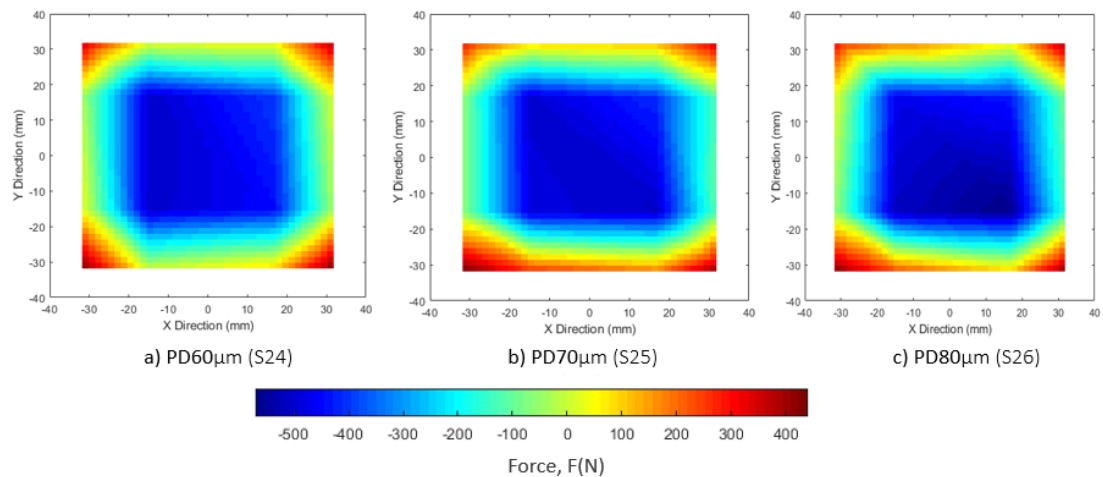


Figure 116: Contour plots of force at the end of each build for square samples S24, S25 and S26. Samples built using the Stripe scan strategy and a $60\ \mu\text{m}$ layer thickness with a variation of point distance from $60\ \mu\text{m}$ to $80\ \mu\text{m}$. See Table 12 for details.

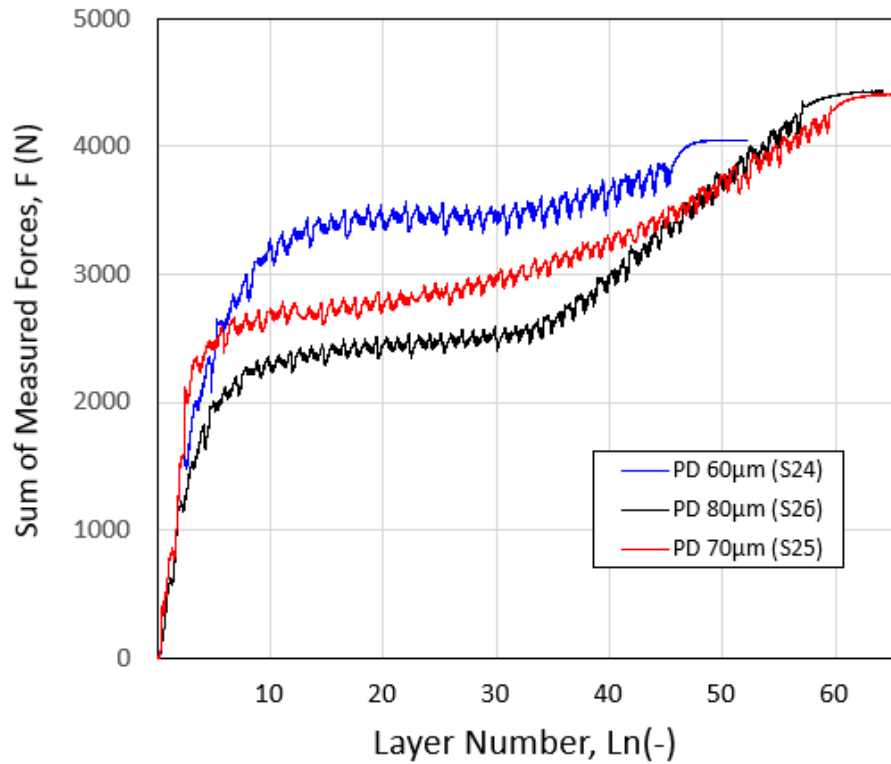


Figure 117: In-situ measurements of resultant forces developed in samples S24, S25 and S26 with variation in point distance (PD) built using Stripe strategy using Inconel 625 metal. Details for the square parts can be found in Table 12.

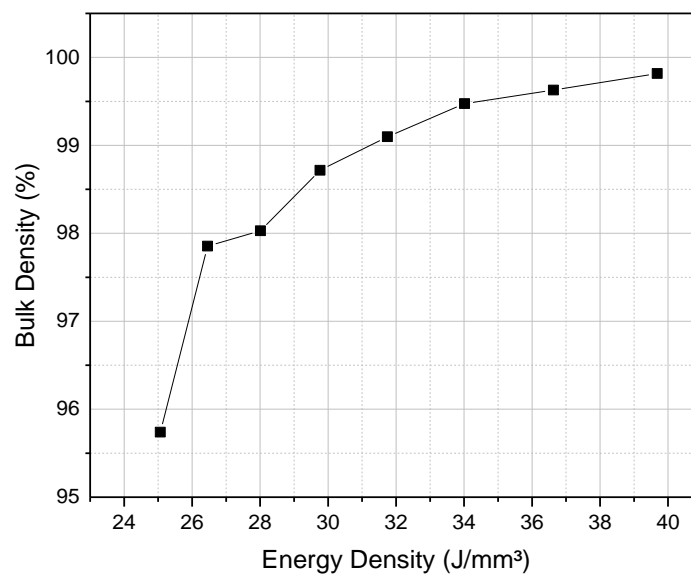


Figure 118: Bulk density as a function of volumetric energy density in square parts built using Stripe scan strategy.

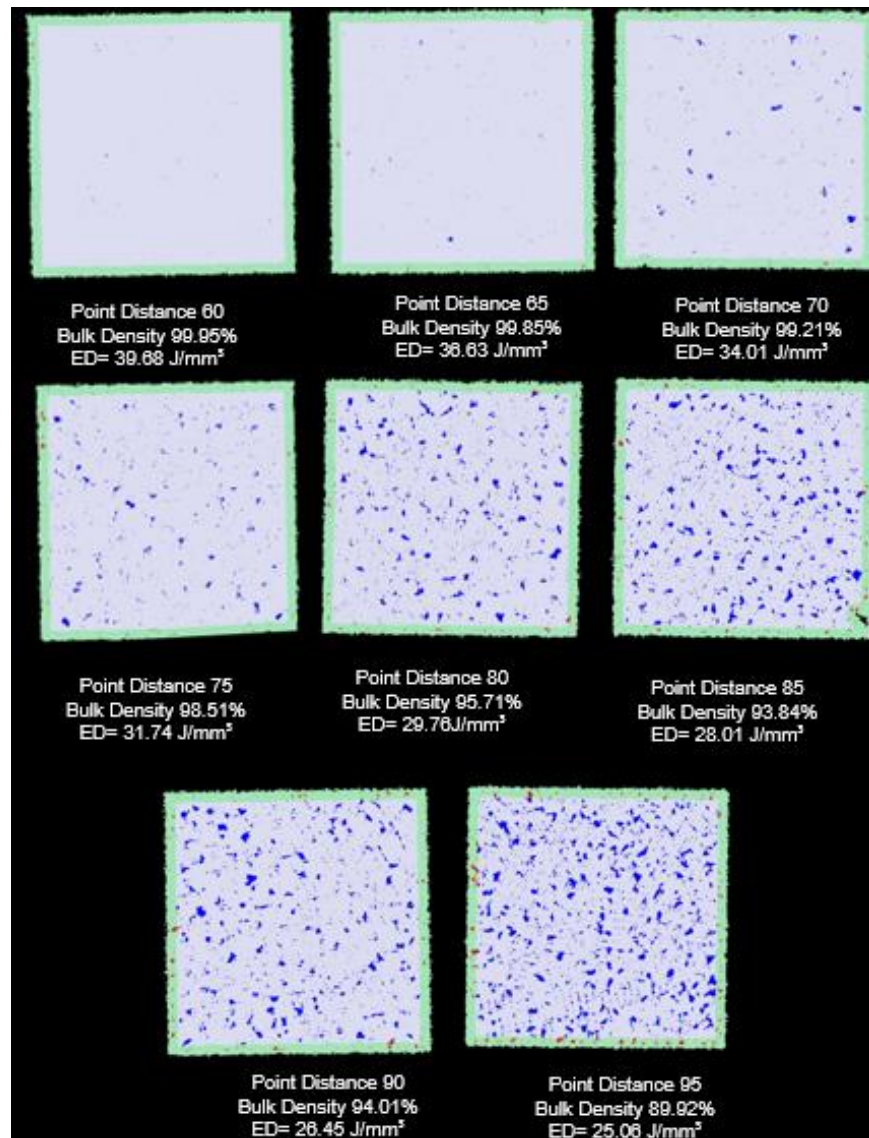


Figure 119: Micrographs showing porosity on a function of point distance in density cubes parts built using Stripe scan strategy in Inconel 625 metal. Details for relative density and volumetric energy density are shown and further details can be found in Table 12

At the same time, the increment in point distance increased the porosity of the part and decreased its relative density, the increase in point distance also caused larger deformation on releasing the part, see Figure 120, smaller elongation to failure and lower ultimate tensile strengths (see Figure 121). These changes in behaviours are connected to changes in the microscale structure of the part characterised by the porosity shown in Figure 119. Imperfections, such as porosity or lack of fusion between layers, can cause deformation and stress relaxation; the loss of metallurgical contact with the previous layers during manufacturing could lead to the re-distribution of stresses within the part [180]. Any heterogeneity in packing density throughout a powder layer can result in non-uniform shrinkage behaviour when one region of the powder layer consolidates more rapidly than

another region. Therefore, the induced porosity in the sample decreases the volume of solidifying material which caused less material shrinkage; thus, the residual stress is reduced [185].

DIC Result for Part Deformation			
Inconel 625	PD 60 μm (S24)	PD 70 μm (S25)	PD 80 μm (S26)
Maximum Deformation (towards the laser)	0.24 mm	0.32 mm	0.53 mm
Maximum Deformation (against the laser)	-0.15 mm	-0.24 mm	-0.24 mm
Absolute Deformation	0.39 mm	0.56 mm	0.81 mm

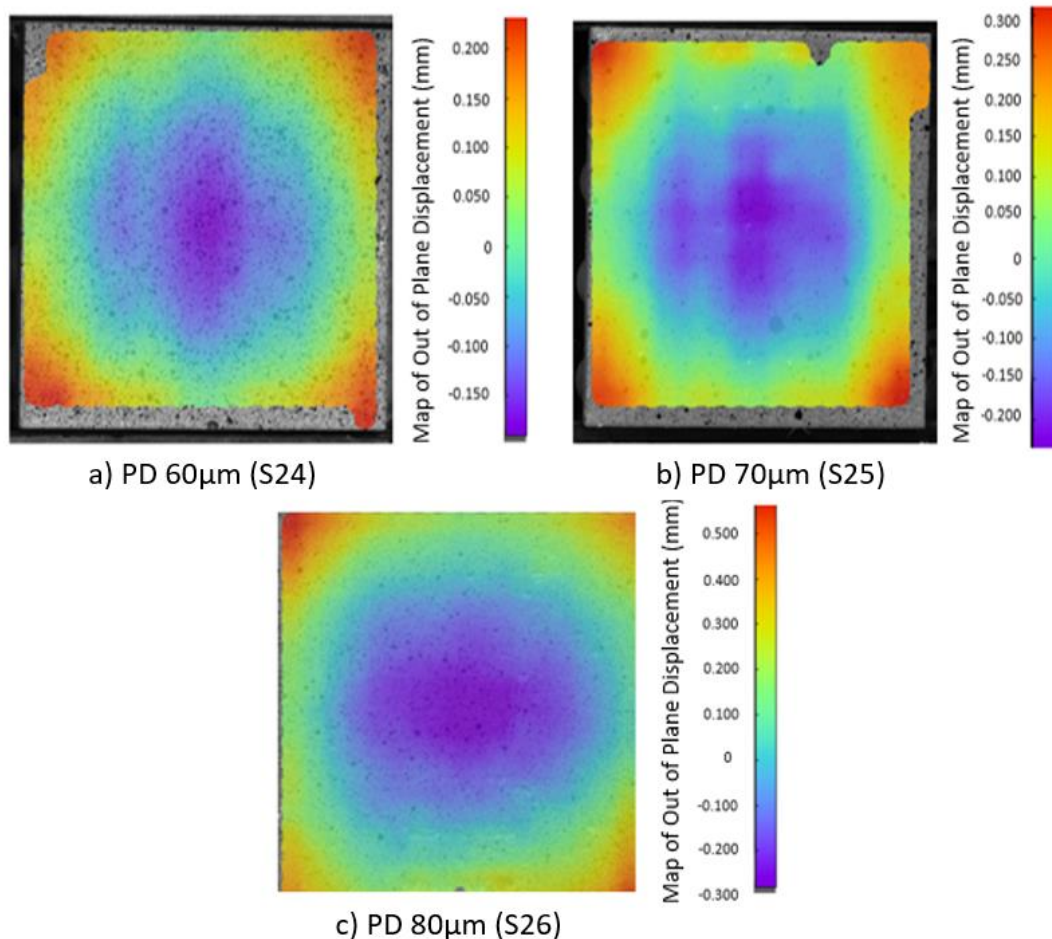


Figure 120: Out of plane displacement map from DIC for square parts with different point distances built using stripe scan strategy in Inconel 625 as detailed in Table 12; together with numerical results (Top).

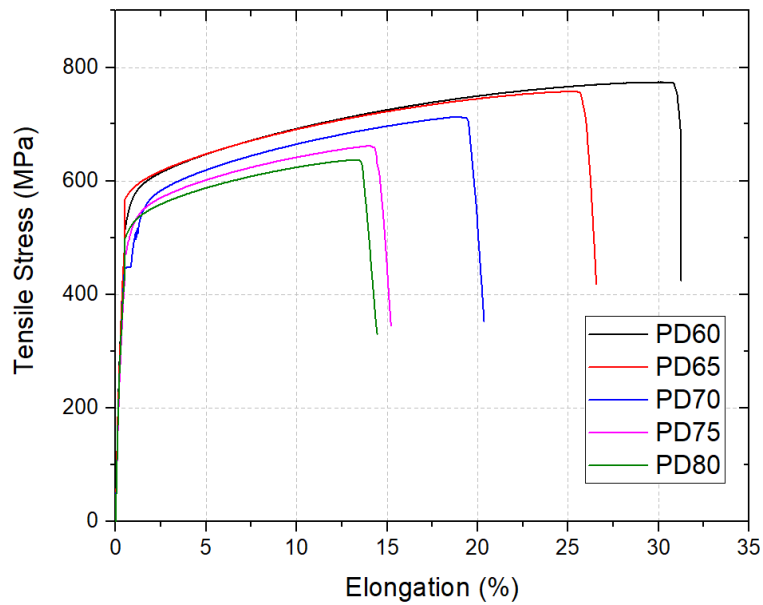


Figure 121: Tensile stress results from samples with different point distance, see Table 12 for more details.

4.3 Melt Pool Characteristics

A better understanding of the melt pool characteristics based on laser - material interactions would help to calibrate the 3DSIM software for other types of simulation and more accurate results. Therefore, in collaboration with Ansys, a study based on the melt pool characterizations was conducted from single tacks built using different metal powders Ti-6Al-4V, Inconel 625 and Maraging steel with multiple laser power and exposure time combinations, as described in Table 13. Depending upon the heat condition of the powder bed, the melt pools of the L-PBF melting metallic powder exhibit a varied size and morphology, even if identical scanning parameters are used. It is known, that the base plate or a solid metal provides high thermal conduction for fusion energy to be dissipated, while thermal conduction from the powder bed is much lower due to gas-filled pores that may reduce thermal conductivity [165]. Thus, the characteristics of the melt pool on a powder bed without any prior layers will have different properties than that developed in prior layers. Comparing both conditions could give additional significant information on the melt pool characteristics. Therefore, single beads with no powder and single beads with a single layer of powder of thickness 30 μm were built over a 2 mm base, but using the same parameters combination shown in the schematic in Figure 72. Measurements were taken of each single bead to determine the melt pool width at the surface, the height of the powder bead from the top of the base and the depth of the melt pool. In order to be far away from the start and the end

of the laser scan motion to avoid the scanning effects caused by speed ramping of the laser galvanometers and the optic effect caused by the edges of the sample, which as can be seen in Figure 122. The samples were cross-sectioned, and measurements were taken from the centre of the part, as described in Figure 72.

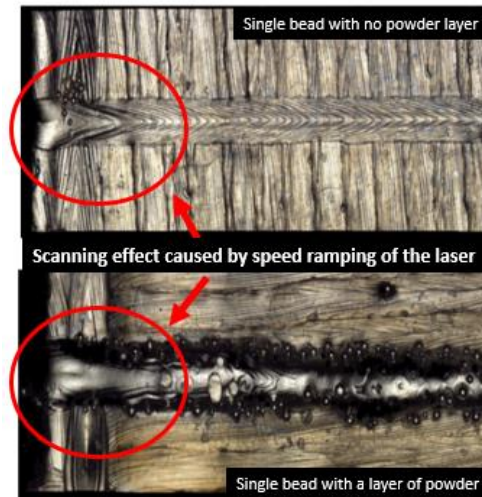


Figure 122: Alicona Infinite Focus image of the surface for a single bead of Ti-6Al4V built with no powder (No.12 in Table 18) (top) and for the single bead (No.12 in Table 19) with powder (bottom), see Table 13 for more details.

4.3.1 Three-dimensional Optical Measurements

The single beads were individually measured using an optical three-dimensional measurement system (Alicona Infinite Focus); each part was measured at two different positions along the single bead to determine the height and the width of the beads. Figure 123 shows an example of the measurement of the height of the bead for a sample with powder. The measurements were taken from the top of the bead to a surface of the base giving a difference in the z-direction of 193.8089 μm for the example in Figure 123. Figure 124 shows an example of the measurement of the height of bead with no powder, at the top of in this case the height of the bead was 12.8242 μm .

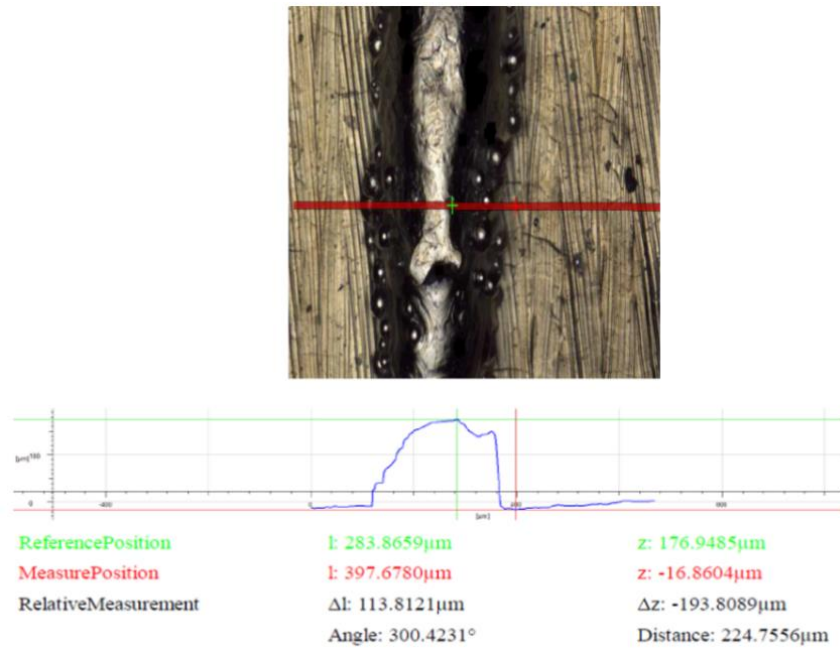


Figure 123: Optical Micrograph (top) for a single bead of Ti-6Al4V built with powder (No.12 in Table 19) and the corresponding height across the marked section (bottom) from which the height of the bead was evaluated.

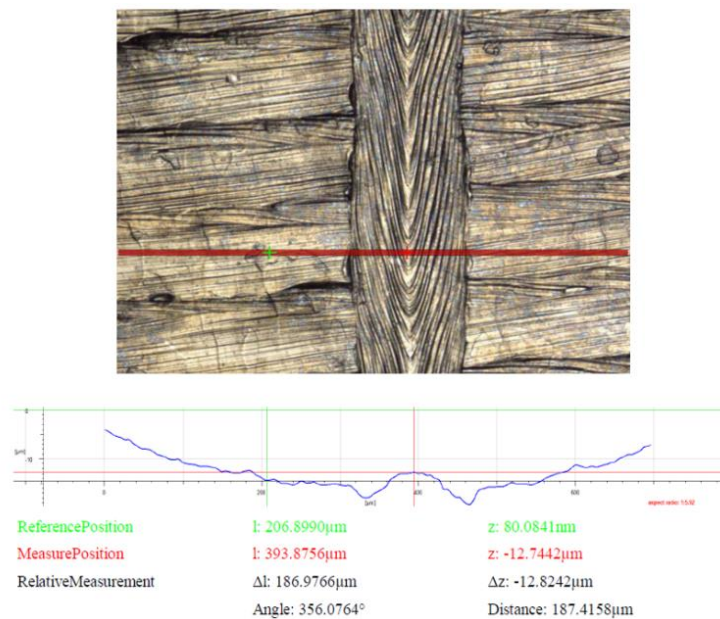


Figure 124: Optical Micrograph (top) for a single bead of Ti-6Al4V built with no powder (No.12 in Table 18) and the corresponding height across the marked section (bottom) from which the height of the bead was evaluated.

For the single beads with no powder, single beads were formed due to the re-melting and solidification of the base material. The single beads were consistent, and without any interruption along the scan, as it can be seen in Figure 122 and Figure 124, thus, the width variation along the bead was not significant. For the powder case, single beads were

generated by melting the metal powder and base plate material and are solidified together. As it can be seen in Figure 122 and Figure 123, there was a higher variation of the width of the single bead along the scan, compared to the single bead formed without powder using the same scan parameters. The surface roughness for the single bead with powder was affected by metal particles attached to both sides of the single bead during the scan, as seen in Figure 123, and is similar to previous studies [162]. In addition, the single tracks from the samples with powder were not consistent along the scan as from the single beads with no scan; some holes can be observed on the surface along the scan that could be produced by the vapours released from the melt pool due to the vaporization of the metal alloy [162], especially on the tracks with lower energy input which presented higher inconsistencies. The results for the measurements of the surface of the single beads produced without powder are shown in Table 18, and the results for the measurements of the top surface from the single beads produced with powder are shown in Table 19. The results show that there is an increase in the bead size with an increase in the exposure time for the single beads with no powder present for all energy levels and a decrease in the bead size for the single beads produced with a layer of powder for all the energy levels. The variation in each bead is greater or equal to the difference between the energy levels. This could be due to the lower thermal conductivity of the powder bed compared to a solid base and to the higher laser absorptivity of the metal powder compared to solid materials [161]. When higher energy is present in the samples with no powder greater thermal conductivity is transferred due to the solid material of the base plate, increasing the size of the melt pool. However, for the samples with powder due to the low thermal conductivity of metallic powder, less thermal energy is conducted downwards to the base while more energy is accumulated in the powder bed resulting in lower dimension of single beads width while increasing the energy levels. As the parts were measured from the top surface only, the height and the width of the single beads could not be measured, for measuring the depth of the melt pool the part must be cross-sectioned and etched. Further analysis using microscopic measurements were performed.

Table 18: Results from the measurements of the top surface for single beads without powder built using Ti-6Al-4V

Single Bead	Laser Power (W)	Exposure Time (μ s)	Height BTM	Width BTM	Height TOP	Width TOP	Average Height (μ m)	Average Width (μ m)
1_NP	160	40	6.6652	137.3554	8.6754	138.4964	7.6703	137.9259
2_NP	160	50	9.1365	144.0348	15.0258	158.244	12.08115	151.1394
3_NP	160	100	18.3954	184.0927	12.3261	175.4627	15.36075	179.7777
4_NP	170	40	9.1087	132.5476	11.8408	150.1546	10.47475	141.3511
5_NP	170	50	12.3228	147.6378	13.6595	160.9651	12.99115	154.30145
6_NP	170	100	15.8507	193.6434	11.4571	175.6488	13.6539	184.6461
7_NP	180	40	9.5176	143.2974	11.0578	148.5852	10.2877	145.9413
8_NP	180	50	6.7948	149.9153	10.4911	165.1645	8.64295	157.5399
9_NP	180	100	12.8558	174.0608	10.9843	191.262	11.92005	182.6614
10_NP	200	40	10.1653	145.1278	15.4237	163.3209	12.7945	154.22435
11_NP	200	50	12.3269	172.1465	16.1124	166.5775	14.21965	169.362
12_NP	200	100	12.1468	189.4862	7.7162	199.7458	9.9315	194.616

Table 19: Results from the measurements of the top surface for single beads with powder built using Ti-6Al-4V

Single Bead	Laser Power (W)	Exposure Time (μ s)	Height BTM	Width BTM	Height TOP	Width TOP	Average Height (μ m)	Average Width (μ m)
1_WP	160	40	193.8089	247.5213	151.3286	204.8904	172.56875	226.20585
2_WP	160	50	126.1025	185.8763	144.5769	173.3911	135.3397	179.6337
3_WP	160	100	138.5803	175.9383	89.4753	101.331	114.0278	138.63465
4_WP	170	40	151.2598	190.1453	146.4455	196.8814	148.85265	193.51335
5_WP	170	50	98.3231	175.2306	115.3651	183.8469	106.8441	179.53875
6_WP	170	100	135.5496	176.3875	99.4697	119.7953	117.50965	148.0914
7_WP	180	40	138.296	209.3847	118.5456	200.2649	128.4208	204.8248
8_WP	180	50	126.3841	183.0336	166.6429	191.699	146.5135	187.3663
9_WP	180	100	176.428	194.3719	134.4481	143.1447	155.43805	168.7583
10_WP	200	40	115.4324	183.1932	132.625	171.6686	124.0287	177.4309
11_WP	200	50	128.0301	156.6407	139.0725	154.7875	133.5513	155.7141
12_WP	200	100	129.5584	163.3495	76.8957	153.2368	103.22705	158.29315

4.3.2 Section Measurements

The Ti-6Al-4V samples were sectioned, mounted, polished and etched using the Keller's etch composition, to allow their features to be measured in a microscope. The diagram on Figure 72 shows the definition of height, width and depth for a single bead. Figure 125 and Figure

126 show the optical micrographs for the samples without and with powder, respectively. Measurements were made on two sections along each using the ImageJ software, and the results are shown in Table 20 and Table 21.

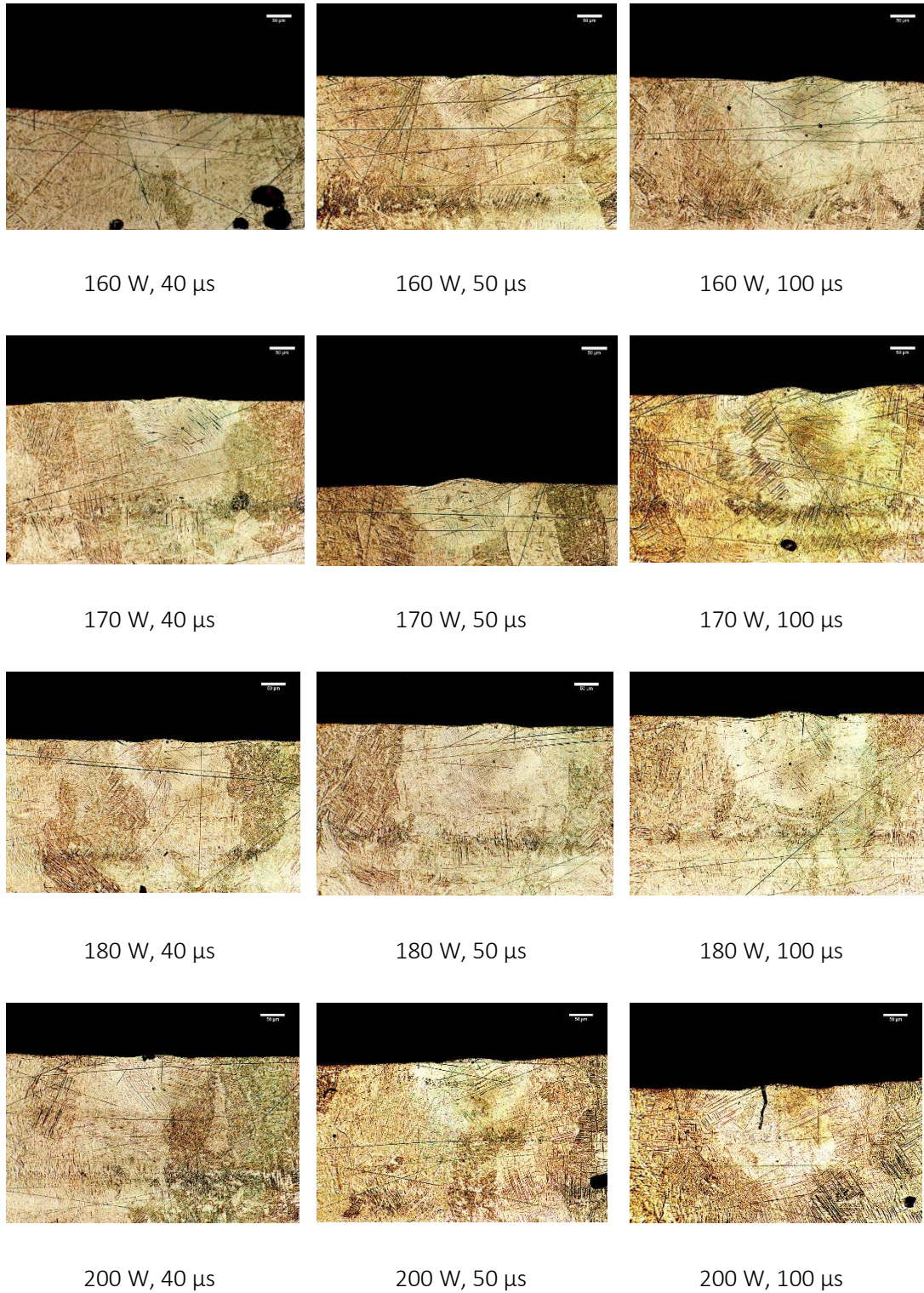


Figure 125: Cross-section of samples showing the melt pool geometry of single beads built using Ti-6Al-4V without powder and with different laser power (vertically) and for exposure times of 40 μ s (left), 50 μ s (middle) and 100 μ s (right). The details of the beads are described in Table 13.

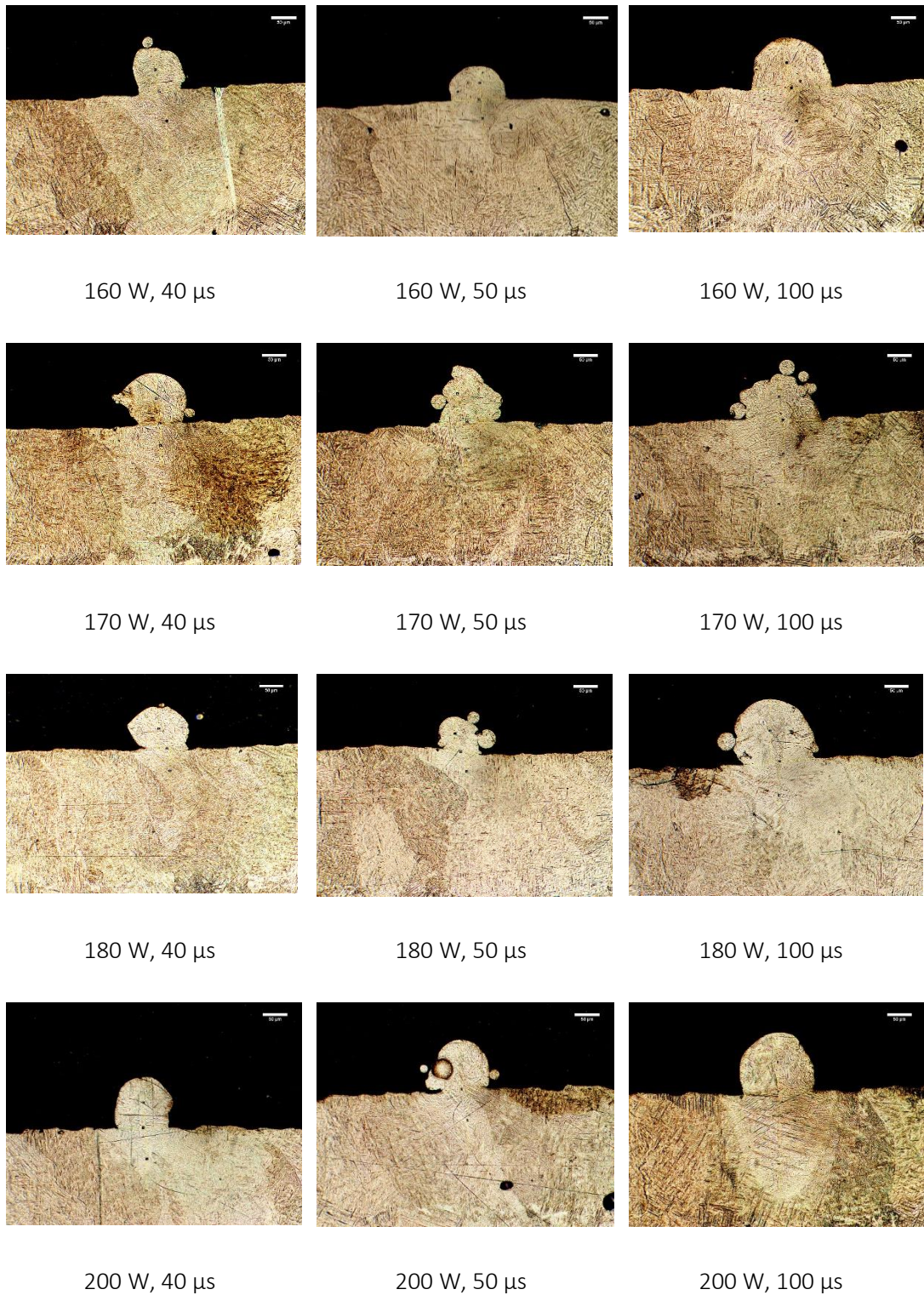


Figure 126: Cross-section samples showing the melt pool geometry of single beads built using Ti-6Al-4V with powder and with different laser power (vertically) and for exposure times of 40 μs (left), 50 μs (middle) and 100 μs (right). The details of the beads are described in Table 13.

Table 20: Results from the measurements of height, width and depth for single beads without powder built with different laser power and exposure times (see Table 13) obtained from the micrographic sections from Figure 125.

Single Bead	Laser Power (W)	Exposure Time (μs)	Average Height (μm)	Average Width (μm)	Average Depth (μm)
1_NP	160	40	6.224	130.1135	122.3915
2_NP	160	50	7.1955	143.5905	135.2065
3_NP	160	100	13.366	141.3405	189.3670
4_NP	170	40	9.435	121.9805	103.3310
5_NP	170	50	10.143	139.1970	126.4875
6_NP	170	100	13.619	162.1770	193.3270
7_NP	180	40	9.1645	122.5270	116.5895
8_NP	180	50	9.901	148.2925	134.7205
9_NP	180	100	13.128	164.2015	155.4470
10_NP	200	40	11.386	139.6110	122.0305
11_NP	200	50	10.9165	146.5620	137.1410
12_NP	200	100	13.8705	191.6130	172.0480

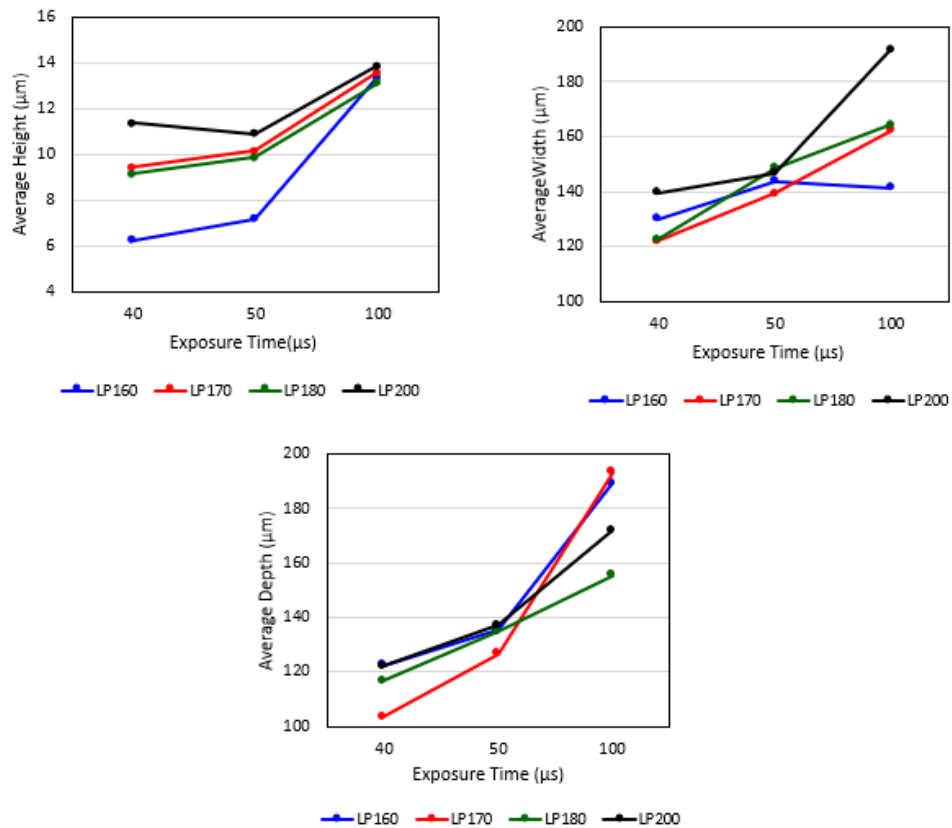


Figure 127: Comparison of measurements results shown in Table 20 from the height, width and depth of single beads built using Ti-6Al-4V with one 30 μm layer of powder with different laser power and exposure times, see Table 13 for more details.

Table 21: Results from the measurements of height, width and depth for single beads with one 30 μm layer of powder built with different laser power and exposure times obtained from the micrographic sections from Figure 126.

Single Bead	Laser Power (W)	Exposure Time (μs)	Average Height (μm)	Average Width (μm)	Average Depth (μm)
1_WP	160	40	75.7610	85.9715	102.5015
2_WP	160	50	69.0675	98.3645	78.9875
3_WP	160	100	99.2795	157.7915	130.716
4_WP	170	40	65.1370	86.0645	87.1470
5_WP	170	50	99.2725	107.0440	98.3385
6_WP	170	100	104.4875	151.4900	136.4190
7_WP	180	40	99.0370	69.9995	73.0265
8_WP	180	50	91.1060	79.7420	80.4720
9_WP	180	100	123.8310	152.6925	118.5780
10_WP	200	40	85.6670	95.8130	99.2585
11_WP	200	50	110.4005	98.3565	98.0250
12_WP	200	100	120.8085	131.0560	201.0295

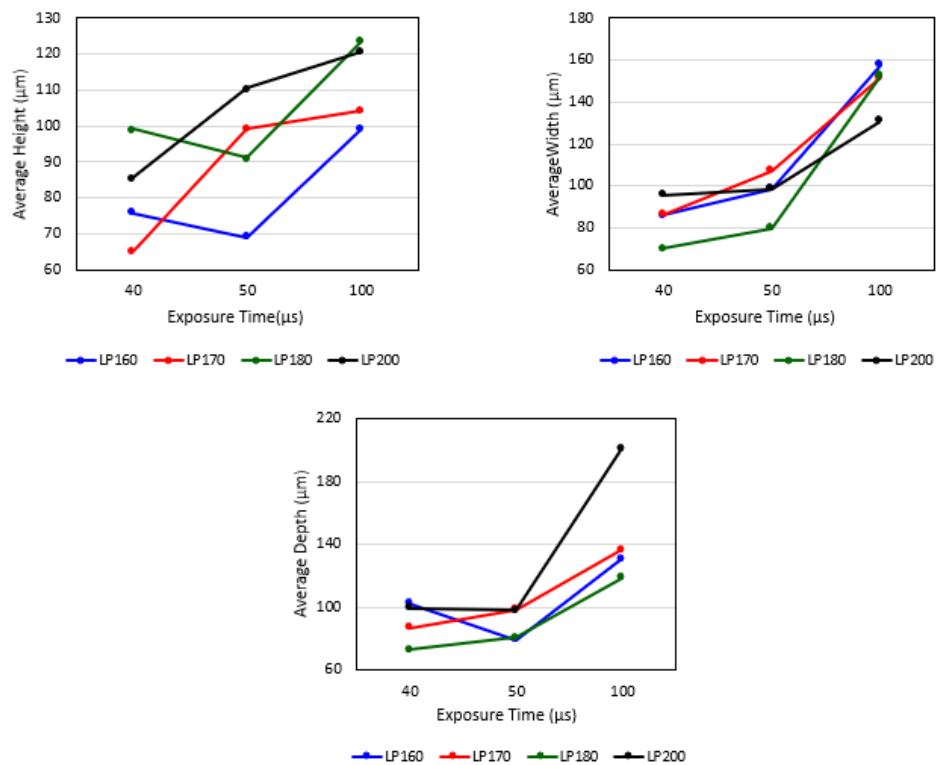


Figure 128: Comparison of measurements results shown in Table 21 from the height, width and depth of single beads built using Ti-6Al-4V with one 30 μm layer of powder with different laser power and exposure times, see Table 13 for more details.

For both cases, the width and depth of the melt pool increased with both laser power and exposure time with the trends being more evident when powder was present as it can be seen from the plots in Figure 127 and Figure 128. However, the absolute depth was greater in the absence of powder; this could be because attributed to the lower thermal conductivity of the powder bed compared to a solid material and the enhanced laser absorptivity of the powder.

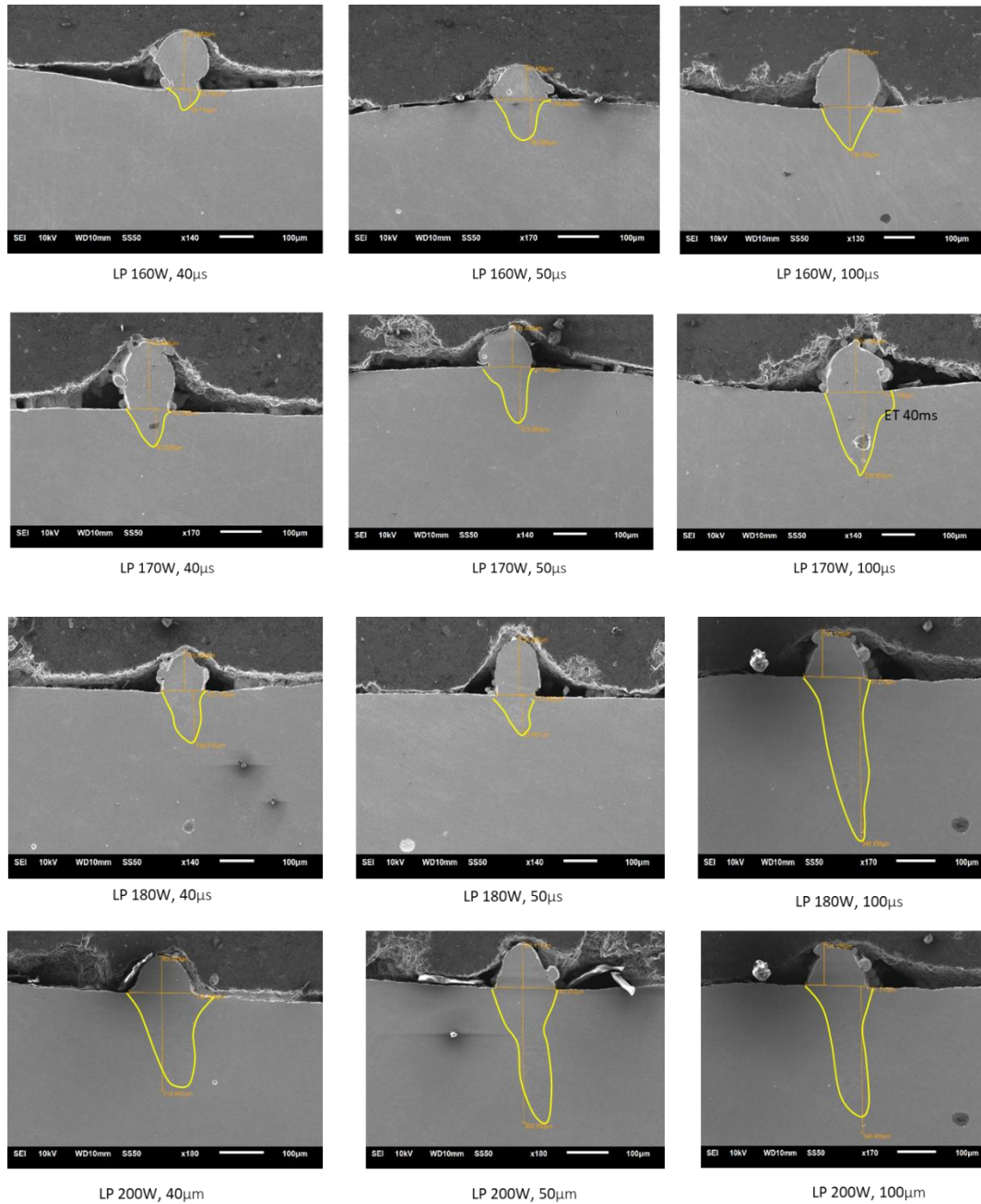


Figure 129: SEM images showing the melt pool geometry for single beads built using Ti-6Al-4V with powder and different laser power and for exposure times of 40 μs (left) 50 μs (middle) and 100 μs (right). The details of the beads are shown in Table 19.

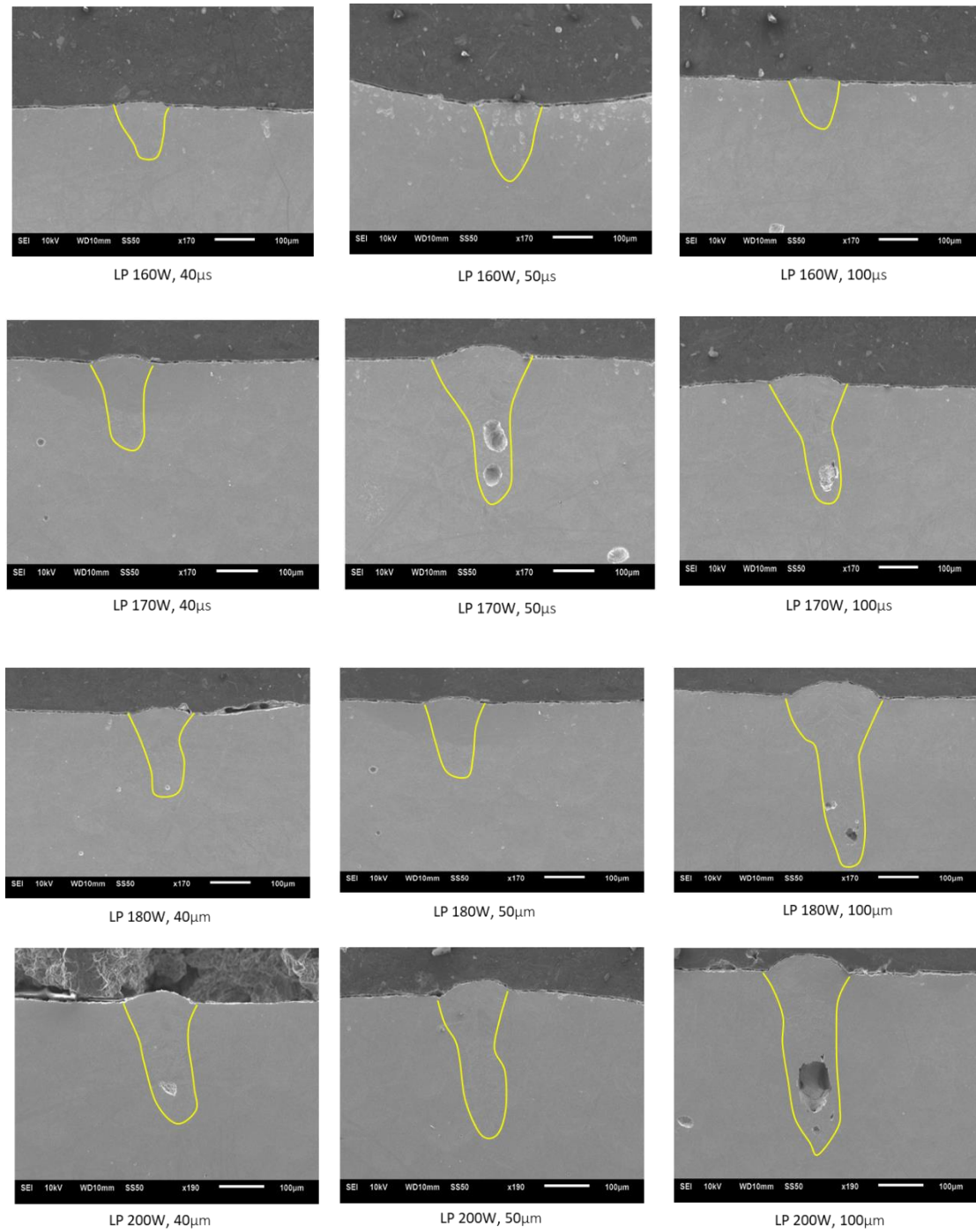


Figure 130: SEM images showing the melt pool geometry for single beads built without powder and different laser power and for exposure times of 40 μs (left) 50 μs (middle) and 100 μs (right). The details of the beads are shown in Table 19.

For single beads created using lowest energy density, the melt pool geometry was hard to observe as very little material melted, while in samples for which a higher laser power and lower scan speed result in large melt pools were observed as shown in Figure 129 and Figure 130. Pores were found in the melt pools with a keyhole geometry in samples with a high energy density input, as shown in the bottom right micrograph in Figure 130. This may be attributed to gas entrapped in the melt pool due to material evaporation [186].

In order to see the effect of the laser-material interaction with respect to the metal alloy properties, the experiments were repeated with the single bead built using different metal powders, i.e. Inconel 625 and Maraging steel; additionally, samples were analysed using Maraging steel built using Nitrogen as the inert gas, as it was noticed from the previous result that it the change in the inert gas could affect the microstructure of the Maraging steel samples. The samples were cross-sectioned perpendicular to the scanning direction and polished and etched for metallography to show dimensional and geometrical features from the melt pool formation. Figure 131, Figure 133 and Figure 135 show the optical micrographs for the samples without powder fabricated using Inconel 625 and Maraging steel (Ar) and Maraging steel (N₂) respectively. Figure 132, Figure 134 and Figure 136 show the optical micrographs for the samples with powder fabricated using Inconel 625 and Maraging steel (Ar) and Maraging steel (N₂) respectively. Measurements were made on two sections along each using the ImageJ software, and the results are shown in Table 22 and Table 23.

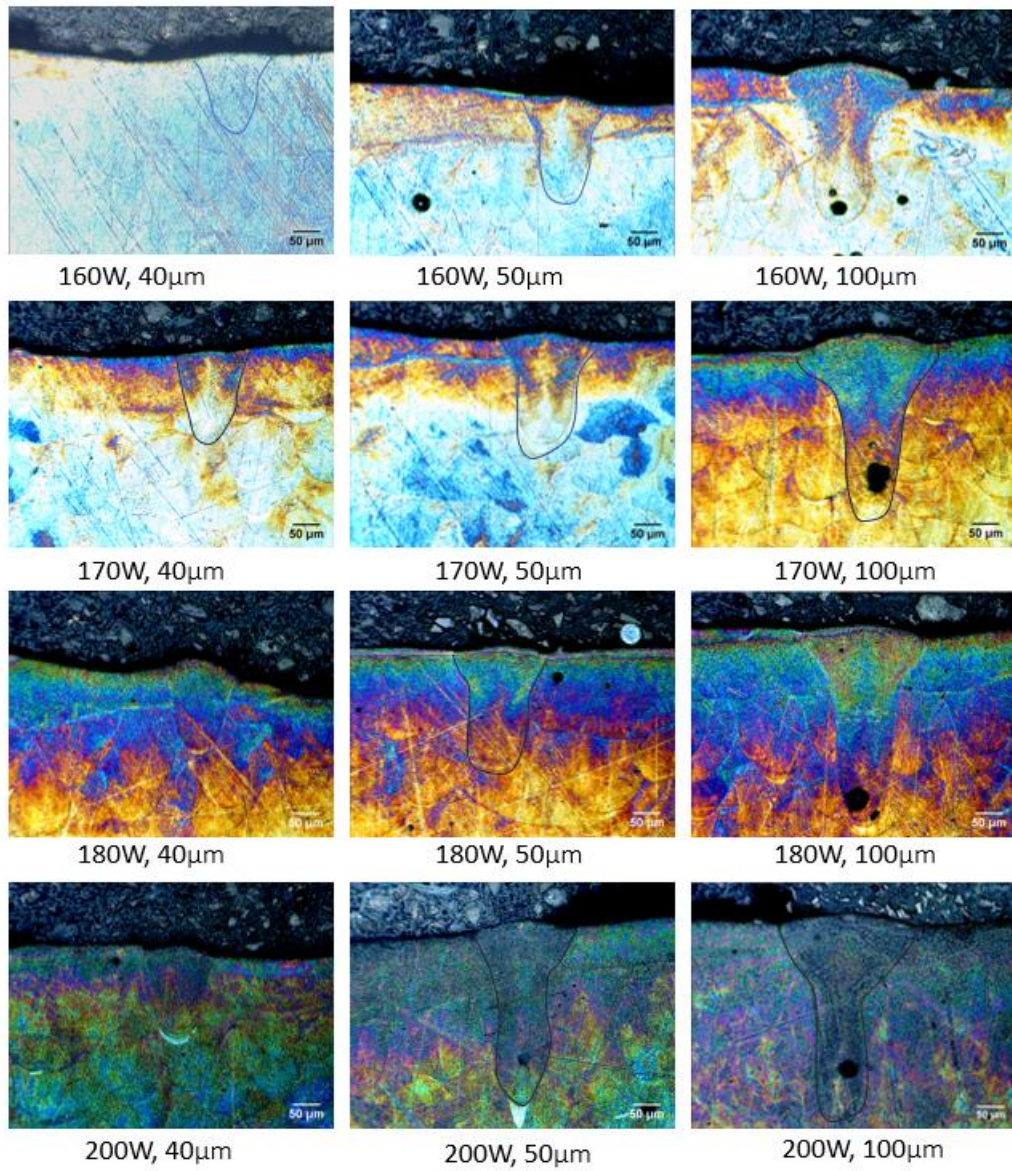


Figure 131: Cross-section samples showing the melt pool geometry of single beads built using Inconel 625 and built without powder and with different laser power (vertically) and for exposure times of 40 µs (left), 50 µs (middle) and 100 µs (right). The details of the beads are described in Table 13.

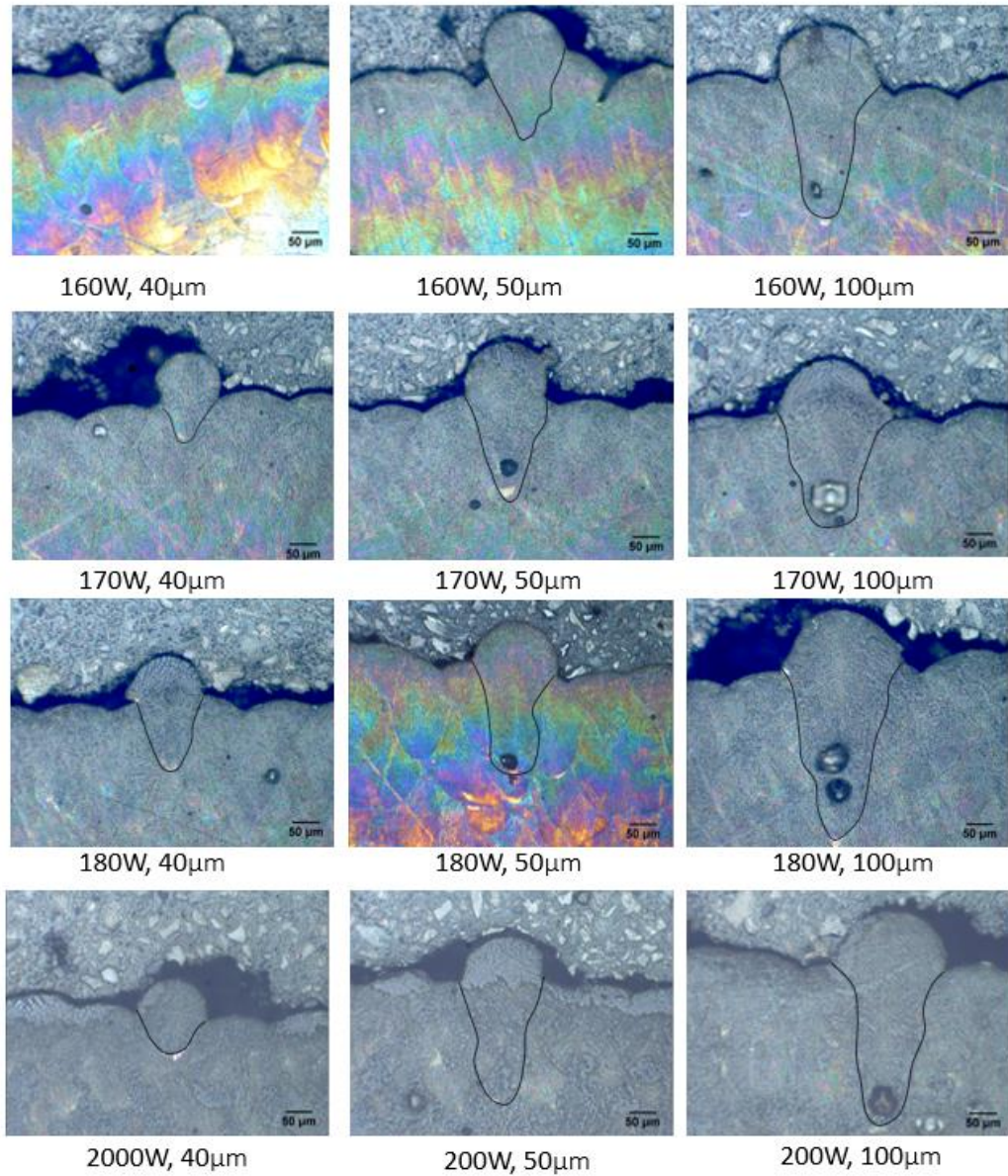


Figure 132: Cross-section samples showing the melt pool geometry of single beads built using Inconel 625 and built with powder and with different laser power (vertically) and for exposure times of 40 μ s (left), 50 μ s (middle) and 100 μ s (right). The details of the beads are described in Table 13.

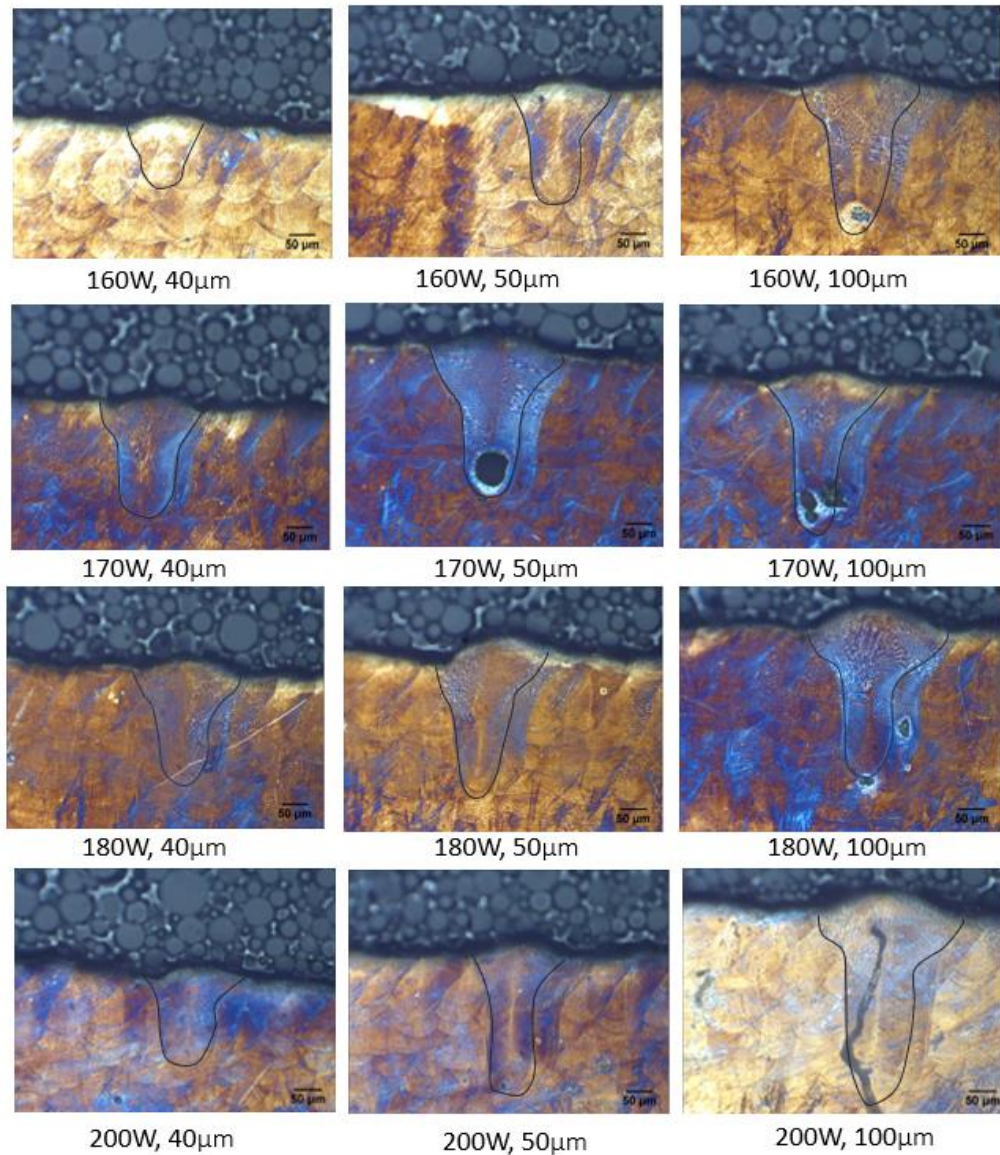


Figure 133: Cross-section samples showing the melt pool geometry of single beads built using Maraging steel and built without powder and with different laser power (vertically) and for exposure times of 40 μ s (left), 50 μ s (middle) and 100 μ s (right). The details of the beads are described in Table 13.

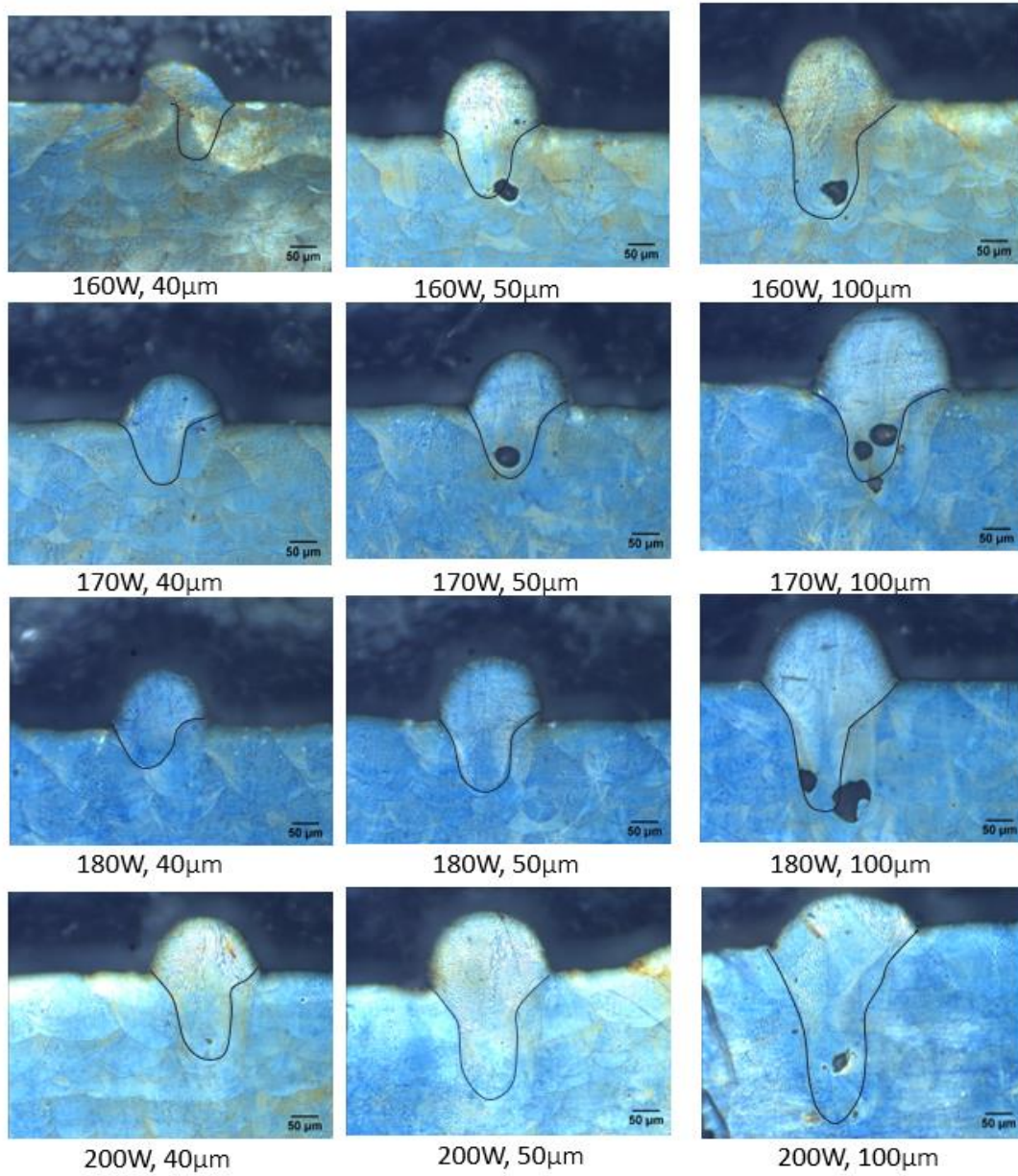


Figure 134: Cross-section samples showing the melt pool geometry of single beads built using Maraging steel and built with powder and with different laser power (vertically) and for exposure times of 40 μs (left), 50 μs (middle) and 100 μs (right). The details of the beads are described in Table 13.

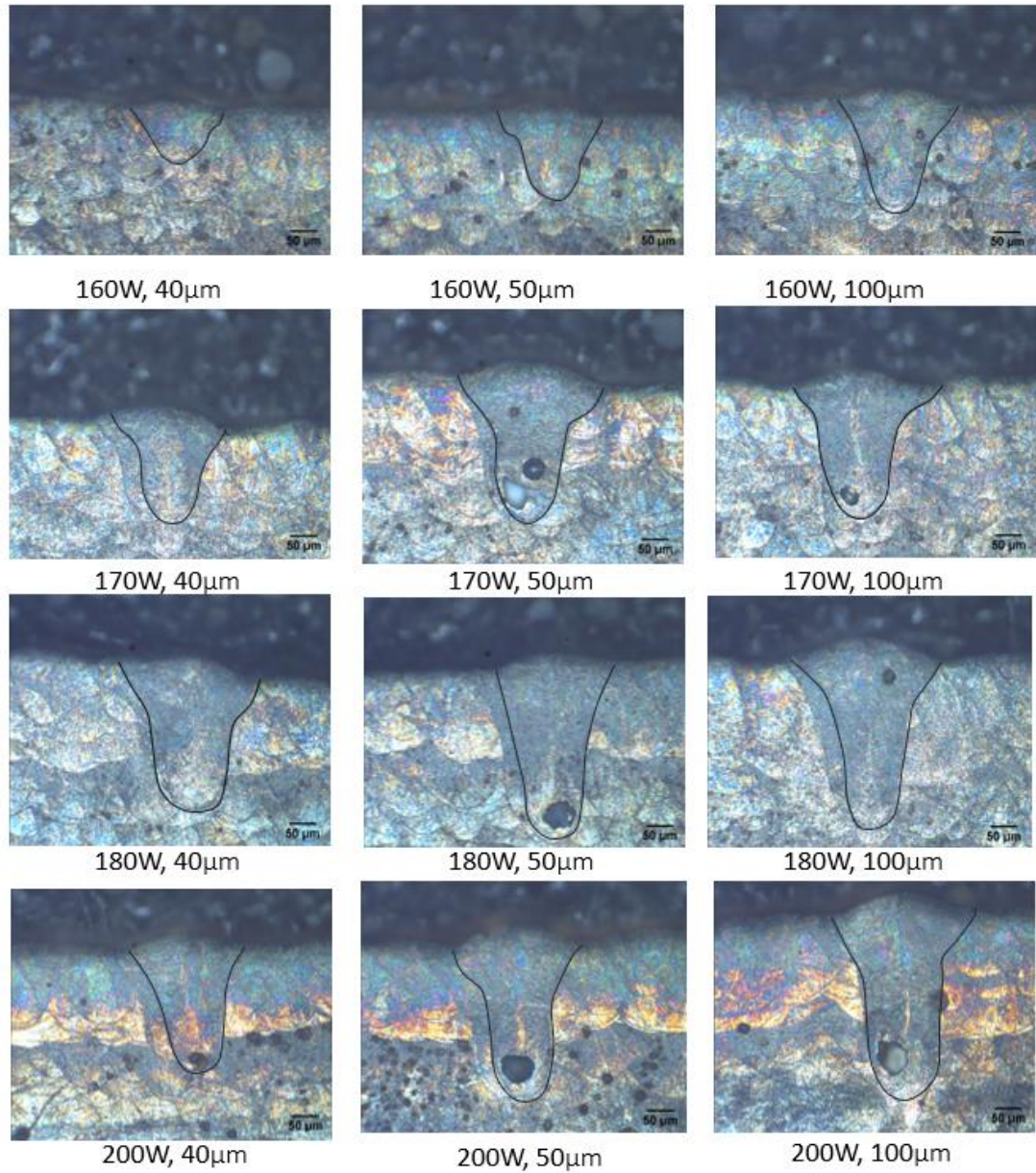


Figure 135: Cross-section samples showing the melt pool geometry of single beads built using Maraging steel with Nitrogen as Inert gas; built without powder and with different laser power (vertically) and for exposure times of 40 μ s (left), 50 μ s (middle) and 100 μ s (right). The details of the beads are described in Table 13.

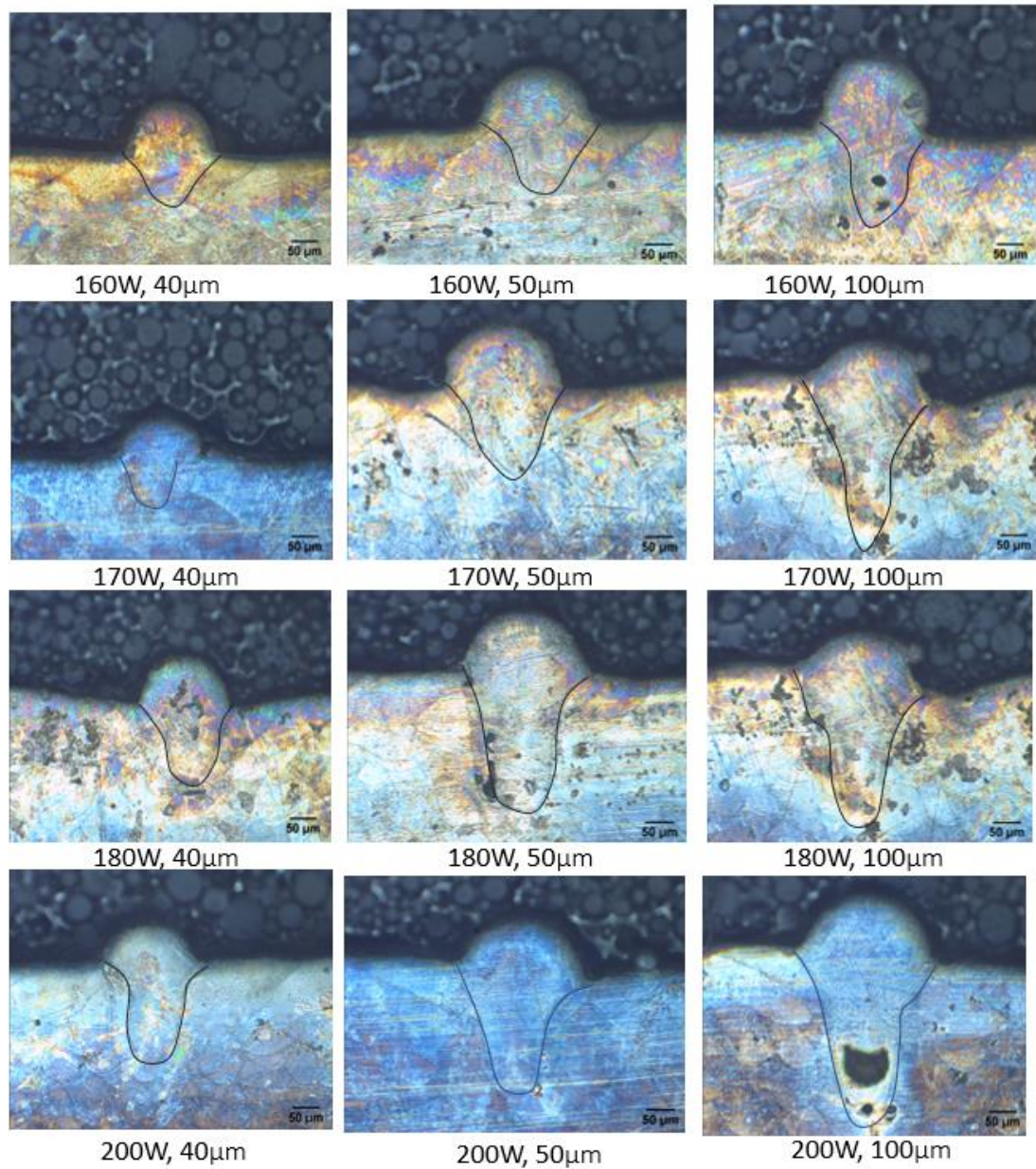


Figure 136: Cross-section samples showing the melt pool geometry of single beads built using Maraging steel with Nitrogen as Inert gas; built with powder and with different laser power (vertically) and for exposure times of 40 μ s (left), 50 μ s (middle) and 100 μ s.

Table 22: Results from the measurements of height, width and depth for single beads with one 60 μm layer of powder built with different laser power and exposure times obtained from the micrographic sections from Figure 132, Figure 134 and Figure 136.

Samples with powder			Average Height (μm)			Average Width (μm)			Average Depth (μm)		
Single Bead	Laser Power (W)	Exposure Time (μs)	Inconel 625	Maraging steel (Ar)	Maraging steel (N)	Inconel 625	Maraging steel (Ar)	Maraging steel (N)	Inconel 625	Maraging steel (Ar)	Maraging steel (N)
1_WP	160	40	60.396	98.44	93.26	100.01	90.37	148.8	52.478	28.13	67.37
2_WP	160	50	99.01	96.22	95.52	157.426	134.71	196.14	170.3	121.46	109.22
3_WP	160	100	104.653	108.1	125.09	205.941	188.02	216.2	201.99	242.76	162.1
4_WP	170	40	80.204	80.69	90.15	135.647	102.16	193.99	121.789	79.36	97.3
5_WP	170	50	100.99	91.05	100.67	138.687	144.33	240.54	186.139	205.95	145.67
6_WP	170	100	108.915	100.67	108.13	203.96	218.37	267.6	237.626	241.31	200.65
7_WP	180	40	67.334	74.75	89.57	116.836	111.02	219.08	192.082	129.56	136.03
8_WP	180	50	86.144	82.18	86.62	147.528	158.73	249.21	225.745	240.57	128.82
9_WP	180	100	114.856	107.32	103.88	206.931	229.01	287.91	348.516	299.01	243.13
10_WP	200	40	89.109	60.69	87.83	143.564	130.27	203.54	191.092	78.12	194.82
11_WP	200	50	107.921	79.95	93.26	151.485	144.36	220.36	237.626	219.82	165.82
12_WP	200	100	116.832	97.7	107.61	236.636	199.84	256.09	353.48	286.44	281.44

Table 23: Results from the measurements of height, width and depth for single beads without powder built with different laser power and exposure times obtained from the micrographic sections from Figure 127, Figure 129, and Figure 131.

Samples without powder			Average Height (μm)			Average Width (μm)			Average Depth (μm)		
Single Bead	Laser Power (W)	Exposure Time (μs)	Inconel 625	Maraging steel (Ar)	Maraging steel (N)	Inconel 625	Maraging steel (Ar)	Maraging steel (N)	Inconel 625	Maraging steel (Ar)	Maraging steel (N)
1_WP	160	40	6.7	17.82	27.38	130.697	143.11	148.8	110.962	106.59	91.11
2_WP	160	50	7.44	25.92	22.22	168.697	173.99	196.14	174.359	190.5	148.8
3_WP	160	100	30.35	37.01	29.64	248.517	220.31	216.2	279.215	247.56	189.84
4_WP	170	40	6.66	21.48	39.23	141.584	194.89	193.99	126.736	194.89	164.31
5_WP	170	50	14.8	31.09	35.9	181.199	201.11	240.54	183.171	252.54	219.14
6_WP	170	100	28.87	33.34	40.71	263.368	242.84	267.6	312.038	253.36	233.92
7_WP	180	40	20.01	28.09	32.78	148.518	178.86	203.54	156.439	199.84	237.59
8_WP	180	50	21.48	31.83	34.79	162.379	183.55	220.36	201.983	233.14	240.57
9_WP	180	100	32.2	48.11	41.34	279.208	244.27	256.09	302.972	252.41	291.62
10_WP	200	40	27.42	23.7	33.31	139.604	160.72	219.08	157.429	160.64	194.82
11_WP	200	50	28.87	26.69	42.16	173.27	205.79	249.24	266.338	245.35	253.95
12_WP	200	100	34.584	45.89	45.91	282.18	276.07	287.91	400.001	331.59	310.89

As can be seen in Figure 137 and Figure 138, even when the same parameters were used for the fabrication of single bead the melt pool characteristics width, height, and depth were different for both cases (with powder and without powder) for the different metal powders i.e. Inconel 625 and Maraging steel. As well as, the melt pool characteristics were different for the samples built using Maraging steel with Argon and Nitrogen as inert gas. This confirms that the change of the inert gas from Argon to Nitrogen affects the microstructure of the samples built using Maraging steel.

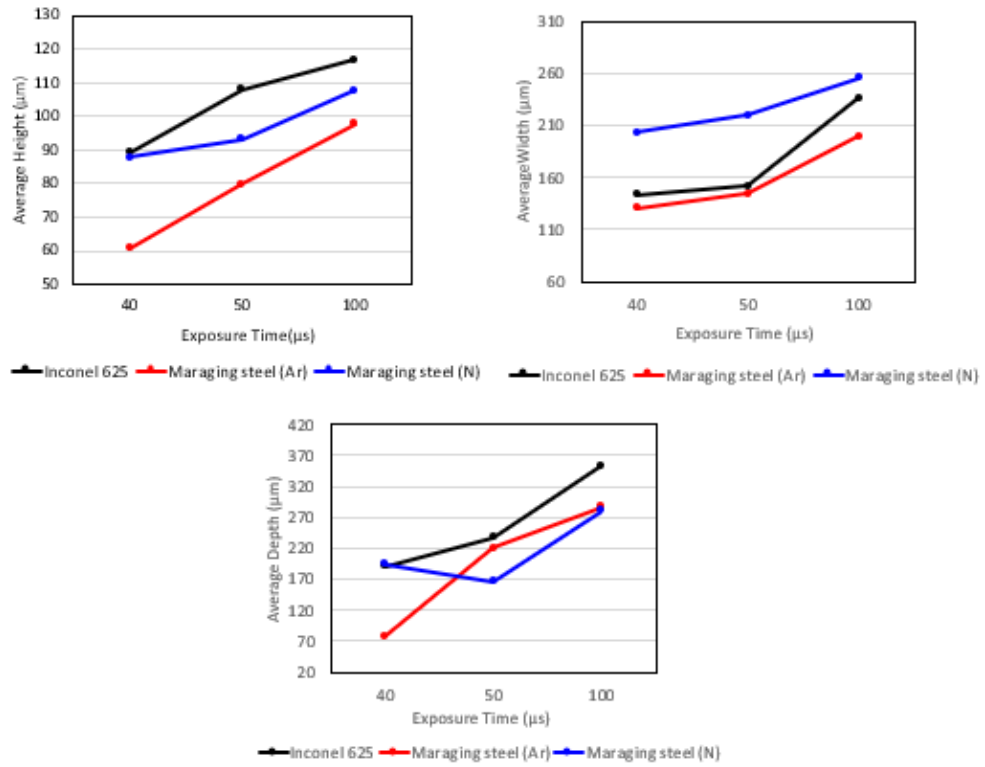


Figure 137: Comparison of measurements results shown in Table 22 from the height, width and depth of single beads built using one 60 μm layer of powder with a laser power of 200 W and an exposure time of 100 μs using different metal powders, see Table 13 for more details.

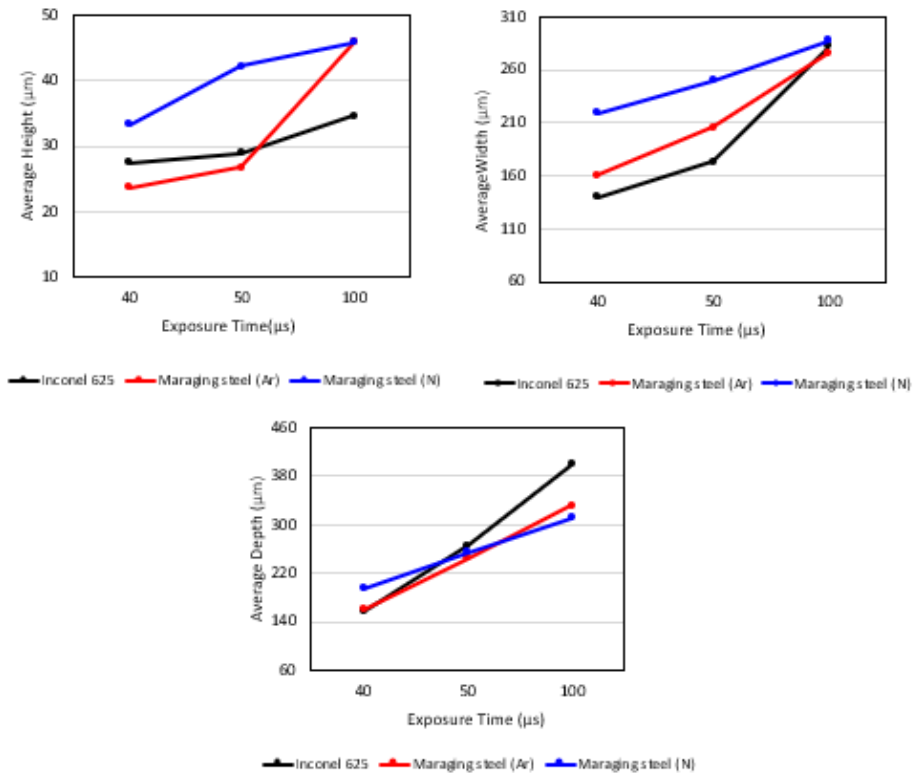


Figure 138: Comparison of measurements results shown in Table 23 from the height, width and depth of single beads built without powder with a laser power of 200 W and exposure time of 100 μs using different metal powders, see Table 13 for more details.

5 Discussion

The aim of this research was to understand the complex evolution of residual stresses in the L-PBF process. In order to accomplish this, the following objectives were addressed:

1. To conduct a literature review of the current understanding of residual stresses developed in L-PBF and the existing measurement methods used to determine the residual stresses in the L-PBF process.
2. To investigate the generation of residual stress in the L-PBF process through the use of a Force Transducer Device (FTD) to explore how residual stresses originate and evolve during the manufacturing process using different metal powders.
3. To explore and identify the key parameters in the build process that result in the formation of residual stresses through in-situ measurements and investigate the effect of the material properties on the development of residual stress.
4. To investigate a correlation between the in-situ measurements, process parameters and material properties in the development of residual stresses in the L-PBF process.

Significant research has been conducted on residual stresses using post-process measurements [87, 92, 113, 187], while very few studies have reported on in-process measurement of residual stresses during the L-PBF process [45, 47, 48]. Previous methods reported in the literature for in-process measurements have provided valuable information on the development of residual stresses in the L-PBF process; however, the reported research has been limited to measurements at single points of a single variable and were focused on a particular material. Therefore, the method proposed by Robinson [119] was used to extend the investigation to a more complete understanding of the development of residual stresses through in-process measurements in the L-PBF process for different metal powders. The method used in this thesis effectively allowed the investigation of the development of residual forces, from which residual stresses can be inferred, for two different part geometries using an array of measurement points to investigate and compare the effects of process parameters and material properties for different metal powders.

5.1 Experimental Results

The experimental work in this thesis was conducted in two phases. The first phase of the project was focused on the study of the effect of the different processing parameters (such as laser power, scan strategy and layer thickness) on the development of residual forces during the L-PBF process and the resulting part deformation. This first stage was conducted using Ti-6Al-4V, which is one of the most common materials used in the L-PBF process, due to the interest in this particular material from the sponsor and collaborators. The second phase of the project extended the study into three Nickel based metal powders: Inconel 625, Inconel 718 and Maraging steel, to investigate the effect of material properties on the development of residual forces during the L-PBF process. Results from the experimental work demonstrate how the processing parameters have a significant impact on the development of residual stress in the L-PBF process. The in-process measurements allowed observation of how the residual stress levels developed during the build vary depending on the energy input, and how varying the process parameters can affect the manufactured parts in different ways depending on the material properties of the metal alloy used. All experiments were performed using a Renishaw AM250 machine. However, the machine is representative of the L-PBF process, which consists of the selective melting and fusing of metallic powders with a laser beam under an inert gas atmosphere layer by layer until completion. Therefore, the experimental work will be applicable to all L-PBF machines including all variations of materials and parameters. Since the operating principle of the L-PBF process will not vary if a different machine is used, all the parameter variations (i.e. laser power, layer thickness and point distance) are capable of being repeated using any other L-PBF machine. If this study was repeated using a different L-PBF machine, the forces developed could be slightly different; however, the fundamental result would be the same.

5.1.1 Effect of the processing parameters for Ti-6AL-4V

The use of the FTD allowed the development of residual forces in the L-PBF process over time to be studied, which revealed inter-layer effects not noticed with post-process measurements. The distribution of the forces in the L-PBF process are not uniform because the sections of the part are heated non-uniformly following the scanning pattern of the laser, such that sections of the part are heated and cooled independently. This makes the magnitude and orientation of the stresses strongly dependent on the scanning strategy used. It can be observed in Figure 73, that the forces measured for the central load cells (6, 7, 10, and 11) and external load cells follow a linear trend after the first layer of the build. The forces on the central load cells are compressive while the forces on the corner load cells are tensile. While the forces registered

by the centre external load cells are much lower than the registered by the corner. Thus, the sum of the forces remains zero, as shown in Figure 73. The distribution of the forces of the in-plane (xy plane) with respect to the build direction (z-direction) are shown in Figure 74 and implies that the part will curl away from the build platform when the constraining forces are released, creating a permanent part distortion, which agrees with previous research on the distribution of developed stresses in the L-PBF process [187-189]. Similar effects occur in different AM processes due to the shrinkage of the material used [190, 191]. In the FDM process, the curling effect occurs due to the behaviour of thermoplastic polymer where, the polymer is warmed up to glass transition temperature and turn into molten state. Then, the molten polymer is extruded through a nozzle and follows the desired deposition path. However, when it becomes cold, the uneven distribution of heat will generate internal stresses causing it to bend in upward direction [190]. Similar, in Stereolithography, shrinkage forces occur mainly in the scanning direction which results in one-sided curling of the parts, therefore, Onuh and Hun [191] showed that the use of an alternating exposure of the layers, i.e. divergent STAR-WEAVE (DSW), resulted in more homogeneous residual stress in the part and to higher part stability than when layers are scanned in only one direction.

As can be seen in Figure 76, the sum of the measured forces oscillates with each layer, the results obtained from the in-process measurements from the FTD suggest that this could be an effect of the thermal gradient mechanism (TGM). When a new layer is added and heated far above the underlying layers, the melted material will first expand uniformly releasing the forces present in the part; this expansion will be restricted by much cooler underlayers in the part. When the heat source moves away from the part, the new layer will cool at a faster rate than the underlying material, resulting in a primary tensile stress in the upper layer and a primary compressive stress in the layers below. The results from the in-situ measurements reported in section 4.2.1 have shown that the forces developed per layer are related to the scan direction and scan vectors length.

The results from the experiments performed in section 4.2.1 demonstrated that the scan strategy has a significant impact on the development of residual forces in the L-PFB process, which vary depending on the vector's orientation, and length and on the energy input. Longitudinal stresses are developed in the direction of the scan track and perpendicular to the scan track, giving strong credence that the primary stress is oriented in the direction of the scanning (parallel to the scan vector), which agrees with previous research [49]. However,

this still needs to be further investigated in order to see if the orientation of the FTD influences the results.

When using a unidirectional scan strategy, higher levels of force were developed with X-direction scan than with Y-direction scan vectors for a rectangular part; this agrees with previous studies [174, 192]. As can be seen in Figure 85 from the sum of the forces registered by the 16 load cells, there is an oscillation per layer, because the forces are relaxed when the laser is scanning the part and, when the laser is off while recoating of the powder for the next layer, the forces increase as the part cools down. This layer by layer oscillation was different for the three scan strategies tested with a constant amplitude of 10 N and 40 N for X and Y direction scanning respectively and a varying amplitude for the 67° rotating scan strategy. These results show that the residual forces developed during the L-PBP are highly dependent on the orientation of the scan vectors, as the layers are not melted uniformly, but rather are dependent on the track of the laser beam. The non-uniform temperature distribution of the scanning pattern results in different cooling rates throughout the part, which agrees with previous research [99, 183]. The use of a rotating scan strategy contributes to reducing the residual stress developed in the process as approaching the part from different directions for each layer will keep a more consistent temperature in the part [166]; hence, it is recommended to use a rotating scan strategy rather than a unidirectional scan strategy [174]. The time elapsed between layers showed an effect on the developed strains, this agrees with previous research [120]; nonetheless further studies were needed for different materials, as previous results showed that the cooling dwell times have an effect on the material properties.

In an additional investigation of the effect of the scan strategies, samples produced using three different scan strategies: Stripe, Chessboard and Meander showed the Meander scan strategy to develop lower forces than the rest of the strategies allowing a higher part to be built before the force on any of the load cells reached the maximum permissible load of 50 Kg. This agrees with previous studies [193] in which single line vectors, from side to side of the part, were found to develop less residual stress than sectioned scanning, but disagrees with others studied [166, 194, 195]. Results for the build height reached for each scan strategy and layer thickness are shown in Figure 95. The Stripe scan strategy with a 30 μm layer thickness showed much faster development of forces than the rest of the scan strategies investigated, thus reducing the part height by 40% of the maximum height built (3.9 mm) using the Meander strategy with a 60 μm layer thickness and single-track scan vector. While the Chessboard strategy with a 30 μm layer thickness was 29% below the maximum height.

The effect of the thickness of the layers was small compared to the scan strategy with a doubling in the thickness producing only a 12% increase in the residual forces. A thicker layer implies fewer layers are required to build the part leading to less number of cycles and hence lower residual forces, despite greater energy input required to melt the thicker layers [98].

For all the scan strategies, there was a linear rate increase in the forces after the first seconds of the build or layer 11 of the build. These consistencies could benefit the prediction of the stresses developed in one scan strategy based on another and to determine a residual stress factor for a particular material. Further investigation was performed to determine if this tendency extends to different metal powders and if the development of residual stresses is characteristic to a particular property of each material rather than of a process parameter.

Lower forces were developed in the Meander scan strategy, which could be related to the volumetric energy input. The Meander scan strategy with a 30 μm layer thickness, had an energy density of 42.328 J/mm^3 , which was lower than the value for the Stripe and Chessboard scan strategies which was 57.720 J/mm^3 . The parameters used to build a sample using the Stripe and Chessboard strategies were the same; however, the sample built using the Stripe strategy reached the maximum workable load for the load cells faster than the sample built using the Chessboard strategy.

The parameters used to build a nearly dense part were the same used for the Stripe and Meander scan strategies using a 60 μm layer thickness with an energy density of 40.93 J/mm^3 . It would be expected that because of using the same parameters, the forces developed would be similar for both samples. However, for the sample built using the Meander strategy, the forces developed were much lower compared to the sample built using the Stripe strategy, as shown in Figure 86. This could be attributed to the less material melted per scan when using single line vectors for the Meander scan strategy compared to the 5mm stripes sections from the Stripe scan strategy; thus, the shrinkage of the solidified material is smaller using the Meander scan strategy developing less tensile forces per layer. In general, the result showed that by reducing the energy input, the total measured force was reduced, which agrees with previous results from Simons et al. [154]; however, the forces developed depend on the scan strategy used being lower using a single line scan rather than a sectioned scan. An extended analysis of the effect of the energy density was performed using Inconel 625, the material had to be changed due to the availability of the machine, and is further discussed in this section.

A limitation to this result is that by using the FTD, in-situ measurements performed in this work were limited into simple part geometries, i.e. square part and rectangular part; therefore, the thermal gradients could vary according to more complex part geometries, and the scan pattern could affect differently on the developed residual stresses for different part geometries.

By reducing the laser power from 200 W to 180 W and 160 W the sum of forces, as can be seen in Figure 77, were affected during the first 12 layers of the builds, particularly the 160 W for which the measured forces were significantly lower than for the 200 W and 180 W samples. As more layers were added, the measured forces increased up to a similar resultant force for the three samples after 50 layers. As can be seen in Figure 78 the contour plots show that the distribution of forces was the same for all samples at the end of each build, being tensile in the corners and compressive in the centre of the part, this agrees with previous literature [179, 196]. The sum of the measured forces followed a nearly linear trend as a function of the laser power (Figure 139) as previously reported by Mukherjee [197]. The higher heat input by using a higher laser power, slightly lowers thermal gradients and allows for a higher temperature increase during the process, thus reduces the residual stresses developed in the part [196].

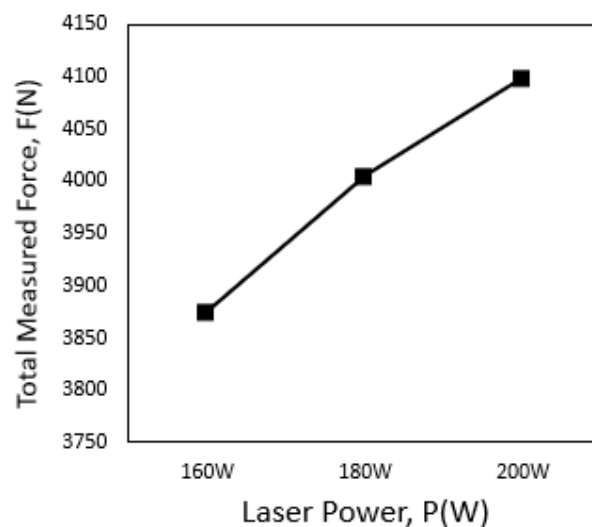


Figure 139: Absolute total measured force (N) from in-situ measurements for a square part in Ti-6Al-4V as a function of laser power (W), from samples S1, S2 and S3, shown in Figure 73.

5.1.2 Effect of the Material Properties

Material properties were found to have a strong effect on the development of residual forces induced in the L-PBF process. Thermal and mechanical properties of the material powder were expected to affect the development of residual stresses in the part, such that materials with lower thermal diffusivity would have higher thermal strains [198]. The coefficient of thermal expansion of the material was expected to be important to the residual stresses developed in the process, with a large thermal expansion coefficient leading to large shrinkage of the material during cooling and higher stresses [116]. In addition, the yield stress at the high temperatures in the process will influence the levels of the residual stress. Amongst the tested materials, Inconel 625 has the highest coefficient of thermal expansion [$12.8 \cdot 10^{-6} K^{-1}$] and exhibited the highest measured force. However, Maraging steel's coefficient of thermal expansion [$10.3 \cdot 10^{-6} K^{-1}$] is greater than Ti-6Al-4V alloy's [$9.3 \cdot 10^{-6} K^{-1}$] and was found to have much lower forces induced during the process, which makes it difficult to define a correlation, as seen in Figure 140.

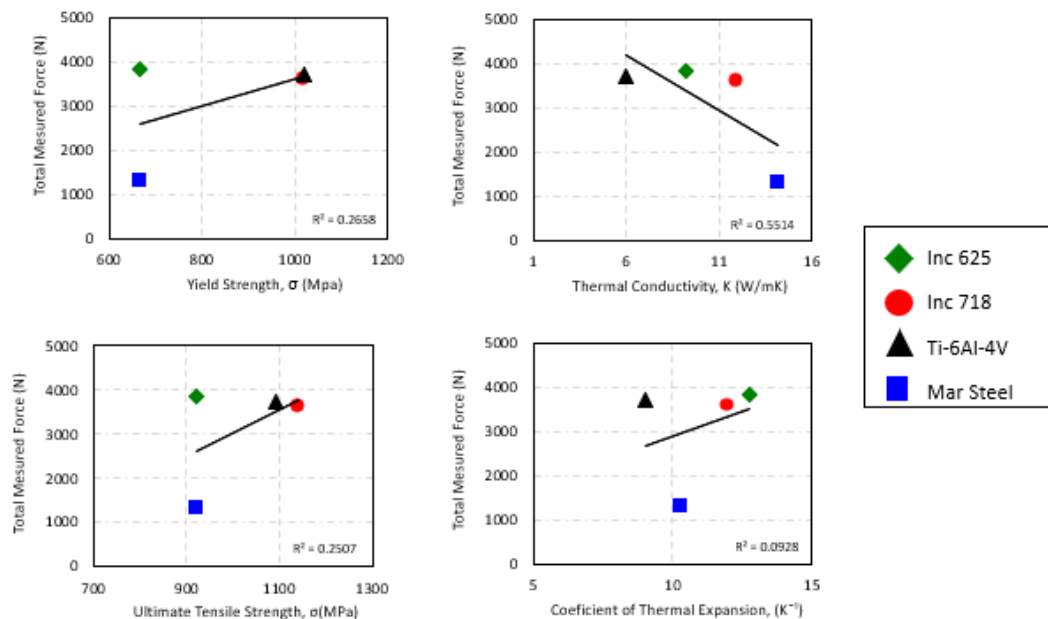


Figure 140: Relationship of measured force to material properties: yield strength, thermal conductivity, ultimate tensile strength and thermal expansion for the different metal powders tested.

Results from the experimental work showed an important effect of the phase transformation on the development of strains and the part deformation not previously shown in literature,

which implies that the Type II stresses, developed in the phase transformation of the material, have a significant effect in the L-PBF. In Maraging steel, allotropic transformations between austenite and martensite occur at much lower temperatures than in other materials. In Maraging steel, martensite is transformed to austenite during continuous heating, this transformation begins (M_s) at about 590 °C and is completed (M_f) at approximately 770 °C. Upon cooling, the structure begins to transform from austenite to martensite at about 154 °C (M_s) and is reported to be completely transformed at about 99 °C (M_f) [184]. Compressive stresses generated by the martensite to austenite and austenite to martensite transformation are large enough to neutralise and overcome the tensile stress, developing much lower forces than the rest of the materials. Potentially, this behaviour will allow the manufacture of complex parts with lower residual stresses and part deformation than other metal powders. However, a dimensional change is anticipated on transforming from one phase to the other, because of the simultaneous contraction associated with the transformation of martensite to austenite and the expansion of the residual martensite [184]. The martensite has an atomic packing factor of 0.68, while the austenite has an atomic packing factor of 0.74. The difference in atomic packing factor leads to a volumetric expansion during cooling and subsequently results in compressive stress [184]. The compressive stresses are large enough to neutralise and overcome the residual tensile stresses, which reduces the overall levels of residual stress. This difference leads to a volumetric expansion during cooling and subsequently results in compressive stress. As it can be seen in the contour plots for the measured forces shown in Figure 106 after the part cools down the forces at the corners changed from being compressive to tensile, which may be caused by the volume expansion due to the transformation of austenite to martensite (Figure 141). This effect supports the theory that differences in dimensional changes observed during the martensite to austenite and austenite to martensite phase transformations produce shape deformation [199, 200].

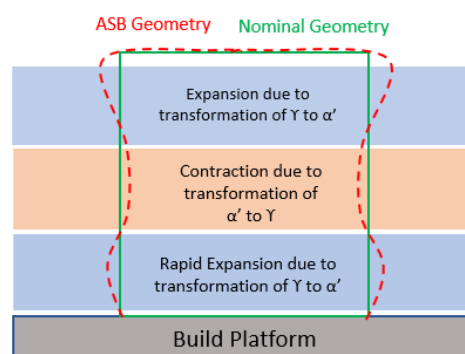


Figure 141: Dimensional part geometry change due to the phase transformation for Maraging steel.

5.1.3 Effect of the inert gas atmosphere

The use of different inert gases for Maraging steel affected the part deformation and force distribution, which might be due to the N_2 gas acting as an austenite stabilizer. The residual strains developed for the Maraging steel were very low compared to the rest of the materials using the same scan strategy in both Argon and Nitrogen gas atmospheres (Figure 102). The sum of the developed forces increased slightly more in the Nitrogen built part as can be seen in Figure 110. This effect of the inert gas has not been previously reported in the literature, and is an additional factor to consider when modelling the L-PBF process and specifying build parameters for parts. The effect of changing the inert gas was not the same for Inconel 625 on the part deformation. However, for the sample built using Inconel 625 and Nitrogen inert gas, the forces developed were lower, which allowed to build a higher part as from previous sample using argon gas, as shown in Figure 114.

As can be seen in Figure 142, the melt pool boundaries differ for the different inert gases, with N_2 producing metastable hexagonal grain boundaries, possibly from the formation of martensite at the lower melt pools due to the retained austenite often found along grain boundaries, as described by Takata et al [173] and in the schematic shown in Figure 143. Further analysis needs to be done on the mechanical properties of the parts built in the different inert gases as the microstructural changes will likely influence the final properties of the parts.

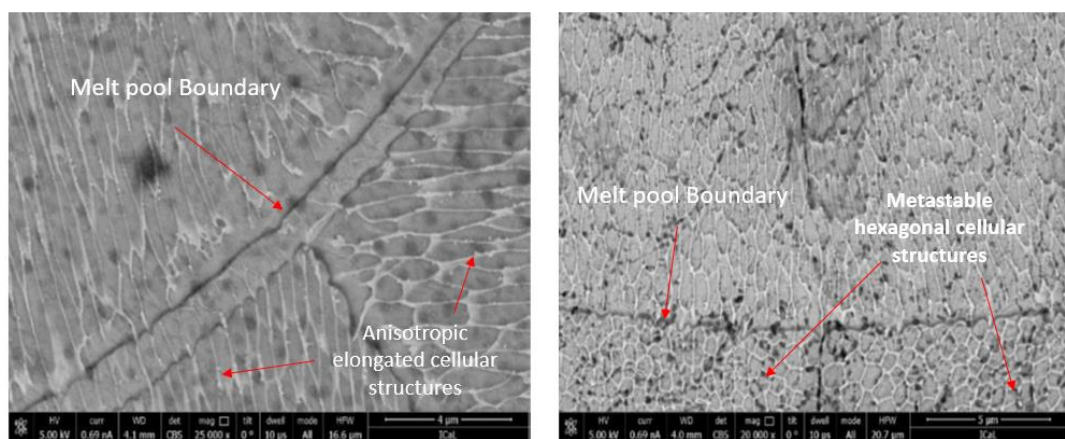


Figure 142: SEM image showing the microstructure of the melt pool boundary from (left) sample with Argon gas (S20) and (right) from sample using Maraging steel with Nitrogen gas (S21) inert atmosphere.

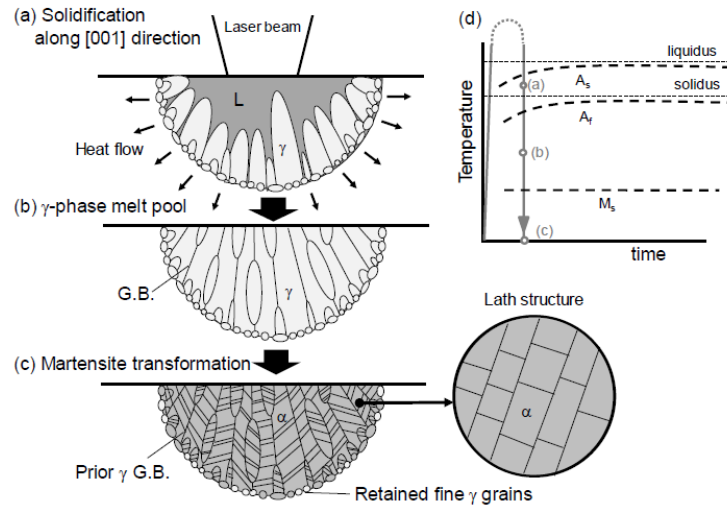


Figure 143: Schematic of the formation process of microstructure in the Maraging steel during L-PBF (from [173])

5.1.4 Effect of the Energy Density

Energy Density (ED) has been shown to influence the development of resultant strains. By reducing the energy input into the part, a lack of fusion of the metal particles can induce porosity into the part that impacts the mechanical properties of the final component. The processing parameters, including the energy input, should be carefully selected to ensure the complete fusion of the metal particles to reduce porosity in the samples and ensure interlayer bonding while avoiding excess energy input that will increase residual stresses due to the increase melt pool size and the Heated Affected Zone (HAZ) [176]. By increasing the point distance, the scan speed is reduced, reducing the energy density induced in the process. By increasing the point distance, the strains developed during the build reduced, producing a linear correlation between energy density and measured forces, as seen in Figure 144. However, the mechanical properties of the samples were also reduced by increasing the point distance, which induced increased porosity and reduced elongation at failure and the ultimate tensile stress (UTS) of the samples.

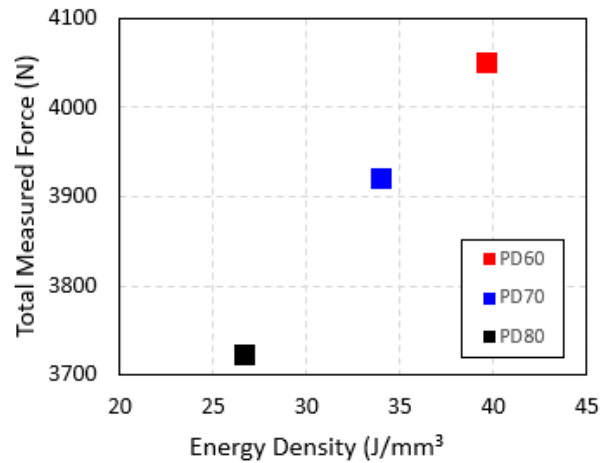


Figure 144: Total measured force vs Energy density from samples with a point distance (PD) variation

The density of the energy input influences the size and the morphology of the melt pool. The characteristics of the melt pool are discussed in the next section; however, the three types of behaviour can be identified based on increasing levels of energy density, i.e. insufficient melting, conduction melting and keyhole melting, as shown in Figure 145. As using high energy densities, the temperature from the melt pool exceeds the boiling point of the metal leading to evaporation and formation of bubbles known as keyhole pores [201]. Hence, the selection of an appropriate energy density is essential to achieve the desired material structure and density.

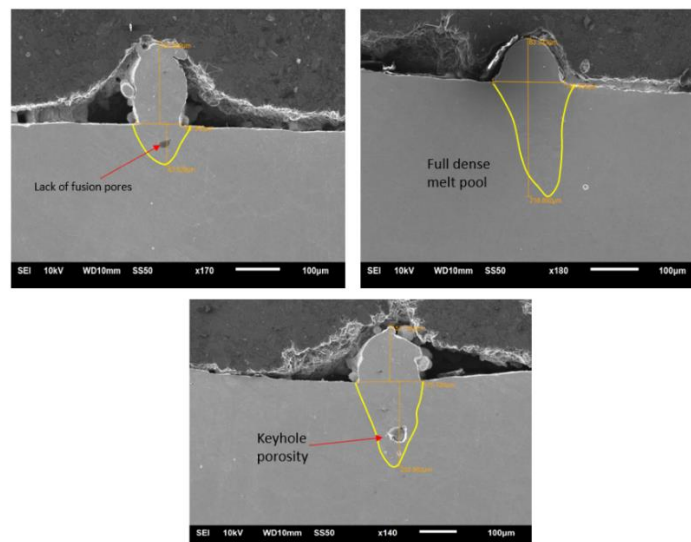


Figure 145: SEM images of the melt pool characteristics with energy input variation from 51.94 J/mm³ (top left), 57.72 J/mm³ (top right), and 115.44 J/mm³ (bottom) for Ti-6Al-4V samples showing porosity in the sample due to lack of fusion (top left), dense melt pool heat conduction (top right) and keyhole porosity (bottom)

5.1.5 Melt pool characteristic

The scanning process in the L-PBF process is based on single-line scanning where the powder particles are melted when a laser beam travels along with a prescribed pattern. When the laser beam melts the powder particles, a single solid track is formed after creating a melt pool shape whose properties are dependent on the parameters used in the L-PBF process. The melt pool size and behaviour directly depend upon the applied energy density. Therefore, the study of the laser powder interaction in the formation of single tracks becomes important to control residual stress development and for process simulations.

The characteristics of the melt pool were studied by examining sections of a part in a scanning electron microscope to obtain images such as those shown in Figure 143. The length, width and depth of the melt pool were measured and found to increase with laser power and exposure time. At the higher levels of power and exposure time, keyholes were observed to have formed, as described in the previous section. The results agree with those found in previous studies [186, 201, 202]. Increasing the scan speed and laser power elongates the melt pool, which could increase the magnitude and anisotropy of the residual stresses on each layer [196]. The microstructure of the samples manufactured using L-PBF is the result of local rapid solidification and cooling, which lead to large thermal gradients, and it is, therefore metastable and unique compared to traditional manufacturing methods. This microstructure could react differently to high temperatures than that of the same material processed via another technique [116]. Material properties such as the coefficient of thermal expansion and thermal diffusivity could affect the melt pool geometries; thus, the thermal gradients induced in the process. Having a good understanding of laser-material interaction could help to determine a correlation between material parameters and the magnitude of residual stresses and can lead to more accurate FE models and simulation results.

The measurements for the single beads were performed manually, which could be slightly different if the process was repeated, and the definition of the melt pool geometries was dependant on a visual judgement. The known geometry could have been slightly inaccurate, and the scaling measurements might not have been precise; therefore, the accuracy of the measurements could be significantly improved by the automatization of the process. As well there were some inconsistencies in the single tracks especially in the cases for the lower laser power and exposure times, if the parts were sectioned at a different position along the track the results could be different, the measurements might not have been consistent enough for





a tendency to be observed. However, it was clear that the melt pool size and behaviour directly depend upon the applied energy density and will influence the developed residual stresses per layer.

As a result of this experimental work, it is clear that the residual stresses developed in a component during the L-PBF process are very complex and result from not only the process parameters but also the material properties; both have an important effect on the residual stresses developed. Further work is needed to improve our understanding of the phase transformation in Maraging steel, as well as the dependence of the individual material properties on the forces developed during the L-PBF process for different metal powders.

5.2 Proposal Design for High-Temperature FTD

Due to the continuous and fast development of technology available in the L-PBF process, new capabilities to expand the process parameters arise, i.e. work with higher laser powers and multi-lasers systems, heated base plates and heated chambers. The use of more than one laser for the manufacturing of a part reduces the production times significantly reducing the thermal gradient effect and could modify the microstructure of the parts and could reduce the residual stresses. The effect of multiple lasers allows developing new scan strategies that might reduce the development of residual stresses. The actual FTD has a limitation on the temperature and maximum load capacity, which makes it impossible to use with multiple laser systems, therefore we need to use load cells capable of working at higher temperatures. A comparison of commercially available load cells can be seen in Table 24. Few commercial load cells were found to be available that work at higher load capacity, but only one was able to work at temperatures up to 200 °C. Therefore, the proposed FTD was designed using a BD-MCL Bi-directional miniature load cell (PMC, UK), shown in Table 24. The BD-MCL miniature bi-directional load cell is produced from either aluminium (400 N) or stainless steel (800 N), is able to be used at temperatures up to 200 °C.

Table 24: High-temperature load cell availability

Product	Load Cell	Features and specifications	Cost
Honeywell Wire Lead Load Cell -53°C +121°C Part No.: 060-1432-07		Force Measured: Compression and Tension Force/ Load Measurement Range: 453.59kg Sensor Type: Miniature Operating Temperature (°C): -53 to +121	£701.37
TE Connectivity Wire Lead Load Cell -40°C +85°		Force Measured: Compression Force/ Load Measurement Range: 226.796kg Operating Temperature (°C): -40 to +85	£98.31
OMEGA Stainless Steel S Beam Load Cell (OMEGA, UK)		Force Measured: Tension or compression forces. Sensor Type: S-Type load cells Force/ Load Measurement Range: 453.59kg Operating temperature (°C): -35 to +65	£ 183.6
BD-MCL Bi-directional miniature load cell (PMC, UK)		Force Measured: Tension or compression forces Force/ Load Measurement Range: 400N and 800N Sensor Type: bi-directional miniature load cell Operating temperature (°C): -54 +200	£896.56

The FTD3 was designed using the same principle as of the previous FTD; a special substrate was designed to accommodate the BD-MCL Bi-directional load cell. A rectangular part will be built on top of cylindrical pegs attached to the load cell, which will be able to be removed after the build is complete. The top cover will be sectioned in three parts in order to give access to the pegs after the build is complete in order for the finished part to be removed Figure 146. The design is composed of 8 load cells as shown in the cross-section in Figure 147 which will allow measuring the forces developed at multiple sections of the part; a schematic of the part geometry is shown in Figure 148. The estimated cost of the FTD is of £1,3957.83. A bill of materials and can be seen in Appendix 2.

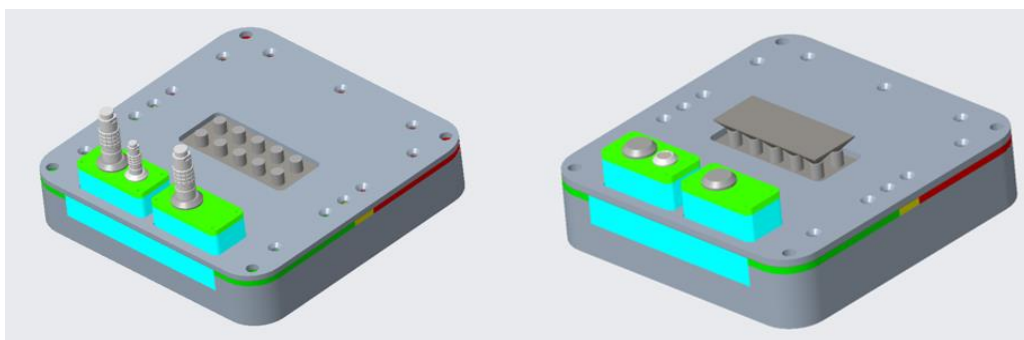


Figure 146: Design of FTD3 for higher temperatures and greater load capacity

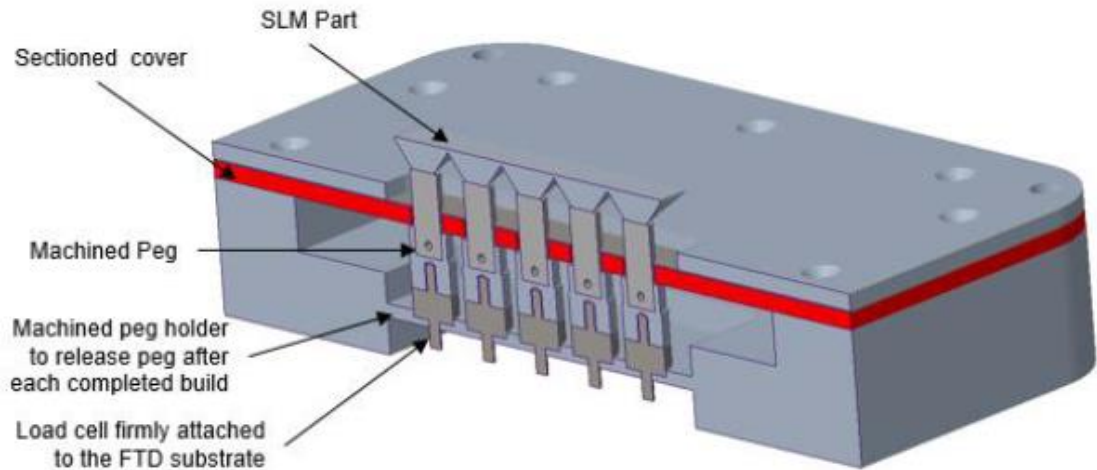


Figure 147: Cross-section of the FTD3

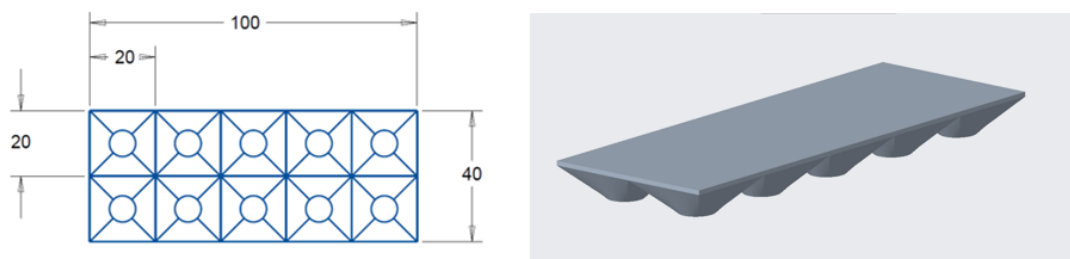


Figure 148: Part geometry for In-situ residual force measurements for the FTD3

The proposed FTD3 with a higher workable temperature load cell will allow for the device to be used on the multiple laser machines, i.e. Renishaw AM500. With the use of multiple laser systems, the possibility to develop new scan strategies is extended and can contribute to reducing the residual stresses developed in the part. Some of the different scan strategies that can be tested to reduce the thermal gradient per layer and measure the effect on residual stress development are shown in Figure 149:

- a) Individual laser scan with different initial points to reduce the thermal gradient effect.
- b) Re-scan with different laser parameters to alleviate residual stresses
- c) Use of different boundary scans to reduce residual stresses part deformation

- d) Use of combined scan strategies to reduce residual stresses and part deformation with different laser scanning parameters, i.e. Use of different laser powers at different sections of the part.

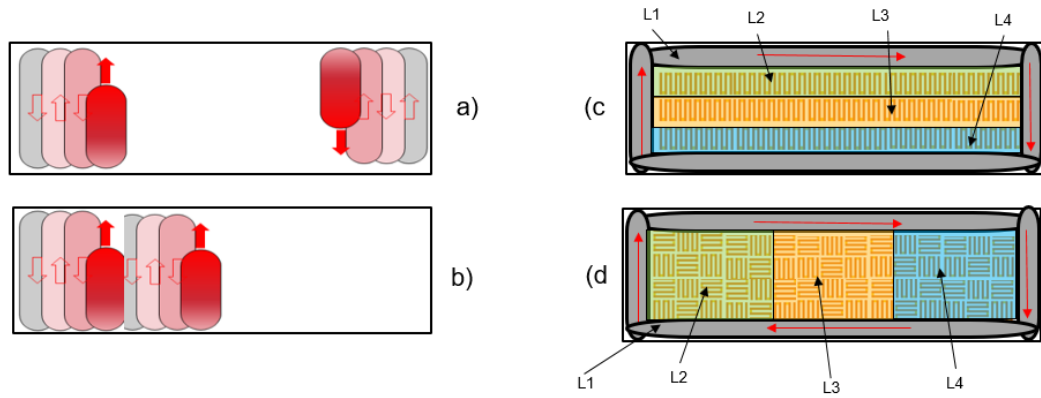


Figure 149: Scan strategies to achieve a lower thermal gradient to be used in the FTD3

6 Conclusions

The aim of this investigation is to understand the complex evolution of residual stresses in the L-PBF process through the use of in-situ measurements and to understand the effect of the process-material relationships on residual stress. A novel method for in-process measurements of the induced forces, from which the residual stresses could be inferred, was used to study the effect of different processing parameters and material properties on the L-PBF process. The results from the experimental work in this thesis illuminate the effects, which are difficult to observe using post-measurement techniques, of different processing parameters, such as scan strategies, layer thickness, energy density, inert gas and material properties in the L-PBF process. These results obtained from in-process measurements were found to contribute to the magnitude and distribution of the developed forces. However, it is difficult to identify a direct correlation between the residual stress and any particular variable, as the processing parameters are dependent on the material properties of the metal powder being used.

In general, forces measured in-situ during the build process using the FTD were tensile at the edges of the part and compressive at the centre, regardless of the scan strategy employed. These forces were released when the part was removed from its baseplate which resulted in the part deforming into a catenoid with the corners curling away from the baseplate.

The magnitude of the forces measured during a build process increased in an approximately linear manner after the first layers of the build were completed; although there was a layer-by-layer oscillation in the forces which could be a result of cyclic heat input caused by movement of the laser to and away from the part.

The magnitudes of the forces measured and their rate of development was dependent on the pattern of scanning used, such that for unidirectional scanning in a layer produced lower levels of force when the scan direction was rotated 67° between layers, than when all layers were scanned in the same direction. In addition, scanning all layers in y-direction induced lower forces than scanning all layers in x-direction, and it was not clear whether this was a bias in the FTD or L-PBF machine, though the literature would imply the latter.

The meander scan strategy avoids this bias by using uni-directional scanning at 45° to the machine's axes. It was found to induce forces that were 40% lower than those induced by sectional scan strategies, i.e. the Stripe and Chessboard strategies.

The influence of the thickness of the layers was found to be less than the scan strategy. Nevertheless, doubling the thickness from 30 μm to 60 μm allowed a higher part to be built before the maximum permissible force on a load cell was exceeded; perhaps because fewer layers and hence fewer thermal cycles were required. And, the sum of the absolute forces in the part was 12% lower for the part built using a layer thickness of 30 μm .

An important process parameter is the point distance which was changed in step with the scan speed, i.e. 10 μm increments in point distance corresponded to 100 mm/s increments in scan speed and approximately 5 J/mm³ reductions in energy density. The forces measured in-situ decreased with increasing point distance and tensile tests showed that the ultimate tensile strength and elongation to failure also decreased. Analysis of section of built parts implied that these changes in mechanical performance were related to an increase in porosity, which the results from the experimental work suggest that was caused by the decrease in energy density and increase in scan speed.

Results from the experimental work in this thesis show the effect of metal properties, such as the phase transformation, has on the development of residual forces that have not been previously studied. Four different materials were investigated: Ti-6Al-4V, Inconel 625, Inconel 718 and Maraging steel; the Maraging steel samples showed the lowest development of restraining force in comparison with the rest of the materials. This was probably due to the low temperature allotropic transformation of martensite to austenite which caused a volume expansion and limited the tensile forces developed during cooling of the parts in the Maraging steel.

In an Argon (Ar) gas inert atmosphere, the direction of part deformation for the Maraging steel sample was the opposite to the rest of the materials and exhibited curling towards the building platform. The effect of changing the inert gas atmosphere from Argon (Ar) to Nitrogen (N₂) for the Maraging steel samples, was shown to have an effect on the development of forces and changed the direction of the part deformation after release. This effect might be due to the Nitrogen acting as an austenite stabiliser promoting austenite reversion.

The use of in-situ measurements has contributed to providing in-process information which is difficult to obtain from post-process analysis for the L-PBF process. These results will be useful in designing scanning strategies and selecting processing parameters that minimise residual stresses in parts built using L-PBF. These activities are often informed by simulations

performed using computational models, and these results will be valuable for validating the predictions from such simulations and for building higher fidelity models.

List of contributions to knowledge:

- The results obtained from the in-process measurements were found to contribute to the magnitude and distribution of the developed forces and allowed to notice inter layer oscillation in the forces which could be a result of cyclic heat input caused by movement of the laser to and away from the part.
- In process measurements shown that the forces induced in the first five layers represented approximately 80% of the maximum on completion of the build and were distributed such as the part deforming into a catenoid with the corners curling away from the baseplate.
- The magnitudes of the forces measured and their rate of development was dependent on the pattern of scanning used. The use of a rotated 67° scan between layers reduced the levels of force than scanning every layer in the same direction.
- Using single vector scanning (Meander scan strategy) was found to induce forces that were 40% lower than those induced by sectional scan strategies (Chessboard and Stripe scan strategies) for the tested part geometry.
- Doubling the thickness from 30 μm to 60 μm reduced the forces developed per layer possible because fewer layers were required and hence fewer thermal cycles are induced.
- The effect of metal properties, such as the phase transformation, has a strong influence on the development of residual forces. Results shown that for Maraging steel sample much lower development of forces was noticed. This could be due to the low temperature allotropic transformation of martensite to austenite which will cause a volume expansion limiting the tensile forces developed during cooling of the parts reducing the residual forces. In addition, the change in the inert gas from Argon to Nitrogen (which promotes austenite formation) for the Maraging steel samples reduced the value and orientation of the forces measured at the end of the build and of the part deformation on release from the substrate.

Future Work

Regardless of all the research that has already been conducted on residual stresses in the L-PBF process, due to the large number of parameters involved in the process the variation of these processing parameters has been found to have different results dependant on the properties of the materials. Hence, it has been difficult to find a correlation between the processing parameters and the material properties. Therefore, there is still a wide area of investigation on how residual stresses develop in L-PBF components. The technological advances in L-PBF process are in constant development. As the L-PBF process capabilities expand, opportunities for conducting research continue to expand in the use of new different parameters, i.e. higher laser power and multiple laser systems.

The experimental work in this project needs to be extended further in understanding the relationship of the process-material interaction. As it was noticed from the results in this research, the material properties have a strong influence on how the process variables will affect the development of residual stresses in the process. The phase transformation of the metal alloys can contribute to minimize the developed residual stresses. However, further investigation needs to be done in the coefficient expansion of Maraging steel and the changes in the part geometry during the phase transformation. As well as, the mechanical properties from the Maraging steel samples manufactured using Argon and Nitrogen gas need to be analysed, as they could be affected by the changes in the microstructure. Additionally, the findings from the benefit of the phase transformation in the reduction of residual stresses could be extended in the design of new metal alloys for the L-PBF process based on this fundamental approach.

This work needs to be extended into the development of an FE model. As this work has shown, residual stresses in the L-PBF process are built up from a layer by layer basis and are dependent on every single track. Therefore, a model should be developed, from the characteristics of the melt pool to capture the influence of the process parameters such as laser power and exposure time, together with the influence of the material phase transformation. In addition, the scan strategies should be taken into consideration for the development of the FE model as scan strategies have a strong influence on the developments of the residual stresses. However, a model of such complexity will require high costs and time implications for such precise simulations. However, these factors should be considered in the design of the L-PBF parts.

It has been demonstrated that preheating the base plate to 170 °C contributes to the reduction of the stresses developed in the process [45, 166]. The in-situ measurements performed in this work were limited to the load cells' maximum operational load and temperature. Therefore, a proposed FTD described in section 5.2, was designed that will allow the investigation of the residual forces developed during the L-PBF process, which could be extended into the effect of heating the base plate and could allow working with L-PBF machines with higher laser powers and/or multiple laser systems.

7 References

1. *ISO/ASTM 52900(en) Additive manufacturing — General principles — Terminology*. Available from: <https://www.iso.org/obp/ui/#iso:std:iso-astm:52900:dis:ed-2:v1:en>.
2. Bartolo, P.J., *Stereolithography*, in *Stereolithography*. 2011, Springer: New York, USA. ISBN 978-0-387-92904-0
3. Murr, L.E., Gaytan, S.M., Ramirez, D.A., Martinez, E., Hernandez, J., Amato, K.N., Shindo, P.W., Medina, F.R. and Wicker, R.B., 2012. Metal fabrication by additive manufacturing using laser and electron beam melting technologies. *Journal of Materials Science & Technology*, **28**(1), pp.1-14. [https://doi.org/10.1016/S1005-0302\(12\)60016-4](https://doi.org/10.1016/S1005-0302(12)60016-4)
4. Standard, A.S.T.M., 2012. Standard terminology for additive manufacturing technologies. ASTM International F2792-12a. Available from: <https://www.astm.org/Standards/F2792.htm>
5. Gibson, I., Rosen, D.W. and Stucker, B., 2010. Photopolymerization processes. In *Additive Manufacturing Technologies* (pp. 78-119). Springer, Boston, MA. ISBN : 978-1-4419-1119-3
6. Pham, D. and Dimov, S.S., 2012. *Rapid manufacturing: the technologies and applications of rapid prototyping and rapid tooling*. Springer Science & Business Media. ISBN 978-1-4471-0703-3
7. Hull, C.W., 1986. Apparatus for production of three-dimensional objects by stereolithography. US 4575330 A, Google Patents. Available from: <https://patents.google.com/patent/US4575330A/en>.
8. Kurzman, C., Janjić, K., Shokoohi-Tabrizi, H., Edelmayer, M., Pensch, M., Moritz, A. and Agis, H., 2017. Evaluation of resins for stereolithographic 3D-printed surgical guides: the response of L929 cells and human gingival fibroblasts. *BioMed research international*, 2017. DOI: 10.1155/2017/4057612
9. Bremen, S., Meiners, W. and Diatlov, A., 2012. Selective laser melting: A manufacturing technology for the future?. *Laser Technik Journal*, **9**(2), pp.33-38. <https://doi.org/10.1002/latj.201290018>
10. Kruth, J.P., 1991. Material increment manufacturing by rapid prototyping techniques. *CIRP annals*, **40**(2), pp.603-614. [https://doi.org/10.1016/S0007-8506\(07\)61136-6](https://doi.org/10.1016/S0007-8506(07)61136-6)
11. Campbell, I., Bourell, D. and Gibson, I., 2012. Additive manufacturing: rapid prototyping comes of age. *Rapid prototyping journal* **18**(4): p. 255-258. <https://doi.org/10.1108/13552541211231563>
12. Brown, C., Lubell, J. and Lipman, R., 2013. Additive manufacturing technical workshop summary report. US Department of Commerce, National Institute of Standards and Technology. <http://dx.doi.org/10.6028/NIST.TN.1823>
13. Huang, S.H., Liu, P., Mokasdar, A. and Hou, L., 2013. Additive manufacturing and its societal impact: a literature review. *The International Journal of Advanced Manufacturing Technology*, **67**(5), pp.1191-1203. <https://doi.org/10.1007/s00170-012-4558-5>
14. *Metal additive manufacturing sector in 'pivotal' year - report*. Daily coverage of the optics & photonics industry and the markets that it serves 2017 [cited 2019 03/03/2019]; Available from: <https://optics.org/news/8/4/1>.
15. Frazier, W.E., 2014. Metal additive manufacturing: a review. *Journal of Materials Engineering and performance*, **23**(6), pp.1917-1928. <https://doi.org/10.1007/s11665-014-0958-z>

16. Koike, M., Greer, P., Owen, K., Lilly, G., Murr, L.E., Gaytan, S.M., Martinez, E. and Okabe, T., 2011. Evaluation of titanium alloys fabricated using rapid prototyping technologies—electron beam melting and laser beam melting. *Materials*, **4**(10), pp.1776-1792. <https://doi.org/10.3390/ma4101776>
17. King, W.E., Anderson, A.T., Ferencz, R.M., Hodge, N.E., Kamath, C., Khairallah, S.A. and Rubenchik, A.M., 2015. Laser powder bed fusion additive manufacturing of metals; physics, computational, and materials challenges. *Applied Physics Reviews*, **2**(4), p.041304. <https://doi.org/10.1063/1.4937809>
18. Guo, N. and Leu, M.C., 2013. Additive manufacturing: technology, applications and research needs. *Frontiers of Mechanical Engineering*, **8**(3), pp.215-243. DOI 10.1007/s11465-013-0248-8
19. Gomet, T.W.a.T., *History of Additive Manufacturing*, in *Wholers Report 2013*. 2013, Wohlers Associates, INC.
20. Meiners, W., Wissenbach, K. and Gasser, A., Fraunhofer Gesellschaft zur Forderung der Angewandten Forschung eV, 2001. Selective laser sintering at melting temperature. U.S. Patent 6,215,093. Available from : <https://patents.google.com/patent/US6215093/en>
21. Lagutkin, S., Achelis, L., Sheikhaliev, S., Uhlenwinkel, V. and Srivastava, V., 2004. Atomization process for metal powder. *Materials Science and Engineering: A*, **383**(1), pp.1-6.
22. Baskoro, A.S. and Supriadi, S., 2019. Review on plasma atomizer technology for metal powder. In *MATEC Web of Conferences* (Vol. 269, p. 05004). EDP Sciences. DOI: <https://doi.org/10.1051/mateconf/201926905004>
23. Entezarian, M., Allaire, F., Tsantrizos, P. and Drew, R.A.L., 1996. Plasma atomization: A new process for the production of fine, spherical powders. *Jom*, **48**(6), pp.53-55. DOI: <https://doi.org/10.1007/BF03222969>
24. Wang, D., Wu, S., Fu, F., Mai, S., Yang, Y., Liu, Y. and Song, C., 2017. Mechanisms and characteristics of spatter generation in SLM processing and its effect on the properties. *Materials & Design*, **117**, pp.121-130. <https://doi.org/10.1016/j.matdes.2016.12.060>
25. Gupta, N., Weber, C. and Newsome, S., 2012. *Additive manufacturing: status and opportunities*. Science and Technology Policy Institute, Washington. Terry Wohlers, Wohlers Associates, Inc.
26. Herderick, E., *Additive manufacturing of metals: A review*. *Materials science and technology*, 2011. **1413**.
27. Song, B., Zhao, X., Li, S., Han, C., Wei, Q., Wen, S., Liu, J. and Shi, Y., 2015. Differences in microstructure and properties between selective laser melting and traditional manufacturing for fabrication of metal parts: A review. *Frontiers of Mechanical Engineering*, **10**(2), pp.111-125. <https://doi.org/10.1007/s11465-015-0341-2>
28. Saunders, M. *Feature article: DfAM essentials - print parts efficiently and effectively*. 2017. Renishaw Plc, Gloucestershire UK. [cited 2019 04/08/2019]. <https://www.renishaw.com/en/dfam-essentials-print-parts-efficiently-and-effectively--43444>
29. Seifi, M., Salem, A., Beuth, J., Harrysson, O. and Lewandowski, J.J., 2016. Overview of materials qualification needs for metal additive manufacturing. *Jom*, **68**(3), pp.747-764. DOI: 10.1007/s11837-015-1810-0
30. Zäh, M.F. and Lutzmann, S., 2010. Modelling and simulation of electron beam melting. *Production Engineering*, **4**(1), pp.15-23. <https://doi.org/10.1007/s11740-009-0197-6>

31. Larson, R., *Method and device for producing three-dimensional bodies*. 1998, Google Patents. US5786562A. Available from: <https://patents.google.com/patent/US5786562A/en>
32. *GE to acquire additive manufacturing firms SLM Solutions and Arcam AB for \$1.4 billion*. 2016. TCT MAG. Rapid News Publications Ltd [cited 2019 04/07/2019]; Available from: <https://www.tctmagazine.com/3d-printing-news/ge-acquires-slm-solutions-and-arcam/>.
33. Griffiths, L. *Bugatti uses SLM Solutions' metal 3D printing to produce optimised functional components*. 2019; TCT MAG. Rapid News Publications Ltd. Available from: <https://www.tctmagazine.com/3d-printing-news/bugatti-slm-solutions-metal-3d-printing/>.
34. Petch, M. *3D printed jet engine certified for use, GE Concept Laser deal update*. 3D Printing Industry 2016 [cited 2019 7 June 2019]; Available from: <https://3dprintingindustry.com/news/3d-printed-jet-engine-certified-use-ge-concept-laser-deal-update-101792/>.
35. Davies, S. *GE Aviation tests 35% additive manufactured Advanced Turboprop engine*. TCT MAG 2016. Rapid News Publications Ltd. [cited 2019 8/8/2019]; Available from: <https://www.tctmagazine.com/3d-printing-news/ge-aviation-tests-additive-manufactured-turboprop-engine/>.
36. Molitch-Hou, M. *Rolls-Royce to Fly Largest 3D Printed Part Ever Flown*. D Printing Industry 2015. [cited 2019 8/8/2019]; Available from: <https://3dprintingindustry.com/news/rolls-royce-to-fly-largest-3d-printed-part-ever-flown-42795/>.
37. O'Connor, D. *The Ultimate Printing Machine - How BMW is applying 3D printing to commercial vehicles*. 2018. TCT MAG Rapid News Publications Ltd. [cited 2019 06/08/2019]; Available from: <https://www.tctmagazine.com/3d-printing-news/the-ultimate-3d-printing-machine-bmw/>.
38. Davies, S. *3D Systems lands \$15m contract to develop new metal 3D printer for US Army*. TCT MAG 2019 Rapid News Publications Ltd. [cited 2019 08/08/2019]; Available from: <https://www.tctmagazine.com/3d-printing-news/3d-systems-15m-contract-new-metal-3d-printer-us-army/>.
39. Russon, M.-A. *UK government invests £100m into developing 3D printing in aerospace technologies*. 2015 IBTimes Co., Ltd. [cited 2019; Available from: <https://www.ibtimes.co.uk/uk-government-invests-100m-into-developing-3d-printing-aerospace-technologies-1507709>.
40. Christensen, A.M., *Method for design and production of a custom-fit prosthesis*. 2011, Google Patents. Patent Number: US8086336B2. Available from <https://patents.google.com/patent/US8086336B2/en>
41. Lipson, H., *The shape of things to come: frontiers in additive manufacturing*. Frontiers of Engineering, 2011: p. 33-43. Symposium, Cornell University, US.
42. Yap, C.Y., Chua, C.K., Dong, Z.L., Liu, Z.H., Zhang, D.Q., Loh, L.E. and Sing, S.L., 2015. Review of selective laser melting: Materials and applications. Applied physics reviews, **2**(4), p.041101. <https://doi.org/10.1063/1.4935926>
43. Kruth, J.P., Badrossamay, M., Yasa, E., Deckers, J., Thijs, L. and Van Humbeeck, J., 2010. Part and material properties in selective laser melting of metals. In Proceedings of the 16th International Symposium on Electromachining (ISEM XVI) (pp. 3-14). SHANGHAI JIAO TONG UNIV PRESS. ISBN: 978-7-313-05630-6
44. Kurzynowski, T., Gruber, K., Stopyra, W., Kuźnicka, B. and Chlebus, E., 2018. Correlation between process parameters, microstructure and properties of 316 L stainless steel processed by selective laser melting. Materials Science and Engineering: A, **718**, pp.64-73. <https://doi.org/10.1016/j.msea.2018.01.103>

45. Shiomi, M., Osakada, K., Nakamura, K., Yamashita, T. and Abe, F., 2004. Residual stress within metallic model made by selective laser melting process. *CIRP Annals*, **53**(1), pp.195-198. [https://doi.org/10.1016/S0007-8506\(07\)60677-5](https://doi.org/10.1016/S0007-8506(07)60677-5)
46. Mercelis, P. and J.P. Kruth, 2006 . *Residual stresses in selective laser sintering and selective laser melting*. *Rapid Prototyping Journal*. **12**(5): p. 254-265. <https://doi.org/10.1108/13552540610707013>
47. Van Belle, L., Vansteenkiste, G. and Boyer, J.C., 2013. Investigation of residual stresses induced during the selective laser melting process. In *Key Engineering Materials* (Vol. 554, pp. 1828-1834). Trans Tech Publications Ltd. <https://doi.org/10.4028/www.scientific.net/KEM.554-557.1828>
48. Dunbar, A.J., Denlinger, E.R., Heigel, J., Michaleris, P., Guerrier, P., Martukanitz, R. and Simpson, T.W., 2016. Development of experimental method for in situ distortion and temperature measurements during the laser powder bed fusion additive manufacturing process. *Additive Manufacturing*, **12**, pp.25-30. <https://doi.org/10.1016/j.addma.2016.04.007>
49. Robinson, J.H., Ashton, I.R.T., Jones, E., Fox, P. and Sutcliffe, C., 2019. The effect of hatch angle rotation on parts manufactured using selective laser melting. *Rapid Prototyping Journal*. **25**(2): p. 289-298. <https://doi.org/10.1108/RPJ-06-2017-0111>
50. Hopkinson, N., Hague, R.J.M. and Dickens, P.M., 2006. *Rapid manufacturing. An Industrial Revolution for the Digital Age*. Chichester, England: John Wiley and Sons, Ltd. ISBN:9780470016138
51. Wohlers, T. and T. Gornet, *History of additive manufacturing*. 2014, Wohlers Associates, INC. Available from <http://www.wohlersassociates.com/history2014.pdf>
52. Marciniak, A. and Miechowicz, S., 2004. Stereolithography-the choice for medical modelling. *Acta of Bioengineering and Biomechanics*, **6**(1), pp.13-24.
53. Wimpenny, D.I., B. Bryden, and I.R. Pashby, 2003. *Rapid laminated tooling*. *Journal of Materials Processing Technology*. **138**(1-3): p. 214-218. [https://doi.org/10.1016/S0924-0136\(03\)00074-8](https://doi.org/10.1016/S0924-0136(03)00074-8)
54. Haghsefat, K. and L. Tingting, *FDM 3D Printing Technology and Its Fundamental Properties*. 2020. ICIRES - International Conference on Innovation and Research in Engineering. Tblisi Georgia.
55. Singh, R., S. Singh, and M.S.J. Hashmi, *Implant Materials and Their Processing Technologies*, in *Reference Module in Materials Science and Materials Engineering*. 2016, Elsevier. ISBN 978-0-12-803249-7
56. *Rolls-Royce selects quad-laser machine for next stage of AM industrialisation*. 2019 Europa Science Ltd. [cited 2019 20/8/2019]; Available from: <https://www.lasersystemseurope.com/news/rolls-royce-selects-quad-laser-machine-next-stage-am-industrialisation>.
57. Wiesner, A. and Schwarze, D., 2014, September. Multi-laser selective laser melting. In *8th International Conference on Photonic Technologies LANE* (pp. 1-3).
58. Li, F., Wang, Z. and Zeng, X., 2017. Microstructures and mechanical properties of Ti6Al4V alloy fabricated by multi-laser beam selective laser melting. *Materials Letters*, **199**, pp.79-83..
59. Carter, L.N., Martin, C., Withers, P.J. and Attallah, M.M., 2014. The influence of the laser scan strategy on grain structure and cracking behaviour in SLM powder-bed fabricated nickel superalloy. *Journal of Alloys and Compounds*, **615**, pp.338-347. <https://doi.org/10.1016/j.jallcom.2014.06.172>
60. Agarwala, M., Bourell, D., Beaman, J., Marcus, H. and Barlow, J., 1995. Direct selective laser sintering of metals. *Rapid Prototyping Journal*. **1**(1): p. 26-36. <https://doi.org/10.1108/13552549510078113>

61. Kumar, S., *Selective laser sintering: a qualitative and objective approach*. Jom, 2003. **55**(10): p. 43-47. <https://doi.org/10.1007/s11837-003-0175-y>
62. Park, J., M.J. Tari, and H.T. Hahn, 2000. *Characterization of the laminated object manufacturing (LOM) process*. Rapid Prototyping Journal. <https://doi.org/10.1108/13552540010309868>
63. Kruth, J.P., Leu, M.C. and Nakagawa, T., 1998. Progress in additive manufacturing and rapid prototyping. *Cirp Annals*, **47**(2), pp.525-540. [https://doi.org/10.1016/S0007-8506\(07\)63240-5](https://doi.org/10.1016/S0007-8506(07)63240-5)
64. Tromans, G., *Additive Manufacturing: opportunities and constraints*. November 2013 . Royal Academy of Engineering, London UK. Available from <https://www.raeng.org.uk/publications/reports/additive-manufacturing>
65. Bourell, D.L., Rosen, D.W. and Leu, M.C., 2014. The roadmap for additive manufacturing and its impact. *3D Printing and Additive Manufacturing*, **1**(1), pp.6-9. <https://doi.org/10.1089/3dp.2013.0002>
66. Carter, W.T. and Jones, M.G., 1993. Direct laser sintering of metals. In 1993 International Solid Freeform Fabrication Symposium. The University of Texas, Austin. <http://hdl.handle.net/2152/65036>
67. Tolosa, I., Garciandía, F., Zubiri, F., Zapirain, F. and Esnaola, A., 2010. Study of mechanical properties of AISI 316 stainless steel processed by “selective laser melting”, following different manufacturing strategies. *The International Journal of Advanced Manufacturing Technology*, **51**(5), pp.639-647. <https://doi.org/10.1007/s00170-010-2631-5>
68. H Becker, T.H. and Dimitrov, D., 2016. The achievable mechanical properties of SLM produced Maraging Steel 300 components. *Rapid Prototyping Journal*. **22**(3): p. 487-494. <https://doi.org/10.1108/RPJ-08-2014-0096>
69. Casalino, G., Campanelli, S.L., Contuzzi, N. and Ludovico, A.D., 2015. Experimental investigation and statistical optimisation of the selective laser melting process of a maraging steel. *Optics & Laser Technology*, **65**, pp.151-158. <https://doi.org/10.1016/j.optlastec.2014.07.021>
70. Bai, Y., Yang, Y., Wang, D. and Zhang, M., 2017. Influence mechanism of parameters process and mechanical properties evolution mechanism of maraging steel 300 by selective laser melting. *Materials Science and Engineering: A*, **703**, pp.116-123. <https://doi.org/10.1016/j.msea.2017.06.033>
71. Murr, L.E., Martinez, E., Hernandez, J., Collins, S., Amato, K.N., Gaytan, S.M. and Shindo, P.W., 2012. Microstructures and properties of 17-4 PH stainless steel fabricated by selective laser melting. *Journal of Materials Research and Technology*, **1**(3), pp.167-177. [https://doi.org/10.1016/S2238-7854\(12\)70029-7](https://doi.org/10.1016/S2238-7854(12)70029-7)
72. Averyanova, M., Cicala, E., Bertrand, P. and Grevey, D., 2012. Experimental design approach to optimize selective laser melting of martensitic 17 - 4 PH powder: part I – single laser tracks and first layer. *Rapid Prototyping Journal*. **18**(1): p. 28-37. <https://doi.org/10.1108/13552541211193476>
73. Garcia, M.A., Garcia-Pando, C. and Marto, C., 2011. Conformal cooling in moulds with special geometry. *Innovative developments in virtual and physical prototyping*, pp.409-412. ISBN 978-0-415-68418-7
74. Wong, M., Tsopanos, S., Sutcliffe, C.J. and Owen, I., 2007. Selective laser melting of heat transfer devices. *Rapid Prototyping Journal*. **13**(5): p. 291-297. <https://doi.org/10.1108/13552540710824797>
75. Kruth, J.P., Vandenbroucke, B., Van Vaerenbergh, J. and Naert, I., 2005, September. Digital manufacturing of biocompatible metal frameworks for complex dental prostheses by means of SLS/SLM. In *Proc. of 2nd Int. Conf. on Advanced Research in Virtual and Rapid Prototyping*, Leiria (pp. 139-145).

76. Li, R., Liu, J., Shi, Y., Du, M. and Xie, Z., 2010. 316L stainless steel with gradient porosity fabricated by selective laser melting. *Journal of Materials Engineering and Performance*, **19**(5), pp.666-671. <https://doi.org/10.1007/s11665-009-9535-2>
77. Gu, D., Hagedorn, Y.C., Meiners, W., Meng, G., Batista, R.J.S., Wissenbach, K. and Poprawe, R., 2012. Densification behavior, microstructure evolution, and wear performance of selective laser melting processed commercially pure titanium. *Acta Materialia*, **60**(9), pp.3849-3860. <https://doi.org/10.1016/j.actamat.2012.04.006>
78. Vandenbroucke, B. and Kruth, J.P., 2007. Selective laser melting of biocompatible metals for rapid manufacturing of medical parts. *Rapid Prototyping Journal*. **13**(4): p. 196-203. <https://doi.org/10.1108/13552540710776142>
79. Zhang, L.C. and Attar, H., 2016. Selective laser melting of titanium alloys and titanium matrix composites for biomedical applications: a review. *Advanced engineering materials*, **18**(4), pp.463-475. <https://doi.org/10.1002/adem.201500419>
80. Stamp, R., Fox, P., O'neill, W., Jones, E. and Sutcliffe, C., 2009. The development of a scanning strategy for the manufacture of porous biomaterials by selective laser melting. *Journal of Materials Science: Materials in Medicine*, **20**(9), p.1839. DOI 10.1007/s10856-009-3763-8
81. Lin, C.Y., Wirtz, T., LaMarca, F. and Hollister, S.J., 2007. Structural and mechanical evaluations of a topology optimized titanium interbody fusion cage fabricated by selective laser melting process. *Journal of Biomedical Materials Research Part A: An Official Journal of The Society for Biomaterials, The Japanese Society for Biomaterials, and The Australian Society for Biomaterials and the Korean Society for Biomaterials*, **83**(2), pp.272-279. <https://doi.org/10.1002/jbm.a.31231>
82. Mullen, L., Stamp, R.C., Brooks, W.K., Jones, E. and Sutcliffe, C.J., 2009. Selective Laser Melting: A regular unit cell approach for the manufacture of porous, titanium, bone in - growth constructs, suitable for orthopedic applications. *Journal of Biomedical Materials Research Part B: Applied Biomaterials: An Official Journal of The Society for Biomaterials, The Japanese Society for Biomaterials, and The Australian Society for Biomaterials and the Korean Society for Biomaterials*, **89**(2), pp.325-334. <https://doi.org/10.1002/jbm.b.31219>
83. Murr, L.E., Quinones, S.A., Gaytan, S.M., Lopez, M.I., Rodela, A., Martinez, E.Y., Hernandez, D.H., Martinez, E., Medina, F. and Wicker, R.B., 2009. Microstructure and mechanical behavior of Ti-6Al-4V produced by rapid-layer manufacturing, for biomedical applications. *Journal of the mechanical behavior of biomedical materials*, **2**(1), pp.20-32. <https://doi.org/10.1016/j.jmbbm.2008.05.004>
84. Habijan, T., Haberland, C., Meier, H., Frenzel, J., Wittsiepe, J., Wuwer, C., Greulich, C., Schildhauer, T.A. and Köller, M., 2013. The biocompatibility of dense and porous nickel-titanium produced by selective laser melting. *Materials Science and Engineering: C*, **33**(1), pp.419-426. <https://doi.org/10.1016/j.msec.2012.09.008>
85. Amato, K.N., Gaytan, S.M., Murr, L.E., Martinez, E., Shindo, P.W., Hernandez, J., Collins, S. and Medina, F., 2012. Microstructures and mechanical behavior of Inconel 718 fabricated by selective laser melting. *Acta Materialia*, **60**(5), pp.2229-2239. <https://doi.org/10.1016/j.actamat.2011.12.032>
86. Soller, S., Barata, A., Beyer, S., Dahlhaus, A., Guichard, D., Humbert, E., Kretschmer, J. and Zeiss, W., 2016. Selective laser melting (SLM) of Inconel 718 and stainless steel injectors for liquid rocket engines. *Space Propulsion 2016 Proceedings*.
87. Noyan, I.C. and J.B. Cohen, *Residual stress: measurement by diffraction and interpretation*. 2013: Springer. ISBN 978-1-4613-9571-3
88. Withers, P.J. and H.K.D.H. Bhadeshia, *Residual stress. Part 2 – Nature and origins*. *Materials Science and Technology*, 2001. **17**(4): p. 366-375. <https://doi.org/10.1179/026708301101510087>

89. Withers, P.J., 2007. Residual stress and its role in failure. Reports on progress in physics, **70**(12), p.2211. <https://doi.org/10.1088/0034-4885/70/12/R04>
90. Bartlett, J.L. and Li, X., 2019. An overview of residual stresses in metal powder bed fusion. Additive Manufacturing, **27**, pp.131-149. <https://doi.org/10.1016/j.addma.2019.02.020>
91. Mercelis, P. and Kruth, J.P., 2006. Residual stresses in selective laser sintering and selective laser melting. Rapid prototyping journal. <https://doi.org/10.1108/13552540610707013>
92. Kandil, F.A., Lord, J D, Fry, A T, Grant, P V, *A review of residual stress measurement methods - a guide to technique selection*, N.M. Centre, Editor. 2001, National Physical Laboratory: NPL Report MATC(A)04. <http://eprintspublications.npl.co.uk/id/eprint/1873>
93. Leuders, S., Thöne, M., Riemer, A., Niendorf, T., Tröster, T., Richard, H.A. and Maier, H.J., 2013. On the mechanical behaviour of titanium alloy TiAl6V4 manufactured by selective laser melting: Fatigue resistance and crack growth performance. International Journal of Fatigue, **48**, pp.300-307. <https://doi.org/10.1016/j.ijfatigue.2012.11.011>
94. Mercelis, P. and Kruth, J.P., 2006. Residual stresses in selective laser sintering and selective laser melting. Rapid prototyping journal. <https://doi.org/10.1108/13552540610707013>
95. Zaeh, M.F. and Branner, G., 2010. Investigations on residual stresses and deformations in selective laser melting. Production Engineering, **4**(1), pp.35-45. DOI: 10.1007/s11740-009-0192-y
96. Thijs, L., Sistiaga, M.L.M., Wauthle, R., Xie, Q., Kruth, J.P. and Van Humbeeck, J., 2013. Strong morphological and crystallographic texture and resulting yield strength anisotropy in selective laser melted tantalum. Acta Materialia, **61**(12), pp.4657-4668. <https://doi.org/10.1016/j.actamat.2013.04.036>
97. Liu, Y., Yang, Y. and Wang, D., 2016. A study on the residual stress during selective laser melting (SLM) of metallic powder. The International Journal of Advanced Manufacturing Technology, **87**(1), pp.647-656. <https://doi.org/10.1007/s00170-016-8466-y>
98. Vrancken, B., PhD Thesis: *Study of residual stresses in selective laser melting*, in *Faculty of Engineering Science*. 2016, ARENBERG DOCTORAL SCHOOL: KU Leuven.
99. Anderson, L.S., Venter, A.M., Vrancken, B., Marais, D., Van Humbeeck, J. and Becker, T.H., 2018, April. Investigating the residual stress distribution in selective laser melting produced Ti-6Al-4V using neutron diffraction. In Mater. Res. Proc (Vol. **4**, pp. 73-78). DOI 10.21741/9781945291678-11
100. Gusarov, A.V., Pavlov, M. and Smurov, I., 2011. Residual stresses at laser surface remelting and additive manufacturing. Physics Procedia, **12**, pp.248-254. <https://doi.org/10.1016/j.phpro.2011.03.032>
101. Moat, R.J., Pinkerton, A.J., Li, L., Withers, P.J. and Preuss, M., 2011. Residual stresses in laser direct metal deposited Waspaloy. Materials Science and Engineering: A, **528**(6), pp.2288-2298. <https://doi.org/10.1016/j.msea.2010.12.010>
102. Rangaswamy, P., Griffith, M.L., Prime, M.B., Holden, T.M., Rogge, R.B., Edwards, J.M. and Sebring, R.J., 2005. Residual stresses in LENS® components using neutron diffraction and contour method. Materials Science and Engineering: A, **399**(1-2), pp.72-83. <https://doi.org/10.1016/j.msea.2005.02.019>
103. Vrancken, B., Cain, V., Knutsen, R. and Van Humbeeck, J., 2014. Residual stress via the contour method in compact tension specimens produced via selective laser melting. Scripta Materialia, **87**, pp.29-32. <https://doi.org/10.1016/j.scriptamat.2014.05.016>

104. Denlinger, E.R., Gouge, M., Irwin, J. and Michaleris, P., 2017. Thermomechanical model development and in situ experimental validation of the Laser Powder-Bed Fusion process. *Additive Manufacturing*, **16**, pp.73-80.
<https://doi.org/10.1016/j.addma.2017.05.001>
105. Withers, P.J. and Bhadeshia, H.K.D.H., 2001. Residual stress. Part 1—measurement techniques. *Materials science and Technology*, **17**(4), pp.355-365.
<https://doi.org/10.1179/026708301101509980>
106. ASTM 837-13, A.E., *Standard method for determining residual stresses by the hole-drilling strain gage method*. 1981., Annual Book of ASTM Standards. Available from: <https://sint-technology.com/astm-e837/>
107. Knowles, C.R., Becker, T.H. and Tait, R.B., 2012. Residual stress measurements and structural integrity implications for selective laser melted Ti-6Al-4V. *South African Journal of Industrial Engineering*, **23**(3), pp.119-129. ISSN 2224-7890
108. Salmi, A., Atzeni, E., Iuliano, L. and Galati, M., 2017. Experimental analysis of residual stresses on AlSi10Mg parts produced by means of Selective Laser Melting (SLM). *Procedia CIRP*, **62**, pp.458-463. <https://doi.org/10.1016/j.procir.2016.06.030>
109. Casavola, C., Campanelli, S.L. and Pappalettere, C., 2008, June. Experimental analysis of residual stresses in the selective laser melting process. In *Proceedings of the XIth International Congress and Exposition, Orlando, Florida, USA*.
110. Stoney, G.G., 1909. The tension of metallic films deposited by electrolysis. *Proceedings of the Royal Society of London. Series A, Containing Papers of a Mathematical and Physical Character*, **82**(553), pp.172-175.
<https://doi.org/10.1098/rspa.1909.0021>
111. Kruth, J.P., Deckers, J., Yasa, E. and Wauthlé, R., 2012. Assessing and comparing influencing factors of residual stresses in selective laser melting using a novel analysis method. *Proceedings of the institution of mechanical engineers, Part B: Journal of Engineering Manufacture*, **226**(6), pp.980-991.
<https://doi.org/10.1177/0954405412437085>
112. Mishurova, T., Cabeza, S., Artzt, K., Haubrich, J., Klaus, M., Genzel, C., Requena, G. and Bruno, G., 2017. An assessment of subsurface residual stress analysis in SLM Ti-6Al-4V. *Materials*, **10**(4), p.348. <https://doi.org/10.3390/ma10040348>
113. Bagg, S.D., Sochalski-Kolbus, L.M. and Bunn, J.R., 2016. The effect of laser scan strategy on distortion and residual stresses of arches made with selective laser melting. *NASA Technical Reports M16-5377*. DOI 20160009706.pdf
114. Reid, R.G., PhD Thesis: *The Measurement of Longitudinal Residual Stresses in Unidirectional Glass Fibre Reinforced Plastic*. 2009, University of the Witwatersrand.
115. Balasingh, C. and Singh, A.K., 2000. Residual Stresses and Their Measurements by X-ray Diffraction Methods. *Metals materials and Processes*, **12**(2/3), pp.269-280.
116. V Vrancken, B., Wauthlé, R., Kruth, J.P. and Van Humbeeck, J., 2013. Study of the influence of material properties on residual stress in selective laser melting. In *Proceedings of the solid freeform fabrication symposium* (pp. 393-407).
117. Hutchings, M.T., Withers, P.J., Holden, T.M., and Lorentzen T. 2005. *Introduction to the characterization of residual stress by neutron diffraction*. Taylor and Francis CRC press. Florida, USA. ISBN 10:0-415-31000-8
118. Sochalski-Kolbus, L.M., Payzant, E.A., Cornwell, P.A., Watkins, T.R., Babu, S.S., Dehoff, R.R., Lorenz, M., Ovchinnikova, O. and Duty, C., 2015. Comparison of residual stresses in Inconel 718 simple parts made by electron beam melting and direct laser metal sintering. *Metallurgical and Materials Transactions A*, **46**(3), pp.1419-1432.
<https://doi.org/10.1007/s11661-014-2722-2>

119. Robinson, J., PhD Thesis: *Optimisation of Selective Laser Melting Process for the Production of Hybrid Orthopaedic Devices*. 2014, University of Liverpool: Liverpool UK.
120. Denlinger, E.R., Heigel, J.C., Michaleris, P. and Palmer, T.A., 2015. Effect of inter-layer dwell time on distortion and residual stress in additive manufacturing of titanium and nickel alloys. *Journal of Materials Processing Technology*, 215, pp.123-131. <https://doi.org/10.1016/j.jmatprotec.2014.07.030>
121. Yakout, M., Elbestawi, M.A., Veldhuis, S.C. and Nangle-Smith, S., 2020. Influence of thermal properties on residual stresses in SLM of aerospace alloys. *Rapid Prototyping Journal*. <https://doi.org/10.1108/RPJ-03-2019-0065>
122. Doubenskaia, M.A., Zhirnov, I.V., Teleshevskiy, V.I., Bertrand, P. and Smurov, I.Y., 2015. Determination of true temperature in selective laser melting of metal powder using infrared camera. In *Materials science forum* (Vol. 834, pp. 93-102). Trans Tech Publications Ltd. <https://doi.org/10.4028/www.scientific.net/MSF.834.93>
123. Rodriguez, E., Mireles, J., Terrazas, C.A., Espalin, D., Perez, M.A. and Wicker, R.B., 2015. Approximation of absolute surface temperature measurements of powder bed fusion additive manufacturing technology using in situ infrared thermography. *Additive Manufacturing*, 5, pp.31-39. <https://doi.org/10.1016/j.addma.2014.12.001>
124. Roberts, I.A., Wang, C.J., Esterlein, R., Stanford, M. and Mynors, D.J., 2009. A three-dimensional finite element analysis of the temperature field during laser melting of metal powders in additive layer manufacturing. *International Journal of Machine Tools and Manufacture*, 49(12-13), pp.916-923. <https://doi.org/10.1016/j.ijmachtools.2009.07.004>
125. Childs, T.H.C. and Hauser, C., 2005. Raster scan selective laser melting of the surface layer of a tool steel powder bed. *Proceedings of the Institution of Mechanical Engineers, Part B: Journal of Engineering Manufacture*, 219(4), pp.379-384. <https://doi.org/10.1243/095440505X32201>
126. Childs, T.H.C., Hauser, C. and Badrossamay, M., 2005. Selective laser sintering (melting) of stainless and tool steel powders: experiments and modelling. *Proceedings of the Institution of Mechanical Engineers, Part B: Journal of Engineering Manufacture*, 219(4), pp.339-357. <https://doi.org/10.1243/095440505X8109>
127. Song, B., Dong, S., Liao, H. and Coddet, C., 2012. Process parameter selection for selective laser melting of Ti6Al4V based on temperature distribution simulation and experimental sintering. *The International Journal of Advanced Manufacturing Technology*, 61(9), pp.967-974. <https://doi.org/10.1007/s00170-011-3776-6>
128. Zhang, D.Q., Cai, Q.Z., Liu, J.H., Zhang, L. and Li, R.D., 2010. Select laser melting of W–Ni–Fe powders: simulation and experimental study. *The International Journal of Advanced Manufacturing Technology*, 51(5-8), pp.649-658. DOI 10.1007/s00170-010-2641-3
129. Gusarov, A.V., Yadroitsev, I., Bertrand, P. and Smurov, I., 2007. Heat transfer modelling and stability analysis of selective laser melting. *Applied Surface Science*, 254(4), pp.975-979. <https://doi.org/10.1016/j.apsusc.2007.08.074>
130. Konrad, C., Zhang, Y. and Xiao, B., 2005. Analysis of melting and resolidification in a two-component metal powder bed subjected to temporal Gaussian heat flux. *International Journal of Heat and Mass Transfer*, 48(19-20), pp.3932-3944. <https://doi.org/10.1016/j.ijheatmasstransfer.2005.04.010>
131. Zeng, K., Pal, D. and Stucker, B., 2012, August. A review of thermal analysis methods in laser sintering and selective laser melting. In *Proceedings of Solid Freeform Fabrication Symposium Austin, TX* (Vol. 60, pp. 796-814).

132. Labudovic, M., Hu, D. and Kovacevic, R., 2003. A three dimensional model for direct laser metal powder deposition and rapid prototyping. *Journal of materials science*, **38**(1), pp.35-49. <https://doi.org/10.1023/A:1021153513925>
133. Li, C., Wang, Y., Zhan, H., Han, T., Han, B. and Zhao, W., 2010. Three-dimensional finite element analysis of temperatures and stresses in wide-band laser surface melting processing. *Materials & Design*, **31**(7), pp.3366-3373. <https://doi.org/10.1016/j.matdes.2010.01.054>
134. Dai, K., Li, X.X. and Shaw, L.L., 2004. Comparisons between thermal modeling and experiments: effects of substrate preheating. *Rapid Prototyping Journal*. <https://doi.org/10.1108/13552540410512507>
135. Dai, K. and Shaw, L., 2005. Finite element analysis of the effect of volume shrinkage during laser densification. *Acta materialia*, **53**(18), pp.4743-4754. <https://doi.org/10.1016/j.actamat.2005.06.014>
136. Jiang, W. and Dalgarno, K.W., 2002. Finite element analysis of residual stresses and deformations in direct metal SLS process. In 2002 International Solid Freeform Fabrication Symposium. <http://dx.doi.org/10.26153/tsw/4492>
137. Matsumoto, M., Shiomi, M., Osakada, K. and Abe, F., 2002. Finite element analysis of single layer forming on metallic powder bed in rapid prototyping by selective laser processing. *International Journal of Machine Tools and Manufacture*, **42**(1), pp.61-67. [https://doi.org/10.1016/S0890-6955\(01\)00093-1](https://doi.org/10.1016/S0890-6955(01)00093-1)
138. Ma, L. and Bin, H., 2007. Temperature and stress analysis and simulation in fractal scanning-based laser sintering. *The International Journal of Advanced Manufacturing Technology*, **34**(9-10), pp.898-903. DOI 10.1007/s00170-006-0665-5
139. Dai, K. and Shaw, L., 2002. Distortion minimization of laser - processed components through control of laser scanning patterns. *Rapid Prototyping Journal*. **8**(5): p. 270-276. <https://doi.org/10.1108/13552540210451732>
140. Shiomi, M., Yoshidome, A., Abe, F. and Osakada, K., 1999. Finite element analysis of melting and solidifying processes in laser rapid prototyping of metallic powders. *International Journal of Machine Tools and Manufacture*, **39**(2), pp.237-252. [https://doi.org/10.1016/S0890-6955\(98\)00036-4](https://doi.org/10.1016/S0890-6955(98)00036-4)
141. Luo, Z. and Zhao, Y., 2018. A survey of finite element analysis of temperature and thermal stress fields in powder bed fusion additive manufacturing. *Additive Manufacturing*, **21**, pp.318-332. <https://doi.org/10.1016/j.addma.2018.03.022>
142. Parry, L., Ashcroft, I.A. and Wildman, R.D., 2016. Understanding the effect of laser scan strategy on residual stress in selective laser melting through thermo-mechanical simulation. *Additive Manufacturing*, **12**, pp.1-15. <https://doi.org/10.1016/j.addma.2016.05.014>
143. Cheng, B., Shrestha, S. and Chou, K., 2016. Stress and deformation evaluations of scanning strategy effect in selective laser melting. *Additive Manufacturing*, **12**, pp.240-251. <https://doi.org/10.1016/j.addma.2016.05.007>
144. Ali, H., Ghadbeigi, H. and Mumtaz, K., 2018. Effect of scanning strategies on residual stress and mechanical properties of Selective Laser Melted Ti6Al4V. *Materials Science and Engineering: A*, **712**, pp.175-187. <https://doi.org/10.1016/j.msea.2017.11.103>
145. Xiao, B. and Zhang, Y., 2007. Laser sintering of metal powders on top of sintered layers under multiple-line laser scanning. *Journal of Physics D: Applied Physics*, **40**(21), p.6725. <https://doi.org/10.1088/0022-3727/40/21/036>
146. Poirier D.R., Geiger G.H. (2016) *Conduction of Heat in Solids*. In: *Transport Phenomena in Materials Processing*. Springer, Cham. https://doi.org/10.1007/978-3-319-48090-9_9. ISBN978-3-319-48090-9

147. Prabhakar, P., Sames, W.J., Dehoff, R. and Babu, S.S., 2015. Computational modeling of residual stress formation during the electron beam melting process for Inconel 718. *Additive Manufacturing*, **7**, pp.83-91.
<https://doi.org/10.1016/j.addma.2015.03.003>
148. Fu, C. and Guo, Y., 2014, August. 3-dimensional finite element modeling of selective laser melting Ti-6Al-4V alloy. In 25th Annual International Solid Freeform Fabrication Symposium (pp. 1129-1144).
149. Zhirnov, I.V., Podrabinnik, P.A., Tokbergenov, M., Okunkova, A.A. and Smurov, I.Y., 2015. Optical monitoring and diagnostics of SLM processing for single track formation from Co-Cr alloy. In *Materials Science Forum* (Vol. 834, pp. 51-60). Trans Tech Publications Ltd. <https://doi.org/10.4028/www.scientific.net/MSF.834.51>
150. Gong, H., Rafi, K., Karthik, N., Starr, T. and Stucker, B., 2013, August. Defect morphology in Ti-6Al-4V parts fabricated by selective laser melting and electron beam melting. In 24rd Annual International Solid Freeform Fabrication Symposium—An Additive Manufacturing Conference, Austin, TX, Aug (pp. 12-14).
151. King, W.E., Barth, H.D., Castillo, V.M., Gallegos, G.F., Gibbs, J.W., Hahn, D.E., Kamath, C. and Rubenchik, A.M., 2014. Observation of keyhole-mode laser melting in laser powder-bed fusion additive manufacturing. *Journal of Materials Processing Technology*, **214**(12), pp.2915-2925.
<https://doi.org/10.1016/j.jmatprotec.2014.06.005>
152. Darvish, K., Chen, Z.W. and Pasang, T., 2016. Reducing lack of fusion during selective laser melting of CoCrMo alloy: Effect of laser power on geometrical features of tracks. *Materials & Design*, **112**, pp.357-366.
<https://doi.org/10.1016/j.matdes.2016.09.086>
153. Thijs, L., Verhaeghe, F., Craeghs, T., Van Humbeeck, J. and Kruth, J.P., 2010. A study of the microstructural evolution during selective laser melting of Ti-6Al-4V. *Acta materialia*, **58**(9), pp.3303-3312. <https://doi.org/10.1016/j.actamat.2010.02.004>
154. Simson, T., Emmel, A., Dwars, A. and Böhm, J., 2017. Residual stress measurements on AISI 316L samples manufactured by selective laser melting. *Additive Manufacturing*, **17**, pp.183-189. <https://doi.org/10.1016/j.addma.2017.07.007>
155. Yadroitsev, I., Yadroitsava, I., Bertrand, P. and Smurov, I., 2012. Factor analysis of selective laser melting process parameters and geometrical characteristics of synthesized single tracks. *Rapid Prototyping Journal*.
<https://doi.org/10.1108/13552541211218117>
156. Li, R., Liu, J., Shi, Y., Wang, L. and Jiang, W., 2012. Balling behavior of stainless steel and nickel powder during selective laser melting process. *The International Journal of Advanced Manufacturing Technology*, **59**(9), pp.1025-1035.
<https://doi.org/10.1007/s00170-011-3566-1>
157. Manvatkar, V., De, A. and DebRoy, T., 2015. Spatial variation of melt pool geometry, peak temperature and solidification parameters during laser assisted additive manufacturing process. *Materials Science and Technology*, **31**(8), pp.924-930.
<https://doi.org/10.1179/1743284714Y.0000000701>
158. Wu, A.S., Brown, D.W., Kumar, M., Gallegos, G.F. and King, W.E., 2014. An experimental investigation into additive manufacturing-induced residual stresses in 316L stainless steel. *Metallurgical and Materials Transactions A*, **45**(13), pp.6260-6270. <https://doi.org/10.1007/s11661-014-2549-x>
159. Vasinonta, A., J.L. Beuth, and M. Griffith, *Process maps for predicting residual stress and melt pool size in the laser-based fabrication of thin-walled structures*. *Journal of Manufacturing Science and Engineering*, 2007. **129**(1): p. 101-109.
<https://doi.org/10.1115/1.2335852>

160. Brückner, F., D. Lepski, and E. Beyer, *Modeling the influence of process parameters and additional heat sources on residual stresses in laser cladding*. Journal of thermal spray technology, 2007. **16**(3): p. 355-373. DOI: 10.1007/s11666-007-9026-7
161. Heeling, T., M. Cloots, and K. Wegener, *Melt pool simulation for the evaluation of process parameters in selective laser melting*. Additive Manufacturing, 2017. **14**: p. 116-125. <https://doi.org/10.1016/j.addma.2017.02.003>
162. Gong, H., Gu, H., Zeng, K., Dilip, J.J.S., Pal, D., Stucker, B., Christiansen, D., Beuth, J. and Lewandowski, J.J., 2014, August. Melt pool characterization for selective laser melting of Ti-6Al-4V pre-alloyed powder. In Solid freeform fabrication symposium (pp. 256-267).
163. Casavola, C., Campanelli, S.L. and Pappalettere, C., 2008, June. Experimental analysis of residual stresses in the selective laser melting process. In Proceedings of the XIth International Congress and Exposition, Orlando, Florida, USA.
164. Vasinonta, A., Beuth, J.L. and Griffith, M.L., 2001. A process map for consistent build conditions in the solid freeform fabrication of thin-walled structures. J. Manuf. Sci. Eng., **123**(4), pp.615-622. <https://doi.org/10.1115/1.1370497>
165. Jhabvala, J., Boillat, E., Antignac, T. and Glardon, R., 2010. On the effect of scanning strategies in the selective laser melting process. Virtual and physical prototyping, **5**(2), pp.99-109. <https://doi.org/10.1080/17452751003688368>
166. Kruth, J.P., Deckers, J., Yasa, E. and Wauthlé, R., 2012. Assessing and comparing influencing factors of residual stresses in selective laser melting using a novel analysis method. Proceedings of the institution of mechanical engineers, Part B: Journal of Engineering Manufacture, **226**(6), pp.980-991. <https://doi.org/10.1177/0954405412437085>
167. Evren Yasa, J.D., Jean-Pierre Kruth, Marleen Rombouts and Jan Luyten, *Investigation of Sectoral Scanning in Selective Laser Melting*, in *ASME 2010 10th Biennial Conference on Engineering Systems Design and Analysis*. 2010. <https://doi.org/10.1115/ESDA2010-24621>
168. Bo, Q., Yu-sheng, S., Qing-song, W. and Hai-bo, W., 2012. The helix scan strategy applied to the selective laser melting. The International Journal of Advanced Manufacturing Technology, **63**(5), pp.631-640. <https://doi.org/10.1007/s00170-012-3922-9>
169. Quick start guide: QuantAM Material Editor 2019 V5.1 , *Renishaw QuantAM Material Editor*. Renishaw Plc. 2019. UK Available from: <https://resources.renishaw.com/en/details/quick-start-guide-quantam-material-editor-2019-v51--109734>
170. Jacobs, P.F., 1992. Rapid prototyping & manufacturing: fundamentals of stereolithography. Society of Manufacturing Engineers. ISBN 0872634256, 9780872634251
171. *ELECTRICAL DISCHARGE MACHINING (EDM)*. Header Die and Tool Inc. 2020; Available from: <https://www.header.com/capabilities/edm>.
172. Mishurova, T., Cabeza, S., Thiede, T., Nadammal, N., Kromm, A., Klaus, M., Genzel, C., Haberland, C. and Bruno, G., 2018. The influence of the support structure on residual stress and distortion in SLM Inconel 718 parts. Metallurgical and Materials Transactions A, **49**(7), pp.3038-3046. <https://doi.org/10.1007/s11661-018-4653-9>
173. Yadroitsev, I. and Yadroitsava, I., 2015. Evaluation of residual stress in stainless steel 316L and Ti6Al4V samples produced by selective laser melting. Virtual and Physical Prototyping, **10**(2), pp.67-76. <https://doi.org/10.1080/17452759.2015.1026045>
174. Parry, L., Ashcroft, I.A. and Wildman, R.D., 2016. Understanding the effect of laser scan strategy on residual stress in selective laser melting through thermo-mechanical simulation. Additive Manufacturing, **12**, pp.1-15.

- <https://doi.org/10.1016/j.addma.2016.05.014>
175. Gong, Haijun, Chong Teng, Kai Zeng, Deepankar Pal, Brent Stucker, J. J.S. Dilip, Jack Beuth, John J. Lewandowski. 2016. "Single Track of Selective Laser Melting Ti-6Al-4V Powder on Support Structure." Proceedings of the International Solid Freeform Fabrication Symposium – An Additive Manufacturing Conference: 1621-1633. <http://sffsymposium.engr.utexas.edu/sites/default/files/2016/131-Gong.pdf>
 176. Yadroitsev, I., Yadroitsava, I., Bertrand, P. and Smurov, I., 2012. Factor analysis of selective laser melting process parameters and geometrical characteristics of synthesized single tracks. Rapid Prototyping Journal. <https://doi.org/10.1108/13552541211218117>
 177. Anderson, L.S., Venter, A.M., Vrancken, B., Marais, D., Van Humbeeck, J. and Becker, T.H., 2018, April. Investigating the residual stress distribution in selective laser melting produced Ti-6Al-4V using neutron diffraction. In Mater. Res. Proc (Vol. 4, pp. 73-78). DOI 10.21741/9781945291678-11
 178. Dotcheva, M., Thomas, D. and Millward, H., 2009. An evaluation of rapid manufactured cellular structures to enhance injection moulding tool performance. International Journal of Materials Engineering and Technology, **1**(2), pp.105-127.
 179. Li, C., Liu, Z.Y., Fang, X.Y. and Guo, Y.B., 2018. On the simulation scalability of predicting residual stress and distortion in selective laser melting. Journal of Manufacturing Science and Engineering, **140**(4). <https://doi.org/10.1115/1.4038893>
 180. van Zyl, I., Yadroitsava, I. and Yadroitsev, I., 2016. Residual stress in Ti6Al4V objects produced by direct metal laser sintering. South African Journal of Industrial Engineering, **27**(4), pp.134-141. <http://dx.doi.org/10.7166/27-4-1468>
 181. Alimardani, M., Toyserkani, E., Huissoon, J.P. and Paul, C.P., 2009. On the delamination and crack formation in a thin wall fabricated using laser solid freeform fabrication process: an experimental–numerical investigation. Optics and lasers in engineering, **47**(11), pp.1160-1168. <https://doi.org/10.1016/j.optlaseng.2009.06.010>
 182. Saunders, M. *Are your borders secure?* 2019 Group Strategic Development, Renishaw Plc. [cited 2019 09/09/2019]; Available from: <https://www.linkedin.com/pulse/your-borders-secure-marc-saunders/>.
 183. Li, C., Fu, C.H., Guo, Y.B. and Fang, F.Z., 2015. Fast prediction and validation of part distortion in selective laser melting. Procedia Manufacturing, **1**, pp.355-365. <https://doi.org/10.1016/j.promfg.2015.09.042>
 184. Kranzlein, H.H., 1964. Anisotropic dilatation during annealing of 18 percent nickel maraging steel. NASA Technical Memorandum (TM) TM-X-53184. NASA Marshall Space Flight Center Huntsville, AL, United States. 19650007939.pdf
 185. Xiao, Z., Chen, C., Zhu, H., Hu, Z., Nagarajan, B., Guo, L. and Zeng, X., 2020. Study of residual stress in selective laser melting of Ti6Al4V. Materials & Design, **193**, p.108846. <https://doi.org/10.1016/j.matdes.2020.108846>
 186. Gong, H., Gu, H., Zeng, K., Dilip, J.J.S., Pal, D., Stucker, B., Christiansen, D., Beuth, J. and Lewandowski, J.J., 2014, August. Melt pool characterization for selective laser melting of Ti-6Al-4V pre-alloyed powder. In Solid freeform fabrication symposium (pp. 256-267).
 187. Rangaswamy, P., Griffith, M.L., Prime, M.B., Holden, T.M., Rogge, R.B., Edwards, J.M. and Sebring, R.J., 2005. Residual stresses in LENS® components using neutron diffraction and contour method. Materials Science and Engineering: A, **399**(1-2), pp.72-83. <https://doi.org/10.1016/j.msea.2005.02.019>
 188. Ali, H., Ma, L., Ghadbeigi, H. and Mumtaz, K., 2017. In-situ residual stress reduction, martensitic decomposition and mechanical properties enhancement through high temperature powder bed pre-heating of Selective Laser Melted Ti6Al4V. Materials Science and Engineering: A, **695**, pp.211-220.

- <https://doi.org/10.1016/j.msea.2017.04.033>
189. Pohl, H., Simchi, A., Issa, M. and Dias, H.C., 2001. Thermal stresses in direct metal laser sintering. In 2001 International Solid Freeform Fabrication Symposium. , Texas, US. <http://dx.doi.org/10.26153/tsw/3329>
 190. Sardinha, M., Vicente, C.M., Frutuoso, N., Leite, M., Ribeiro, R. and Reis, L., 2021. Effect of the ironing process on ABS parts produced by FDM. *Material Design & Processing Communications*, **3**(2), p.e151. <https://doi.org/10.1002/mdp2.151>
 191. Onuh, S.O. and Hon, K.K.B., 1998. An experimental investigation into the effect of hatch pattern in stereolithography. *CIRP Annals*, **47**(1), pp.157-160. [https://doi.org/10.1016/S0007-8506\(07\)62807-8](https://doi.org/10.1016/S0007-8506(07)62807-8)
 192. Robinson, J., Ashton, I., Fox, P., Jones, E. and Sutcliffe, C., 2018. Determination of the effect of scan strategy on residual stress in laser powder bed fusion additive manufacturing. *Additive Manufacturing*, **23**, pp.13-24. <https://doi.org/10.1016/j.addma.2018.07.001>
 193. Cheng, B., Shrestha, S. and Chou, K., 2016. Stress and deformation evaluations of scanning strategy effect in selective laser melting. *Additive Manufacturing*, **12**, pp.240-251. <https://doi.org/10.1016/j.addma.2016.05.007>
 194. Kruth, J.P., Froyen, L., Van Vaerenbergh, J., Mercelis, P., Rombouts, M. and Lauwers, B., 2004. Selective laser melting of iron-based powder. *Journal of materials processing technology*, **149**(1-3), pp.616-622. <https://doi.org/10.1016/j.jmatprotec.2003.11.051>
 195. Lu, Y., Wu, S., Gan, Y., Huang, T., Yang, C., Junjie, L. and Lin, J., 2015. Study on the microstructure, mechanical property and residual stress of SLM Inconel-718 alloy manufactured by differing island scanning strategy. *Optics & Laser Technology*, **75**, pp.197-206. <https://doi.org/10.1016/j.optlastec.2015.07.009>
 196. Vrancken, B., Cain, V., Knutsen, R. and Van Humbeeck, J., 2014. Residual stress via the contour method in compact tension specimens produced via selective laser melting. *Scripta Materialia*, **87**, pp.29-32. <https://doi.org/10.1016/j.scriptamat.2014.05.016>
 197. Mukherjee, T., Manvatkar, V., De, A. and DebRoy, T., 2017. Mitigation of thermal distortion during additive manufacturing. *Scripta materialia*, **127**, pp.79-83. <https://doi.org/10.1016/j.scriptamat.2016.09.001>
 198. Dieter, G.E. and D.J. Bacon, *Mechanical metallurgy*. Vol. 3. 1986: McGraw-hill New York. <http://books.google.com/books?id=hlabmB3e8XwC>. ISBN: 881205378
 199. Ramana, P.V., Reddy, G.M., Mohandas, T. and Gupta, A.V.S.S.K.S., 2010. Microstructure and residual stress distribution of similar and dissimilar electron beam welds–Maraging steel to medium alloy medium carbon steel. *Materials & Design*, **31**(2), pp.749-760. <https://doi.org/10.1016/j.matdes.2009.08.007>
 200. Takata, N., Nishida, R., Suzuki, A., Kobashi, M. and Kato, M., 2018. Crystallographic features of microstructure in maraging steel fabricated by selective laser melting. *Metals*, **8**(6), p.440. <https://doi.org/10.3390/met8060440>
 201. Shrestha, S., Starr, T. and Chou, K., 2019. A study of keyhole porosity in selective laser melting: single-track scanning with micro-CT analysis. *Journal of Manufacturing Science and Engineering*, **141**(7). <https://doi.org/10.1115/1.4043622>
 202. Heigel, J.C. and Lane, B.M., 2018. Measurement of the melt pool length during single scan tracks in a commercial laser powder bed fusion process. *Journal of Manufacturing Science and Engineering*, **140**(5). <https://doi.org/10.1115/1.4037571>

Appendix 1

- Data Sheet Ti-6Al-4V

Data sheet



Ti6Al4V ELI-0406 powder for additive manufacturing

Process specification

Powder description	Titanium alloy powder
Layer thickness	30 µm and 60 µm
Laser power	200 W
Additive manufacturing system	AM250

Material description

Ti6Al4V ELI-0406 alloy comprises titanium mass fraction up to 90% alloyed with aluminium up to 6.75% and vanadium up to 4.5%, along with other minor elements. Ti6Al4V grade 23 is otherwise referred to as Extra Low Interstitial (ELI) with regards to the interstitial impurities oxygen, carbon, and nitrogen. It is a higher purity version of the most commonly used titanium alloy Ti6Al4V grade 5. The reduced interstitial elements in grade 23 lead to an increase in both ductility and fracture toughness.

Ti6Al4V ELI-0406 has excellent specific strength (strength to weight ratio) which makes it an ideal choice where weight saving load structures are required. It has good corrosion resistance, it is also biocompatible, so can be used for a range of surgical and dental applications. For medical and dental applications Renishaw supplies Ti DG1 powder, for more information refer to document H-5983-9026.

Material properties

- High specific strength
- High corrosion resistance
- Excellent biocompatibility
- Good osseointegration
- Low thermal expansion
- Low thermal conductivity

Applications

- Medical and dental (Refer to document H-5983-9026)
- Aerospace and defence
- Motor sport
- Jewellery and art
- Maritime applications
- High-end sports equipment

Generic data - wrought material

Density	4.42 g/cm ³
Thermal conductivity	6 W/mK to 8 W/mK
Melting range	1635 °C to 1665 °C
Coefficient of thermal expansion (see note 1)	8 × 10 ⁻⁶ K ⁻¹ to 9 × 10 ⁻⁶ K ⁻¹

Note 1 In the range of 0 °C to 100 °C.

Note 2 Annealed at 850 °C ±10 °C for 2 hr.

Note 3 Tested at ambient temperature to ASTM E8. Machined before testing. Values based on a sample size of 6.

Note 4 Tested to ASTM E384-11, after polishing.

Note 5 Tested to JIS B 0601-2001 (ISO 97), after bead blasting.

Note 6 HIP (hot isostatic pressing).

For further information or support please contact Renishaw or visit www.renishaw.com/additive

Composition of powder

Element	Mass (%)
Titanium	Balance
Aluminium	5.50 to 6.50
Vanadium	3.50 to 4.50
Iron	≤ 0.25
Oxygen	≤ 0.13
Carbon	≤ 0.08
Nitrogen	≤ 0.05
Hydrogen	≤ 0.012
Yttrium	≤ 0.005
Residuals	≤ 0.10 each, ≤ 0.40 total

*ASTM standard composition powder. Renishaw powders are supplied to a tighter specification to minimise batch-to-batch variations. Results quoted in this data sheet are from samples produced using Renishaw's tighter specification powder. Please contact Renishaw for further information about specifications or if you require support in qualifying non-Renishaw powders.

Mechanical properties of additively manufactured components processed in 30 µm layers

	Heat treated (See note 2)		HIP treated (see note 6)	
	Mean	Standard deviation ($\pm 1\sigma$)	Mean	Standard deviation ($\pm 1\sigma$)
Ultimate tensile strength (UTS) (See note 3)				
Horizontal direction (XY)	1089 MPa	7 MPa	1033 MPa	4 MPa
Vertical direction (Z)	1085 MPa	12 MPa	1034 MPa	7 MPa
Yield strength (see note 3)				
Horizontal direction (XY)	1007 MPa	5 MPa	947 MPa	4 MPa
Vertical direction (Z)	985 MPa	23 MPa	923 MPa	21 MPa
Elongation at break (See note 3)				
Horizontal direction (XY)	16%	1%	16%	1%
Vertical direction (Z)	14%	1%	17%	1%
Modulus of elasticity (see note 3)				
Horizontal direction (XY)	129 GPa	7 GPa	127 GPa	3 GPa
Vertical direction (Z)	126 GPa	15 GPa	125 GPa	4 GPa
Hardness (Vickers) (see note 4)				
Horizontal direction (XY)	368 HV0.5	10 HV0.5	352 HV0.5	9 HV0.5
Vertical direction (Z)	372 HV0.5	7 HV0.5	360 HV0.5	7 HV0.5
Surface roughness (R_a) (See note 5)				
Horizontal direction (XY)	4 µm to 6 µm			
Vertical direction (Z)	4 µm to 7 µm			

Density of additively manufactured Ti6Al4V is typically 99.8%, measured optically on a 10 mm x 10 mm x 10 mm sample at 75x magnification.

Renishaw plc
 Stone Business Park
 Brooms Road, Stone
 Staffordshire, ST15 0SH
 United Kingdom

T +44 (0)1785 285000
F +44 (0)1785 285001
E uk@renishaw.com
www.renishaw.com

RENISHAW
 apply innovation™

Mechanical properties of additively manufactured components processed in 60 µm layers

	Heat treated (see note 2)		HIP treated (see note 6)	
	Mean	Standard deviation ($\pm 1\sigma$)	Mean	Standard deviation ($\pm 1\sigma$)
Ultimate tensile strength (UTS) (see note 3)				
Horizontal direction (XY)	1091 MPa	6 MPa	1052 MPa	3 MPa
Vertical direction (Z)	1084 MPa	8 MPa	1058 MPa	9 MPa
Yield strength (see note 3)				
Horizontal direction (XY)	1020 MPa	25 MPa	957 MPa	2 MPa
Vertical direction (Z)	987 MPa	22 MPa	973 MPa	24 MPa
Elongation at break (see note 3)				
Horizontal direction (XY)	16%	1%	16%	1%
Vertical direction (Z)	17%	1%	18%	1%
Modulus of elasticity (see note 3)				
Horizontal direction (XY)	132 GPa	9 GPa	127 GPa	3 GPa
Vertical direction (Z)	128 GPa	7 GPa	131 GPa	6 GPa
Hardness (Vickers) (see note 4)				
Horizontal direction (XY)	363 HV0.5	11 HV0.5	361 HV0.5	7 HV0.5
Vertical direction (Z)	363 HV0.5	13 HV0.5	360 HV0.5	10 HV0.5
Surface roughness (R_a) (see note 5)				
Horizontal direction (XY)	3 µm to 4 µm			
Vertical direction (Z)	5 µm to 7 µm			

Density of additively manufactured Ti6Al4V is typically 99.8%, measured optically on a 10 mm x 10 mm x 10 mm sample at 75x magnification.

For worldwide contact details, please visit www.renishaw.com/contact

RENISHAW HAS MADE CONSIDERABLE EFFORTS TO ENSURE THE CONTENT OF THIS DOCUMENT IS CORRECT AT THE DATE OF PUBLICATION BUT MAKES NO WARRANTIES OR REPRESENTATIONS REGARDING THE CONTENT. RENISHAW EXCLUDES LIABILITY, HOWSOEVER ARISING, FOR ANY INACCURACIES IN THIS DOCUMENT.

© 2017 Renishaw plc. All rights reserved.

Issued: 06.2017



H - 5800 - 1086 - 04 - C

- Data Sheet Inconel 625

Data sheet

RENISHAW 
 apply innovation™

In625-0402 powder for additive manufacturing

Process specification

Powder description	Nickel alloy powder
Layer thickness	30 µm and 60 µm
Laser power	200 W
Additive manufacturing system	AM250

Material description

In625-0402 alloy comprises nickel alloyed with chromium of mass fraction up to 23% and molybdenum up to 10%, along with other minor elements. The addition of niobium, acting with molybdenum, gives the alloy high strength and toughness in the annealed condition.

In625-0402 has a wide range of applications within industry and is particularly suitable for seawater applications and applications where corrosion and oxidation resistance at high temperatures is required. Similar to In718-0405 which is suitable for applications where good tensile, creep, and rupture strength is required.

Material properties

- High creep resistance
- Very high corrosion and oxidation resistance at high temperatures
- High fatigue strength in seawater
- Excellent welding characteristics
- Nonmagnetic

Applications

- Automotive
- Aerospace and defence
- Chemical process industry
- Marine engineering
- Oil and gas industry
- Nuclear
- Seawater heat exchangers

Generic data - wrought material

Density	8.44 g/cm ³
Thermal conductivity	9.2 W/mK to 10.7 W/mK
Melting range	1290 °C to 1350 °C
Coefficient of thermal expansion (see note 1)	12.8 10 ⁻⁶ K ⁻¹

Note 1 In the range of 20 °C to 200 °C.

Note 2 Annealed at 1048 °C for 1 hr followed by furnace cool.

Note 3 Tested at ambient temperature to ASTM E8. Machined prior to testing. Values based on a sample size of 8.

Note 4 Tested to ASTM E384-11, after polishing.

Note 5 Tested to JIS B 0601-2001 (ISO 97). As built after bead blasting.

For further information or support please contact Renishaw or visit www.renishaw.com/additive

Composition of powder

Element	Mass (%)
Nickel	Balance
Chromium	20.00 to 23.00
Molybdenum	8.00 to 10.00
Iron	≤ 5.00
Niobium	3.15 to 4.15
Cobalt	≤ 1.00
Copper	≤ 0.50
Manganese	≤ 0.50
Silicon	≤ 0.50
Aluminium	≤ 0.40
Titanium	≤ 0.40
Carbon	≤ 0.10
Tantalum	≤ 0.05
Nitrogen	≤ 0.02
Oxygen	≤ 0.02
Phosphorus	≤ 0.015
Sulphur	≤ 0.015

*ASTM standard composition powder. Renishaw powders are supplied to a tighter specification to minimise batch-to-batch variations. Results quoted in this data sheet are from samples produced using Renishaw's tighter specification powder. Please contact Renishaw for further information about specifications or if you require support in qualifying non-Renishaw powders.

Mechanical properties of additively manufactured components built using 30 µm layer thickness

	As built		Heat treated (see note 2)	
	Mean	Standard deviation ($\pm 1\sigma$)	Mean	Standard deviation ($\pm 1\sigma$)
Ultimate Tensile strength (UTS) (See note 3)				
Horizontal direction (XY)	1055 MPa	3 MPa	1020 MPa	1 MPa
Vertical direction (Z)	964 MPa	2 MPa	955 MPa	2 MPa
Yield strength (see note 3)				
Horizontal direction (XY)	767 MPa	9 MPa	633 MPa	1 MPa
Vertical direction (Z)	676 MPa	7 MPa	598 MPa	2 MPa
Elongation at break (see note 3)				
Horizontal direction (XY)	34%	1%	39%	1%
Vertical direction (Z)	42%	1%	43%	1%
Modulus of elasticity (see note 3)				
Horizontal direction (XY)	205 GPa	10 GPa	206 GPa	3 GPa
Vertical direction (Z)	186 GPa	11 GPa	200 GPa	2 GPa
Hardness (Vickers) (See note 4)				
Horizontal direction (XY)	331 HV0.5	8 HV0.5	251 HV0.5	13 HV0.5
Vertical direction (Z)	332 HV0.5	8 HV0.5	254 HV0.5	16 HV0.5
Surface roughness (R_a) (See note 5)				
Horizontal direction (XY)	2 µm to 3 µm			
Vertical direction (Z)	6 µm to 7 µm			

Density of additively manufactured In625 is typically 99.8%, measured optically on a 10 mm x 10 mm x 10 mm sample at 75x magnification.

Mechanical properties of additively manufactured components built using 60 µm layer thickness

	As built		Heat treated (see note 2)	
	Mean	Standard deviation ($\pm 1\sigma$)	Mean	Standard deviation ($\pm 1\sigma$)
Ultimate Tensile strength (UTS) (See note 3)				
Horizontal direction (XY)	922 MPa	9 MPa	1005 MPa	6 MPa
Vertical direction (Z)	770 MPa	56 MPa	985 MPa	10 MPa
Yield strength (see note 3)				
Horizontal direction (XY)	667 MPa	11 MPa	600 MPa	4 MPa
Vertical direction (Z)	536 MPa	34 MPa	583 MPa	2 MPa
Elongation at break (see note 3)				
Horizontal direction (XY)	18%	2%	31%	2 %
Vertical direction (Z)	11%	4%	32%	4 %
Modulus of elasticity (see note 3)				
Horizontal direction (XY)	175 GPa	16 GPa	208 GPa	4 GPa
Vertical direction (Z)	176 GPa	9 GPa	209 GPa	6 GPa
Hardness (Vickers) (See note 4)				
Horizontal direction (XY)	302 HV0.5	13 HV0.5	279 HV0.5	7 HV0.5
Vertical direction (Z)	308 HV0.5	6 HV0.5	290 HV0.5	8 HV0.5
Surface roughness (R_a) (See note 5)				
Horizontal direction (XY)	1.5 µm to 2 µm			
Vertical direction (Z)	6 µm to 7 µm			

Density of additively manufactured In625 is typically 99.8%, measured optically on a 10 mm x 10 mm x 10 mm sample at 75x magnification.

For worldwide contact details, please visit www.renishaw.com/contact

RENISHAW HAS MADE CONSIDERABLE EFFORTS TO ENSURE THE CONTENT OF THIS DOCUMENT IS CORRECT AT THE DATE OF PUBLICATION BUT MAKES NO WARRANTIES OR REPRESENTATIONS REGARDING THE CONTENT. RENISHAW EXCLUDES LIABILITY, HOWSOEVER ARISING, FOR ANY INACCURACIES IN THIS DOCUMENT.

© 2017 Renishaw plc. All rights reserved.

Issued: 09.2017



H - 5800 - 1105 - 02 - B

- Data Sheet Maraging M300

Data sheet

RENISHAW 
 apply innovation™

Maraging steel M300 powder for additive manufacturing

Process specification

Powder description	Maraging steel
Layer thickness	40 µm
Laser power	200 W
Additive manufacturing system	AM250 and AM 400

Material description

Maraging steels form a class of iron alloys. This group of materials has a martensitic crystal structure and is strengthened via aging at approximately 500 °C (900 °F), hence the name 'maraging'. These ultra-low carbon alloys have very high strength and hardness properties derived from precipitation of intermetallic compounds rather than carbon content.

Nickel is the main alloying element, with cobalt, molybdenum, and titanium as secondary intermetallic alloying metals.

Maraging steel M300 is also commonly referred to as 1.2709.

Material properties

- High strength
- High hardness
- High fatigue strength
- Good machinability

Applications

- Tooling inserts
- Mould and die
- High strength components

Generic data - wrought material

Density	8.1 g/cm ³
Thermal conductivity	14.2 W/mK at 20 °C, 21.0 W/mK at 600 °C, 28.6 W/mK at 1300 °C
Melting point	1413 °C
Coefficient of thermal expansion	10.3 10 ⁻⁶ K ⁻¹

Note 1 Age hardening conditions: 1. Heat up to 500 °C ±10 °C over the course of 60 minutes to 90 minutes, hold temperature for 6 hours; 2. Furnace cool to 300 °C; 3. Air cool.

Note 2 Tested at ambient temperature to ASTM E8. Machined prior to testing. Values based on a sample size of 6.

Note 3 Tested to ASTM E384-11, after polishing.

Note 4 Tested to JIS B 0601-2001 (ISO 97). As built after bead blasting.

For further information or support please contact Renishaw or visit www.renishaw.com/additive

Renishaw plc
Stone Business Park
Brooms Road, Stone
Staffordshire, ST15 0SH
United Kingdom

T +44 (0)1785 285000
F +44 (0)1785 285001
E uk@renishaw.com
www.renishaw.com

RENISHAW 
apply innovation™

Composition of powder

Element	Mass / max. %
Iron	Balance
Nickel	17.00 to 19.00
Cobalt	7.00 to 10.00
Molybdenum	4.50 to 5.20
Titanium	0.30-1.20
Silicon	≤ 0.10
Manganese	≤ 0.15
Carbon	≤ 0.03
Phosphorous	≤ 0.01
Sulphur	≤ 0.01

*ASTM standard composition powder. Renishaw powders are supplied to a tighter specification to minimise batch-to-batch variations. Results quoted in this data sheet are from samples produced using Renishaw's tighter specification powder. Please contact Renishaw for further information about specifications or if you require support in qualifying non-Renishaw powders.

Mechanical properties of additively manufactured parts

	As built	Standard deviation ($\pm 1\sigma$)	Age hardened (See note 1)	Standard deviation ($\pm 1\sigma$)
Tensile strength (UTS) (See note 2)				
Horizontal direction (XY)	1141 MPa	7 MPa	1806 MPa	6 MPa
Vertical direction (Z)	1122 MPa	14 MPa	1794 MPa	9 MPa
Yield strength (see note 2)				
Horizontal direction (XY)	1016 MPa	8 MPa	1753 MPa	20 MPa
Vertical direction (Z)	999 MPa	20 MPa	1730 MPa	20 MPa
Elongation at break (see note 2)				
Horizontal direction (XY)	7.3%	1%	5.5%	1%
Vertical direction (Z)	7.5%	1%	7%	1%
Modulus of elasticity (see note 2)				
Horizontal direction (XY)	160 GPa	5 GPa	170 GPa	8 GPa
Vertical direction (Z)	162 GPa	10 GPa	175 GPa	11 GPa
Hardness (Vickers) (see note 3)				
Horizontal direction (XY)	363 HV0.5	5 HV0.5	542 HV0.5	7 HV0.5
Vertical direction (Z)	355 HV0.5	7 HV0.5	543 HV0.5	8 HV0.5
Surface roughness (R_a) (See note 4)				
Horizontal direction (XY)	3.5 μm to 5 μm			
Vertical direction (Z)	4 μm to 6 μm			

Density of additively manufactured maraging steel M300 is typically 99.8%, measured optically on a 10 mm x 10 mm x 10 mm sample at 75x magnification.

For worldwide contact details, visit www.renishaw.com/contact

RENISHAW HAS MADE CONSIDERABLE EFFORTS TO ENSURE THE CONTENT OF THIS DOCUMENT IS CORRECT AT THE DATE OF PUBLICATION BUT MAKES NO WARRANTIES OR REPRESENTATIONS REGARDING THE CONTENT. RENISHAW EXCLUDES LIABILITY, HOWSOEVER ARISING, FOR ANY INACCURACIES IN THIS DOCUMENT.

© 2017 Renishaw plc. All rights reserved.

Issued: 09.2017



H - 5800 - 3429 - 03 - A

- Data Sheet Inconel 718

Data sheet

RENISHAW
 apply innovation™

In718-0405 powder for additive manufacturing

Process specification

Powder description	Nickel alloy powder
Layer thickness	30 µm and 60 µm
Laser power	200 W
Additive manufacturing system	AM250

Material description

In718-0405 alloy comprises nickel mass fraction up to 55% alloyed with iron up to 21% and chromium up to 21%, along with other minor elements. Properties include high strength, excellent corrosion resistance and a working temperature range between -250 °C and 650 °C (-418 °F to 1200 °F). It is also age-hardenable.

In718-0405 has a wide range of applications within industry and is particularly suitable for applications where good tensile, creep, and rupture strength is required. Similar to In625-0402 which is suitable for applications where corrosion and oxidation resistance at high temperatures is required. Its excellent welding characteristics and resistance to cracking makes it an ideal material for additive manufacturing.

Material properties

- Retains strength up to 650 °C
- High creep resistance
- High corrosion resistance
- Solidification properties suit additive manufacture

Applications

- Aerospace and defence
- Gas turbine blades
- Exhaust manifolds
- Rocket motors
- Heat exchangers
- Nuclear

Generic data - wrought material

Density	8.19 g/cm ³
Thermal conductivity	6 W/mK to 12 W/mK
Melting range	1260 °C to 1336 °C
Coefficient of thermal expansion (see note 1)	12 µm/mK to 16 µm/mK

Note 1 In the range of 25 °C to 760 °C.

Note 2 Heat treated conditions: 1. Solution treated at 980 °C ± 10 °C for 1 hr 2. Aged at 720 °C ± 10 °C for 8 hr, and further aged at 620 °C ± 10 °C for 8 hr.

Note 3 Hot isostatically pressed.

Note 4 Tested at ambient temperature to ASTM E8. Machined before testing. Values based on a sample size of 6.

Note 5 Tested to ASTM E384-11, after polishing.

Note 6 Tested to JIS B 0601-2001 (ISO 97), after bead blasting.

For further information or support please contact Renishaw or visit www.renishaw.com/additive

Renishaw plc
Stone Business Park
Brooms Road, Stone
Staffordshire, ST15 0SH
United Kingdom

T +44 (0)1785 285000
F +44 (0)1785 285001
E uk@renishaw.com
www.renishaw.com

RENISHAW 
apply innovation™

Composition of powder

Element	Mass (%)
Nickel	50.00 to 55.00
Chromium	17.00 to 21.00
Iron	Balance
Niobium and Tantalum	4.75 to 5.5
Molybdenum	2.80 to 3.30
Titanium	0.65 to 1.15
Cobalt	≤ 1.00
Aluminium	0.20 to 0.80
Manganese	≤ 0.35
Silicon	≤ 0.35
Copper	≤ 0.30
Carbon	0.02 to 0.05
Nitrogen	≤ 0.03
Oxygen	≤ 0.03
Phosphorus	≤ 0.015
Sulphur	≤ 0.015
Calcium	≤ 0.01
Magnesium	≤ 0.01
Selenium	≤ 0.005
Boron	≤ 0.005

*ASTM standard composition powder. Renishaw powders are supplied to a tighter specification to minimise batch-to-batch variations. Results quoted in this data sheet are from samples produced using Renishaw's tighter specification powder. Please contact Renishaw for further information about specifications or if you require support in qualifying non-Renishaw powders.

Mechanical properties of additively manufactured components using 30 µm layers

	As built		Solution treated and aged (See note 2)		HIP treated (See note 3)	
	Mean	Standard deviation ($\pm 1\sigma$)	Mean	Standard deviation ($\pm 1\sigma$)	Mean	Standard deviation ($\pm 1\sigma$)
Ultimate tensile strength (UTS) (See note 4)						
Horizontal direction (XY)	1040 MPa	7 MPa	1467 MPa	6 MPa	1379 MPa	3 MPa
Vertical direction (Z)	971 MPa	3 MPa	1391 MPa	9 MPa	1346 MPa	5 MPa
Yield strength (see note 4)						
Horizontal direction (XY)	758 MPa	4 MPa	1259 MPa	5 MPa	1088 MPa	26 MPa
Vertical direction (Z)	636 MPa	19 MPa	1202 MPa	15 MPa	1052 MPa	4 MPa
Elongation at break (see note 4)						
Horizontal direction (XY)	30%	1%	17%	1%	25%	1%
Vertical direction (Z)	36%	1%	17%	1%	24%	1%
Modulus of elasticity (see note 4)						
Horizontal direction (XY)	186 GPa	5 GPa	195 GPa	13 GPa	207 GPa	4 GPa
Vertical direction (Z)	158 GPa	18 GPa	186 GPa	15 GPa	201 GPa	3 GPa
Hardness (Vickers) (see note 5)						
Horizontal direction (XY)	277 HV0.5	9 HV0.5	418 HV0.5	9 HV0.5	456 HV0.5	11 HV0.5
Vertical direction (Z)	302 HV0.5	8 HV0.5	488 HV0.5	11 HV0.5	463 HV0.5	7 HV0.5
Surface roughness (R_a) (See note 6)						
Horizontal direction (XY)	1.28 µm to 1.36 µm					
Vertical direction (Z)	1.72 µm to 1.96 µm					

Density of additively manufactured In718 is typically 99.8%, measured optically on a 10 mm × 10 mm × 10 mm sample at 75x magnification.

Mechanical properties of additively manufactured components using 60 µm layers

	As built		Solution treated and aged (See note 2)		HIP treated (See note 3)	
	Mean	Standard deviation ($\pm 1\sigma$)	Mean	Standard deviation ($\pm 1\sigma$)	Mean	Standard deviation ($\pm 1\sigma$)
Ultimate tensile strength (UTS) (See note 4)						
Horizontal direction (XY)	1057 MPa	11 MPa	1504 MPa	3 MPa	1289 MPa	4 MPa
Vertical direction (Z)	943 MPa	38 MPa	1439 MPa	11 MPa	1228 MPa	24 MPa
Yield strength (see note 4)						
Horizontal direction (XY)	753 MPa	8 MPa	1306 MPa	10 MPa	958 MPa	8 MPa
Vertical direction (Z)	639 MPa	13 MPa	1231 MPa	10 MPa	929 MPa	10 MPa
Elongation at break (see note 4)						
Horizontal direction (XY)	25%	3%	16%	2%	23%	2 %
Vertical direction (Z)	19%	8%	16%	2%	17%	4%
Modulus of elasticity (see note 4)						
Horizontal direction (XY)	203 GPa	10 GPa	202 GPa	4 GPa	219 GPa	6 GPa
Vertical direction (Z)	191 GPa	9 GPa	198 GPa	11 GPa	214 GPa	7 GPa
Hardness (Vickers) (see note 5)						
Horizontal direction (XY)	275 HV0.5	14 HV0.5	465 HV0.5	28 HV0.5	408 HV0.5	11 HV0.5
Vertical direction (Z)	295 HV0.5	11 HV0.5	467 HV0.5	20 HV0.5	418 HV0.5	16 HV0.5
Surface roughness (R_a) (See note 6)						
Horizontal direction (XY)	1.14 µm to 1.70 µm					
Vertical direction (Z)	2.36 µm to 3.0 µm					

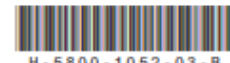
Density of additively manufactured In718 is typically 99.8%, measured optically on a 10 mm x 10 mm x 10 mm sample at 75x magnification.

For worldwide contact details, please visit www.renishaw.com/contact

RENISHAW HAS MADE CONSIDERABLE EFFORTS TO ENSURE THE CONTENT OF THIS DOCUMENT IS CORRECT AT THE DATE OF PUBLICATION BUT MAKES NO WARRANTIES OR REPRESENTATIONS REGARDING THE CONTENT. RENISHAW EXCLUDES LIABILITY, HOWSOEVER ARISING, FOR ANY INACCURACIES IN THIS DOCUMENT.

© 2017 Renishaw plc. All rights reserved.

Issued: 07.2017



H - 5 8 0 0 - 1 0 5 2 - 0 3 - B

Appendix 2

Sub-assembly	Part Name	Manufacturer	Manu. Part No.	Supplier	Part	Cost	Qty.	Line Cost
Chassis	FTD Base plate	Proto Labs	N/A	ProtoLabs	FTD base plate	£1,572	1	£1,572
Load Cell	BD-MCL Bi-directional miniature load cell (PMC, UK)	PMC, UK	BD-MCL 0813	PMC	bi-directional Load Cell	£996.56	8	£7,972.48
Data Logger	INET-100HC	InstruNet	90303310	OMEGA	A/D BOX W/SCREW TRM 15MA/10KPF	£1,090.00	3	£3,270.00
USB Controllers	INET-240	InstruNet	90309085	OMEGA	INET CONTROLLER, USB 2.0	£880.00	1	£880.00
Cable Box	Enclosure	Hammond	15988BK	Farnell	HAMMOND 15988BK Enclosure,	£7.66	1	£7.66
Overflow Interface	20 Core Cable	Pro Power	PP000266	Farnell	PRO POWER PP000266 Multicore Unscreened Cable, Black, 20 Core, 0.22 mm ² , 82.021 Ft, 25 m	£40.02	1	£40.02
Overflow Interface	Cable Gland	TE CONNECTIVITY / AMP	1478769-6	Farnell	TE CONNECTIVITY / AMP 32MM BLK Cable Gland, 18 mm, 25 mm, M32, Nylon 6 (Polyamide 6), Black	£1.95	1	£1.95
Overflow Interface	Signal Plug	Lemo	FGG.2K.319-CLAC80Z	Lemo	Circular Push Pull Connectors STRAIGHT PLUG MALE	£38.04	2	£76.08
FTD Interface	Signal Socket	Lemo	EGG.2K.319-CLL	Lemo	Circular Push Pull Connectors FIXED RECEPTACLE NUT FIXING	£90.95	2	£181.90
FTD Interface	Signal Socket	Lemo	GMA.2B.080.DN	Lemo	Circular Connector Clamp	£1.59	1	£1.59
FTD Interface	Signal Socket	Lemo	GMA.2B.080.DS	Lemo	Circular Connector Clamp	£1.59	1	£1.59
FTD Interface	Thermo Socket	Lemo	EGG.0K.302-CLL	Lemo	Circular Push Pull Connectors 2P STRAIGHT FEMALE	£9.42	1	£9.42
Overflow Interface	Thermo Plug	Lemo	FGG.0K.302-CLAC25Z	Lemo	2 Position Circular Connector Plug, Male	£11.61	1	£11.61
Overflow Interface	Thermo Plug Strain Relief	Lemo	GMA.0B.025.DN	Lemo	Circular Connector Clamp	£1.00	1	£1.00
Overflow Interface	Thermo Plug Strain Relief	Lemo	GMA.0B.025.DS	Lemo	Circular Connector Clamp	£1.00	1	£1.00
Overflow Interface	25 way D-sub plug	MH Connectors	765-9508	RS	25 Way D-Sub Plug Connector Kit	£4.72	2	£9.44
Overflow Interface	Thermocouple cable	RS Pro	827-5716	RS	Thermocouple & Extension Wire Typ K 2 Core PFA Teflon Sheath 10m	£23.09	1	£23.09
Overflow Interface	KF40 Stub	Scanwel	KFSU40AL	Scanwel	Flanges	£17.00	1	£17.00
Total Cost								£13,957.83